Laboratory Studies of Halogen-Containing and Organic Species of Atmospheric Importance

A thesis submitted in partial fulfillment of the requirements
of the degree of Doctor of Philosophy

by

Kirsten Wagner

Linacre College, Oxford

Trinity Term, 2003

"Even a blind dog can find a bone every so often."

Alexi Sayle

"Wagner a de beaux moments, mais de mauvais quart d'heures."

Translation: "Wagner has lovely moments but awful quarters of an hour."

Gioacchino Rossini (1792 – 1868)

Acknowledgements

There are so many people that I would like to thank for their support during my PhD. First, Richard, for giving me the opportunity to come to Oxford in the first place; Carlos, for his patience and ideas; and Pete, for his rubbish teatime jokes and help with the mass spec at the beginning of the project. Next, come the individuals who set me on the right track when I first arrived: Ali, Queen of the *double entendre*, thanks for your guidance with the IO work and for making the first few months so much fun; Dina, for always being there to answer my questions and to fiddle (oo-er) with the I lamp; Eimear, for showing me how to use the 0-50 flow tube and how to annoy your neighbours at 3 o'clock in the morning (I'm glad I didn't live next door to you); and Mark, for lifting the heavy stuff, having hairy arms and doing on-the-floor-dancing. Thanks also to the Part IIs in my first year for the top nights out and lengthy tea break chats, particularly Mike, the whistling old fool, I'm not sure I will ever quite forgive you for what you did in my wardrobe; Maz, my one-legged dance partner (you're soooo clever); and Chris — it really was all good stuff. Other group members to thank are Caroline, for helping me survive the meat-filled, dog-do fest that was Obernai 2001; Craigious, my OCAK dancing Queen, for gratuitous use of the phrase 'ohmigod!!!' (one day we will look back at our time spent with that mass spec and laugh); Stew 'Bum' Vaughan, King of Cheese and freaky thumbs, for the lengthy Cl discussions; Frinster, for always sneezing twice, answering back to RPW and spilling your food down your front at lunch; Christian, for trying to teach me German filth; and Alex, for always paying attention and filling my last months in the lab with dodgy rock music. I would also like to thank Dan from the Hancock group for the loan of the pump, for coming to find me when something on my side of the lab exploded, and for the good (bad) luck charm. An extra special thanks goes to several other members of the PTCL, namely, Pete, Paul, Sarah and Gerald in 0-43; John and Neville in electronics; Roger, Charlie and Les in workshops; Merv and John in stores; and Dave in IT. Without your help, the job would have been extremely difficult, if not impossible.

A big thank you goes to the staff of Linacre College: always friendly and accommodating, you helped me when I needed you most. Thanks also to all my Linacre pals, Markee, Sarah, Schmoo, Hector, Simon, Dave and the rest (you know who you are), for making me laugh and showing me a good time. I must mention Ellie – you know I wouldn't have survived that year at CC without you. And of course, Tom, thank you for your kindness and patience, and for putting up with my considerable whinging.

Finally, I would like to thank my mum for being there every single day of the last 27½ years, and my sister, Janine, for her support too. I couldn't have done it without you both.

Abstract

Laboratory Studies of Halogen-Containing and Organic Species of Atmospheric Importance

by Kirsten Wagner

Submitted for the degree of Doctor of Philosophy

Linacre College, Oxford — Trinity Term, 2003

This thesis describes laboratory studies of the kinetics of some reactions of atmospheric significance. The species of interest were Cl atoms, IO radicals and several organic compounds. In particular, the chemistry of acetone and the acetonylperoxy radical was investigated. These species are of importance in the troposphere and the stratosphere, where they may influence the concentrations of HO_x, NO_x and O_3.

The experiments were performed using low-pressure discharge–flow tubes coupled to a variety of detection techniques, including conventional methods such as resonance fluorescence (RF) and electron-impact mass spectrometry (EIMS). However, much of the thesis is concerned with the development of techniques that offer a greater sensitivity and selectivity, namely, laser-induced fluorescence (LIF) and chemical-ionization mass spectrometry (CIMS).

The reactions of Cl atoms with acetone and butanone were monitored with Cl RF. The study of the former reaction was extended in order to obtain information about the chemistry of the acetonylperoxy radical. IO was observed with LIF. This work involved the first reported coupling of IO LIF to a discharge-flow tube. The system was shown to be a suitable method by which to study reactions of IO. The results of these investigations demonstrate that reaction with Cl and IO may be an important sink for several organic compounds in the marine boundary layer.

The design, construction and commissioning of the EIMS system is described. The apparatus was used in an attempt to follow the self-reaction of the acetonylperoxy radical by monitoring the products. The complications that arose during the study illustrated the need for a more versatile form of MS. It was decided to convert the instrument to a CIMS system that would allow direct observation of the peroxy radical. The construction of two ion sources, one employing a cartridge of polonium-210 and the other a simple discharge, as well as an electrostatic ion guide, is described. The discharge source was shown to be better suited to the low-pressure conditions.

Contents

Chapter 2 Experimental techniques

Chapter 3 Laser-induced fluorescence of IO and the kinetics of some reactions of the radical

Chapter 1 Atmospheric chemistry

1.1 Introduction

The laboratory experiments described in this thesis are designed to investigate reactions of species that are potentially important in the atmosphere. Such studies, combined with outdoor measurements and modelling work, make up the field of atmospheric chemistry research. The aims of this research are to better understand the chemistry of the natural atmosphere and to assess the impact of Man's activities upon it. Stratospheric ozone depletion, global climate change, acid rain and photochemical smog are terms encountered in everyday life for chemical and physical phenomena in the atmosphere that are a consequence of Man-made emissions. These processes have either a potential or realized ability to degrade the environment and reduce human well-being. Thus it is vitally important that we develop our knowledge of atmospheric processes.

This thesis is concerned with the reactions of several halogen-containing and organic compounds. Such chemistry is of importance in the lower parts of the atmosphere: the troposphere and the stratosphere. The species were monitored in the laboratory with a variety of techniques, including conventional methods such as resonance fluorescence and electron-impact mass spectrometry. However, much of the thesis describes the development of less well-established detection systems, namely chemical-ionization mass spectrometry to monitor organic compounds, and laser-induced fluorescence to observe the IO radical.

This first chapter aims to discuss the chemistry of the species investigated. Following an introduction to the general features of the atmosphere, the chemistry of the stratosphere is considered and then the main processes in the troposphere are described. Ozone will be shown to be an extremely important constituent in both these regions. The chemistry of the species of interest is then discussed. The chapter ends by introducing the aims of the research undertaken.

1.2 Structure and composition of the atmosphere

The atmosphere is the gaseous envelope that surrounds the Earth. The term 'atmosphere' is derived from the Greek words 'atmos' and 'sphaira', which mean 'vapour' and 'ball', respectively. The Earth's atmosphere is apparently unique in that it supports life. This life also partly determines the composition of the atmosphere. Interactions with the oceans and land also control the composition. The atmosphere is 78.1% N_2, 20.9% O_2 and 0.9% Ar (Wayne, 2000). The amount of water vapour is highly variable, ranging from up to 4% in the tropics to less than 1% in polar and desert regions. A small fraction of the atmosphere consists of a huge diversity of trace gases. Despite their low abundance, trace species play crucial roles in defining many atmospheric characteristics. Some of these processes are discussed in the following sections.

The total mass of the atmosphere is 5.3×10^8 kg (Wayne, 2000). Owing to gravitational forces, most of this mass is near the Earth's surface. Indeed, half of the atmospheric mass lies below about 5.5 km, and 99% is found below 30 km. The pressure profile of an atmosphere is described by the hydrostatic equation:

$$p = p_0 \exp\left\{-\int_0^z \frac{\mathrm{d}z}{(kT/mg)}\right\} \qquad \text{(E1.1)}$$

where p is the pressure at altitude z, p_0 is the pressure at the planet's surface, k is the Boltzmann constant, T is the temperature, m is the average mass of air and g is the acceleration due to gravity.

The temperature profile of the Earth's atmosphere is depicted in figure 1.1. It can be seen that in the lowest region, the temperature decreases with increasing altitude. The radiative heating of the atmosphere reduces as the distance from the surface increases, so that there would be a drop in temperature as altitude increases from this effect alone. However, there is a second factor, of thermodynamic origin, that must also be considered. As the pressure of the atmosphere reduces with increasing altitude, a rising air parcel will expand, perform work on its surroundings, and therefore, cool down. The temperature

Figure 1.1. The temperature profile of the Earth's atmosphere.

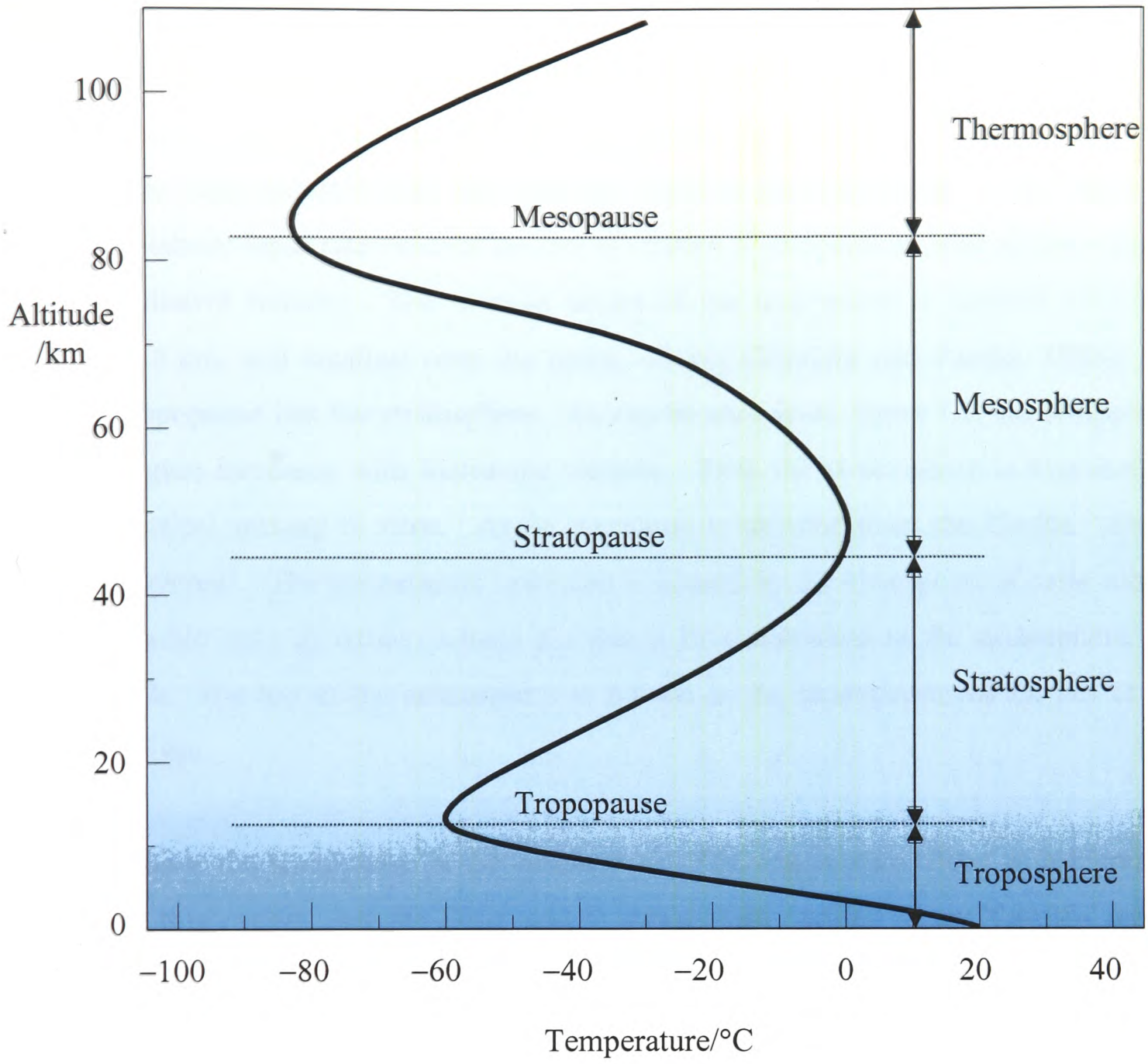

decrease with altitude resulting from the expansion of a dry air parcel is described by the dry adiabatic lapse rate, Γ_d (Wayne, 2000):

$$\Gamma_d = -\frac{dT}{dz} = \frac{g}{c_p} \qquad \text{(E1.2)}$$

where c_p is the specific heat capacity at constant pressure. For Earth, $\Gamma_d = 9.8\ \text{K km}^{-1}$. In the lower atmosphere, the predicted temperature resulting from radiative heating drops off more rapidly than Γ_d. If, in reality, gas parcels possessed a temperature lower than that predicted by Γ_d, they would tend to sink, so that convection currents will tend to maintain the adiabatic lapse rate. These convection processes mean that the lower atmosphere is

turbulent. It is from this characteristic that this region derives its name — the troposphere. 'Tropos' is Greek for 'turning'.

The troposphere can be divided into the planetary (continental or marine) boundary layer, and the free troposphere. The former extends from the Earth's surface up to about 1 km. The latter extends from the boundary layer to the tropopause — the region where the adiabatic lapse rate exceeds the rate of change of temperature with altitude predicted from radiative transfer. The average height of the tropopause is greatest over the equator, ~18 km, and smallest over the poles, ~8 km (Seinfeld and Pandis, 1998). Above the tropopause lies the stratosphere. As can be seen from figure 1.1, the temperature of this region increases with increasing altitude. Thus the stratosphere is extremely stable, as vertical mixing is slow. Again the name is derived from the Greek: 'stratus' means 'layered'. The temperature inversion is caused by the absorption of solar ultraviolet and visible light by ozone, a trace gas that is most abundant in the stratosphere: see section 1.3. The top of the stratosphere is known as the stratopause, which lies at about 45 – 55 km.

Above the stratopause is the mesosphere. The temperature drops with increasing height in this region, and the lapse rate is subadiabatic, which means that the mesosphere is stable with respect to convective motions (Wayne, 2000). The coldest point in the atmosphere is the mesopause. The thermosphere and the exosphere make up the outer parts of the atmosphere. The upper mesosphere and lower thermosphere contain the ionosphere, so-called because the absorption of radiation may result in significant ion production. The exosphere, which lies above ~500 km in altitude, is the region from which gases with sufficient energy can escape into space.

1.3 Stratospheric ozone

Most of the ozone in the atmosphere is found in a layer, about 20 km thick and centred on an altitude of about 25 – 30 km, within the stratosphere. Mixing ratios peak at ~10 ppm in this region (Seinfeld and Pandis, 1998). Despite its low abundance, ozone is the most important trace gas in the atmosphere. It absorbs virtually all of the solar ultraviolet radiation in the range wavelength 240 – 290 nm. Such radiation is lethal to unicellular

organisms, and the surface cells of higher animals and plants, as it can damage macromolecules such as proteins and DNA. As previously stated, the absorption of radiation by ozone is also responsible for the temperature inversion in the stratosphere.

A mechanism for ozone production and destruction in the stratosphere was first proposed by Chapman in 1930 (Finlayson-Pitts and Pitts Jr., 2000):

$$O_2 + h\nu \rightarrow 2O \qquad \text{(R1.1)}$$

$$O + O_2 + M \rightarrow O_3 + M \qquad \text{(R1.2)}$$

$$O_3 + h\nu \rightarrow O + O_2 \qquad \text{(R1.3)}$$

$$O + O_3 \rightarrow 2O_2. \qquad \text{(R1.4)}$$

However, in the 1960s, model studies demonstrated that the Chapman mechanism predicted $[O_3]$ that were much greater than the observed levels. Catalytic loss processes involving HO_x[a] had been proposed as early as 1950, but the real breakthrough in understanding came in the 1970s when Crutzen and Johnston elucidated the role of nitrogen oxides in the depletion of stratospheric ozone. Shortly after, Cicerone, Molina and Rowland suggested that chlorine chemistry had a similar effect. The mechanism of ozone destruction takes the form of a catalytic cycle:

$$X + O_3 \rightarrow XO + O_2 \qquad \text{(R1.5)}$$

$$XO + O \rightarrow X + O_2 \qquad \text{(R1.6)}$$

$$\text{Net: } O + O_3 \rightarrow 2O_2 \qquad \text{(R1.4)}$$

where X is H, OH, NO, Cl and Br (Seinfeld and Pandis, 1998).

It was thought that the factors controlling the abundance of stratospheric ozone were well understood. Thus the atmospheric science community was shocked when, in 1985, a team of scientists from the British Antarctic Survey reported a massive decrease in the total ozone column over their station at Halley Bay (Seinfeld and Pandis, 1998). The losses had been occurring since about 1977 and were confined to the polar spring (September to November). Analysis of satellite data soon revealed that the ozone

[a] The term 'HO_x' represents the oxides of hydrogen where $x = 0$, 1 or 2.

depletion extended over the entire Antarctic continent. The October mean total ozone column was shown to have dropped from more than 300 Dobson units (DU) in the mid-1970s to about 200 DU in 1985. Ozone vertical profiles obtained from balloon measurements showed that the depletion was primarily located at altitudes between 10 and 20 km.

Intensive research in the late '80s and the '90s revealed the cause of the Antarctic ozone hole. The mechanism was found to be a complex combination of homogeneous and heterogeneous processes involving chlorine- and nitrogen-containing compounds, which occur under specific meteorological conditions. Only a brief discussion is required for the purpose of this thesis. As the air cools during the Antarctic winter, it descends and develops a westerly direction (Seinfeld and Pandis, 1998). The resulting polar vortex has an extremely cold core (as low as –90°C), which allows polar stratospheric clouds (PSCs) to form. PSCs consist of various combinations of H_2O, HNO_3 and H_2SO_4 in either liquid or solid form. These clouds provide surfaces on which heterogeneous processes can take place. In particular, reactions that liberate photolytically active forms of chlorine from reservoir compounds are possible. (Note that such reactions are very slow in the gas phase). For example, following the adsorption of HCl by PSCs, reaction with $ClONO_2$ results in the release of gaseous Cl_2:

$$HCl(s) + ClONO_2 \rightarrow Cl_2 + HNO_3(s). \qquad \text{(R1.7)}$$

When the sun rises in the polar spring, the molecular chlorine that has accumulated during the winter is photolysed and the resulting Cl atoms destroy ozone:

$$Cl_2 + h\nu \rightarrow 2Cl \qquad \text{(R1.8)}$$

$$2(Cl + O_3 \rightarrow ClO + O_2). \qquad \text{(R1.9)}$$

However, it is not possible for a catalytic cycle of the kind described earlier by reactions 1.5 and 1.6 to occur because of the low abundance of O atoms in the polar stratosphere in the spring. Instead, the massive losses of ozone are the result of a catalytic process involving the self-reaction of ClO:

$$ClO + ClO + M \rightarrow ClOOCl + M \quad \text{(R1.10)}$$

$$ClOOCl + h\nu \rightarrow Cl + ClOO \quad \text{(R1.11)}$$

$$ClOO + M \rightarrow Cl + O_2 + M \quad \text{(R1.12)}$$

$$2(Cl + O_3 \rightarrow ClO + O_2) \quad \text{(R1.9)}$$

$$\text{Net: } 2O_3 \rightarrow 3O_2. \quad \text{(R1.13)}$$

Note that the ClOOCl dimer is only stable at low temperatures, such as those prevailing in the Antarctic lower stratosphere (Wayne, 2000). Note also that ozone depletion *via* the ClO cycle is facilitated by processes involving nitrogen-containing compounds. A major sink of ClO in the atmosphere is reaction with NO_2 to form $ClONO_2$. However, the formation of PSCs results in the removal of NO_x[b] (in the form of HNO_3) from the stratosphere. Reaction 1.7 also sequesters nitrogen as the HNO_3 product is retained in the PSC. Thus, more chlorine remains in its ozone-destroying form. Finally, it should be stated that following the break up of the polar vortex in November, the ozone abundance returns to normal levels.

In recent years, the Antarctic ozone hole has grown larger and total ozone columns of less than 100 DU are commonly observed (Wayne, 2000). The 'Montreal Protocol on Substances that Deplete the Ozone Layer', which came into force in 1989 and was amended several times during the '90s, aims to control the release of ozone-destroying substances to the atmosphere. However, current models show that even if the conditions of the protocol are adhered to, ozone depletion in the Antarctic stratosphere will continue to be a problem well into the second half of the 21st century.

1.4 Tropospheric chemistry

This thesis is mostly concerned with processes that occur in the troposphere. The daytime chemistry of this region is dominated by reactions of the hydroxyl radical, whereas at night the nitrate radical is the major oxidant (Wayne, 2000). It is the chemistry of the daytime that is of interest in this work.

---

[b] The term 'NO_x' represents NO and NO_2. Note that 'NO_y' is used to refer to NO_x and all other reactive nitrogen-containing species, e.g. NO_3, N_2O_5, HNO_3, HONO, $ClONO_2$ and organic nitrates.

1.4.1 OH chemistry

The hydroxyl radical is highly reactive towards most of the trace gases, both natural and man-made, that are emitted to the atmosphere. Oxidation by OH initiates chain reactions that result in the chemical conversion (removal) of the trace species. Thus OH greatly influences the composition of the troposphere. The primary source of the hydroxyl radical is the photolysis of ozone followed by reaction of the excited O atom product with water (Seinfeld and Pandis, 1998):

$$O_3 + h\nu \rightarrow O_2 + O(^1D) \qquad \text{(R1.14)}$$

$$O(^1D) + H_2O \rightarrow 2OH. \qquad \text{(R1.15)}$$

Thus the oxidizing or cleansing capacity of the troposphere, and its composition, are ultimately linked to the abundance of tropospheric ozone. The main source of this ozone is:

$$NO_2 + h\nu \rightarrow NO + O \qquad \text{(R1.16)}$$

followed by:

$$O + O_2 + M \rightarrow O_3 + M. \qquad \text{(R1.2)}$$

Ozone is also transported to the troposphere from the stratospheric ozone layer.

Hydroxyl radicals mainly react with carbon dioxide and methane (Wayne, 2000):

$$OH + CO \rightarrow H + CO_2 \qquad \text{(R1.17)}$$

$$OH + CH_4 \rightarrow CH_3 + H_2O \qquad \text{(R1.18)}$$

and the radical products add to molecular oxygen to form peroxy radicals:

$$H + O_2 + M \rightarrow HO_2 + M \qquad \text{(R1.19)}$$

$$CH_3 + O_2 + M \rightarrow CH_3O_2 + M. \qquad \text{(R1.20)}$$

In low [NO_x] environments these radicals are consumed by the reactions:

$$HO_2 + HO_2 \rightarrow H_2O_2 + O_2 \qquad \text{(R1.21)}$$

$$CH_3O_2 + HO_2 \rightarrow CH_3OOH + O_2 \qquad \text{(R1.22)}$$

and the hydrogen peroxide and methyl hydroperoxide products may be removed from the atmosphere *via* wet deposition. If NO_x is present then the peroxy radicals can react with NO:

$$HO_2 + NO \rightarrow OH + NO_2 \qquad \text{(R1.23)}$$

$$CH_3O_2 + NO \rightarrow CH_3O + NO_2. \qquad \text{(R1.24)}$$

Note that R1.23 regenerates OH and that both reactions produce NO_2, the source of ozone. The methoxy radical reacts with O_2:

$$CH_3O + O_2 \rightarrow HCHO + HO_2 \qquad \text{(R1.25)}$$

to form formaldehyde, which is photolysed:

$$HCHO + h\nu \rightarrow H + HCO. \qquad \text{(R1.26)}$$

The HCO product reacts with O_2:

$$HCO + O_2 \rightarrow CO + HO_2 \qquad \text{(R1.27)}$$

to generate CO, which is oxidized by OH *via* R1.17. The hydroperoxy radicals produced in R1.25 and R1.27 can react *via* R1.23, and the hydrogen atom generated in R1.26 is oxidized *via* R1.19.

The mechanism of methane oxidation just described can also be applied to other volatile organic compounds (VOCs) that are released into the troposphere (Jenkin, 1999). The main processes are summarized in figure 1.2. It can be seen that the completion of one cycle results in the production of two molecules of NO_2, and hence potentially O_3, and the

regeneration of the OH radical, whilst the VOC is degraded to a lower compound. Note that other reactions of RO_2 and HO_2, some of which are shown in the figure, compete with the reactions with NO. These processes are of interest as they inhibit ozone formation.

Figure 1.2. A summary of the mechanism of the OH-initiated oxidation of VOCs in the troposphere (Jenkin, 1999).

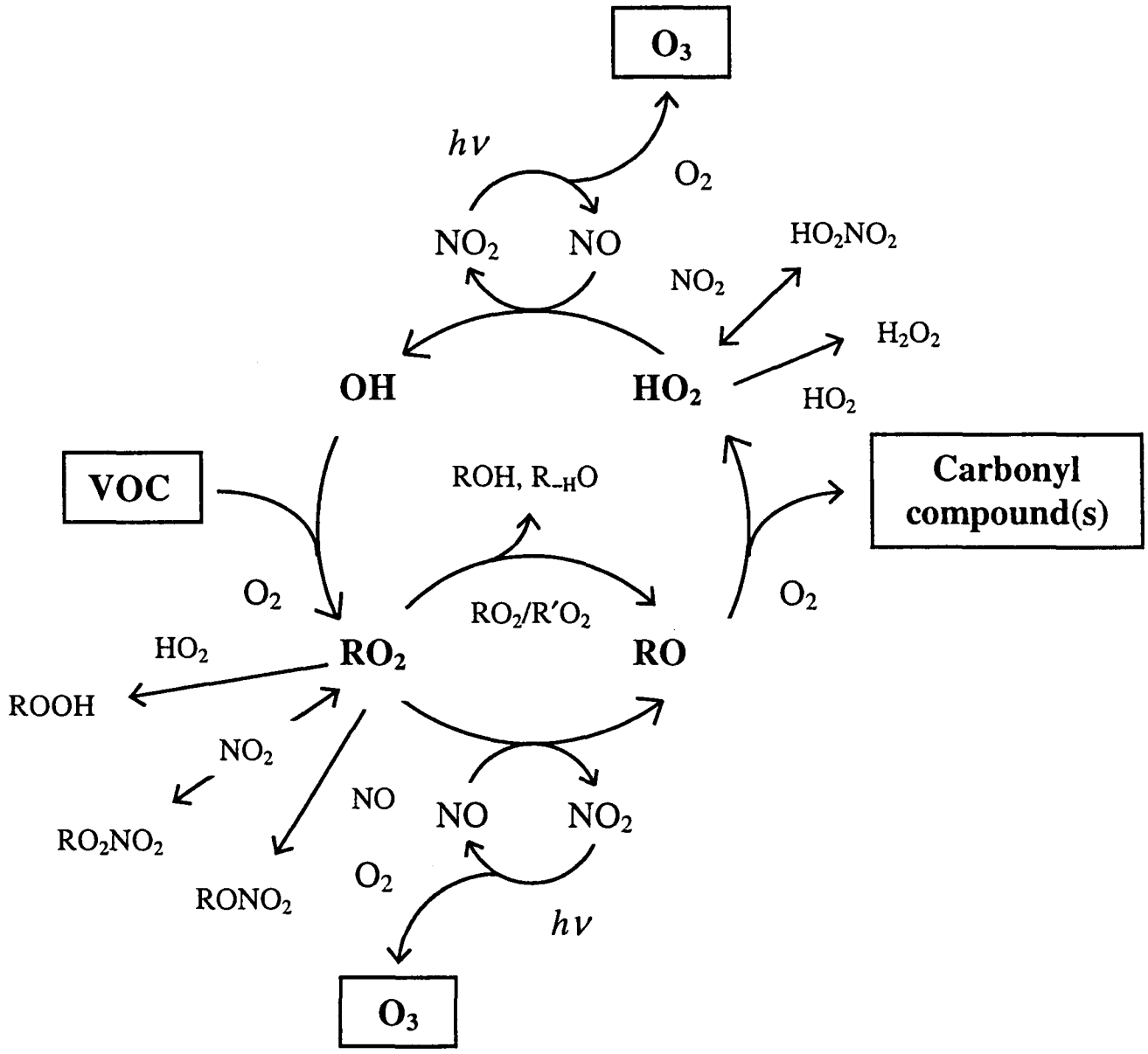

The reactions of several VOCs are considered in this thesis. The species of interest were acetone, butanone, dimethylsulphide (DMS), isoprene and *trans*-2-butene. The atmospheric chemistry of these compounds is discussed in the following section. Acetone chemistry is a recurrent theme in the thesis and so will be described in some detail. The other VOCs will only be considered briefly.

1.4.2 Volatile organic compounds (VOCs)

1.4.2.1 Acetone

Acetone (CH_3COCH_3) has received considerable attention as an atmospheric trace gas in recent years. It has been found to be ubiquitous to the entire troposphere and is probably the most abundant oxygenated hydrocarbon in the atmosphere. Acetone has been shown to have important functions in the troposphere, contributing to [NO_x], [HO_x] and the ozone budget.

1.4.2.1.1 The importance of atmospheric acetone

The photolysis of acetone results in the production of HO_x:

$$CH_3COCH_3 + h\nu \rightarrow CH_3CO + CH_3 \quad \text{(R1.28)}$$

$$CH_3CO + O_2 + M \rightarrow CH_3COO_2 + M \quad \text{(R1.29)}$$

$$CH_3COO_2 + NO \rightarrow CH_3 + CO_2 + NO_2 \quad \text{(R1.30)}$$

$$CH_3 + O_2 + M \rightarrow CH_3O_2 + M \quad \text{(R1.20)}$$

$$CH_3O_2 + NO \rightarrow CH_3O + NO_2 \quad \text{(R1.24)}$$

$$CH_3O + O_2 \rightarrow HCHO + HO_2 \quad \text{(R1.25)}$$

$$HCHO + h\nu \rightarrow H + HCO \quad \text{(R1.26)}$$

$$H + O_2 + M \rightarrow HO_2 + M \quad \text{(R1.19)}$$

$$HCO + O_2 \rightarrow HO_2 + CO. \quad \text{(R1.27)}$$

Singh *et al.* (1997), Arnold *et al.* (1997) and Wennberg *et al.* (1998) found this mechanism to be responsible for a large proportion of the HO_x present in the troposphere, particularly the upper troposphere where [H_2O] is low. Calculations demonstrated that in this region acetone photolysis could generate up to five times more HO_x than the reaction of $O(^1D)$ with H_2O. As previously discussed, the reaction of HO_2 with NO produces NO_2, photolysis of which results in O_3 production. Thus acetone photolysis enhances [O_3].

Acetone photochemistry can also contribute to the formation of peroxyacetyl nitrate (PAN), *via* reaction of the acetylperoxy radical, produced in R1.29, with NO_2:

$$CH_3COO_2 + NO_2 + M \rightarrow CH_3COO_2NO_2 + M. \qquad (R1.31)$$

Modelling work by Singh *et al.* (1995) revealed that a considerable proportion, possibly up to 50%, of observed tropospheric PAN could be attributed to acetone photolysis. PAN is a temporary reservoir of NO_x. Its formation leads to a reduction in ozone production and enables the long-range transport of NO_x.

1.4.2.1.2 Atmospheric abundance

Table 1.1. Some examples of acetone mixing ratios observed in the atmosphere.

Atmospheric region	Geographical location and season	Mean mixing ratio /pptv	Mixing ratio range /pptv	Reference
BL and FT	N America Summer	1140 ± 413	357 – 2310	Singh *et al.* (1994)
UT/LS	N Europe Winter	Tropopause 480		Arnold *et al.* (1997)
	W Europe Summer	Tropopause 700	UT/LS 200 – 1500	
LS	Pacific Ocean Spring	152.9 ± 73.6		Singh *et al.* (1997)
UT/LS	N Atlantic Ocean Autumn		UT 200 – 2200 LS 100 – 200	Wohlfrom *et al.* (1999)
BL and FT	Indian Ocean Spring		BL 300 – 2500 FT 300 – 1000	Sprung *et al.* (2001)

Notes: BL – boundary layer; FT – free troposphere; UT – upper troposphere; LS – lower stratosphere; pptv – parts per trillion by volume.

Some examples of field measurements of acetone are presented in table 1.1. It can be seen that large quantities have been detected throughout the lower atmosphere, in several different locations and seasons. Singh *et al.* (1994) were surprised to discover that, during their entire field study, acetone was found in greater concentrations than ethane, which was though to be the most abundant non-methane organic species in the global atmosphere. Arnold *et al.* (1997) and Wohlfrom *et al.* (1999) state that they frequently observed mixing ratios as high as 2200 and 3000 pptv respectively in the upper troposphere. The much lower quantities detected in the lower stratosphere reflect the combined action of high photolysis rates in this region and slow vertical exchange with respect to the lifetime of acetone.

1.4.2.1.3 Sources of acetone

Acetone has many sources. Jacob *et al.* (2002) compiled a global source inventory: see table 1.2. The direct emission from vegetation was found to provide the greatest contribution: many plant species emit acetone as a by-product of metabolic processes. The oceans release large quantities *via* the photochemical degradation of dissolved organic matter. The atmospheric oxidation of various organic compounds also results in the production of acetone. Propane is the most important precursor:

$$CH_3CH_2CH_3 + OH + O_2 \rightarrow CH_3CHO_2CH_3 + H_2O \quad (80\%) \quad \text{(R1.32a)}$$

$$\rightarrow CH_3CH_2CH_2O_2 + H_2O \quad (20\%) \quad \text{(R1.32b)}$$

$$CH_3CHO_2CH_3 + NO + O_2 \rightarrow CH_3COCH_3 + NO_2 + HO_2 \quad \text{(R1.33)}$$

$$CH_3CHO_2CH_3 + HO_2 \rightarrow CH_3CHOOHCH_3 + O_2 \quad \text{(R1.34)}$$

$$CH_3CHOOHCH_3 + h\nu \rightarrow CH_3CHOCH_3 + OH \quad \text{(R1.35)}$$

$$CH_3CHOCH_3 + O_2 \rightarrow CH_3COCH_3 + HO_2. \quad \text{(R1.36)}$$

Other precursors include isobutane, isopentane, monoterpenes such as myrcene and α- and β-pinene, and methylbutenol. Forest fires, abiotic processes occurring in decaying plant matter, and microbial processes occurring in soil also generate a small quantity of acetone; anthropogenic sources include automobile exhausts and losses through its use as a solvent.

Table 1.2. A global source inventory for acetone (Jacob *et al.* 2002).

Source	**Global annual emissions /Tg yr^{-1}**
Terrestrial vegetation	33 ± 9
Oceans	27 ± 6
Alkane oxidation	21 ± 5
Monoterpene/methylbutenol oxidation	7 ± 3
Biomass burning	4.5 ± 1.6
Dead/decaying plant matter	2 ± 5
Anthropogenic emissions	1.1 ± 0.5
Total source strength	**95 ± 15**

1.4.2.1.4 Sinks of acetone and chemistry of the acetonylperoxy radical

Photolysis and reaction with OH are the major loss processes for acetone. Modelling work by Jacob *et al.* (2002) revealed that globally 45% of acetone is lost *via* photolysis, 30% by reaction with OH, 15% is taken up by the oceans and 10% is lost *via* dry deposition to the land. A global mean lifetime of 15 days was derived.

The oxidation of acetone generates a range of species in the atmosphere. Photolysis results in the formation of compounds such as HO_x and PAN (as has already been discussed), which have been the subject of much research. The products of the OH-initiated oxidation of acetone have, however, received much less attention. The reaction of OH with acetone generates the acetonyl radical, which is rapidly oxidized to form the acetonylperoxy radical:

$$CH_3COCH_3 + OH \rightarrow CH_3COCH_2 + H_2O \qquad \text{(R1.37)}$$

$$CH_3COCH_2 + O_2 + M \rightarrow CH_3COCH_2O_2 + M. \qquad \text{(R1.38)}$$

There have been no field measurements of the acetonylperoxy radical because of the lack of detection techniques that are capable of speciating peroxy radicals. However, with

acetone as its precursor, the possibility exists that it is a widespread and important free radical, so that its chemistry could have significant impacts.

The acetonylperoxy radical reacts rapidly with NO and NO_2:

$$CH_3COCH_2O_2 + NO \rightarrow CH_3COCH_2O + NO_2 \quad \text{(R1.39)}$$

$$CH_3COCH_2O_2 + NO_2 + M \rightarrow CH_3COCH_2O_2NO_2 + M. \quad \text{(R1.40)}$$

The production of NO_2 *via* R1.39 can, of course, increase $[O_3]$. Sehested *et al.* (1998) found that the peroxy nitrate formed in R1.40 decomposes thermally back to the original reactants. The workers state that the lifetime of the nitrate with respect to this process is sufficiently small, even at the lower temperatures of the upper troposphere, to prevent it participating, in a manner similar to PAN, in the long-range transport of NO_x.

In remote areas where $[NO_x]$ may be low, the reactions of $CH_3COCH_2O_2$ with HO_2 and other peroxy species may be significant. Jenkin *et al.* (1993) determined the products of the reactions:

$$CH_3COCH_2O_2 + HO_2 \rightarrow CH_3COCH_2O_2H + O_2 \quad \text{(R1.41)}$$

$$CH_3COCH_2O_2 + CH_3O_2 \rightarrow CH_3COCH_2O + CH_3O + O_2 \quad \text{(R1.42a)}$$

$$\rightarrow CH_3COCH_2OH + HCHO + O_2 \quad \text{(R1.42b)}$$

$$\rightarrow CH_3COCHO + CH_3OH + O_2 \quad \text{(R1.42c)}$$

$$CH_3COCH_2O_2 + CH_3COO_2 \rightarrow CH_3COCH_2O + CH_3 + CO_2 + O_2 \quad \text{(R1.43a)}$$

$$\rightarrow CH_3COCHO + CH_3COOH + O_2. \quad \text{(R1.43b)}$$

Cox *et al.* (1990) suggested that the self-reaction of acetonylperoxy radical may also be of importance in the atmosphere:

$$2CH_3COCH_2O_2 \rightarrow 2CH_3COCH_2O + O_2 \quad \text{(R1.44a)}$$

$$\rightarrow CH_3COCHO + CH_3COCH_2OH + O_2. \quad \text{(R1.44b)}$$

These reactions generate a range of oxygenated species, including formaldehyde, methyl glyoxal and methanol. The hydroperoxide formed in R1.41 will be photolysed in the

atmosphere to produce OH. Thus HO_2 is converted to OH in the absence of NO. The acetonoxy radical produced in reactions 1.42a, 1.43a and 1.44a decomposes to form acetyl radicals. Along with the methyl radicals also produced in R1.43a, the acetyl radicals will react with oxygen to generate more RO_2.

Previous laboratory studies of acetonylperoxy radical chemistry are described in more detail in chapter 6. The products of the reactions require verification, and the branching ratios and rate constants are also poorly defined. Highly selective and sensitive detection techniques for the radical are required to improve the laboratory work and make field measurements possible. Only then can the impacts of the OH-initiated oxidation of acetone on the atmosphere be fully characterized.

1.4.2.2 Butanone

Butanone, $CH_3COCH_2CH_3$, has received much less attention than acetone as an atmospheric trace gas. It has been observed in the troposphere of alpine forest and Antarctic regions (Schubert *et al.*, 1999; Ciccioli *et al.*, 1996). The atmospheric chemistry of butanone is expected to be similar to that of acetone. Terrestrial vegetation has been identified as a source: de Gouw *et al.* (1999) observed butanone in emissions from cut and drying grass and clover, and Isidorov *et al.* (1985) identified several plant species that directly released the ketone. Ciccioli *et al.* (1996) also suggested that the oceans are a likely source. The major sinks of butanone are reaction with OH and photolysis. Unlike acetone, it is probable that the former is of greatest importance (Seinfeld and Pandis, 1998).

1.4.2.3 Dimethylsulphide (DMS)

Sulphur-containing compounds exert a profound influence on the chemistry of the atmosphere and, possibly, on climatological processes. DMS (CH_3SCH_3) is the dominant sulphur compound emitted from biogenic sources. Large quantities, 15 – 25 Tg yr^{-1}, are released from the oceans as a result of the actions of phytoplankton and bacteria (Seinfeld and Pandis, 1998). Typical concentrations of DMS in the marine boundary layer are 80 to 110 ppt. Smaller quantities are observed in the continental boundary layer (8 – 60 ppt) and the free troposphere (1.5 – 15 ppt). The principle sinks are reaction with OH and

NO_3. The observed products of the oxidation of DMS are dimethylsulphoxide (DMSO), COS, SO_2, H_2SO_4, methane sulphonic acid (MSA) and dimethylsulphone ($DMSO_2$). In fact, DMS is the only source of MSA in the atmosphere and the dominant source of SO_2 in marine regions. SO_2 and H_2SO_4 act as aerosol precursors, may affect cloud production and may also be of climatological significance (Wayne, 2000). H_2SO_4 also lowers the pH of rainwater. The H_2SO_4 derived from DMS oxidation is thought to constitute at least 25% of the acid deposited over Europe. COS is the main source of sulphur to the stratosphere. This sulphur influences the temperature profile of the lower stratosphere and may affect ozone concentrations.

1.4.2.4 Isoprene

Isoprene ($CH_2CCH_3CHCH_2$) is thought to be the dominant VOC emitted by vegetation. It is estimated that about 500 Tg yr^{-1} are released as a by-product of photosynthesis and/or respiration in plants (Finlayson-Pitts and Pitts Jr., 2000). Isoprene has a very short tropospheric lifetime, of the order of hours, as a result of its rapid reaction with OH, NO_3 and O_3. All three reactions proceed *via* addition of the oxidant to the carbon double bonds. The chemistry initiated by these oxidants is highly complex as the presence of the two double bonds in isoprene permits a number of possible sites of attack. A variety of peroxy radicals are generated as intermediates. Final products of isoprene oxidation include formaldehyde, methacrolein (CH_2CCH_3CHO) and methyl vinyl ketone ($CH_3COCHCH_2$). In the case of the reaction with NO_3, nitrato-substituted C_4 and C_5 carbonyl compounds are generated. Reaction with O_3 also produces large quantities of OH (Wayne, 2000).

1.4.2.5 *Trans*-2-butene

Alkenes, such as *trans*-2-butene ($CH_3CHCHCH_3$), are typically released to the atmosphere from anthropogenic sources including exhausts from automobiles (Seinfeld and Pandis, 1998). *Trans*-2-butene has been observed in urban and remote regions, and has a short atmospheric lifetime (minutes to hours) owing to rapid reaction with OH, O_3 and NO_3 (Finlayson-Pitts and Pitts Jr., 2000). Like the reactions of the other unsaturated compound described in this section, isoprene, the mechanisms involve addition of the

oxidant to the double bond. Again, peroxy radicals are generated as intermediate species and the products include carbonyl compounds.

1.4.3 Halogen-containing species

The chemistry of halogen-containing compounds is another theme of the thesis. Two species are considered, namely the IO radical and the Cl atom. Although the role of chlorine-containing species in stratospheric ozone depletion has been thoroughly studied, the impact of such compounds on the abundance of tropospheric ozone has received less attention. The effect of iodine compounds on the concentration of ozone in both the troposphere and the stratosphere is also not as well understood.

Atomic I (the precursor of IO) and Cl are both capable of destroying ozone directly *via* catalytic cycles. In competition with these cycles, both atoms can also react with other trace gases to form reservoir compounds. However, the behaviour of the two elements is really quite different in the troposphere. Iodine is less electronegative than chlorine. Thus it reacts less readily and forms compounds that are easily photolysed in the lower atmosphere (Chameides and Davis, 1980). In contrast, Cl reacts quickly with many species to form reservoir compounds that are much more stable. Consequently, a higher percentage of the iodine than the chlorine in the troposphere is present in its active form and therefore I has the greater potential to deplete tropospheric ozone (Solomon *et al.*, 1994). However, Cl can also perturb the abundance of O_3 indirectly as a result of interactions with VOCs: it is capable of initiating the oxidation of these species in a similar manner to OH. The chemistry of Cl and IO in the troposphere is now described in some detail. The possible role of iodine compounds in stratospheric ozone depletion is also considered.

1.4.3.1 Chlorine atoms

There has been recurring speculation over the years about the role of atomic chlorine in the troposphere. Many studies have indicated that Cl atoms contribute significantly to, or even locally dominate, the oxidative capacity of the marine boundary layer (MBL).

1.4.3.1.1 Sources of Cl atoms

The major source of Cl atoms to the troposphere is the oceans, or more precisely, processes involving seasalt aerosols (Finlayson-Pitts and Pitts Jr., 2000). The formation of such aerosols is initiated by the actions of waves. Droplets of seawater are flung into the air and the water evaporates to leave behind a suspended particle of seasalt. This aerosol mainly consists of NaCl. Reaction with species such as N_2O_5 and $ClONO_2$ at the aerosol surface releases the chlorine into the gas phase (Finlayson-Pitts *et al.*, 1989):

$$N_2O_{5(g)} + NaCl_{(s)} \rightarrow ClNO_{2(g)} + NaNO_{3(s)} \quad \text{(R1.45)}$$

$$ClONO_{2(g)} + NaCl_{(s)} \rightarrow Cl_{2(g)} + NaNO_{3(s)}. \quad \text{(R1.46)}$$

These reactions can also occur in the aqueous phase, in competition with the hydrolysis of N_2O_5 and $ClONO_2$. The chlorine-containing products are photolysed to generate Cl atoms:

$$ClNO_2 + h\nu \rightarrow Cl + NO_2 \quad \text{(R1.47)}$$

$$Cl_2 + h\nu \rightarrow 2Cl. \quad \text{(R1.8)}$$

Other mechanisms for the production of gaseous, photochemically active, forms of chlorine from seasalt aerosols have been proposed. Experiments by Oum *et al.* (1998) indicate that the reaction of ozone with aqueous aerosols in the presence of light generates Cl_2. Vogt *et al.* (1996) also suggest a mechanism that involves the scavenging of gaseous HOBr by aerosols and the subsequent generation and release of BrCl, a species that undergoes rapid photolysis. This mechanism presents a source of Cl atoms in the unpolluted MBL as NO_x is not required.

1.4.3.1.2 Tropospheric abundance

Atomic chlorine has not been observed in the troposphere because a detection technique of sufficient sensitivity has yet to be developed. However, estimates of [Cl] have been inferred from measurements of the precursor species. Spicer *et al.* (1998) measured nighttime Cl_2 mixing ratios of ~40 to ~150 ppt off the east coast of the USA. The

concentration dropped rapidly at dawn to reach a daytime low of <15 ppt: modelling work demonstrated that the resultant [Cl] reached a maximum of 1.3×10^5 atom cm^{-3} shortly after sunrise. Pszenny *et al.* (1993) performed similar experiments at a North American coastal site that also suggested a noontime [Cl] of $10^4 - 10^5$ atom cm^{-3}.

Measurements of organic species have also been used to estimate [Cl]. Jobson *et al.* (1994) observed NMHCs in the Arctic lower troposphere. They found that the relative rates of decay of these species could not be the result of attack by OH alone. Indeed, they observed a correlation between the loss of the organic species and the rate constants for reaction with Cl. A maximum concentration of Cl of 8×10^4 atom cm^{-3} was inferred. Wingenter *et al.* (1996) measured changes in the abundance of a selection of hydrocarbons and halocarbons in the North Atlantic MBL and estimated an average Cl concentration of $\sim 3 \times 10^4$ atom cm^{-3} for the 5 hour period from 6 am to 11 am, and a noontime concentration of $\sim 7 \times 10^4$ atom cm^{-3}. However, a similar study by Rudolph *et al.* (1996) highlighted how Cl-atom chemistry is confined to the MBL. The workers inferred the global average concentration of Cl atoms in the troposphere to be $\leq 10^3$ atom cm^{-3}. Such concentrations mean that, on a global scale, reactions of Cl are of minor importance.

1.4.3.1.3 Cl-atom chemistry in the MBL

As just discussed, Cl-atom chemistry in the MBL involves reactions with organic species. Cl can initiate the oxidation of such compounds by either abstracting a hydrogen atom, in a manner similar to OH as described in section 1.4.1, or reacting *via* an addition-elimination reaction. These reactions are significant, despite the fact that even at the elevated concentrations found in the MBL the abundance of Cl atoms is lower than that of OH radicals, because Cl reacts more rapidly than OH with organic species. For example, Spicer *et al.* (1998) compared the loss of ethane as a result of reaction with the two oxidants. Their model showed that shortly after sunrise, when [Cl] was at a maximum (1.3×10^5 atom cm^{-3}), the concentration of OH was three times greater (3.9×10^5 molecule cm^{-3}). However, the rate of loss of ethane as a result of reaction with Cl was 7.2×10^{-6} s^{-1}, whereas the rate of loss owing to oxidation by OH was about two orders of magnitude smaller (8.6×10^{-8} s^{-1}). Modelling work by Pszenny *et al.* (1993)

also found [OH] to be greater than [Cl], in some cases by two orders of magnitude, but again they discovered that oxidation by Cl accounted for significant fractions of the loss of organic species, such as ethane and propane.

Cl atoms are also capable of modifying the ozone budget directly in the MBL. Rapid O_3 loss can occur *via* the following sequence:

$$Cl + O_3 \rightarrow ClO + O_2 \qquad \text{(R1.9)}$$

$$ClO + HO_2 \rightarrow HOCl + O_2 \qquad \text{(R1.48)}$$

$$HOCl + h\nu \rightarrow OH + Cl \qquad \text{(R1.49)}$$

$$\text{Net: } HO_2 + O_3 \rightarrow OH + 2O_2. \qquad \text{(R1.50)}$$

However, this loss can be offset by the production of ozone *via* the reaction of Cl with organic species in the presence of NO_x. Pszenny *et al.* (1993) found that the net effect of Cl chemistry in the MBL was to increase O_3 loss when the NO_x concentration was less than 20 pptv and to stimulate O_3 generation at higher [NO_x].

1.4.3.2 IO radicals

The IO radical has been the subject of much research in recent years as a result of its possible effect on the ozone concentration in both the troposphere and stratosphere.

1.4.3.2.1 Sources of IO

IO is formed in the atmosphere following the photolysis of iodine-containing compounds (Chameides and Davis, 1980). The principal sources of these compounds are biogenic processes taking place in the oceans. Macroalgae and phytoplankton generate a variety of halocarbons, including CH_3I, C_2H_5I and CH_2I_2, as metabolic byproducts (Carpenter *et al.*, 1999). These species are transferred to the seawater and then released into the atmosphere. The most abundant alkyl iodide is CH_3I. Concentrations of about 1 pptv have been observed in the free troposphere (Davis *et al.*, 1996), although much higher levels (43 pptv) have been measured in the MBL (Oram and Penkett, 1994). The global

source strength of CH_3I is estimated to be 1 – 2 Tg yr^{-1}. Biomass burning and industrial emissions are also thought to be minor sources of iodocarbons (Solomon *et al.*, 1994).

Methyl iodide is photolysed to release I, which can react with O_3 to form IO:

$$CH_3I + h\nu \rightarrow CH_3 + I \qquad \text{(R1.51)}$$

$$I + O_3 \rightarrow IO + O_2. \qquad \text{(R1.52)}$$

Recent studies have highlighted the contribution of other halocarbons to the generation of I and IO. Carpenter *et al.* (1999) suggest that species such as CH_2I_2 and CH_2IBr provide a much greater flux of iodine atoms to the atmosphere because they are photodissociated more rapidly than CH_3I.

1.4.3.2.2 Tropospheric abundance

There have been several observations of IO in the troposphere. Alicke *et al.* (1999) measured a noontime maximum of about 6 ppt in the MBL at Mace Head, Ireland. The workers observed a strong correlation between the intensity of solar radiation and the highest [IO], so providing evidence for the photolytic nature of the source. Carpenter *et al.* (1999) also demonstrated that the greatest abundance was associated with large fluxes of the precursor species. Allen *et al.* (2000) measured daytime mixing ratios of IO of ≤ 0.2 – 4 ppt in the boundary layer at three different coastal sites. The average concentration was about 1 ppt. Measurements performed by Frieß *et al.* (2000) indicate that [IO] may reach ~10 ppt in the MBL off the coast of Antarctica. The highest levels were observed in the summer months.

1.4.3.2.3 IO chemistry in the troposphere

IO can either be photolysed or react with various trace gases. Photolysis results in the production of O and the regeneration of I:

$$IO + h\nu \rightarrow I + O. \qquad \text{(R1.53)}$$

This process may of course be followed by the consumption of more ozone to reform IO *via* R1.52. However, this loss is offset by the reaction of O with O_2 to produce ozone. Consequently, IO photolysis has no net effects (Chameides and Davis, 1980). By contrast, the reactions of IO with itself and other trace gases, such as HO_2 and NO_2, can result in ozone depletion (McFiggans *et al.*, 2000):

IO cycle:

$$IO + IO\ (+ M) \rightarrow I_2O_2 + M \quad \text{(R1.54a)}$$

$$\rightarrow OIO + I \quad \text{(R1.54b)}$$

$$I_2O_2 + h\nu \rightarrow 2I + O_2 \quad \text{(R1.55)}$$

$$OIO + h\nu \rightarrow I + O_2 \quad \text{(R1.56)}$$

$$2I + 2O_3 \rightarrow 2IO + 2O_2 \quad \text{(R1.52)}$$

$$\text{Net: } 2O_3 \rightarrow 3O_2 \quad \text{(R1.13)}$$

HO_2 cycle:

$$IO + HO_2 \rightarrow HOI + O_2 \quad \text{(R1.57)}$$

$$HOI + h\nu \rightarrow OH + I \quad \text{(R1.58)}$$

$$I + O_3 \rightarrow IO + O_2 \quad \text{(R1.52)}$$

$$\text{Net: } HO_2 + O_3 \rightarrow OH + 2O_2 \quad \text{(R1.50)}$$

NO_2 cycle:

$$IO + NO_2 + M \rightarrow IONO_2 + M \quad \text{(R1.59)}$$

$$IONO_2 + h\nu \rightarrow I + NO_3 \quad \text{(R1.60)}$$

$$NO_3 + h\nu \rightarrow NO + O_2 \quad \text{(R1.61)}$$

$$NO + O_3 \rightarrow NO_2 + O_2 \quad \text{(R1.62)}$$

$$I + O_3 \rightarrow IO + O_2 \quad \text{(R1.52)}$$

$$\text{Net: } 2O_3 \rightarrow 3O_2. \quad \text{(R1.13)}$$

It can be seen that the ozone destruction in the second cycle is accompanied by the conversion of HO_2 to OH. IO can also convert NO to NO_2:

$$IO + NO \rightarrow I + NO_2. \quad \text{(R1.63)}$$

Several studies have attempted to quantify the impact of iodine chemistry upon the abundance of O_3, HO_x and NO_x. For example, Davis *et al.* (1996) calculated that a

mixing ratio of between 1.5 and 7 pptv of inorganic iodine would increase the rate of depletion of the total ozone column in the troposphere by 6 to 30 %. The maximum changes in the $[HO_2]/[OH]$ and $[NO_2]/[NO]$ ratios were estimated to be –24% and +11% respectively. McFiggans *et al.* (2000) found IO to be responsible for up to 13% of the total ozone destruction taking place. The workers also suggested that the uptake of $IONO_2$ by aerosols followed by the deposition of these particles to the Earth's surface constituted a significant pathway for the removal of NO_x from the atmosphere.

1.4.3.2.4 IO chemistry in the stratosphere

A possible role for IO in stratospheric ozone depletion was first suggested by Solomon *et al.* (1994). It had previously been thought that iodine-containing compounds could not reach the stratosphere because of their short lifetimes with respect to photolysis followed by deposition. However, the workers proposed that such compounds could be rapidly transported to the upper troposphere and possibly the lower stratosphere *via* convective clouds. Model results showed that if the total concentration of all iodine-containing compounds in these regions was 1 ppt, there would be a significant impact on the abundance of ozone. Cycles such as those described with reference to tropospheric chemistry were responsible for this loss, although the interactions of IO with other halogenated species were highlighted for their contribution. For example, the chemistry of iodine and bromine can combine to destroy ozone (Finlayson-Pitts and Pitts Jr., 2000):

$$I + O_3 \rightarrow IO + O_2 \qquad \text{(R1.52)}$$

$$Br + O_3 \rightarrow BrO + O_2 \qquad \text{(R1.64)}$$

$$IO + BrO \rightarrow OIO + Br \qquad \text{(R1.65)}$$

$$OIO + h\nu \rightarrow I + O_2 \qquad \text{(R1.56)}$$

$$\text{Net: } 2O_3 \rightarrow 3O_2. \qquad \text{(R1.13)}$$

The first stratospheric measurements showed iodine-containing compounds to be present in only very small quantities. For example, Wennberg *et al.* (1997) observed the total concentration of iodine species at mid-latitudes to be ~0.2 ppt, and Pundt *et al.* (1998) derived a stratospheric abundance of IO of <0.2 ppt at high latitudes. Thus it was thought that iodine chemistry could not contribute greatly to stratospheric ozone depletion.

However, Wittrock *et al.* (2000) reopened the debate by publishing data that showed IO to be present at much higher concentrations — 0.65 to 0.80 ppt in polar regions in the spring. These measurements imply that iodine compounds do indeed play a part in ozone destruction in the stratosphere.

1.5 Thesis aims and layout

The work reported in this thesis aimed to determine the rate constants of some reactions of the organic and halogen-containing compounds just described. In chapter 3, the reactions of IO with itself, NO, DMS, isoprene and *trans*-2-butene are considered. In chapter 4, the reactions of Cl with acetone and butanone are thoroughly investigated. The study of the reaction with acetone is extended in order to obtain information about the chemistry of the acetonylperoxy radical. In chapter 6, it is the self-reaction of this peroxy species that is under investigation.

These reactions were studied through the use of discharge–flow tubes coupled to a variety of detection techniques. Two conventional detection methods were employed: resonance fluorescence was used to monitor Cl atoms, and the acetonylperoxy radical self-reaction was followed with electron-impact mass spectrometry. Chapter 5 describes the design, construction and commissioning of this latter piece of apparatus. However, much of the thesis is concerned with the development of more sensitive and selective detection systems. Chapter 3 reports the use of laser-induced fluorescence to observe IO, and chapter 7 describes the conversion of the mass spectrometer from an electron-impact to a chemical-ionization instrument for the direct detection of the acetonylperoxy radical.

Before the details of this research are reported, the principles of the detection techniques and the discharge–flow tubes employed are discussed in the next chapter. The methods of data analysis are also presented.

1.6 References

- Alicke, B., K. Hebestreit, J. Stutz and U. Platt, *Nature*, 1999, **397**, 572
- Arnold, F., V. Burger, B. Droste-Fanke, F. Grimm, A. Krieger, J. Schneider and T. Stilp, *Geophys. Res. Lett.*, 1997, **24**(23), 3017
- Bloss, W. J., D. M. Rowley, R. A. Cox and R. L. Jones, *J. Phys. Chem. A*, 2001, **105**, 1840
- Carpenter, L. J., W. T. Sturges, S. A. Penkett, P. S. Liss, B. Alicke, K. Hebestreit and U. Platt, *J. Geophys. Res.*, 1999, **104 (D1)**, 1679
- Cox R. A., J. Munk, O. J. Nielsen, P. Pagsberg and E. Ratajczak, *Chem. Phys. Lett.*, 1990, **173**(2,3), 206
- Ciccioli, P., A. Cecinato, E. Brancaleoni, M. Frattoni, F. Bruner and M. Maione, *Intern. J. Environ. Anal. Chem.*, 1996, **62**, 245
- Davis, D., J. Crawford, S. Liu, S. McKeen, A. Brandy, D. Thornton, F. Rowland and D. Blake, *J. Geophys. Res.*, 1996, **101 (D1)**, 2135
- de Gouw, J. A., C. J. Howard, T. G. Custer and R. Fall, *Geophys. Res. Lett.*, 1999, **26**, 811
- Chameides, W. L. and D. D. Davis, *J. Geophys. Res.*, 1980, **85 (C12)**, 7383
- Finlayson-Pitts, B. J., M. J. Ezell and J. N. Pitts Jr., *Nature*, 1989, **337**, 241
- Finlayson-Pitts, B. J. and J. N. Pitts Jr., *Chemistry of the Upper and Lower Atmosphere*, Academic Press, San Diego, 2000
- Freiß, U., T. Wagner, I. Pundt, K. Pfeilsticker and U. Platt, *Geophys. Res. Lett.*, 2000, **28**, 1941
- Isidorov, V. A., I. G. Zenkevich and B. V. Ioffe, *Atmospheric Environment*, 1985, **19**, 1
- Jacob, D. J., B. D. Field, E. M. Jin, I. Bey, Q. Li, J. A. Logan, R. M. Yantosca and H. B. Singh, *J. Geophys. Res.*, 2002, **107**(D10), ACH5
- Jenkin, M. E., R. A. Cox, M. Emrich and G. K. Moortgat, *J. Chem. Soc. Faraday Trans.*, 1993, **89**(16), 2983
- Jenkin, M. E. in *Proceedings of EUROTRAC Symposium '98*, ed. P. M. Borrell and P. Borrell, WIT PRESS, Southampton, 1999, 33
- Jobson, B. T., H. Niki, Y. Yokouchi, J. Bottenheim, F. Hopper and R. Leaitch, *J. Geophys. Res.*, 1994, **99 (D12)**, 25355

- McFiggans, G., J. M. C. Plane, B. J. Allan, L. J. Carpenter, H. Coe and C. O'Dowd, *J. Geophys. Res.*, 2000, **105 (D11)**, 14371
- Oram, D. E. and S. A. Penkett, *Atmos. Environ.*, 1994, **28**, 1159
- Oum, K. W., M. J. Lakin, D. O. DeHaan, T. Brauers and B. J. Finlayson-Pitts, *Science*, 1998, **279**, 74
- Pszenny, A. A. P., W. C. Keene, D. J. Jacob, S. Fan, J. R. Maben, M. P. Zetwo, M. Springer-Young and J. N. Galloway, *Geophys. Res. Lett.*, 1993, **20**, 699
- Pundt, I., J.-P. Pommereau, C. Phillips and E. Lateltin, *J. Atmos Chem.*, 1998, **30**, 173
- Rudolph, J., R. Koppmann and Ch. Plass-Dülmer, *Atmos. Environ.*, 1996, **30**, 1887
- Sehested, J., L. K. Christensen, O. J. Nielsen, M. Bilde, T. J. Wallington, W. F. Schneider, J. J. Orlando and G. S. Tyndall, *Int. J. Chem. Kinet.*, 1998, **30**, 475
- Seinfeld, J. H. and S. N. Pandis, *Atmospheric Chemistry and Physics*, John Wiley and Sons, Toronto, 1998
- Singh, H. B., D. O'Hara, D. Herlth, W. Sachse, D. R. Blake, J. D. Bradshaw, M. Kanakidou and P. J. Crutzen, *J. Geophys. Res.*, 1994, **99**, 1805
- Singh, H. B., M. Kanakidou, P. J. Crutzen and D. J. Jacob, *Nature*, 1995, **378**, 50
- Singh, H. B., Y. Chen, G. L. Gregory, G. W. Sachse, R. Talbot, D. R. Blake, Y. Kondo, J. D. Bradshaw, B. Heikes and D. Thornton, *Geophys. Res. Lett.*, 1997, **24**(2), 127
- Solomon, S., R. R. Garcia and A. R. Ravishankara, *J. Geophys. Res.*, 1994, **99 (D10)**, 20491
- Spicer, C. W., E. G. Chapman, B. J. Finlayson-Pitts, R. A. Plastridge, J. M. Hubbe, J. D. Fast and C. M. Berkowitz, *Nature*, 1998, **394**, 353
- Sprung, D., C. Jost, T. Reiner, A. Hansel and A. Wisthaler, *J. Geophys. Res.*, 2001, **106**(D22), 28511
- Vogt, R., P. J. Crutzen and R. Sander, *Nature*, 1996, **383**, 327
- Wayne, R. P., *Chemistry of Atmospheres*, 3rd Edition, Oxford University Press, Oxford, 2000
- Wennberg, P. O., J. W. Brault, T. F. Hanisco, R. J. Salawitch and G. H. Mount, *J. Geophys. Res.*, 1997, **102 (D7)**, 8887
- Wennberg, P. O., T. F. Hanisco, L. Jaegle, D. J. Jacob, E. J. Hintsa, E. J. Lazendorf, J. G. Anderson, R. S. Gao, E. R. Keim, S. G. Donnelly, L. A. Del Negro, D. W. Fahey, S. A. McKeen, R. J. Salawitch, C. R. Webster, R. D. May, R. L. Herman, M. H.

Proffitt, J. J. Margitan, E. L. Atlas, S. M. Schauffler, F. Flocke, C. T. McElroy and T. P. Bui, *Science*, 1998, **279**, 49

- Wingenter, O. W., M. K. Kubo, N. J. Blake, T. W. Smith Jr., D. R. Blake and F. S. Rowland, *J. Geophys. Res.*, 1996, **101 (D2)**, 4331
- Wittrock, F., R. Müller, A. Richter, H. Bovensmann and J. P. Burrows, *Geophys. Res. Lett.*, 2000, **27**, 1471
- Wohlfrom, K. H., T. Hauler, F. Arnold and H. Singh, *Geophys. Res. Lett.*, 1999, **26**(D18), 2849

Chapter 2 Experimental techniques

2.1 Introduction

The basic data of kinetic investigations are the concentrations of reactants and/or products as a function of time since the reaction was initiated. Such data were obtained in the experiments reported in this thesis through the use of discharge–flow tubes coupled to a variety of detection techniques, namely, resonance fluorescence, laser-induced fluorescence and electron-impact mass spectrometry. The development of a chemical-ionization mass spectrometer is also reported. These pieces of apparatus are discussed in the following sections. The chapter ends with a description of the methods of data analysis used to extract the kinetic information.

2.2 The discharge–flow technique

The discharge–flow technique is a common method of determining absolute rate constants. The basic principle of operation is as follows: reactants are introduced to the upstream end of a flow tube; the reaction occurs as the gases travel along the tube at high speeds; and then the reactants and/or products are detected at the downstream end. The length of time that the reaction has proceeded is proportional to the distance between the points where the reactants mixed and where they were detected.

Schematic diagrams of the discharge–flow tubes used in this work are presented in figures 3.1 and 4.1. The tubes were constructed of Pyrex, and were 1.1 m long and 2.6 – 3.6 cm in internal diameter. Helium was used as the carrier gas. This gas was introduced to the upstream end and pumped through the tube. The carrier gas is the main component in the tube and thus serves to define the physical properties of the gas stream, such as the pressure, flow velocity and viscosity (Howard, 1979). It also maintains the reactants at the same temperature as the flow tube walls, controls diffusion and acts as the third body in termolecular reactions. Helium is a common choice as a result of its inertness, high thermal conductivity and excellent diffusion characteristics. The reactants entered the flow tube *via* ports and side arms. One of the tubes was also fitted with a sliding injector.

Additional flows of helium were often used to flush the reactants into the tube. Atoms were generated with microwave discharges or by thermal dissociation. These species were used to create the radicals of interest *via* titration reactions (for example, see section 4.2.2 for details of the titration reaction used to generate Cl atoms). Kinetic measurements were made by varying the distance that the reactants were in contact, either through the use of several different ports or by repeatedly adjusting the position of the sliding injector. The internal surfaces of the flow tube and the sliding injector were coated with an inert halocarbon wax to minimize the loss of reactive species to the walls.

An important characteristic of a gas stream, such as that which passes through a flow tube, is the Reynold's number, R_e, a dimensionless number that is a function of the internal radius of the flow tube, r, and the average linear flow velocity, u, the density, ρ, and the viscosity, η, of the gas:

$$R_e = \frac{2ru\rho}{\eta}. \qquad \text{(E2.1)}$$

For values of R_e of less than about 2000, the flow is said to be laminar. Values greater than 2000 correspond to turbulent flow. The flow tubes in this work were operated at $R_e < 50$, i.e. under laminar flow conditions. The velocity profile of a gas stream under such a regime is parabolic; that is, the gases near the centre of the flow tube travel faster than those near the walls (Brown, 1978). Consequently, it is possible for a radial concentration gradient of the reactant species to exist, as the length of time that the reaction has been proceeding in the middle of the tube is shorter than the reaction time at the edges. This gradient can be exacerbated by wall reactions. However, if the radial diffusion of the gases is fast compared to the homogeneous and heterogeneous losses, then the concentration gradient can be counteracted. As a result, the behaviour of the gas stream in the tube can be approximated to a 'plug flow', where all species are assumed to be travelling along the flow tube with the same linear flow velocity.

The axial diffusion of reactants is also possible in a flow tube (Howard, 1979). This phenomenon is a consequence of the decrease in concentration of the reactants that, by the very nature of flow experiments, exists along the length of the tube. Axial diffusion

causes the reactants to travel at a greater velocity than the other gases. For the plug-flow approximation to be valid, the effects of axial diffusion must be insignificant.

The plug-flow assumption permits the distance, d, that the reactants have been in contact to be related to the reaction time, t, *via* the simple expression:

$$t = \frac{d}{u} \qquad \text{(E2.2)}$$

However, there may be some instances when the plug-flow approximation is not appropriate. In these cases, the values of t obtained through the application of E2.2 will be incorrect. Fortunately, this situation is easily rectified. Details of the necessary corrections for axial and radial diffusion are presented in section 2.4.4.

The average linear flow velocity, u, is defined as:

$$u = \frac{\mathrm{d}v}{\mathrm{d}t} \Big/ A \qquad \text{(E2.3)}$$

where $\mathrm{d}v/\mathrm{d}t$ is the volume flow with time and A is the cross-sectional area of the flow tube, equal to πr^2. E2.3 may also be expressed as:

$$u = \frac{F\,T\,R}{P\,A\,N_{\mathrm{A}}} \qquad \text{(E2.4)}$$

where F is the total flow of gas, T is the temperature, R is the gas constant, P is the flow-tube pressure and N_{A} is Avogadro's constant.

It should be noted that the gas pressure in a discharge–flow tube is not uniform: as the gases are introduced at one end and are pumped from the other, a small pressure drop necessarily exists along the length of the tube. Thus care is required when determining the pressure. Ideally, measurements should be made in the middle of the region in which the reaction is takes place, in order to obtain a representative value. If measurements are made at an alternative position, then they can be corrected with the Poiseuille equation:

$$P_1^2 - P_2^2 = \frac{16\,F\,l\,\eta\,RT}{\pi\,r^4\,N_A} \qquad \text{(E2.5)}$$

where P_1 is the pressure at the ideal position, P_2 is the pressure at the alternative position and l is the distance between the two.

The concentration of a species X added to the flow tube can be determined by:

$$[\mathrm{X}] = \frac{f_X\,N_A\,P}{F\,R\,T} \qquad \text{(E2.6)}$$

where f_X is the flow rate of X. Concentrations of species generated in the flow tube can be monitored at the downstream end. It is possible to couple a variety of detection methods to discharge–flow tubes; several of the techniques are described in the next section.

2.3 Detection techniques

This thesis reports the use of fluorescence and mass spectrometric detection methods. As much of the work was concerned with the construction of several of these systems, the following discussion is presented in some detail.

2.3.1 Fluorescence

An electronically excited species may lose energy in several ways. A common process is physical quenching, which involves the transfer of energy to surrounding molecules as vibrational, rotational and translational energy (Atkins, 1994). Excited species may also undergo a chemical change (Wayne, 1988). For example, section 2.3.2.2.1 describes a molecule losing energy *via* both the expulsion of an electron and dissociation, following excitation by electron impact. Energy may also be lost *via* a radiative decay process such as fluorescence.

The initial step in fluorescence is the absorption of a photon that promotes the molecule (or atom) to an electronically excited state. Should the neighbouring molecules not be able to accept the large quantum of energy required to return the excited molecule to its ground electronic state, the energy may be lost as a spontaneous emission of radiation, known as fluorescence. If the excited species is vibrationally quenched before it fluoresces, the emitted light is of a longer wavelength than the incident radiation. However, if fluorescence occurs before vibrational deactivation, the emitted light may include photons of the same wavelength as the exciting radiation. Such emission is known as resonance fluorescence (RF). Atoms and simple molecules at low pressures in the gas phase exhibit RF (Wayne, 1988). Low pressures ensure that the spontaneous emission rate exceeds the collision frequency. RF of complex molecules is rare because other options for energy transfer, e.g. dissociation, are possible.

Two fluorescence methods were employed in the work presented in chapters 3 and 4, namely, RF and laser-induced fluorescent (LIF).

2.3.1.1 Resonance fluorescence (RF)

RF has been used to observe several atomic and molecular species, for example, H, N, Cl, I and OH (Pilling and Seakins, 1999). The apparatus is comprised of a lamp, a cell fitted to the flow tube, and a detector. The lamp is positioned perpendicular to the cell and consists of a Pyrex tube fitted with a microwave-discharge cavity. An inert carrier gas, such as helium or argon, and trace quantities of a precursor species (e.g. H_2, Cl_2 or H_2O) are passed through the lamp at a pressure of <1 Torr. The gases are excited in the cavity and some of the resulting atoms or molecules derived from the precursor species are electronically excited by collisions with energetic carrier gas atoms or electrons. These excited species fluoresce and the light is directed into the cell. Some of the flow-tube gases passing through the cell that are identical to the fluorescing species in the lamp will absorb the radiation. These atoms or molecules undergo RF, emitting light in all directions. The fluorescence is monitored with a detector, such as a photomultiplier tube (PMT) (see section 2.3.1.3), positioned at right angles to the lamp.

RF is a highly specific, sensitive and simple technique. Its specificity arises from the sharpness of atomic transitions: it is unlikely that two atomic species will fluoresce at the

same wavelengths. RF involving molecular species is less specific as molecular transitions are much broader. The sensitivity of the technique arises from the ability to monitor the fluorescence at right angles to the lamp which means that the excitation radiation does not contribute to the signal and only the RF is measured (Finlayson-Pitts and Pitts Jr, 1986). (In practice, some scattered lamp light will be detected but collimation of the incident light and blackening of the internal surfaces of the cell can reduce the intensity of this interference). Thus RF can offer a greater sensitivity than can be achieved with an absorption method of equal simplicity, as such techniques require small changes in the highly intense incident radiation to be measured. However, RF does have one particular disadvantage when compared to absorption methods in that it only provides a relative measure of the abundance of a species. To determine absolute concentrations the system must be calibrated.

2.3.1.2 Laser-induced fluorescence (LIF)

Fluorescence detection techniques can be made even more sensitive through the use of lasers as the source of the incident radiation. This enhanced sensitivity is the result of the high intensity of laser light — it causes more molecules to be electronically excited and thus increases the intensity of the resulting fluorescence (Finlayson-Pitts and Pitts Jr, 1986). LIF has found great application in the selective detection of a variety of molecular species, such as OH, NO_2 and CH_3O, as the wavelength of the laser light can be precisely tuned to match a particular rovibronic transition (Mellouki and Le Bras, 1999). The LIF apparatus is comprised of a laser system, a detection cell and a detector. The detector used in the LIF equipment described in this thesis was a PMT: see section 2.3.1.3. The principles of laser action are now briefly discussed.

2.3.1.2.1 Lasers

The word 'laser' is an acronym that stands for **l**ight **a**mplification by stimulated **e**mission of **r**adiation (Hollas, 1993). As previously discussed, an excited molecule may emit radiation spontaneously to return to the ground state. However, an excited species can also be stimulated to emit a photon by the presence of radiation of the same frequency. It is this process upon which the action of lasers depends.

When exposed to light, the probability that a molecule will undergo absorption or stimulated emission is exactly the same (Atkins, 1994). Thus at thermal equilibrium there will be a net absorption of the incident radiation because most of the molecules will be in the ground state. For stimulated emission to be the dominant process, it is necessary for a population inversion to exist. This inversion is created by 'pumping' (exciting) the molecules by applying optical or electrical energy. It is also necessary for the molecules to have several upper energy levels, as pumping a system with only one upper state will initially cause the population of the upper and ground states to be the same, and then further pumping will result in equal rates of absorption and stimulated emission. One of the lasers employed in the work reported in chapter 3 has four energy levels: three upper and one ground (*Quanta-Ray GCR-11 Pulsed Nd:YAG Laser Instruction Manual*, 1990). A schematic diagram of this system is depicted in figure 2.1. The active medium is pumped from the ground state E_1 to the excited state E_2. Relaxation back to the ground state is a slow process, and instead the excited species quickly reach level E_3 by losing some energy *via* non-radiative decay. This state is relatively long-lived, which allows the population to rapidly increase. As level E_4 was initially unoccupied, a population inversion has been created and the application of a photon can stimulate a radiative transition between E_3 and E_4. The population inversion is maintained by the fast relaxation of the excited species from E_4 to the ground state.

The active material is housed in the laser cavity, which is essentially a region bounded by two highly reflective mirrors (Hollas, 1993). Following pumping, a photon may be emitted spontaneously, and travel through the medium. It may stimulate the emission of another photon, which may in turn stimulate further emissions. The photons are reflected back and forth through the cavity. The cavity mirrors are precisely aligned so that only certain wavelengths of radiation are resonant. Any other frequencies present undergo destructive interference. One of the mirrors is less reflective than the other so as to allow 1 – 10 % of the radiation to emerge as a laser beam. As a result of the processes just described, the beam is of a high intensity, monochromatic and coherent. It is also highly collimated as only photons that travel parallel to the axis of the cavity are able to undergo multiple reflections (Atkins, 1994).

Lasers such as the four-level devices described earlier operate at discrete frequencies. A variety of techniques exist that allow the laser light to be precisely tuned to match a

Figure 2.1. A schematic diagram of the transition scheme of a four-level laser.

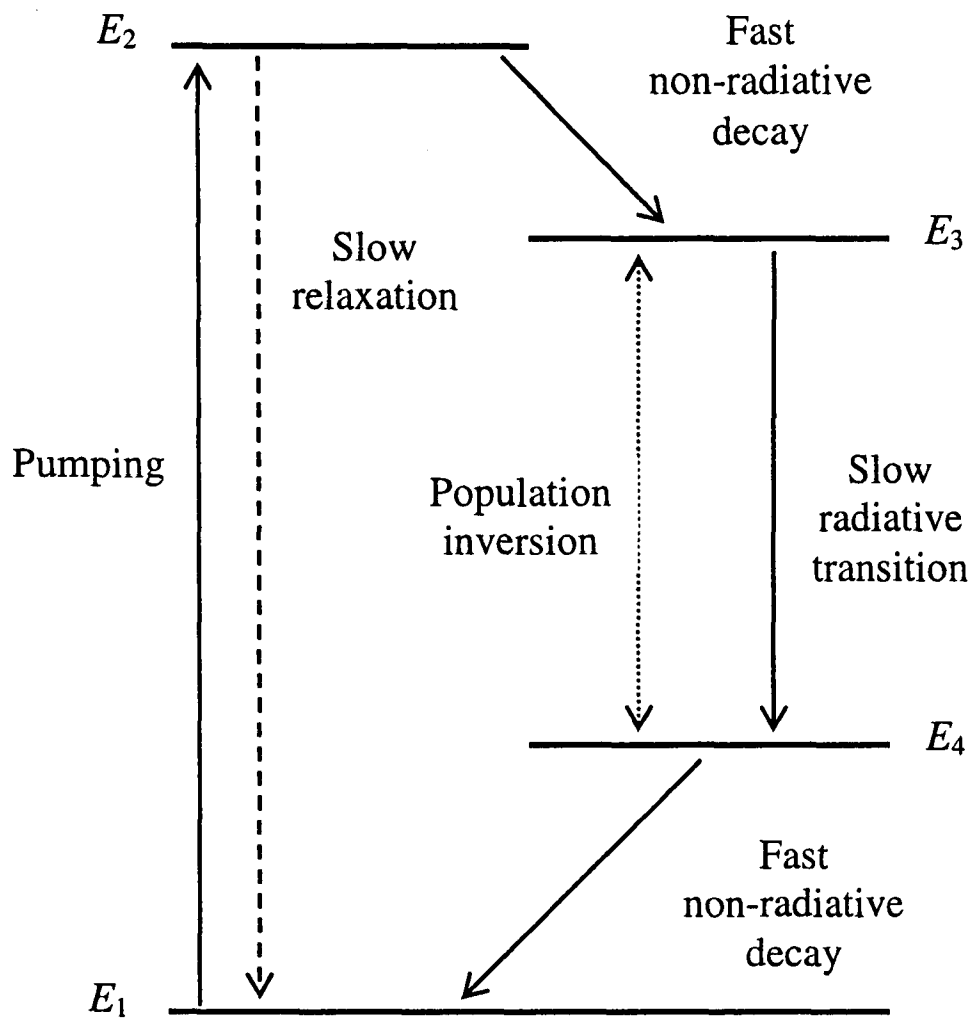

particular transition in the species of interest. Second, third and fourth harmonics can be generated by passing the beam through suitable crystals (Hollas, 1993). The inclusion of a dye laser will also permit the system to be tuned over a narrow range of frequencies. The active materials in this type of laser are large organic compounds containing conjugated bonds. The absorption of radiation by these dye molecules causes their π electrons to be excited from the ground state, S_0, to the first excited singlet state, S_1 (*Quanta-Ray PDL-3 Pulsed Dye Laser Instruction Manual*, 1989). The dye compounds quickly return to S_0 by spontaneously emitting photons. Although only two electronic levels are involved, dye lasers are formally four-level devices because transitions between the rovibronic sublevels of S_0 and S_1 take place. Dye lasers have broad spectral outputs (~20 – 30 nm) because first, a large number of transitions between the excited and ground states are possible, and secondly, these transitions are broadened by interactions with the solvent in which the dye is dissolved. Dye lasers are generally pumped by another laser.

The dye solution flows through the cavity and a diffraction grating is used to select the desired wavelength.

The laser system described in chapter 3 employed both doubling and mixing crystals, and a dye laser to produce the required excitation wavelength. These devices are not very efficient (Hollas, 1993) and thus high-intensity pumping was necessary to generate a laser beam of reasonable power. The intensity of the pump radiation was increased by Q-switching (*Quanta-Ray GCR-11 Pulsed Nd:YAG Laser Instruction Manual*, 1990). This technique involves lowering the quality of the resonance cavity to prevent photons oscillating between the mirrors and stimulating the emission of other photons. As a result, a large population inversion is achieved. The resonance characteristics of the cavity are briefly restored to produce a short pulse of high-intensity light.

2.3.1.3 Detection of fluorescence

The detector used in the RF and LIF systems described in this thesis was a photomultiplier tube (PMT). This device consists of a photocathode, focusing electrodes, an electron multiplier and an anode, all housed in a vacuum tube (Hamamatsu, 1988). When light falls upon the photocathode, electrons are released as a result of the photoelectric effect. These electrons are directed towards the electron multiplier by the focusing electrodes. The electrons strike the first dynode of the multiplier, causing the ejection of secondary electrons. This process is repeated at each dynode in the multiplier. The resulting current is collected on the anode and converted to a voltage. PMTs can detect very low intensities of radiation and are widely used for fluorescence detection.

2.3.2 Mass Spectrometry

Mass spectrometry involves the following procedures:

- Sample introduction
- Ionization
- Mass analysis
- Detection.

These operations can be achieved by a wide variety of techniques. Chapters 5 and 7 report the design and construction of an electron-impact mass spectrometer (EIMS) and a chemical-ionization mass spectrometer (CIMS). The techniques employed in these instruments are now discussed.

2.3.2.1 Sample introduction

All mass spectrometers operate at high vacuum. This condition is necessary to allow the ions to reach the detector. Higher pressures would cause collisions with other gaseous molecules, which would knock the ions off trajectory. Such collisions would reduce ion transmission and peak resolution, and may also result in reaction, so complicating the mass spectrum (de Hoffmann and Stroobant, 2002).

When coupling a mass spectrometer to a higher-pressure system, such as a discharge–flow tube, a means of introducing the sample is required that does not compromise the vacuum. A pinhole or nozzle can be used to admit a sample of the flow-tube gases continuously and an efficient pumping system maintains the high vacuum.

2.3.2.2 Ionization

Two types of ionization were employed in this work, electron impact (EI) and chemical ionization (CI). EI is one of the simplest ionization methods but is a very energetic process, which can cause molecular ions to dissociate extensively. CI allows greater control over the molecular ions produced and the energy involved but is more complex.

2.3.2.2.1 Electron impact (EI)

EI involves bombarding the sample with high-energy electrons. During the collision event, sufficient energy is transferred to the sample molecules (or atoms) to cause an electron to be expelled, resulting in the production of the parent molecular cation:

$$M + e^- \rightarrow M^+ + 2e^-. \qquad \text{(R2.1)}$$

An electron energy of 70 eV is typically used in EI, with approximately 20 eV being absorbed by the molecule during the collision (Watson, 1997). As the ionization energies of many compounds are only about 10 eV, the molecule absorbs more energy than is required for ionization. The excess energy can cause spontaneous dissociation of the ion. The fragmentation may be so extensive that the parent molecular ion does not appear in the mass spectrum.

The EI source consists of a tungsten or rhenium filament ribbon and several electrostatic plates or lenses (Chapman, 1995). The electrons are generated by thermionic emission from the filament and are accelerated by an anode plate into the path of the sample molecules where they collide and form ions. The electron current is measured on the anode and held constant by feedback control of the heating current in order to generate a constant ion current. The potential difference between the filament cathode and the anode plate dictates the electron energy. The ions are extracted from the ionization region and accelerated towards the mass analyser by several electrostatic plates.

The extensive fragmentation and complicated spectra characteristic of EI mean that the technique is not ideal for the detection of species, particularly large organic molecules, in complicated mixtures of gases. Alternative forms of ionization, such as chemical ionization, have been found to be more appropriate for the analysis of such mixtures.

2.3.2.2.2 Chemical ionization (CI)

CI is a method of producing ions with little excess energy. Thus less fragmentation occurs and the parent molecular ion peak is very intense in the mass spectrum. Ionization takes place *via* reaction of reagent ions with the sample molecules. Many different types of CI reaction are possible. Some examples are listed in table 2.1.

The reagent ions are often generated by EI. Consequently, the CI source can be similar to the EI source, with the exception that the operating pressure is several orders of magnitude higher (Watson, 1997). EI is performed at low pressures, typically 10^{-5} Torr, to minimise ion–molecule collisions. Ionization by CI is dependent on such collisions, so the pressure in the source must be much higher (>1 Torr). This high-pressure

Table 2.1 . Typical CI ion–molecule reactions. Note that many other types of reaction and reagent ions are possible.

Reaction	Example	
Charge transfer	$M + Ar^+ \rightarrow M^+ + Ar$	(R2.2)
Electron capture	$M + e^- \rightarrow M^-$	(R2.3)
Proton transfer	$M + CH_5^+ \rightarrow (M + H)^+ + CH_4$	(R2.4)
Cl^- attachment	$M + Cl^- \rightarrow (M + Cl)^-$	(R2.5)
Adduct formation	$M + CH_3CO^+ \rightarrow (M + CH_3CO)^+$	(R2.6)

requirement has two main consequences. First, the electron energy must be greater than that used in EI to ensure efficient penetration of the electrons into the gas. Secondly, the ion source must be separated from the rest of the mass spectrometer so that the high vacuum can be maintained. The source can either be located in another chamber or in an enclosure within the MS chambers.

The reagent and sample gases are often introduced to the source simultaneously. However, the reagent gas is present in a large excess (typically the partial pressure of the sample gas will be 10^{-5} Torr if that of the reagent gas is 1 Torr) so that it is preferentially ionized by the electrons. The resulting ions mostly collide with other reagent molecules to produce reagent ions characteristic of the reagent gas used. For example, the reagent ion for H_2–CI is H_3^+ (de Hoffmann and Stroobant, 2002), generated as follows:

$$H_2 + e^- \rightarrow H_2^+ + 2e^- \quad \text{(R2.7)}$$

$$H_2^+ + H_2 \rightarrow H_3^+ + H \quad \text{(R2.8)}$$

$$H + H_2^+ \rightarrow H_3^+. \quad \text{(R2.9)}$$

Ionization by H_3^+ will produce a protonated molecule. As can be seen from table 2.1, many different forms of the molecular ion are possible in CI, including the molecular cation and anion, and adduct species.

In addition to the ability to choose the type of molecular ion, control of the degree of internal excitation, and hence fragmentation, of the molecular ion is possible with CI. This control is achieved by careful selection of the reagent ion. For example, consider proton-transfer CI of acetone using H_3^+ and H_3O^+. Note that the latter reagent ion is generated from H_2O. The proton affinity (PA), the negative of the enthalpy change for the protonation reaction, can be used to calculate the enthalpies of these CI reactions. The PA of H_2 is 4.37 eV, the PA of H_2O is 7.22 eV and the PA of acetone is 8.42 eV. Thus, reaction with both reagent ions occurs exothermically:

$$CH_3COCH_3 + H_3^+ \rightarrow (CH_3COCH_3{+}H)^+ + H_2 \qquad \text{(R2.10)}$$

$$\Delta H_{reaction} = -(8.42 - 4.37\ \text{eV}) = -4.05\ \text{eV} \qquad \text{(E2.7)}$$

$$CH_3COCH_3 + H_3O^+ \rightarrow (CH_3COCH_3{+}H)^+ + H_2O. \qquad \text{(R2.11)}$$

$$\Delta H_{reaction} = -(8.42 - 7.22\ \text{eV}) = -1.20\ \text{eV} \qquad \text{(E2.8)}$$

However, the acetone mass spectra produced by the two CI processes are vastly different. The excess energy of the H_2–CI reaction is just over 4 eV. It lodges principally in the protonated acetone molecule and causes extensive dissociation (Lambert *et al.,* 1998). The exothermicity of the H_2O–CI reaction is 1.2 eV, which is less than the enthalpies of the bonds in acetone and thus fragmentation does not occur (Sprung *et al.,* 2001).

2.3.2.3 Mass analysis

Mass analysers separate ions according to their mass-to-charge ratios. Several different types of analyser are available, which use either electric or magnetic fields to achieve separation. The mass spectrometer described in this thesis employs a quadrupole filter, which separates ions using a combination of direct-current (DC) and radiofrequency (RF) fields.

The quadrupole filter consists of four parallel rods of circular, or ideally hyperbolic, cross-section (Lambert *et al.,* 1998). A schematic diagram is shown in figure 2.2. Diagonally opposite poles are electrically connected. A DC voltage of opposite sign is applied to the each pair. An oscillating RF voltage is also applied to the poles. The ions,

which have been accelerated out of the source and towards the analyser, enter the central space between the rods and are subjected to the quadrupole field. Positive ions will be drawn towards negative rods and repelled by positive rods. When the RF voltage causes the polarity to change, the ions move in the opposite direction. Thus, the ions perform complex motions through the quadrupole as the RF voltage oscillates. For a given magnitude of DC and RF voltages, only ions of a particular *m/z* ratio will successfully traverse the quadrupole to reach the detector. All other ions will perform unstable oscillations and collide with the rods.

Figure 2.2. (a) A schematic diagram of a quadrupole mass spectrometer. The dashed line indicates the path of an ion performing stable oscillations. (b) The voltages applied to the pairs of poles. U is the DC potential, V is the amplitude of the RF potential, ω is the angular frequency of the RF field and t is time. When the polarity of the RF voltage changes, the polarities of the poles change.

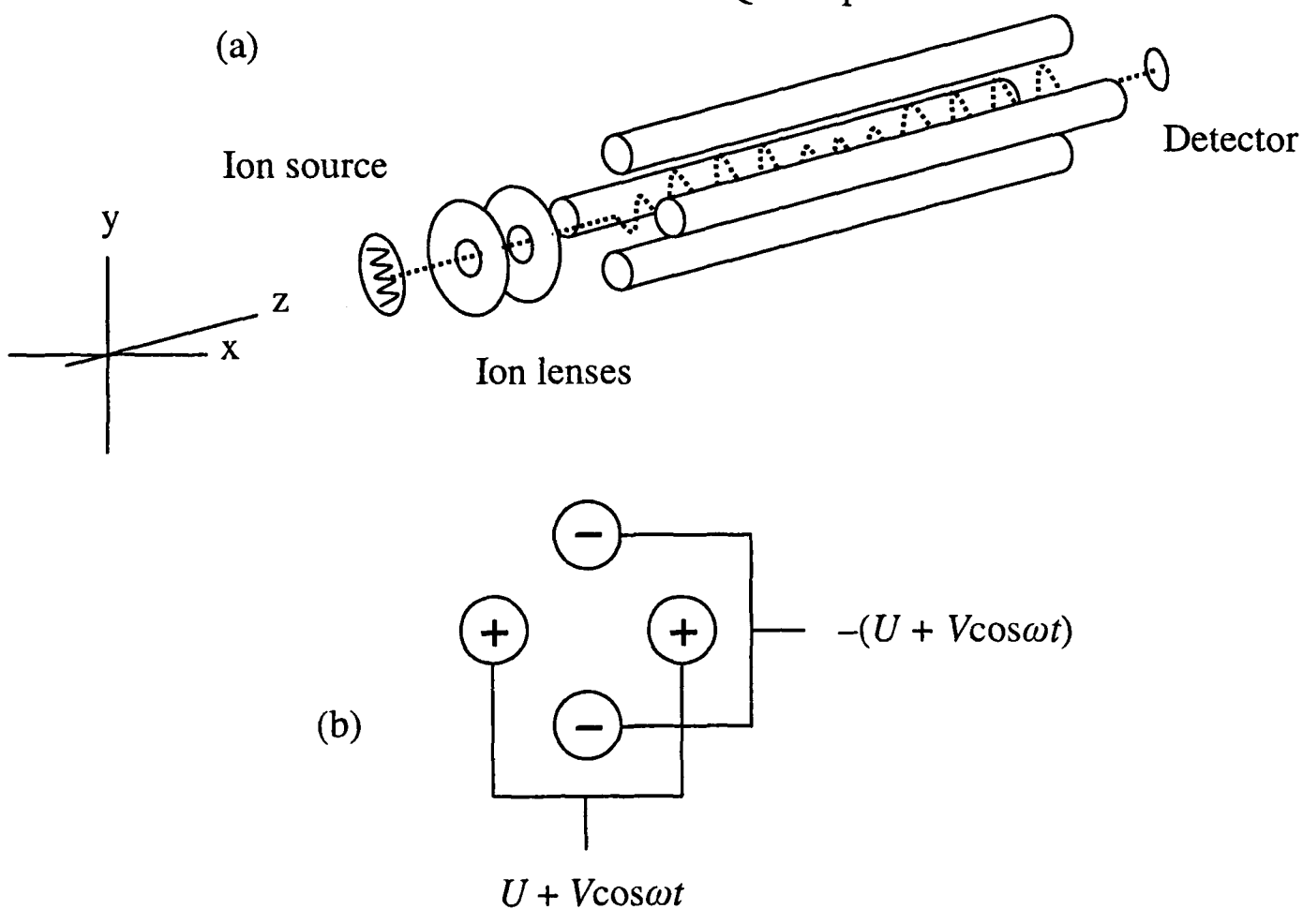

The motions of ions in the quadrupole are fully described by the Mathieu equation:

$$\frac{d^2u}{d\xi^2} + (a_u - 2q_u \cos 2\xi)u = 0 \qquad \text{(E2.9)}$$

where

$$a_u = 8zeU/mr_0^2\omega^2 \qquad \text{(E2.10)}$$

$$q_u = 4zeV/mr_0^2\omega^2 \qquad \text{(E2.11)}$$

$$\xi = \omega t/2. \qquad \text{(E2.12)}$$

The term u represents the position of the ion along the x or y axis, ξ is a function of time, and a_u and q_u are dimensionless parameters related to the DC and RF voltages, respectively. z is the charge of the ion, e is electronic charge, U is the DC potential, V is the amplitude of the RF potential, m is the mass of the ion, r_0 is the radius of the quadrupole, ω is the angular frequency of the RF field and is equal to $2\pi\nu$, where ν is the frequency of the RF, and t is time (Dawson and Douglas, 2000).

For a given quadrupole, r_0 is constant, ω is held constant and U and V are variables. Solutions of the Mathieu equation for a particular ion are of two types: those where the displacement of the ion along the x and y axes is less than r_0, indicating that the ion avoids the poles, and those where the displacement is greater than r_0, representing an unstable trajectory. The conditions for stability can be represented on an a_u–q_u diagram (de Hoffmann and Stroobant, 2002). A representation of such a diagram is shown in figure 2.3. It can be seen that a range of a_u and q_u values exist that relate to stable ion trajectories. However, in practice the values of a_u and q_u are limited by operating the quadrupole at a fixed ratio of DC and RF potentials. Thus the only masses to perform stable oscillations are those that correspond to the region where the operating line intersects the area of stability. In this way, an ion of m/z = 100 will be transmitted and ions of m/z = 99 and 101 will not. The resolution can be adjusted by changing the ratio of DC and RF voltages, which moves the operating line further into or out of the area of stability. The theoretical 'infinite' resolution is, in fact, obtained for $U/V \sim 0.168$, but such a value also implies zero transmission (*Extranuclear Laboratories Quadrupole*

Power Supply Instruction Manual, 1974). In practice, a ratio of DC to RF is used that is a compromise between resolution with transmission.

Figure 2.3. A representation of an a_u–q_u diagram for a quadrupole filter. The shaded area indicates all values of a_u and q_u that correspond to stable trajectories of an ion through the quadrupole field.

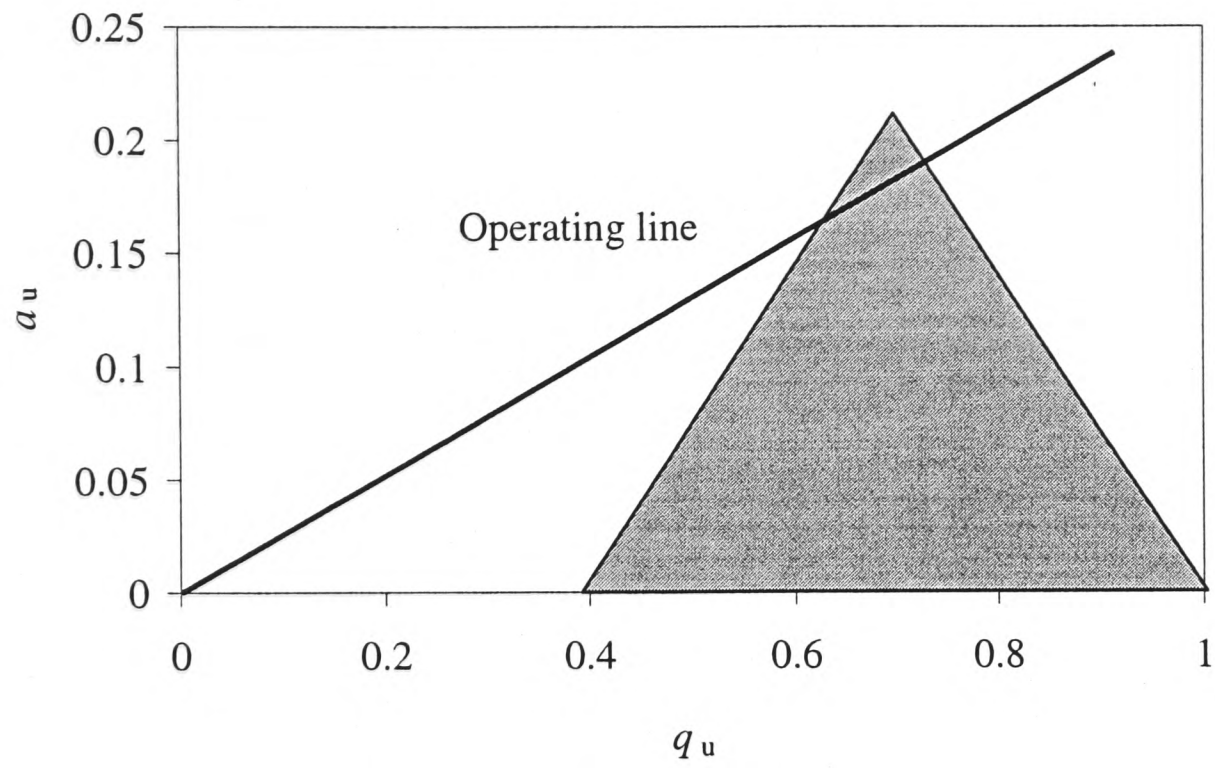

A mass spectrum is obtained by scanning the magnitude of the DC and RF voltages whilst keeping the ratio constant. As can be seen from the definitions of a_u and q_u, U and V are proportional to m/z, and so increasing the magnitude of the voltages brings ions of increasing mass into the area of stability.

2.3.2.4 Detection of ions

The MS described in this thesis employs a continuous electron multiplier (CEM), also known as a channel electron multiplier, to detect the ions that pass through the quadrupole filter. The CEM is a continuous dynode made of a tube of lead-doped glass, a material with good secondary emission properties and high electrical resistivity

(Chapman, 1995). The latter characteristic allows voltages to be applied to the ends of the tube so generating a potential gradient along its length. The beam of ions exiting the mass analyser is directed into one end of the CEM. When an ion of suitable kinetic energy collides with the inner surface of the multiplier, secondary electrons are expelled. These electrons are accelerated by the voltage gradient into the CEM, where they also collide with the walls, causing the ejection of more secondary electrons. This process is repeated many times, causing a cascade of electrons to be released. The resulting current (properly speaking, charge) is converted to a voltage by a pre-amplifier. The gain of the CEM depends on the applied voltage. At a potential difference of 2.5 kV, one ion can cause 10^8 electrons to be ejected.

2.4 Data analysis

The aim of a kinetic experiment is to determine the rate constant for a reaction. Consider a simple bimolecular reaction:

$$A + B \rightarrow C + D. \qquad \text{(R2.12)}$$

The rate of this process may be related to the concentrations of the reactants *via* the rate law (Atkins, 1994):

$$Rate = k_{2.12}[A][B] \qquad \text{(E2.13)}$$

where $k_{2.12}$ is the rate constant. Measures of the rate of R2.12 are the rate of consumption of the reactants A and B, and the rate of formation of the products C and D:

$$Rate = -\frac{d[A]}{dt} = -\frac{d[B]}{dt} = \frac{d[C]}{dt} = \frac{d[D]}{dt}. \qquad \text{(E2.14)}$$

The rate constant was generally derived in the work reported in this thesis by following the decay of the reactants.

2.4.1 *Pseudo*-first-order analysis

The determination of $k_{2.12}$ can be simplified by application of the isolation method, in which one of the reactants, say B, is present in such a large excess that its concentration can be effectively regarded as remaining constant throughout the course of the reaction (Pilling and Seakins, 1999). The change in concentration of the other reactant, A, referred to as the kinetic species, is monitored as a function of time. The data can then be treated with a simple *pseudo*-first-order analysis. The rate law can be expressed as:

$$-\frac{\mathrm{d[A]}}{\mathrm{d}t} = k'_{2.12}[\mathrm{A}] \tag{E2.15}$$

where

$$k'_{2.12} = k_{2.12}[\mathrm{B}]_0 . \tag{E2.16}$$

$k'_{2.12}$ is the *pseudo*-first-order rate constant and $[\mathrm{B}]_0$ is the initial concentration of B. Separation of the variables [A] and t in E2.15, followed by integration between $t = 0$ and $t = t$:

$$\int_{[\mathrm{A}]_0}^{[\mathrm{A}]} -\frac{\mathrm{d[A]}}{[\mathrm{A}]} = \int_0^t k'_{2.12}\mathrm{d}t \tag{E2.17}$$

yields:

$$\ln\frac{[\mathrm{A}]_0}{[\mathrm{A}]} = k'_{2.12}t \tag{E2.18}$$

where $[\mathrm{A}]_0$ is the initial concentration of A. A plot of $\ln([\mathrm{A}]_0/[\mathrm{A}])$ versus t, a 'first-order plot', should yield a straight line of gradient $k'_{2.12}$. The value of the second-order rate constant $k_{2.12}$, may then be calculated from E2.16. Usually, several measurements of $k'_{2.12}$

are made for different excess concentrations of B, and a 'second-order plot' of $k'_{2.12}$ versus [B], with a straight line of slope $k_{2.12}$ is derived.

However, the kinetic species may also be lost *via* wall reactions:

$$\text{A + wall} \rightarrow \text{products.} \tag{R2.13}$$

The rate law for this process is:

$$-\frac{\mathrm{d[A]}}{\mathrm{d}t} = k_{\mathrm{w}}[\mathrm{A}] \tag{E2.19}$$

where k_{w} is the first-order rate constant for wall loss. Integration yields:

$$\ln\frac{[\mathrm{A}]_0}{[\mathrm{A}]_{\mathrm{w}}} = k_{\mathrm{w}}t \tag{E2.20}$$

where $[\mathrm{A}]_{\mathrm{w}}$ is the concentration of A remaining after wall losses over time t. The rate law that describes the loss of A as a result of reaction with both B and the walls is:

$$-\frac{\mathrm{d[A]}}{\mathrm{d}t} = \left(k'_{2.12} + k_{\mathrm{w}}\right)[\mathrm{A}] \tag{E2.21}$$

which may by integrated to give:

$$\ln\frac{[\mathrm{A}]_0}{[\mathrm{A}]} = \left(k'_{2.12} + k_{\mathrm{w}}\right)t\,. \tag{E2.22}$$

Substitution of E2.20 into E2.22 yields:

$$\ln\frac{[\mathrm{A}]_{\mathrm{w}}}{[\mathrm{A}]} = k'_{2.12}t\,. \tag{E2.23}$$

E2.23 is the actual *pseudo*-first order expression used to analyse data as it eliminates the need to quantify k_w. Measurements of [A] in the presence and absence of B after time t are taken. A first-order plot of $\ln([A]_w/[A])$ versus t yields a straight line of slope $k'_{2.12}$, and a second-order plot of $k'_{2.12}$ versus $[B]_0$ gives a straight line of gradient $k_{2.12}$. However, this treatment is only valid if k_w is not affected by the presence of B. An additional benefit of the *pseudo*-first-order treatment is that it is not necessary to quantify concentrations of A absolutely. All that is required is the ratio of the magnitude of the signals that correspond to $[A]_w$ and [A]. (Although an approximation of the absolute concentration is needed in order to ensure that the *pseudo*-first-order condition ([B]>>[A]) is achieved). Finally, it should be noted that in the rest of this work, E2.23 is expressed, through convention, as being equivalent to E2.18.

2.4.2 Second-order analysis

There may be cases where it is not possible to derive a rate constant with a *pseudo*-first-order treatment. For example, the self-reaction of a species:

$$A + A \rightarrow \text{products.} \qquad \text{(R2.14)}$$

demands a second-order analysis. The rate law for this process is:

$$-\frac{d[A]}{dt} = 2k_{2.14}[A]^2 \qquad \text{(E2.24)}$$

which has the integrated solution (Laidler, 1987):

$$\frac{1}{[A]} = \frac{1}{[A]_0} + 2k_{2.14}t\,. \qquad \text{(E2.25)}$$

A plot of 1/[A] versus t will yield a straight line of slope $2k_{2.14}$ and intercept $1/[A]_0$.

A second-order analysis is also obviously required when deriving the rate constant for:

$$A + B \rightarrow C + D \qquad \text{(R2.12)}$$

but when neither reactant is in a suitable excess. The integrated rate equation is:

$$\frac{1}{[B]_0 - [A]_0} \ln\left(\frac{[B]/[B]_0}{[A]/[A]_0}\right) = k_{2.12} t\,. \qquad \text{(E2.26)}$$

2.4.3 Simultaneous reactions

In some experiments, a reactant may be consumed by two or more reactions, for example:

$$A + B \rightarrow C + D \qquad \text{(R2.12)}$$

$$A + A \rightarrow \text{products.} \qquad \text{(R2.14)}$$

If reactant B is present in a suitable excess, then R2.12 may be considered as *pseudo*-first order. The rate of loss of A can be described by a mixed *pseudo*-first-order and second-order rate law (Pilling and Seakins, 1999):

$$-\frac{d[A]}{dt} = k'_{2.12}[A] + 2k_{2.14}[A]^2\,. \qquad \text{(E2.27)}$$

Integration yields:

$$\frac{[A]}{[A]_0} = \frac{k_{2.12}}{(2k_{2.14}[A]_0 + k_1)\exp(k_{2.12}t) - 2k_{2.14}[A]_0}\,. \qquad \text{(E2.28)}$$

If $k_{2.14}$ is known, then the value of $k_{2.12}$ may be easily calculated. However, if both rate constants are unknown, then E2.28 may be solved by employing a computer program to perform a non-linear two-parameter fit, which minimizes the sum of the squares of the differences between experimental and calculated ratios of $[A]/[A]_0$ as a function of time.

2.4.4 Diffusion corrections

The radial and axial diffusion of gases in a flow tube was previously discussed in section 2.2. In some cases, these processes may cause the plug-flow assumption to be invalid. Under such conditions, the reaction time will be erroneously calculated. However, this problem can be easily rectified for first-order conditions by adjustment of the value of the observed first-order rate constant, k'_{obs}, with the expression (Kaufman, 1984):

$$k'_{corr} = k'_{obs}\left(1 + \frac{k'_{obs}D}{u} + \frac{k'_{obs}r^2}{48D}\right) \qquad \text{(E2.29)}$$

where k'_{corr} is the corrected first-order rate constant, D is the diffusion coefficient of the reactant, u is the average linear flow velocity and r is the internal radius of the flow tube.

2.5 References

- Atkins, P. W., *Physical Chemistry*, 5th Edition, Oxford University Press, Oxford, 1994
- Brown, R. L., *J. Res. Natl. Bur. Stand. (US)*, 1978, **83**, 1
- Chapman, J. R., *Practical Organic Mass Spectrometry*, 2nd Edition, John Wiley and Sons, UK, 1995
- Dawson, P. H. and D. J. Douglas in *Encyclopedia of Spectroscopy and Spectrometry*, ed. J. C. Lindon, G. E. Tranter and J. L. Holmes, Academic Press, California, 2000, **3**, 1921
- de Hoffmann, E. and V. Stroobant, *Mass Spectrometry, Principles and Applications*, 2nd Edition, John Wiley and Sons, England, 2002
- *Extranuclear Laboratories Quadrupole Power Supply Instruction Manual,* Extranuclear laboratories, Pittsburgh, 1974
- Finlayson-Pitts, B. J. and J. N. Pitts Jr, *Atmospheric Chemistry: Fundamentals and Experimental Techniques,* John Wiley and Sons, New York, 1986
- *Photomultiplier Tubes*, Hamamatsu, Japan, 1988
- Hollas, J. M., *Modern Spectroscopy*, 2nd Edition, John Wiley and Sons, Chichester, 1993
- Howard, C. J., *J. Phys. Chem.*, 1979, **83**, 3

- Laidler, K. J., *Chemical Kinetics*, Harper and Row, New York, 1987
- Lambert, J. B., H. F. Shurvell, D. A. Lightner and R. G. Cooks, *Organic Structural Spectroscopy*, Prentice Hall, New Jersey, 1998
- Mellouki, A. and G. Le Bras, *Mater. Sci. Forum.*, 1999, **301**, 47
- Pilling, M. J. and P. W. Seakins, *Reaction Kinetics*, Oxford University Press, Oxford, 1999
- *Quanta-Ray PDL-3 Pulsed Dye Laser Instruction Manual*, Spectra-Physics, California, 1989
- *Quanta-Ray GCR-11 Pulsed Nd:YAG Laser Instruction Manual,* Spectra-Physics, California, 1990
- Sprung, D., C. Jost, T. Reiner, A. Hansel and A. Wisthaler, *J. Geophys. Res.*, 2001, **106**(D22), 28511
- Watson, J. T., *Introduction to Mass Spectrometry*, 3rd Edition, Lippincott-Raven, Philadelphia, 1997
- Wayne, R. P., *Principles and Applications of Photochemistry*, Oxford University Press, Oxford, 1988

Chapter 3 Laser-induced fluorescence of IO and the kinetics of some reactions of the radical

3.1 Introduction

The primary aim of the work described in this chapter was to detect IO radicals by laser-induced fluorescence (LIF). The LIF system would be coupled to a discharge–flow tube. A second aim was to explore the potential for the equipment to obtain kinetic information about some reactions of the IO radical. This aim took the form of a scoping exercise because the laser system was only available on loan from the Rutherford Appleton Laboratory for three months. If the discharge–flow tube/LIF apparatus proved itself to be a valuable tool for such studies, another application for a laser loan would be made.

Prior to this work, three other research groups had detected IO radicals with LIF and used the technique to obtain kinetic data (Inoue *et al.*, 1983; Turnipseed *et al.*, 1995; Hölscher *et al.*, 1998). Only two of the groups reported satisfactory sensitivities: Turnipseed *et al.* (1995) quoted a sensitivity of ~1×10^9 molecule cm^{-3} when averaging 100 laser shots for S/N = 1, and Hölscher *et al.* (1998) stated a sensitivity of 5×10^9 molecule cm^{-3} for S/N = 1. Since the work described in this chapter was undertaken, two other research groups have also successfully employed IO LIF (Allan and Plane, 2002; Dillon and Heard, 2003). All of these studies have involved the production of IO by pulsed-laser photolysis. The work presented here is the first report of the coupling of IO LIF to a discharge–flow tube.

The atmospheric chemistry of IO is discussed in chapter 1. Reactions of the radical with itself and other species, such as HO_2, NO_2, BrO and ClO, form parts of catalytic cycles that can deplete ozone in the troposphere and possibly in the stratosphere. Reaction with NO can also affect the ratio of NO_2 to NO in the atmosphere. Some of these reactions had already been studied using IO LIF. Two of these reactions:

$$IO + NO \rightarrow I + NO_2 \quad \text{(R3.1)}$$

$$IO + IO \rightarrow 2I + O_2 \quad \text{(R3.2a)}$$

$$\rightarrow OIO + I \quad \text{(R3.2b)}$$

$$\rightarrow I_2 + O_2 \quad \text{(R3.2c)}$$

$$+M \rightarrow I_2O_2 + M \quad \text{(R3.2d)}$$

were re-investigated. The rate constant for R3.1 is $(1.82 \pm 0.1) \times 10^{-11}$ cm^3 molecule^{-1} s^{-1} (Dillon and Heard, 2003). There is some disagreement between the values of $k_{3.2}$ listed in the literature. The most recent derivations of the rate constant lie in the range $(8 - 10) \times 10^{-11}$ cm^3 molecule^{-1} s^{-1} (e.g. Atkinson *et al.*, 1999; Vipond *et al.*, 2002), whereas earlier studies found $k_{3.2}$ to be equal to $(3 - 7) \times 10^{-11}$ cm^3 molecule^{-1} s^{-1} (e.g. Martin *et al.*, 1987; Barnes *et al.*, 1991). R3.2 is thought to proceed *via* four channels, although the branching ratios are still the subject of debate.

The reactions of IO with dimethylsulphide (DMS), isoprene and *trans*-2-butene:

$$IO + CH_3SCH_3 \rightarrow I + CH_3SOCH_3 \quad \text{(R3.3)}$$

$$IO + CH_2CCH_3CHCH_2 \rightarrow \text{products} \quad \text{(R3.4)}$$

$$IO + CH_3CHCHCH_3 \rightarrow \text{products} \quad \text{(R3.5)}$$

were also investigated. The chemistry of these organic species has been described in chapter 1. DMS is the main reduced-sulphur compound present in the marine boundary layer. Reaction with IO could potentially influence the rate of oxidation of DMS if the concentration of IO is sufficiently large (Finlayson-Pitts and Pitts Jr., 2000). The iodine atoms that are released will react with O_3 to regenerate IO, which can further oxidize DMS. This cycle also results in the depletion of ozone. The rate constant for R3.3 is small: $(1.6 \pm 0.1) \times 10^{-14}$ cm^3 molecule^{-1} s^{-1} (Knight and Crowley, 2001). Isoprene is the dominant VOC emitted by plants. *Trans*-2-butene is a VOC typically released from anthropogenic sources. The reactions of these two alkenes with the IO radical have not previously been studied.

3.2 Experimental details

3.2.1 The flow tube

A schematic diagram of the discharge–flow tube is shown in figure 3.1. The apparatus consisted of a Pyrex tube, 1.1 m long, with an internal diameter of 36.8 mm. Gases were introduced *via* a double-nested sliding injector, two large side arms and six smaller ports. The injectors and the internal surface of the flow tube were coated with a halocarbon wax (KMZ Chemicals Ltd) to create an inert surface that minimized the loss of radical species to the walls. The tube was pumped by a Rootes pump (Edwards EH250) backed by a two-stage rotary pump (Edwards E2M80). A butterfly valve was used to adjust the pumping efficiency. The FTP was measured using a 10 Torr capacitance manometer (Edwards Barocel 600) located approximately halfway along the section of the flow tube used to obtain kinetic data.

The upstream end of the flow tube was sealed with an aluminium block, which had a hole bored through the centre to allow passage of the outer sliding injector. The injector was a 1.5 m long, 8 mm internal diameter Pyrex tube. Its movement allowed reactants to be introduced at different positions along the length of the flow tube. A vacuum seal between the block and the injector was achieved with two O-rings (Youngs Scientific). The gap between the O-rings was evacuated with a rotary pump (AEI Ltd, Metrovac) to prevent air leaking into the flow tube. The inner sliding injector was a Pyrex tube of 1.5 m in length and 4 mm in internal diameter. Altering its position permitted control of the contact time between reactants inside the outer injector before they entered the flow tube. The inner injector was connected to the outer by a ¼ – ½ inch Cajon vacuum adapter.

The helium carrier gas (BOC, 99.996 %) flowed directly from the cylinder, through a series of purification traps (silica gel, diphosphorus pentoxide, and sodium and calcium aluminosilicate molecular sieve (4A, 5A and 13X) cooled with liquid nitrogen (all trap materials were supplied by BDH)), and into the flow tube *via* a side arm. A 10 SLPM mass flow controller (Brooks 5816-1A21) — a valve coupled to a thermal-conductivity flow sensor — regulated the flow, and the backing pressure was monitored with a dial manometer (De Wit). Additional flows of carrier gas were employed when the sliding

injector or the other side arm were in use. ~2.5 SLPM ball flow-meters (Jencons RS2) fitted with needle valves (Nupro) were used to regulate this helium.

Figure 3.1. A schematic diagram of the discharge–flow tube.

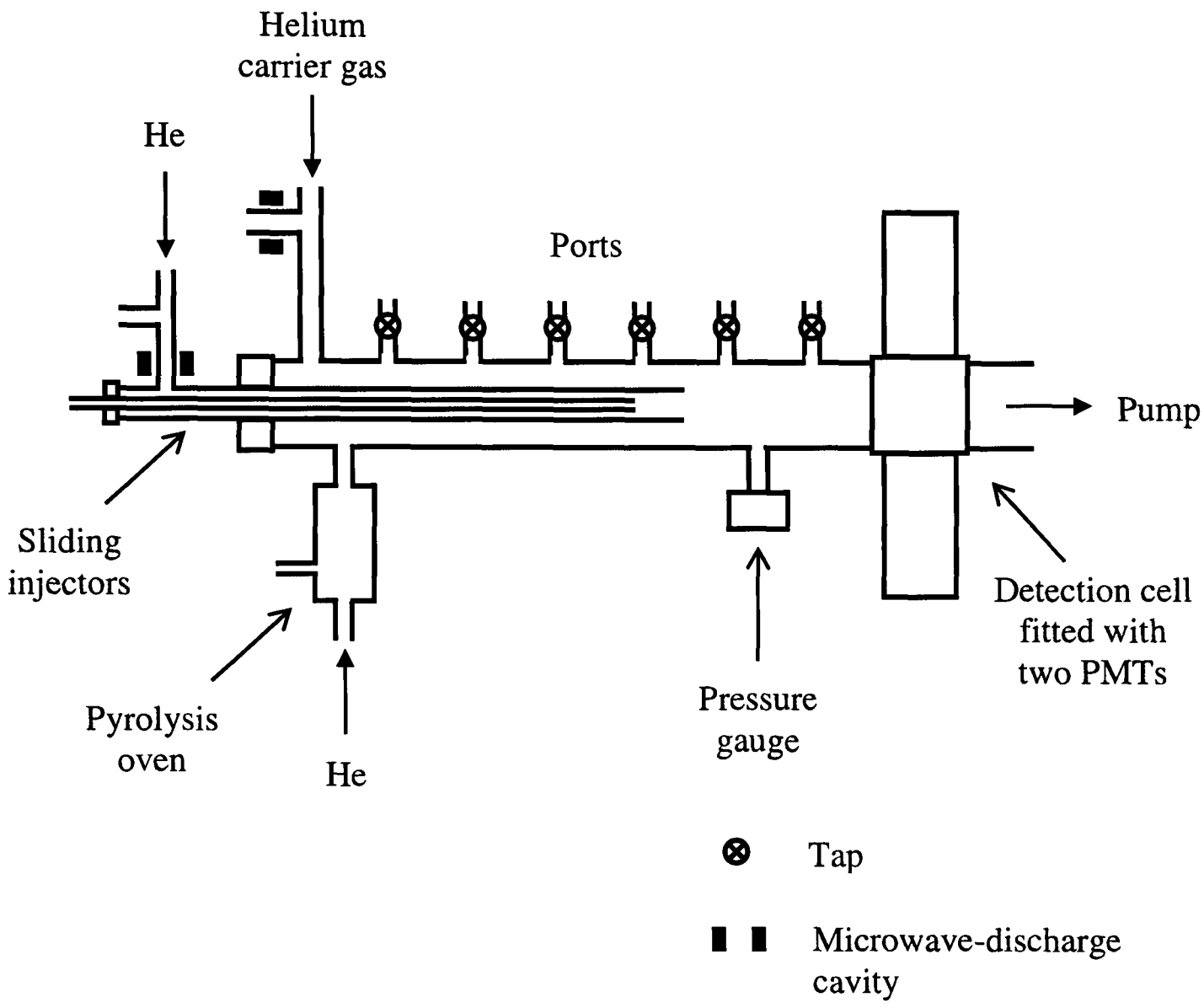

Note: the pyrolysis oven could also be attached to the sliding injector.

The flows of all other gases were also controlled by ball flow-meters (~0.05 and ~2.5 SLPM) (Jencons RS1 and RS2) fitted with needle valves. The backing pressures were monitored by 1000 Torr capacitance manometers (Data Instruments) or, as in the case of oxygen, with a 'bubbler' — a trap filled with dimethyl phthlate (BDH) through which the gas could escape and thus keep the pressure in the line equal to the atmospheric pressure. Oxygen (BOC, 99.5 %) was delivered directly from the cylinder and purified in the same manner as helium, expect that the molecular sieve was not cooled. Gaseous mixtures of

CF_3I (Fluorochem, >97 %), NO (Messer Griesheim, >99.5 %), NO_2 (BDH, >99.5 %), isoprene (Aldrich, 99 %), *trans*-2-butene (Aldrich, >99.9 %) and DMS (Aldrich, 99.5%) were stored in 6 L bulbs. These gases were purified and the mixtures prepared by the techniques described in Appendix I. I_2 was introduced to the flow tube by passing helium through a trap that contained iodine crystals (BDH, 99.9 %). Mixtures of O_3 in O_2 were prepared by passing O_2 through an ozonizer (Argentox GCX10). These mixtures were further diluted with helium. The concentration of ozone was about 5 %.

Radical species were generated at the upstream end of the flow tube by passing the precursor gases through either a microwave-discharge cavity or the pyrolysis oven. Two cavities were fitted to the flow tube: one to a sidearm and the other to the outer sliding injector. The cavities were powered by EMS Microtron 200 generators operating at about 35 Watts. The pyrolysis oven could be fitted to either the other side arm or the sliding injector. The oven consisted of a 25 cm long, 2.5 cm wide Pyrex tube with two gas inlets: one for the carrier gas and the other for the reactant. The tube was heated by a coil of wire that was wrapped around the outside. The temperature was selected by a control unit (Cal Controls, CAL3200). Co-reactants were injected into the flow tube *via* the ports.

3.2.2 Generation of IO radicals

The IO radical was generally produced in the sliding injector. Several different methods were used. The first was the reaction of molecular iodine with O atoms:

$$I_2 + O \rightarrow IO + I. \qquad \text{(R3.6)}$$

Atomic oxygen was generated in the outer sliding injector by passing a small quantity of molecular oxygen and a flow of He through the microwave cavity. The O_2 concentration was $(2 - 7) \times 10^{12}$ molecule cm^{-3}. I_2 was introduced through the inner injector. The rate constant for R3.6 is 1.3×10^{-10} cm^3 $molecule^{-1}$ s^{-1} (Hölscher *et al.*, 1998). It was necessary to add an excess of I_2 to ensure that all of the O atoms had been consumed before the gases mixed with a co-reactant, such as NO or isoprene, in the main flow. However, it was difficult to quantify the concentration of molecular iodine because of the manner in which it needed to be delivered to the flow tube. Instead, O atoms were

monitored with NO_2 chemiluminescence: see section 3.2.2.1. The flow of I_2 and/or the contact time of I_2 and O were increased until O atoms were no longer detected.

The second method of production was the reaction of CF_3I with O:

$$CF_3I + O \rightarrow CF_3 + IO. \qquad \text{(R3.7)}$$

The rate constant for this reaction is 4.3×10^{-12} cm^3 molecule^{-1} s^{-1} (Gilles *et al.*, 1996). The concentrations of O_2 and CF_3I were $(4 - 8) \times 10^{12}$ and $(5 - 11) \times 10^{13}$ molecule cm^{-3}, respectively. O was generated in the outer injector and CF_3I introduced *via* the inner injector. Again, the complete consumption of O atoms was achieved by adjusting the flow of CF_3I and/or the contact time of the two reactants whilst monitoring the signal from NO_2 chemiluminescence. A disadvantage of using R3.7 to generate IO radicals is the presence of a minor channel. Gilles *et al.* (1996) suggested that ~10 % of the reaction does not result in the production of IO. The products of the minor channel have not yet been identified. It is possible that they could complicate the chemistry occurring in the flow tube.

The final technique used to produce the IO radical was the reaction of atomic iodine with ozone:

$$I + O_3 \rightarrow IO + O_2. \qquad \text{(R3.8)}$$

The rate constant for R3.8 is 1.3×10^{-12} cm^3 molecule^{-1} s^{-1} (Hölscher *et al.*, 1998). I atoms were generated in the outer sliding injector either by passing I_2 in a flow of helium through a microwave-discharge cavity or by pyrolysing CF_3I at 950 K:

$$I_2 \rightarrow 2I \qquad \text{(R3.9)}$$

$$CF_3I + M + \Delta \rightarrow CF_3 + I + M. \qquad \text{(R3.10)}$$

The CF_3I was introduced to the pyrolysis oven as a mixture in helium. A further flow of carrier gas was also passed through the oven. The concentration of CF_3I was $(6 - 12) \times 10^{12}$ molecule cm^{-3}. Large quantities of ozone $(4 - 9) \times 10^{13}$ molecule cm^{-3} were added

through the inner injector to completely consume the iodine atoms. R3.8 was not the preferred method of generating IO because it is known to lead to the reformation of the radical further downstream — two of the channels of the IO self-reaction result in the production of I atoms, which react with the excess ozone present in the system to regenerate IO (Martin *et al.*, 1987).

It should be noted that there are further potential problems with all three methods of IO production because reactive species other than IO, namely, I and CF_3, are also generated.

3.2.2.1 Detection of O atoms

As stated in the previous section, when using O atoms to generate IO radicals, it is necessary to ensure the complete consumption of O before a co-reactant, such as NO or isoprene, is introduced into the main flow. If this condition is not satisfied, IO production can continue in the presence of the co-reactant and the oxygen atoms may also react with the co-reactant. O atoms were monitored by observing the chemiluminescence of excited NO_2 formed by the reaction of O with NO:

$$O + NO \rightarrow NO_2^*. \qquad (R3.11)$$

This reaction is known as the airglow reaction. The excited NO_2 emits radiation of wavelengths from 370 to 900 nm (Kaufman, 1961).

The apparatus for the detection of NO_2 chemiluminescence consisted of a photomultiplier (PMT) (EMI 9893/350QB) attached to the detection cell. A quartz window separated these two components. The PMT also had a quartz window and a K-Cs photocathode, and could detection radiation in the range ~150 – 650 nm. The PMT was operated at ~1.5 kV. The signal was fed to an amplifier (in-house built) and monitored on a chart recorder (Venture Servoscribe).

The complete consumption of O atoms was demonstrated as follows. The end of the sliding injector was positioned about 8 cm upstream of the detection point. A large amount of NO $(1 - 3) \times 10^{14}$ molecule cm^{-3} was added through one of the ports. The

flow of CF_3I or I_2 and/or the contact time of the reactants were increased until NO_2 chemiluminescence was no longer detected.

3.2.3 LIF detection of IO

3.2.3.1 Previous studies employing IO LIF

As discussed in the introduction, prior to this work, three other research groups had detected IO with LIF and used the technique to obtain kinetic data. In these studies, fluorescence was induced in the radical by exciting several transitions from the ground $X^2\Pi_{3/2}$ level to the $A^2\Pi_{3/2}$ upper state. These transitions are displayed in table 3.1, along with the excitation wavelengths required. The (2, 0) band was found to produce the most intense fluorescence (Turnipseed *et al.*, 1995).

Table 3.1. Some previous laboratory studies employing LIF detection of the IO radical.

Fluorescent excitation transitions of IO observed ($A^2\Pi_{3/2} \leftarrow X^2\Pi_{3/2}$) ($\upsilon'$, υ'')	**$\lambda_{excitation}$/nm**	**Reference**
(2, 0)	~445	Inoue *et al.* (1983)
(0, 0)	~465	
(2, 0)	~445	Turnipseed *et al.* (1995)
(2, 1)	~459	
(0, 0)	~465	
(3, 0)	~436	
(2, 0)	~445	Hölscher *et al.* (1998)
(3, 0)	~436	

Note: transitions are listed in order of fluorescence intensity, with the most intense first.

The following sections describe the set-up of the laser system that could be tuned to generate 445 nm radiation, the detection of the fluorescence, and the signal processing.

3.2.3.2 The laser system

The excitation radiation was generated by a Nd–YAG-pumped dye laser. A schematic diagram of the apparatus is depicted in figure 3.2. Section 2.3.1.2.3 describes the operating principles of such a laser system.

Figure 3.2. A schematic diagram of the laser system used for IO LIF.

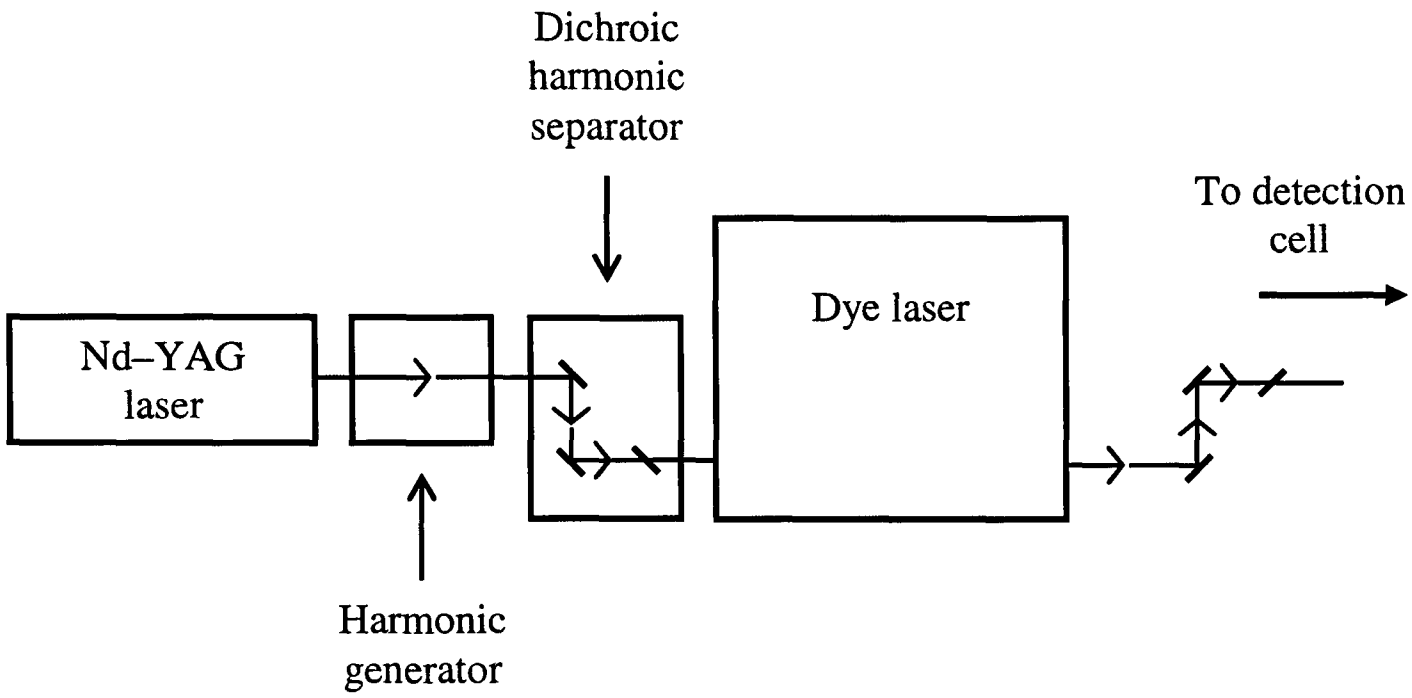

The Nd–YAG laser (Spectra-Physics, Quanta-Ray GCR-11) is a four-level laser (Atkins, 1994). The active medium is triply-ionized neodymium, which is embedded in a crystal of yttrium aluminium garnet ($Y_3Al_5O_{12}$), also known as YAG. The Nd^{3+} ions are optically pumped by a flash lamp with a red/infra-red output to create the population inversion. The lasing transition generates radiation with a wavelength of 1064 nm. The Nd–YAG laser produced pulses of light, the intensity of which were increased by Q-switching (*Quanta-Ray GCR-11 Pulsed Nd:YAG Laser Instruction Manual*, 1990). Q-switching was necessary as several processes were required to convert the wavelength of the laser radiation from 1064 nm to ~445 nm. These processes are not very efficient (Hollas, 1993) and therefore to achieve excitation radiation of a reasonable power, high-intensity incident light was required. In Q-switching mode, the pulse width of the Nd–YAG laser beam is ~9 ns and the pulse energy is about 300 mJ. The laser was triggered by a pulse generator (in-house built). The pulse frequency was set to 10 Hz.

The Nd–YAG laser beam was directed into a harmonic generator (Spectra-Physics, HG-2). This device contained two crystals of potassium dideuterium phosphate (KD*P). The first crystal doubled the frequency of the incident light to produce radiation with a wavelength equal to 532 nm. The second crystal mixed the 532 nm and residual 1064 nm radiation to generate light with a wavelength of 355 nm (*Quanta-Ray GCR-11 Pulsed Nd:YAG Laser Instruction Manual*, 1990). The laser beam was then passed into the dichroic harmonic separator (Spectra-Physics, DHS-1), which contained several dichroic mirrors. These mirrors were arranged to prevent the 532 nm and the 1064 nm radiation from entering the dye laser. Only the 355 nm light was able to pass through.

A solution of Coumarin 440 (Exciton) in methanol (Fisher Chemicals, 99.93%) was continuously passed through the cavity of the dye laser (Spectra-Physics, Quanta Ray PDL-3) by a small pump (Spectra-Physics, TSC-2). The dye solution was capable of producing radiation in the range 425 – 457 nm, with a maximum intensity at 440 nm. The desired wavelength was selected with a diffraction grating. The energy of the laser beam was typically 2 mJ. The beam was directed into the detection cell *via* a series of prisms.

3.2.3.3 Fluorescence detection

The detection cell was constructed from stainless steel. The laser beam entered the cell through a quartz window mounted on a flange. The window was set at the Brewster angle to the polarization of the laser beam so as to minimize reflections that would normally arise from a sudden change in refractive index of the medium containing the beam. A series of metal rings was used to collimate the beam. The internal surfaces of the cell were blackened to reduce the intensity of scattered light.

The output of the dye laser was tuned to match an absorption peak of the IO radical (see section 3.3.1 for further details). Some of the resulting fluorescence passed through a quartz window and a cut-off filter (Schott Glass, GG-495, $\lambda > 495$nm), and was focused onto a PMT (EMI B2F/RF16443) by a quartz lens. The filter transmitted IO fluorescence whilst discriminating against any scattered laser light. The PMT was positioned at right angles to the incident beam and was operated at about 1.3 kV.

Note that two studies, published after the work detailed here was undertaken, state the wavelengths at which IO LIF was monitored: Allen and Plane (2002) detected the intensity of 458.6 nm radiation, and Bloss *et al.* (2003) observed fluorescent wavelengths in the range 500 – 600 nm.

3.2.3.4 Signal processing

The PMT output consisted of a series of signal pulses that corresponded to the fluorescence of a species following excitation by the laser pulses. This output was passed to a boxcar integrator (EG & G, 162). This device allowed only the fluorescence pulses, and not the noise in between them, to be monitored by positioning a 'gate' over part of the fluorescence decay curve. The output of the boxcar integrator was an average measurement of several of these fluorescence pulses. The signal was recorded on a chart recorder (Venture Servoscribe) and also passed to a digital storage adapter (Thurlby DSA524) for further processing before being displayed on an oscilloscope (Tektronix 454).

3.3 Results and discussion

3.3.1 IO LIF performance

As previously stated, the laser system was capable of being tuned over the range 425 – 457 nm, with a maximum beam intensity at 440 nm. The IO radical has four absorption bands within this range, namely (1, 0) at ~454 nm, (2, 0) at ~445 nm, (3, 0) at ~436 nm and (4, 0) at ~427 nm (Himmelmann *et al.*, 1996). IO LIF was successfully observed at $\lambda_{excitation}$ = 445 nm. A very weak signal was also seen at $\lambda_{excitation}$ = 436 nm. No signal was observed at the limits of the laser range, which correspond to the (4, 0) and (1, 0) transitions. These observations are in agreement with those of Turnipseed *et al.* (1995). These workers found the fluorescence intensity from the (2, 0) band to be about 100 times greater than that from the (3, 0). They also could not detect fluorescence from the (4, 0) and (1, 0) transitions.

The IO LIF signal was calibrated by titrating the radical with NO:

$$IO + NO \rightarrow I + NO_2 \qquad (R3.1)$$

and observing LIF of the NO_2 product. $k_{3.1}$ is $(1.82 \pm 0.1) \times 10^{-11}$ cm^3 molecule^{-1} s^{-1} (Dillon and Heard, 2003). NO_2 has broadband absorption in the UV/vis region and fluorescence has been observed at excitation wavelengths from 398 nm to above 750 nm (Okabe, 1978). The method of calibration was as follows. The IO LIF signal was measured at $\lambda_{excitation}$ = 445 nm. Then the laser output was tuned to 430 nm. This excitation wavelength was found to produce a large NO_2 LIF signal and, as just stated, did not induce IO fluorescence. An excess of NO ($5 - 9 \times 10^{13}$ molecule cm $^{-3}$) was added through an upstream port (IO was produced in the sliding injector) and the NO_2 LIF signal was recorded. This procedure was repeated for several different IO LIF signals. The NO_2 LIF system was then calibrated by passing a known quantity of NO_2 through the flow tube. Based on the assumption that IO:NO_2 = 1, a calibration curve could be produced, an example of which is shown in figure 3.3. The calibration factor in this case was 6.2×10^{11} molecule cm^{-3} V^{-1}. The sensitivity of the IO LIF system was ~5×10^9 molecule cm $^{-3}$ for S/N = 1 and an integration time of 60 s.

3.3.2 The reaction of IO with NO (R3.1)

Although the detection of NO_2 LIF enabled the IO LIF system to be calibrated, it obviously interfered with the study of the reaction of IO with NO. The signal at $\lambda_{excitation}$ = 445 nm increased on addition of NO to the flow tube when IO was present ([IO] ≈ 2×10^{11} molecule cm^{-3}, [NO] ≈ 2×10^{13} molecule cm^{-3}, FTP ≈ 2 Torr, contact time ≈ 15 ms). Several attempts to reduce the intensity of NO_2 LIF were made.

First, the FTP was increased in an attempt to selectively quench excited NO_2. The intensity of the IO LIF signal would not be greatly affected because the lifetime of excited IO is very short, <10 ns, which means that collisional quenching can not compete with fluorescence (Inoue *et al.*, 1983). By contrast, the lifetime of NO_2 excited by 445 nm radiation is much longer, ~55 μs, and thus increasing the FTP will quench fluorescence

Figure 3.3. An example of an IO LIF calibration curve.

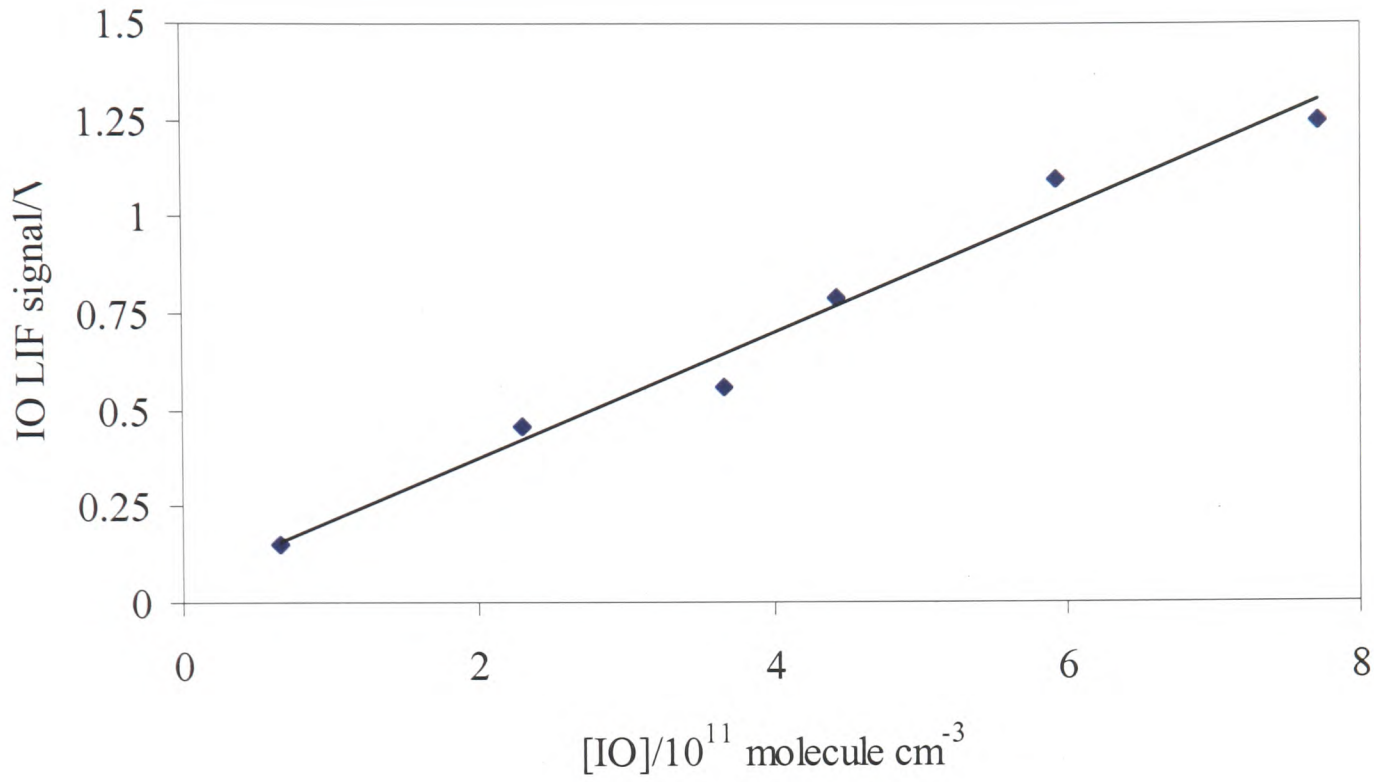

(Okabe, 1978). The effect of pressure was investigated by passing just NO_2 through the flow tube. The pressure was increased from 2 to 10 Torr, which is close to the maximum value at which the tube could be operated, by partially closing the valve at the end of the flow tube. However, the NO_2 LIF signal only decreased by about 20 %. Also, the LFV was greatly reduced to about 500 cm s^{-1}.

The second attempt to reduce the interference involved adding a large quantity of another quencher. Molecular oxygen (~1 × 10^{15} molecule cm^{-3}) was added but the NO_2 LIF signal only reduced by about 15 % (FTP ≈ 2.5 Torr).

The final attempt to remove NO_2 LIF from the signal involved changing the filter that was positioned before the PMT. The cut-off filter, which transmitted wavelengths greater than 495nm, was replaced with an interference filter (Coherent 35-3425-000), which passed wavelengths of (470 ± 7) nm. It was thought that this filter would discriminate against some of the NO_2 fluorescence. Indeed, the NO_2 LIF signal was reduced by about 90%. However, on returning to the reaction of IO with NO, it was found that the S/N ratio of the IO LIF signal had greatly reduced. The interference filter transmitted fewer

fluorescent wavelengths of IO and more of the scattered laser light. At this point, the investigation of the R3.1 was halted because the time to return the laser system to the loan pool was fast approaching.

The reaction of IO with NO has been studied several times. Prior to this work, Inoue *et al.* (1983) and Turnipseed *et al.* (1995) had successfully determined the rate constant by monitoring IO with LIF. The latter study did not suffer from NO_2 interference as most experiments were conducted at 100 Torr of N_2, although two experiments were conducted at lower pressures (5 and 23 Torr) but there is no mention of any problems. The detection system only employed cut-off filters that transmitted wavelengths greater than 475 or 495 nm and therefore NO_2 LIF should have been detected. Inoue *et al.* (1983) performed their experiments at very low pressures, <1 Torr of helium, but again do not discuss any problems of NO_2 interference. The transmission range of the filter employed is not known. Since the work described in this chapter was undertaken, two other IO-LIF studies of R3.1 have been published. Hölscher and Zellner (2002) are the only group of workers to discuss explicitly the problem of LIF of the NO_2 product. They report that the NO_2 fluorescence was quenched by performing experiments at pressures of ~10 to ~100 Torr of synthetic air. They also used a combination of interference (λ = 470 nm) and cut-off (λ > 475 nm) filters to prevent transmission of any remaining NO_2 fluorescence and scattered laser light. Dillon and Heard (2003) also avoided problems by conducting their experiments at higher pressures (64 – 130 Torr of N_2 or synthetic air).

It is highly probable that $k_{3.1}$ could be determined using the low-pressure flow tube/IO LIF apparatus by employing the combination of filters used by Hölscher and Zellner (2002). The ability to greatly reduce the interference of NO_2 LIF implies that it may also be possible to study the reaction of IO with NO_2. A much larger concentration of NO_2 would be required compared to the quantity generated by R3.1 in order to conduct the experiment under first-order conditions. However, it is likely that the interference could be removed. Another method that might possibly allow the reactions of IO with NO and NO_2 to be studied is to use the boxcar integrator to distinguish between IO and NO_2 fluorescence. As previously mentioned, the lifetime of excited IO is much shorter than that of excited NO_2. The boxcar integrator could be operated with two gates: one to

monitor the combined IO/NO_2 LIF signal, and the other to measure a later part of the fluorescence decay that only corresponds to NO_2 LIF. Calibration of the NO_2 signal at both gate positions would allow the IO signal to be calculated.

3.3.3 The IO self-reaction (R3.2)

The self-reaction of the IO radical was briefly investigated. Experiments were conducted at a temperature of ~295 K, an FTP of ~2 Torr and an LFV of ~2500 cm s^{-1}. IO was generated in the sliding injector. Contact times in the main flow of 2 – 21 ms were employed. Figure 3.4 shows an example of the decay of IO as a function of time. In this particular experiment, IO was generated by the reaction of CF_3I with O. It can be seen that the initial decay of the radical appears to be slower than that at contact times greater than about 5 ms. It is likely that this feature is the result of a continuation of IO production in the main flow — the complete consumption of O atoms in the sliding injector was not checked for in this experiment.

The data were subjected to a simple second-order analysis:

$$\frac{1}{[IO]_t} = \frac{1}{[IO]_0} + 2k_{3.2}t \qquad \text{(E3.1)}$$

where $[IO]_0$ is the initial concentration of the radical, and $[IO]_t$ is the concentration after time t. Data taken at t <5 ms were excluded. However, a plot of $1/[IO]_t$ versus t produced a curve instead of a straight line: see figure 3.5. Such curvature is indicative of the existence of other processes that consume IO. Indeed, a linear fit to the data yielded a rate constant of 4.4×10^{-10} cm^3 $molecule^{-1}$ s^{-1}. This value is much higher than the literature values: see table 3.2.

Figure 3.4. An example of the decay of the IO radical as a function of time.

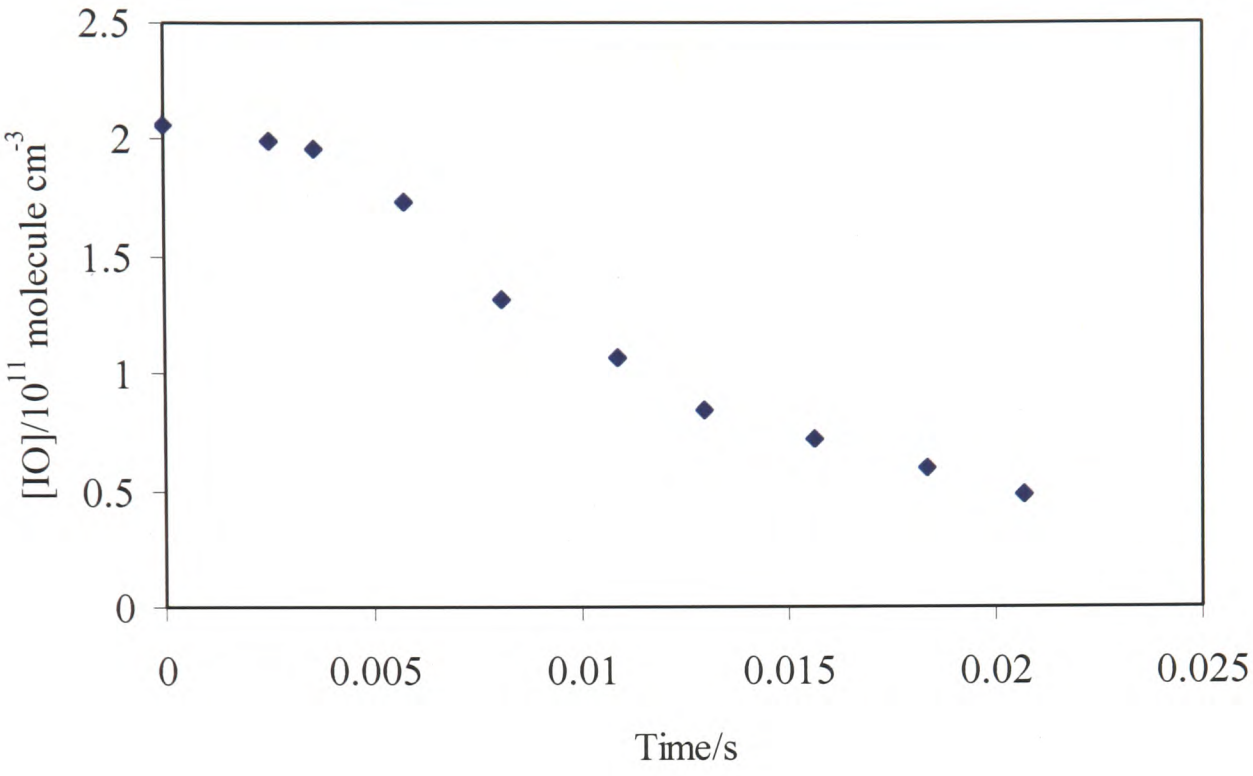

Figure 3.5. A second-order plot for the loss of IO radicals. This analysis assumes that the only chemistry taking place is the self-reaction. The upward curvature of the data indicates that other processes are consuming IO.

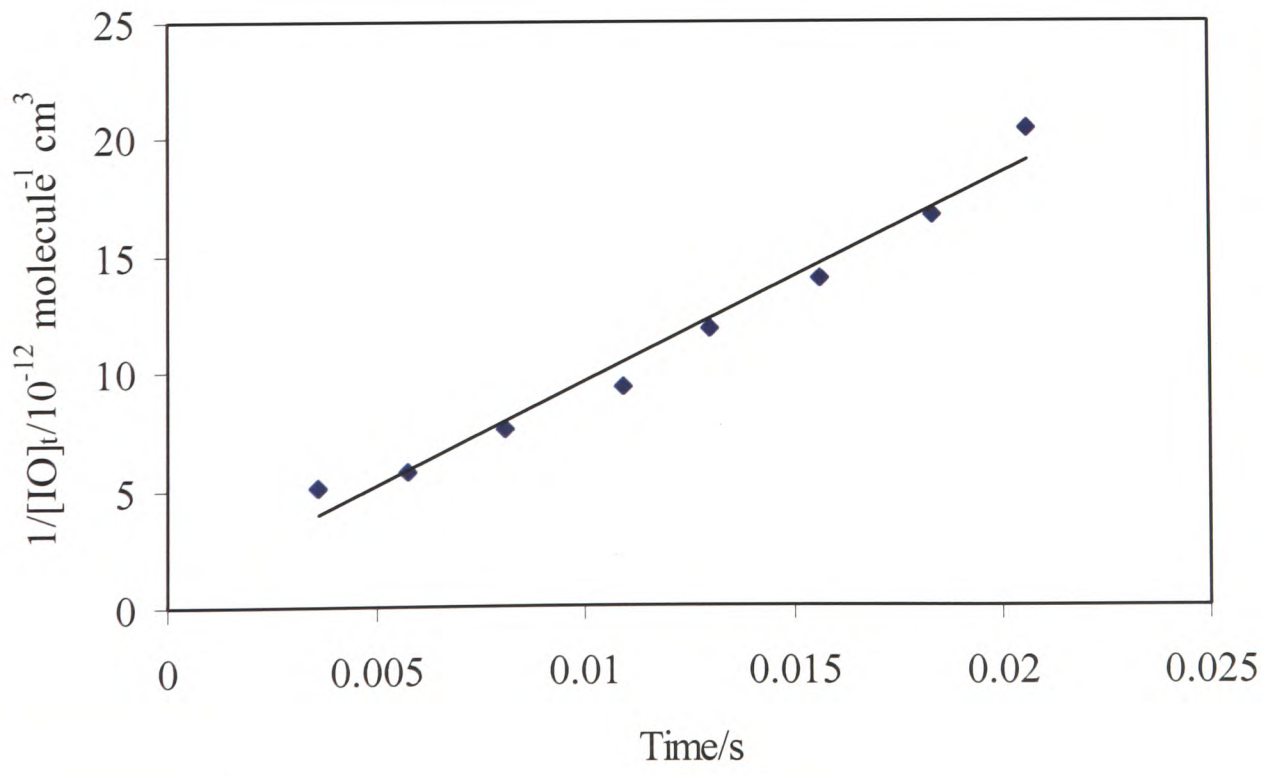

Table 3.2. Some of the values of $k_{3.2}$ listed in the literature.

Method	$k_{3.2}/10^{-11}$ **cm^3 molecule^{-1} s^{-1}**	**Reference**
Discharge–flow tube/RF	(9.3 ± 1.9)	Vipond *et al.* (2002)
Pulsed-laser photolysis/ UV–vis absorption	(8.2 ± 1.3)	Bloss *et al.* (2001)
Pulsed-laser photolysis/CRDS	(10 ± 3)	Atkinson *et al.* (1999)
Discharge–flow tube/MS	(5.5 ± 0.8)	Barnes *et al.* (1991)
Discharge–flow tube/MS	(3.0 ± 0.5)	Martin *et al.* (1987)

Notes: 1) There are several more values listed in the literature. As stated in the introduction, there is a degree of disagreement between some of the studies. However, all of the literature values lie in the range $(3 - 10) \times 10^{-11}$ cm^3 molecule^{-1} s^{-1}. 2) CRDS – cavity ring-down spectroscopy

In an attempt to estimate the magnitude of the loss of IO *via* processes other than its self-reaction, a simple numerical model was generated with the FACSIMILE software package (version 3.0.30, AEA Technology): see appendix II. The model contained only two reactions:

$$\mathrm{IO} + \mathrm{IO} \rightarrow \text{products} \qquad \text{(R3.2)}$$

$$\mathrm{IO} \rightarrow \text{products.} \qquad \text{(R3.12)}$$

The rate constant for R3.2 used was that obtained by Vipond *et al.* (2002). The initial concentration of IO was estimated by extrapolating the concentration–time profiles (excluding the data taken at t <5 ms) to t = 0 s. A value of $[\mathrm{IO}]_0 = 2.6 \times 10^{11}$ molecule cm^{-3} was derived. The parameter-fitting option was used to extract $k_{3.12}$ from the experimental data. The rate constant was calculated to be (50 ± 6) s^{-1}. The quoted errors are the 90 % confidence limits. This loss rate is much greater than that expected to result from the heterogeneous reaction of IO with the flow-tube walls. Although the wall loss was not quantified in this work, previous measurements for the discharge-flow tube employed lie in the range 6 – 8 s^{-1} (Vipond *et al.*, 2002). Other chemistry must have been

occurring. The model was modified in an attempt to identify the important processes. The chemistry of the other product of the reaction used to produce IO, namely CF_3, was included:

$$IO + CF_3 \rightarrow I + CF_3O \qquad \text{(R3.13)}$$

$$CF_3 + CF_3 \rightarrow C_2F_6. \qquad \text{(R3.14)}$$

The initial concentration of CF_3 was taken to be equal to $[IO]_0$. The values of $k_{3.13}$ and $k_{3.14}$ employed were 1.6×10^{-11} and 3.9×10^{-12} cm^3 molecule^{-1} s^{-1}, respectively (Vipond *et al.*, 2002; Vakhtin, 1996). However, it was found that CF_3 chemistry had little impact on the rate of loss of IO, as $k_{3.12}$ was still found to be about 50 s^{-1}. A more likely cause of the increased consumption of IO was reaction with O:

$$IO + O \rightarrow I + O_2. \qquad \text{(R3.15)}$$

This reaction is very fast (1.35×10^{-10} cm^3 molecule^{-1} s^{-1} (Canosa-Mas *et al.*, 1999)) and as previously discussed, it was thought that O atoms were present in the main flow as IO production was evident in the concentration–time profile of the radical. The model was altered to include R3.15 and it was found that an estimated initial concentration of O of 4×10^{11} atom cm^{-3} resulted in a good fit between the experimental and model data. An estimated wall loss of IO of 7 s^{-1} was also included in the model. The data are displayed in figure 3.6. The decay profiles resulting from a model simulation of just the self-reaction of IO, and the self-reaction accompanied by CF_3 chemistry are also shown.

It is highly likely that the agreement between the experimental data and those produced by the model that describes the self-reaction of IO, CF_3 chemistry, IO wall loss and the reaction of the radical with O could be improved by including other chemistry of oxygen atoms, such as reaction with CF_3I and CF_3:

$$CF_3I + O \rightarrow CF_3 + IO \qquad \text{(R3.7)}$$

$$CF_3 + O \rightarrow F + COF_2. \qquad \text{(R3.16)}$$

Figure 3.6. Concentration–time profiles of IO. The experimental data do not include points corresponding to t <5 ms. Three decay curves generated by a model simulation are displayed: one represents the decay resulting from only the self-reaction of IO (R3.2); the second includes CF_3 chemistry (R3.13 and R3.14), and the third includes CF_3 chemistry, a wall loss of IO and the reaction of the radical with O (R3.15). $[IO]_0 = [CF_3]_0 = 2.6 \times 10^{11}$ molecule cm^{-3} and $[O]_0 = 4 \times 10^{11}$ atom cm^{-3}. $k_{3.2} = 9.3 \times 10^{-11}$, $k_{3.13} = 1.6 \times 10^{-11}$, $k_{3.14} = 3.9 \times 10^{-12}$ and $k_{3.15} = 1.35 \times 10^{-10}$ cm^3 molecule^{-1} s^{-1}. $k_{wall} = 7$ s^{-1}.

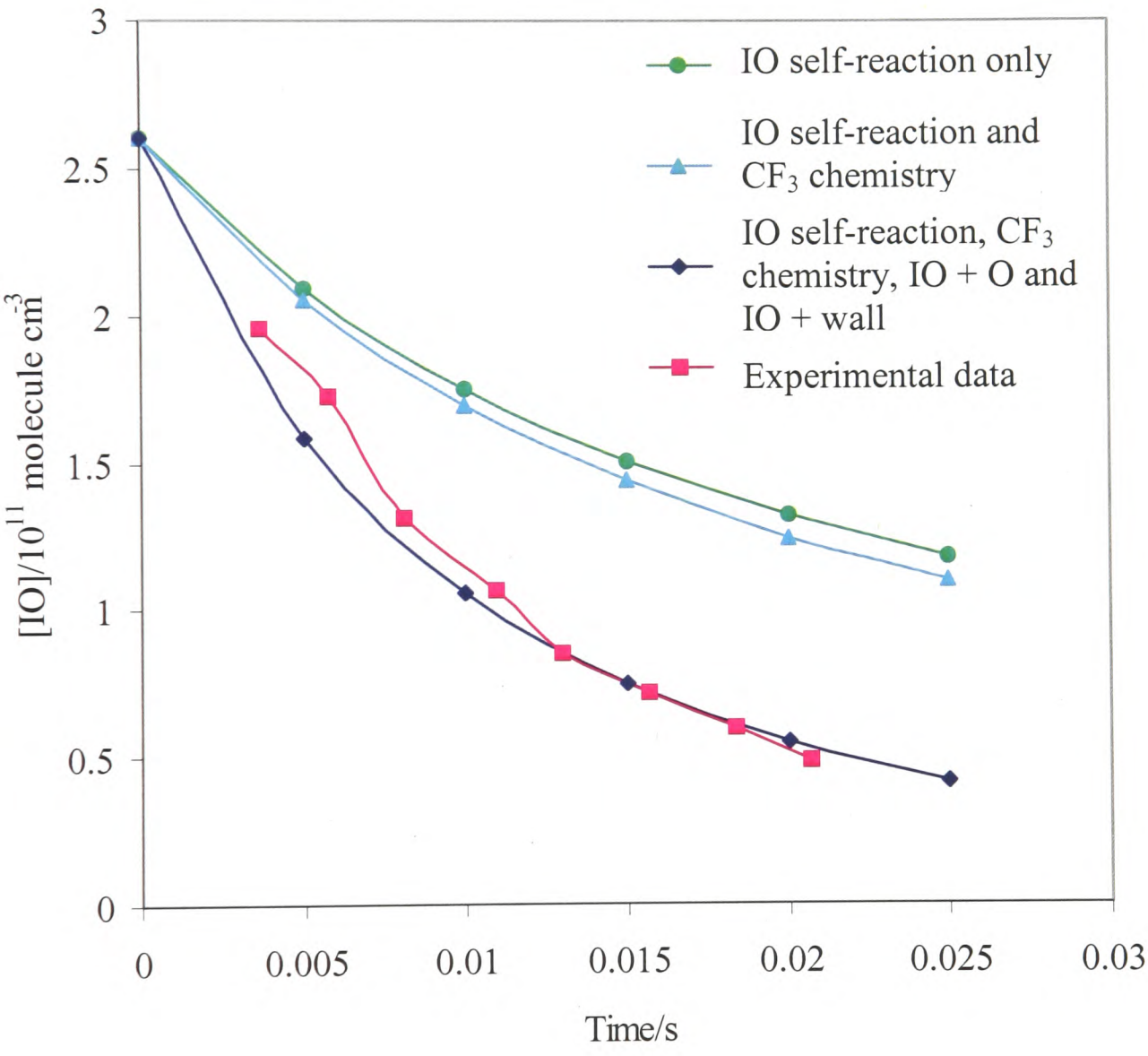

In particular, the inclusion of R3.7 would increase the concentration of IO at shorter contact times. It should also be stated that it might be possible to evaluate $k_{3.2}$ *via* analysis of the data collected at longer contact times, when the effects of secondary chemistry on [IO] would be at a minimum. However, further analysis of the data is not appropriate as the concentration of O was not measured. The main aim of the investigation was achieved, which was to demonstrate that the self-reaction of the IO

radical could be studied with the discharge–flow tube/IO LIF apparatus. Also, the other important processes taking place in the flow tube were identified. A future study of the self-reaction should endeavour to make the interference of O chemistry in the main flow negligible and quantify the wall loss of IO.

3.3.4 The reactions of IO with DMS, isoprene and *trans*-2-butene

The reactions of IO with DMS, isoprene and *trans*-2-butene:

$$IO + CH_3SCH_3 \rightarrow I + CH_3SOCH_3 \qquad (R3.3)$$

$$IO + CH_2CCH_3CHCH_2 \rightarrow \text{products} \qquad (R3.4)$$

$$IO + CH_3CHCHCH_3 \rightarrow \text{products} \qquad (R3.5)$$

were briefly investigated. Experiments were conducted under *pseudo*-first order conditions. IO was generated in the sliding injector and the organic species were introduced *via* an upstream port. Note that the complete consumption of O atoms in the sliding injector was achieved in these experiments. All three reactions were found to proceed slowly as large concentrations of the organic compounds and long contact times were required to see a drop in the IO LIF signal. The drop was time dependent. The experimental conditions were [IO] $\approx 10^{11} - 10^{12}$, [DMS] $\approx 4.0 \times 10^{14}$, [isoprene] $\approx 2.5 \times 10^{14}$ and [*trans*-2-butene] $\approx 7.5 \times 10^{14}$ molecule cm^{-3}. The ambient temperature was ~295 K, the FTP was ~2 Torr and the LFV was ~1700 cm s^{-1}. Contact times of up to ~35 ms were employed.

As there was only time to perform a few experiments, a rigorous determination of $k_{3.3}$, $k_{3.4}$ and $k_{3.5}$ was not possible. Analysis of the available data should take the reactions:

$$IO + \text{organic} \rightarrow \text{products} \qquad (R3.17)$$

$$IO + IO \rightarrow \text{products} \qquad (R3.2)$$

$$IO + \text{wall} \rightarrow \text{products} \qquad (R3.18)$$

into account. However, not all of the relevant parameters were quantified — calibrations of the IO signal and measurements of wall losses were not performed during the

experiments. Only one measurement of the IO LIF signal in the presence and absence of each organic compound was taken. This data can be analysed but only if certain assumptions are made. If the first-order losses of IO are assumed to be more important than the second-order losses (the losses *via* R3.2), then the data can be treated with a simple *pseudo*-first-order analysis:

$$\ln\frac{S_t}{S_{org}} = k't \qquad \text{(E3.2)}$$

where S_t and S_{org} are the IO signals at time t in the absence and presence, respectively, of the organic compound, and $k' = k_{org}[\text{organic}]$. Note that this type of analysis requires neither the wall loss nor the concentration of IO to be known. The derived rate constants were $k_{3.3} = 2.7 \times 10^{-14}$, $k_{3.4} = 1.3 \times 10^{-14}$ and $k_{3.5} = 1.0 \times 10^{-14}$ cm^3 molecule^{-1} s^{-1}. Alternatively, if bimolecular processes are assumed to be important, and unimolecular processes, i.e. the wall loss, are negligible, then the data can be treated with a mixed *pseudo*-first- and second-order expression:

$$\frac{[IO]_{org}}{[IO]_0} = \frac{k'}{(2k_{3.2}[IO]_0 + k')\exp(k't) - 2k_{3.2}[IO]_0} \qquad \text{(E3.3)}$$

where $[IO]_{org}$ is the concentration of IO at time t in the presence of the organic compound. The initial concentration of IO, $[IO]_0$, can be derived from the second-order equation:

$$\frac{1}{[IO]_t} = \frac{1}{[IO]_0} + 2k_{3.2}t\,. \qquad \text{(E3.1)}$$

The rate constant for R3.2 was taken as 9.3×10^{-11} cm^3 molecule^{-1} s^{-1} (Vipond *et al.*, 2002). Initial concentrations of IO were calculated to be $(0.2 - 5) \times 10^{12}$ molecule cm^{-3}. E3.3 was solved for k' using a program written in QBASIC that contained the numerical procedure known as the bisection of the interval. The rate constants were found to be $k_{3.3} = 4.1 \times 10^{-14}$, $k_{3.4} = 1.9 \times 10^{-14}$ and $k_{3.5} = 2.1 \times 10^{-14}$ cm^3 molecule^{-1} s^{-1}. These values are in general agreement with those derived *via* the first method of analysis.

The rate constants obtained in this study are displayed in table 3.3 along with all literature values for the reactions of IO with organic species. Note that the work of Larin *et al.* (2000), and Knight and Crowley (2001) was published after the work described in this chapter was performed. It can be seen that the value of the rate constant for the reaction of IO with DMS derived in this study is in reasonable agreement with the literature data. It should be noted that the results of the two studies published in 1987 are thought to be incorrect because the contributions of the IO self-reaction and wall losses to the consumption of IO were grossly underestimated. The rate constants for the reactions of IO with isoprene and *trans*-2-butene have not been previously determined.

Table 3.3. Rate constants for the reactions of IO with organic compounds obtained in this work and listed in the literature.

Organic co-reactant	***k*/cm^3 molecule^{-1} s^{-1}**	**Reference**
DMS	2.7×10^{-14}	This work (E3.2)
	4.1×10^{-14}	This work (E3.3)
	$(3.0 \pm 1.5) \times 10^{-11}$	Barnes *et al.* (1987)
	$(1.5 \pm 0.5) \times 10^{-11}$	Martin *et al.* (1987)
	$\leq 3.5 \times 10^{-14}$	Daykin and Wine (1990)
	$(1.5 \pm 0.2) \times 10^{-14}$	Maguin *et al.* (1991)
	$(8.8 \pm 2.1) \times 10^{-15}$	Barnes *et al.* (1991)
	$\leq 2.5 \times 10^{-14}$	Larin *et al.* (2000)
	$(1.6 \pm 0.3) \times 10^{-14}$	Knight and Crowley (2001)
Isoprene	1.3×10^{-14}	This work (E3.2)
	1.9×10^{-14}	This work (E3.3)
Trans-2-butene	1.0×10^{-14}	This work (E3.2)
	2.1×10^{-14}	This work (E3.3)
CH_3SH	$(6.6 \pm 1.3) \times 10^{-16}$	Maguin *et al.* (1991)
C_2H_4	$\leq 2 \times 10^{-16}$	Maguin *et al.* (1991)
C_3H_6	$\leq 2 \times 10^{-16}$	Maguin *et al.* (1991)

3.3.4.1 Atmospheric implications

The main sinks of DMS and unsaturated compounds, such as isoprene and *trans*-2-butene, in the atmosphere are reaction with OH and NO_3 (Finlayson-Pitts and Pitts Jr., 2000). Alkenes also react with O_3. However, as these organic species are present the marine environment — DMS in particular has been observed in large quantities — and as IO has been detected in the MBL, reaction with IO may be of importance. Table 3.4 lists the rates of loss of DMS, isoprene and *trans*-2-butene *via* oxidation by IO, OH and Cl in the MBL, and OH and NO_3 in the global troposphere. Note that Cl atoms, reactions of which are investigated in the next chapter, are a potentially important oxidant in the marine environment. The loss rates for the reactions of the two alkenes with O_3 in the troposphere are also listed.

Table 3.4. The rates of loss of DMS, isoprene and *trans*-2-butene *via* reaction with IO, OH and Cl in the MBL, and OH and NO_3 in the global troposphere. The loss rates for the reactions of the two alkenes with O_3 are also listed.

Co-reactant and location	Rate of loss of organic species/s^{-1} [a]		
	DMS	**Isoprene**	***Trans*-2-butene**
IO MBL[b]	6.2×10^{-6}	2.9×10^{-6}	3.2×10^{-6}
Cl MBL[c]	4.3×10^{-5}	6.6×10^{-5}	4.3×10^{-5}
OH MBL[c]	1.9×10^{-6}	3.9×10^{-5}	2.5×10^{-5}
OH global[d]	7.7×10^{-6}	1.6×10^{-4}	1.0×10^{-4}
NO_3 global[e]	5.5×10^{-4}	3.4×10^{-4}	2.0×10^{-4}
O_3 global[f]	n/a	9.0×10^{-6}	1.3×10^{-4}

Notes: [a] $k_{3.3}$, $k_{3.4}$ and $k_{3.5}$ are taken from this work. The larger of the two values that were derived for each rate constant has been used. $k_{Cl + isoprene} = 5.1 \times 10^{-10}$ (Finlayson-Pitts *et al.*, 1999), and $k_{Cl + trans\text{-}2\text{-}butene} = 3.3 \times 10^{-10}$ cm^3 $molecule^{-1}$ s^{-1} (Ezell *et al.*, 2002). All other rate constants are taken from Atkinson *et al.* (1997): $k_{Cl + DMS} = 3.3 \times 10^{-10}$; $k_{OH + DMS} = 4.8 \times 10^{-12}$; $k_{NO3 + DMS} = 1.1 \times 10^{-12}$; $k_{OH + isoprene} = 1.0 \times 10^{-10}$; $k_{NO3 + isoprene} = 6.8 \times 10^{-13}$; $k_{O3 + isoprene} = 1.3 \times 10^{-17}$; $k_{OH + trans\text{-}2\text{-}butene} = 6.4 \times 10^{-11}$; $k_{NO3 + trans\text{-}2\text{-}butene} = 3.9 \times$

10^{-13} and $k_{O3 + trans\text{-}2\text{-}butene} = 1.9 \times 10^{-16}$ cm^3 molecule^{-1} s^{-1}. [b]The maximum concentration of IO in the MBL is 1.5×10^8 molecule cm^{-3} (Alicke *et al.*, 1999). [c]The concentrations of Cl and OH in the MBL are 1.3×10^5 atom cm^{-3} and 3.9×10^5 molecule cm^{-3}, respectively (Spicer *et al.*, 1998). These are the concentrations shortly after sunrise, when [Cl] is at a maximum. [d]The 12-hour average global concentration of OH in the troposphere is 1.6×10^6 molecule cm^{-3} (Prinn *et al.*, 1995). [e]The 12-hour average concentration of NO_3 in the nighttime troposphere is 5×10^8 molecule cm^{-3} (Shu and Atkinson, 1995). [f]The 24-hour average concentration of O_3 in the troposphere is 7×10^{11} molecule cm^{-3} (Logan, 1985).

It can be seen that reaction with NO_3 is the major loss process in the troposphere for all three organic species. During the day, reaction with OH is a significant sink on a global scale, particularly for isoprene and *trans*-2-butene. However, the rate of loss of DMS *via* this path is rivaled by that resulting from reaction with IO in the MBL. In fact, reaction with IO is of reasonable importance for all three organic compounds in the marine environment, although it can be seen that reaction with Cl is of greater significance. Reaction with OH in the MBL is the least important sink of DMS. Finally, it should be noted that, despite the low reactivity of isoprene and *trans*-2-butene to O_3, the rates of loss of these two compounds *via* this pathway are comparable to those resulting from the other processes listed because of the great abundance of O_3 in the troposphere.

3.4 Conclusions

This chapter describes the successful detection of IO by LIF and the first report of the coupling of such a system to a discharge–flow tube. A level of sensitivity was achieved that is comparable to those stated in other studies. Methods of IO production and the laser set-up are discussed. A technique for the calibration of the IO LIF signal is also described. Exploratory investigations of a variety of reactions of IO were performed. Problems were encountered in the study of the reaction of IO with NO because of interference from LIF of the NO_2 product. Several methods of removing the NO_2 signal were investigated and it is thought that a combination of filters that discriminates against the NO_2 interference and also the scattered laser light would allow the decay of IO to be monitored. It may also be possible to use the boxcar integrator to distinguish between IO and NO_2 fluorescence. The self-reaction of IO was also briefly studied. It was shown

that an investigation of the reaction was possible but that it was important to minimize the concentration of O atoms in the main flow. Finally, the rate constants for the reactions of IO with DMS, isoprene and *trans*-2-butene were obtained. It was shown that these reactions might be of importance in the MBL.

Although the discharge–flow tube/IO LIF apparatus was shown to be suitable for studying the kinetics of reactions of IO, a current research project at Oxford with exactly this aim has not employed the technique. Instead, cavity-enhanced absorption spectroscopy (CEAS) has been coupled to a flow tube. The CEAS system involves using a violet laser diode to produce 410 nm radiation to excite the (6, 0) band of IO. This laser was chosen because it is cheap and compact. The laser system used in the work described in this chapter was more expensive and required a large floor space in the laboratory.

3.5 References

- Alicke, B., K. Hebestreit, J. Stutz and U. Platt, *Nature*, 1999, **397**, 572
- Allen, B. J. and J. M. C. Plane, *J. Phys. Chem. A.*, 2002, **106**, 8634
- Atkins, P. W., *Physical Chemistry*, 5th Edition, Oxford University Press, Oxford, 1994
- Atkinson, D. B., J. W. Hudgens and A. J. Orr-Ewing, *J. Phys. Chem. A.*, 1999, **103**, 6173
- Atkinson, R., D. L. Baulch, R. A. Cox, R. F. Hampson Jr., J. A. Kerr, M. J. Rossi, and J. Troe, *J. Phys. Chem. Ref. Data*, 1997, **26**, 521
- Barnes, I., K. H. Becker, P. Carlier and G. Mouvier, *Int. J. Chem. Kinet.*, 1987, **19**, 489
- Barnes, I., V. Bastian, K. H. Becker and R. D. Overath, *Int. J. Chem. Kinet.*, 1991, **23**, 579
- Bloss, W. J., T. J. Gravestock, D. E. Heard, T. Ingham, G. P. Johnson and J. D. Lee, *J. Environ. Monit.*, 2003, **5**, 21
- Canosa-Mas, C. E., M. L. Flugge, D. Shah, A. Vipond and R. P. Wayne, *J. Atmos. Chem.*, 1999, **34**, 153
- Daykin, E. P. and P. H. Wine, *J. Geophys. Res.*, 1990, **95(D11)**, 18547
- Dillon, T. J. and D. E. Heard, *J. Photochem. Photobiol. A.*, 2003, **157**, 223

- Ezell, M. J., W. H. Wang, A. A. Ezell, G. Soskin and B. J. Finlayson-Pitts, *Phys. Chem. Chem. Phys.*, 2002, **4(23)**, 5813
- Finlayson-Pitts, B. J., C. J. Keoshian, B. Buehler and A. A. Ezell, *Int. J. Chem. Kinet.*, 1999, **31**, 491
- Finlayson-Pitts, B. J. and J. N. Pitts Jr., *Chemistry of the Upper and Lower Atmosphere*, Academic Press, San Diego, 2000
- Gilles, M. K., A. A. Turnipseed, R. K. Talukdar, Y. Rudich, P. W. Villalta, L. G. Huey, J. B. Burkholder and A. R. Ravishankara, *J. Phys. Chem.*, 1996, **100**, 14005
- Himmelmann, S., J. Orphal, H. Bovensmann, A. Richter, A. Ladstätter-Weissenmayer and J. P. Burrows, *Chem. Phys. Letts.*, 1996, **251**, 330
- Hollas, J. M., *Modern Spectroscopy*, 2nd Edition, John Wiley and Sons, Chichester, 1993
- Hölscher, D., Chr. Fockenberg and R. Zellner, *Ber. Bunsenges. Phys. Chem.*, 1998, **102**, 716
- Hölscher, D. and R. Zellner, *Phys. Chem. Chem. Phys.*, 2002, **4**, 1839
- Inoue, G., M. Suzuki and N. Washida, *J. Phys. Chem.*, 1983, **79**, 4730
- Kaufman, F., *Prog. Reac. Kinet.*, 1961, **1**, 1
- Knight, G. P. and J. N. Crowley, *Phys. Chem. Chem. Phys.*, 2001, **3**, 393
- Logan, J. A., *J. Geophys. Res.*, 1985, **90**, 10463
- Maguin, F., A. Mellouki, G. Laverdet, G. Poulet and G. Le Bras, *Int. J. Chem. Kinet.*, 1991, **23**, 237
- Martin, D., J. L. Jourdain, G. Laverdet and G. Le Bras, *Int. J. Chem. Kinet.*, 1987, **19**, 503
- Okabi H, *Photochemistry of Small Molecules*, John Wiley and Sons, New York, 1978
- Prinn, R. G., R. F. Weiss, B. R. Miller, J. Huang, F. N. Alyea, D. M. Cunnold, P. J. Fraser, D. E. Hartley and P. G. Simmonds, *Science*, 1995, **269**, 187
- *Quanta-Ray GCR-11 Pulsed Nd:YAG Laser Instruction Manual,* Spectra-Physics, California, 1990
- Sander, S. P., *J. Phys. Chem.*, 1986, **90**, 2194
- Spicer, C. W., E. G. Chapman, B. J. Finlayson-Pitts, R. A. Plastridge, J. M. Hubbe, J. D. Fast and C. M. Berkowitz, *Nature*, 1998, **394**, 353
- Shu, Y. and R. Atkinson, *J. Geophys. Res.*, 1995, **100**, 7275

- Turnipseed, A. A., M. K. Gilles, J. B. Burkholder and A. R. Ravishankara, *Chem. Phys. Lett.*, 1995, **242**, 427
- Vakhtin, A. B., *Int. J. Chem. Kinet.*, 1996, **28**, 443
- Vipond, A, C. E. Canosa-Mas, M. L. Flugge, D. J. Gray, D. E. Shallcross, D. Shah and R. P. Wayne, *Phys. Chem. Chem. Phys.*, 2002, **4**, 3648

Chapter 4 A discharge–flow tube/resonance fluorescence study of the reaction of atomic chlorine with acetone and butanone

4.1 Introduction

The first aim of the work described in this chapter was to determine the rate constant for the reaction of atomic chlorine with acetone using a discharge–flow tube coupled to a Cl resonance-fluorescence (RF) detection system. As discussed in chapter 1, reaction with Cl is a potentially important sink of volatile organic compounds (VOCs) in the marine boundary layer (MBL), where Cl concentrations of up to 10^4 – 10^5 atom cm^{-3} may be present. Acetone, one of the most abundant VOCs, has been shown to be ubiquitous to the entire troposphere and thus reaction with Cl is likely to contribute to its degradation.

Nielsen *et al.* (2002) found that the reaction proceeds mainly *via* hydrogen abstraction:

$$CH_3COCH_3 + Cl \rightarrow CH_3COCH_2 + HCl \quad k_{4.1a}/k_4 > 0.97 \quad \text{(R4.1a)}$$

$$\rightarrow CH_3COCl + CH_3 \quad k_{4.1b}/k_4 \approx 0.01 \quad \text{(R4.1b)}$$

$$\rightarrow CH_3CO + CH_3Cl. \quad k_{4.1c}/k_4 < 0.02 \quad \text{(R4.1c)}$$

The previous laboratory investigations of $k_{4.1}$ that were published at the time it was decided to undertake the work are listed in table 4.1. Since then, two more studies have been published: see section 4.4.1.2. It can be seen that the values of the rate constant determined with the relative-rate method are in agreement. Only one absolute derivation of $k_{4.1}$ has been undertaken, and that study reports a rate constant that is higher than those found in the relative-rate experiments. Indeed, the value obtained by Notario *et al.* (2000) is twice that obtained by Olsson *et al.* (1997). Wallington *et al.* (1998) suggest that there were possible errors in the measurement of the ketone concentrations by the latter workers, although Ljungström and Hallquist (1998), and Albaladejo *et al.* (2003) reject this argument. It was therefore decided to undertake another absolute determination of $k_{4.1}$.

Table 4.1. Previous laboratory studies of the reaction of Cl with CH_3COCH_3.

Method	**$k_{4.1}/10^{-12}$ cm^3 molecule^{-1} s^{-1}**	**Reference**
RR Photolysis/FTIR	2.37 ± 0.12 [f] (2.37 ± 0.59)	Wallington *et al.* (1990)[a]
RR Pulsed-laser photolysis/absorption	1.69 ± 0.32	Olsson *et al.* (1997)[b]
Absolute Pulsed-laser photolysis/RF	3.06 ± 0.38	Notario *et al.* (2000)[c]
RR Photolysis/FTIR	2.2 ± 0.4	Christensen *et al.* (2000)[d]
RR Photolysis/GC and FTIR	2.20 ± 0.44	Carr *et al.* (in preparation)[e]

Notes: RR – relative rate; [a]295 K and 700 Torr; [b]294 K and 1 atmosphere; [c]298 K and 15 – 60 Torr, [d]296 K and 700 Torr; [e]298K and 760 Torr. [f]The error limits of this rate constant are equal to 2σ and do not include the systematic errors, although the authors estimate these to be ± 20 %. The value in brackets includes these errors.

The second aim was to extend the experiment in an attempt to obtain information concerning the chemistry of $CH_3COCH_2O_2$. The second half of this thesis describes the construction of a mass spectrometer intended for the study of peroxy-radical kinetics. At the time the work described in this chapter was performed, the mass spectrometer was in the design and construction phases. However, it was thought that existing apparatus could be used to study some aspects of the chemistry of the acetonylperoxy radical. The aim was to initiate the reaction:

$$CH_3COCH_2O_2 + Cl \rightarrow \text{products} \qquad \text{(R4.2)}$$

by adding oxygen to the reaction system to generate $CH_3COCH_2O_2$, and increasing the concentration of Cl. The decay of the Cl RF signal as a function of time would be attributable to both reactions 4.1 and 4.2.

The last aim was to investigate the reaction of atomic chlorine with butanone:

$$CH_3COCH_2CH_3 + Cl \rightarrow \text{products.} \qquad \text{(R4.3)}$$

This work formed part of a research project that was concerned with the reactions of Cl atoms with different ketones. As stated in the first chapter, butanone has been observed in the troposphere, albeit at much lower concentrations than acetone. Reaction with Cl atoms may be an important loss process for butanone in the MBL.

4.2 Experimental details

4.2.1 The flow tube

A schematic diagram of the discharge–flow tube is shown in figure 4.1. It consisted of a 1.1 m long, 26 mm internal diameter Pyrex tube. Gases were introduced *via* three large side arms and seven smaller ports. The internal surface of the flow tube was coated with a halocarbon wax (KMZ Chemicals Ltd) to minimize the loss of reactive species to the walls. The tube was pumped by a Rootes pump (Leybold RUVAC WAU251) backed by a two-stage rotary pump (Leybold Trivac D40B). A diaphragm valve (Edwards Speedivalve) was used to adjust the pumping efficiency. The flow-tube pressure (FTP) was measured using a 10 Torr capacitance manometer (MKS Baratron Type 626A) located towards the end of the tube.

The helium carrier gas (BOC, 99.996 %) flowed directly from the cylinder, through purification traps containing sodium and calcium aluminosilicate molecular sieve (BDH, 4A, 5A and 13X) cooled with liquid nitrogen, and into the flow tube through two of the side arms. The gas flows were regulated with a 10 SLPM mass flow controller (Tylan FC2900) and a ~2.5 SLPM ball flow-meter (Jencons RS2) fitted with a needle valve (Nupro). The backing pressure was monitored with a 'bubbler' — a trap filled with

dimethyl phthlate (BDH) through which the gas could escape and thus keep the pressure in the line equal to the atmospheric pressure.

Figure 4.1. A schematic diagram of the discharge–flow tube.

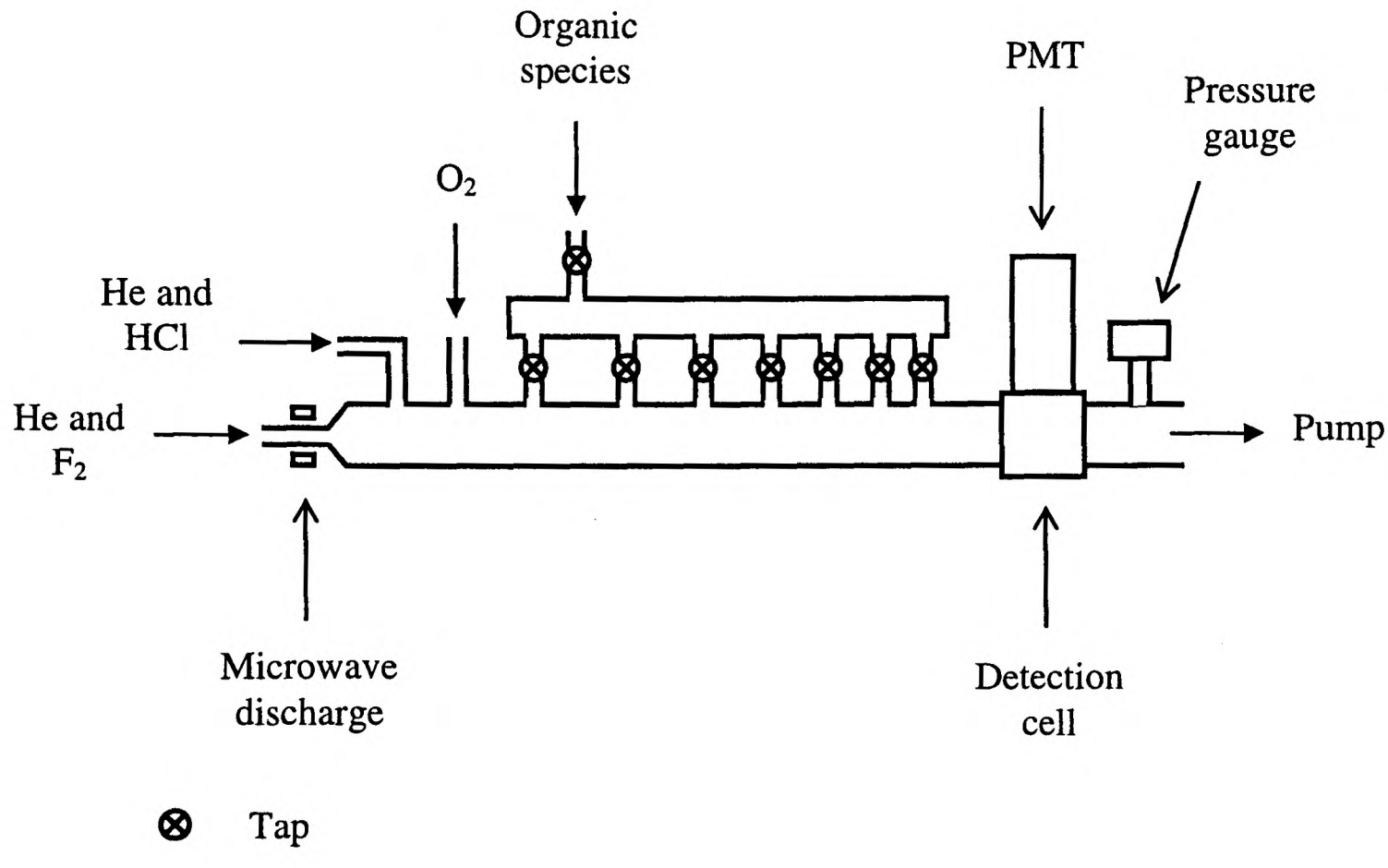

The flows of all other gases were controlled by ~0.05 and ~2.5 SLPM ball flow-meters (Jencons RS1 and RS2) fitted with needle valves. The backing pressures were monitored by 1000 Torr capacitance manometers (Data Instruments) or, as in the case of oxygen, with a bubbler. Oxygen (BOC, 99.5 %) was delivered directly from the cylinder and passed through purification traps containing silica gel, diphosphorus pentoxide and molecular sieve (all trap materials supplied by BDH). Gaseous mixtures of acetone (Aldrich, 99.9+ %), butanone (Aldrich, 99.5+ %), fluorine (Messer Griesheim, 1 % in He) and hydrogen chloride (Aldrich, 99+ %) were stored in 6 L bulbs. These gases were purified and the mixtures prepared by the techniques described in Appendix I. Cl atoms were generated at the upstream end of the flow tube: see the next section. The ketone was added through different ports to vary the contact time. O_2 was passed into the flow tube through one of the side arms.

4.2.2 Generation of Cl atoms

Atomic chlorine was produced *via* the following reaction:

$$F + HCl \rightarrow HF + Cl. \qquad \text{(R4.4)}$$

The fluorine atoms were generated by passing a 1% mixture of F_2 in He, further diluted with another flow of He, through a microwave-discharge cavity powered by a EMS Microtron 200 generator operating at about 35 Watts. The F_2 concentration was (2 – 13) $\times 10^{11}$ molecule cm^{-3}. An excess of HCl, (1 – 5) $\times 10^{13}$ molecule cm^{-3}, was added to ensure the F atoms had been consumed before the first port where the acetone was added. The rate constant for R4.4 is 1.16×10^{-11} cm^3 $molecule^{-1}$ s^{-1} (Baulch *et al.*, 1981).

Chlorine atoms can also be produced by passing molecular chlorine through a discharge. However, this technique was not used because it can lead to the erroneous measurement of [Cl]. The dissociation of Cl_2 in a microwave-discharge cavity is not an efficient process — mass-spectrometric measurements made by Seeley *et al.* (1996) showed that less than 50 % is converted to Cl atoms. The remaining molecular chlorine may react with radical species generated in the flow tube to yield more Cl atoms. Of course, a similar problem may arise with the technique that was employed, as any remaining F_2 molecules could react with radical species to produce F, which would generate chlorine atoms *via* R4.4. However, the dissociation of F_2 in a discharge was thought to occur more efficiently than the dissociation of Cl_2 and thus was considered the preferred technique. Indeed, mass-spectrometric work performed after this study showed that ~95 % of the molecular fluorine was dissociated: see section 6.4.1.

4.2.3 Detection of Cl atoms

The Cl RF apparatus was comprised of a lamp, a detection cell and a detector. A schematic diagram is shown in figure 4.2. The lamp consisted of Pyrex and quartz tubing fitted with a microwave-discharge cavity. A 5 % mixture of Cl_2 (Aldrich, 99.5 %) in CP–He (BOC, 99.999 %) was mixed with a further flow of CP–He and passed through the lamp. The gas flows were regulated by ~0.05 SLPM ball flow-meters (Jencons RS1)

fitted with needle valves (Nupro). The He flowed directly from the cylinder and was purified with an Oxysorb cartridge (Messer Griesheim) and molecular sieve (BDH) cooled with dry ice. The lamp pressure was ~0.8 Torr. The lamp was pumped by a rotary pump (AEI Ltd, Metrovac) and the pressure was measured with a Pirani gauge (Edwards PRM10).

Figure 4.2. A schematic diagram of the Cl RF apparatus.

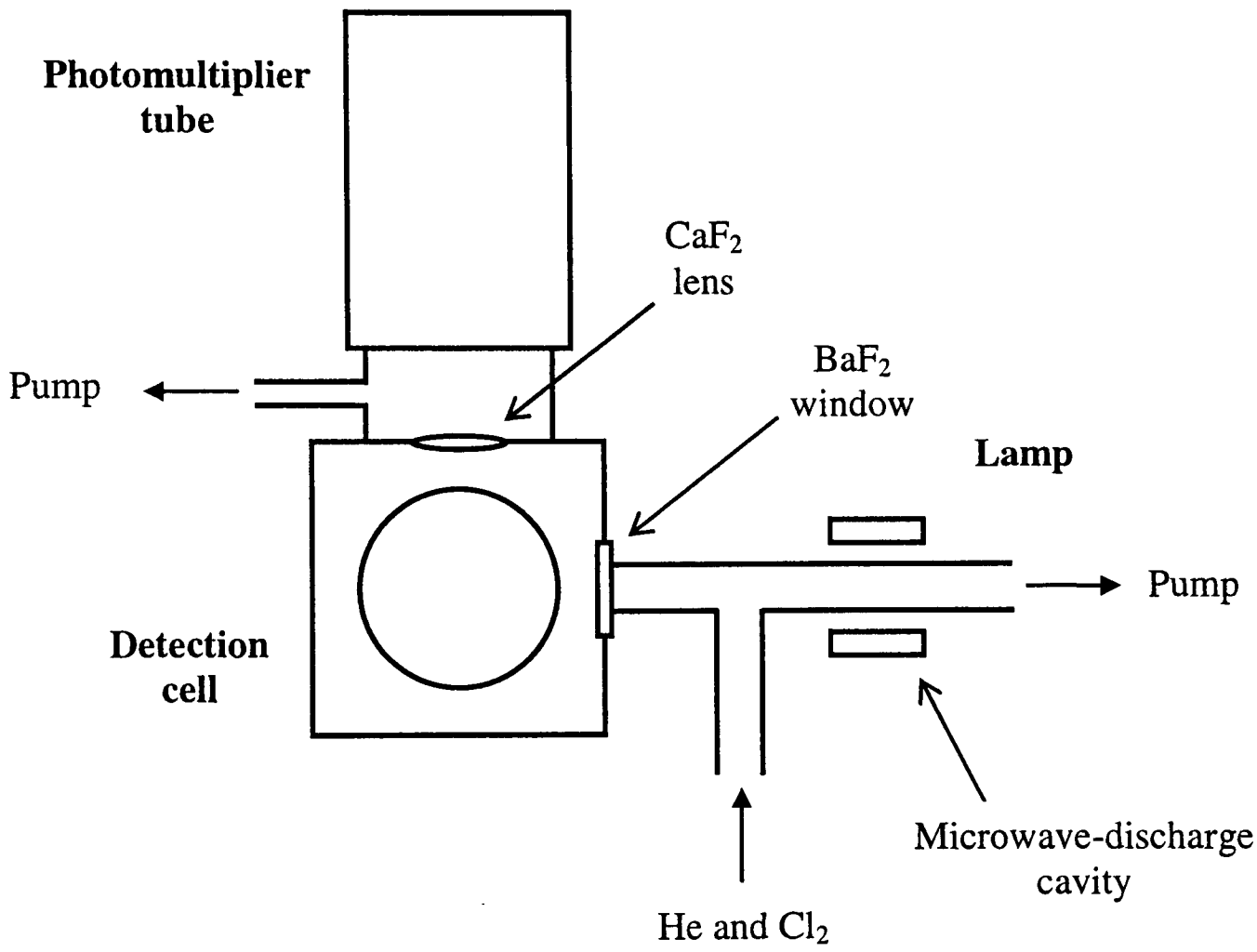

The molecular chlorine flowing through the microwave cavity was dissociated to produce some electronically excited Cl atoms. The discharge was powered by a microwave generator operating at ~40 W. The excited atoms emitted several wavelengths of light in the range 134.7 to 139.7 nm, with the most intense transition occurring at 138.9 nm (Okabe, 1978). Some of this radiation passed through a BaF_2 window and into the detection cell, so causing any Cl atoms present to become excited. These atoms fluoresced and a portion of this RF was focused by a CaF_2 lens onto the photomultiplier (PMT) (Hamamatsu, R1459), which was positioned at right angles to the lamp. The PMT

had an MgF_2 window and a Cs-I photocathode, and could detect radiation in the range 115 – 200 nm, with peak sensitivity at 140 nm. The PMT was operated at ~1.5 kV. The signal was fed to an amplifier (in-house built) and recorded on a chart recorder (Venture Servoscribe).

Several measures were undertaken to prevent other species from interfering with the detection of Cl-atom RF. O_2 absorbs the wavelengths of interest and thus it was necessary to evacuate the gap between the detection cell and the PMT. Also, there was a possibility that O-atom RF would be detected. O_2, present as an impurity in the lamp gases, would be dissociated to produce some electronically excited O atoms. These atoms would emit light in the range 130.2 – 130.6 nm (Okabe, 1978) and cause RF of any oxygen atoms in the detection cell. As previously mentioned, the lamp and flow-tube gases were carefully purified. Also, the intensity of O RF was greatly reduced by the use of a BaF_2 window on the lamp side of the detection cell. (BaF_2 does not transmit light of wavelengths less than ~134 nm).

4.2.3.1 Calibration of the Cl RF signal

It was necessary to quantify the concentration of Cl atoms to ensure that the desired experimental conditions were employed and also to enable the chemistry occurring in the flow tube to be accurately modelled. The method of calibration was to produce large amounts of F atoms in the flow tube and then add small quantities of HCl through the side arm. Thus the HCl was completely converted to Cl, and this 1:1 stoichiometry allowed [Cl] to be derived. A calibration curve was obtained by recording the response of the detection system to various concentrations of Cl (or more precisely, HCl). A typical curve is shown in figure 4.3. The calibration factor in this case was 2.6×10^{12} atom cm $^{-3}$ V^{-1} at an amplification of ×3. The sensitivity of the Cl RF detection system was ~1×10^9 atom cm $^{-3}$ for a signal-to-noise ratio of unity and an integration time of 60 s.

Care was required when applying the calibration factor to measurements made in experiments where oxygen was employed. As previously mentioned, O_2 absorbs the wavelengths of interest. Thus, the Cl-RF calibration no longer holds. The concentration

of chlorine in such experiments was determined by recording the signal before the oxygen was added.

Figure 4.3. A typical calibration curve for a Cl RF detection system. The amplification setting was ×3.

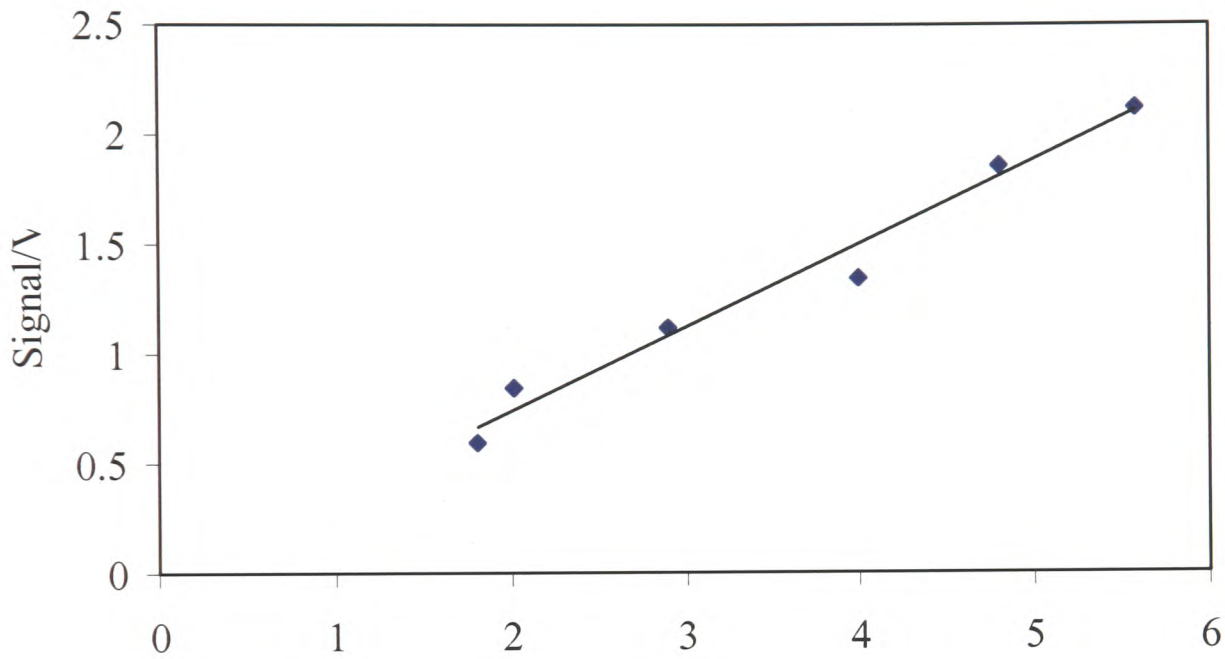

4.2.4 Experimental conditions

The reactions of chlorine atoms with acetone and butanone were carried out under *pseudo*-first-order conditions. Four different experiments involving acetone were performed: one where [Cl] was low; another in which [Cl] was increased and O_2 was added in an attempt to initiate the reaction of Cl atoms with the acetonylperoxy radical; and two control experiments. The first of these employed a higher concentration of chlorine and the second involved low [Cl] and the presence of O_2. The experimental conditions are listed in table 4.2. The concentration of oxygen added to the flow tube was sufficient to ensure that:

$$CH_3COCH_2 + O_2 + M \rightarrow CH_3COCH_2O_2 + M \qquad \text{(R4.5)}$$

occurred at a much higher rate than:

$$CH_3COCH_2 + Cl \rightarrow \text{products.} \qquad \text{(R4.6)}$$

It should be noted that the FTP was corrected to take account of the fact that the pressure measurement was made at the downstream end, and not the middle, of the flow tube. This pressure correction was ≤ 7.3 %. The observed first-order rate constants were also corrected for axial and radial diffusion of Cl atoms. The diffusion coefficient of Cl in He is 5.24×10^{-2} m^2 s^{-1} at 1 Torr (Cotter *et al.,* 2001). A correction factor of ≤ 2 % was employed. (See chapter 2 for a discussion of how these corrections are calculated).

Table 4.2. The experimental conditions employed in the study of the reactions of Cl with CH_3COCH_3 and $CH_3COCH_2CH_3$.

Condition	**Acetone study**	**Butanone study**
[Cl]/10^{10} atom cm^{-3}	1.39 – 3.43 (low [Cl] experiments) 30.1 – 43.1 (high [Cl] experiments)	3.03 – 3.81
[Ketone]/10^{13} molecule cm^{-3}	0.60 – 4.07	0.06 – 0.27
[O_2]/10^{15} molecule cm^{-3}	2.15 – 3.15	
Pressure/Torr	1.58 ± 0.02	1.60 ± 0.03
Temperature/K	300 ± 5	300 ± 2
Linear flow velocity/cm s^{-1}	2032 – 2406	2212 – 3779
Contact time/s	0.008 – 0.039	0.005 – 0.026

4.3 Results

4.3.1 The reaction of Cl with acetone

Typical first-order plots and the second-order plots for the four experiments concerned with acetone are shown in figures 4.4 to 4.11. The second-order rate constants are listed in table 4.3. (See chapter 2 for an explanation of how these plots and the rate constant are derived). Two values of each rate constant are displayed: one with the errors quoted as the 95 % confidence limits and another with an additional ± 10 % equating to the estimated systematic error.

Table 4.3. The second-order rate constants for the four experiments involving the reaction of Cl atoms with acetone.

	$[Cl]/10^{10}$ atom cm^{-3} $[O_2]/10^{15}$ molecule cm^{-3}	**$k \pm 95$ % confidence limits/10^{-12} cm^3 $molecule^{-1}$ s^{-1}**	**$k \pm$ (95 % confidence limits + 10 % systematic error) /10^{-12} cm^3 $molecule^{-1}$ s^{-1}**
1	[Cl] = 1.39 – 3.43 no O_2	2.47 ± 0.16	2.47 ± 0.41
2	[Cl] = 30.1 – 43.1 no O_2	3.01 ± 0.12	3.01 ± 0.42
3	[Cl] = 1.70 – 2.33 $[O_2]$ = 2.25 – 3.15	2.39 ± 0.17	2.39 ± 0.41
4	[Cl] = 32.3 – 37.1 $[O_2]$ = 2.77 – 2.89	2.56 ± 0.13	2.56 ± 0.39

Figure 4.4. A typical first-order plot for the reaction of a low concentration of Cl atoms with acetone in the absence of oxygen. [Cl] = 3.04×10^{10} atom cm^{-3} and [acetone] = 2.17×10^{13} molecule cm^{-3}.

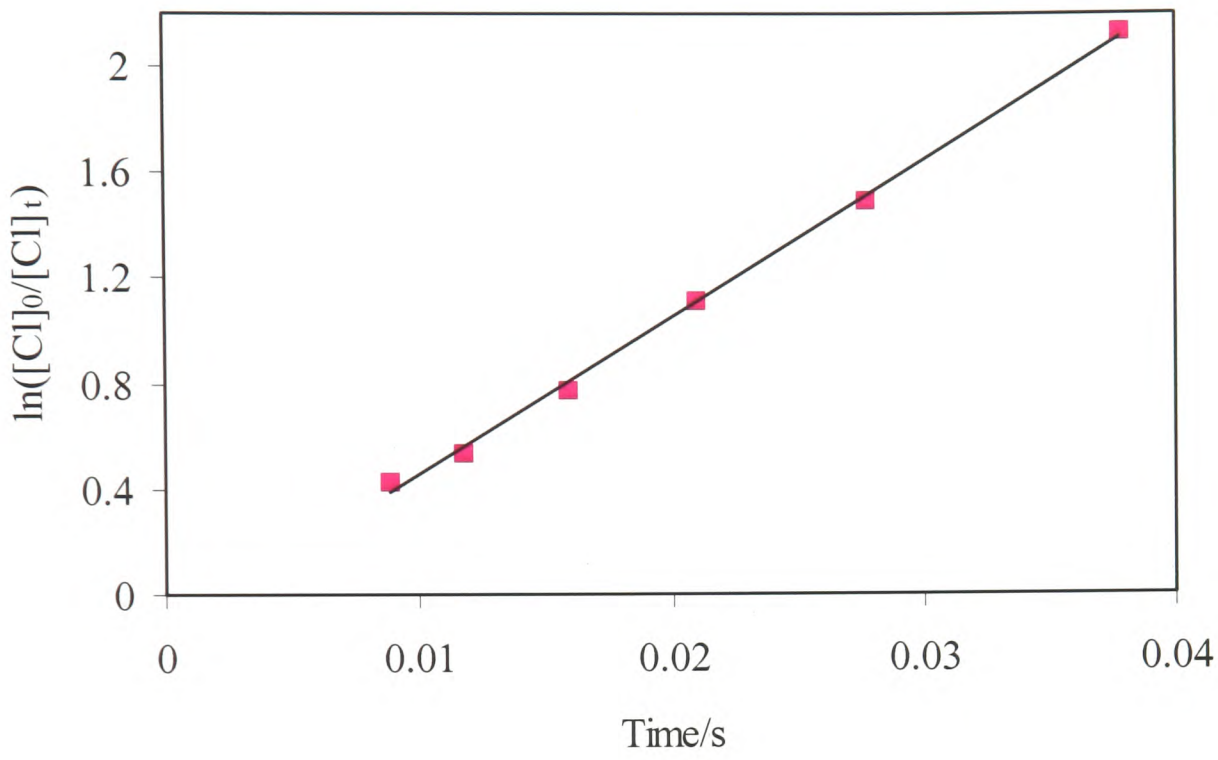

Figure 4.5. A typical first-order plot for the reaction of a high concentration of Cl atoms with acetone in the absence of oxygen. [Cl] = 4.21×10^{11} atom cm^{-3} and [acetone] = 2.32×10^{13} molecule cm^{-3}.

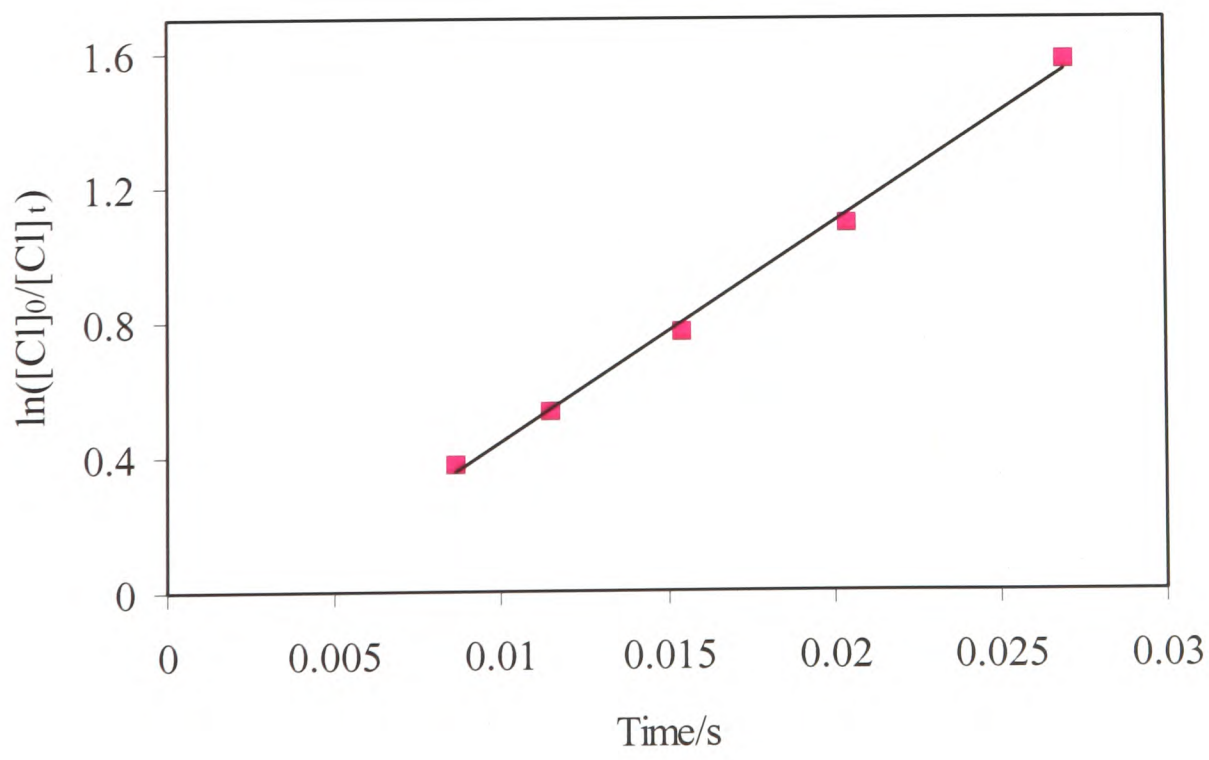

Figure 4.6. A typical first-order plot for the reaction of a low concentration of Cl atoms with acetone in the presence of oxygen. $[Cl] = 2.10 \times 10^{10}$ atom cm^{-3}, [acetone] = 2.37×10^{13} molecule cm^{-3} and $[O_2] = 2.78 \times 10^{15}$ molecule cm^{-3}.

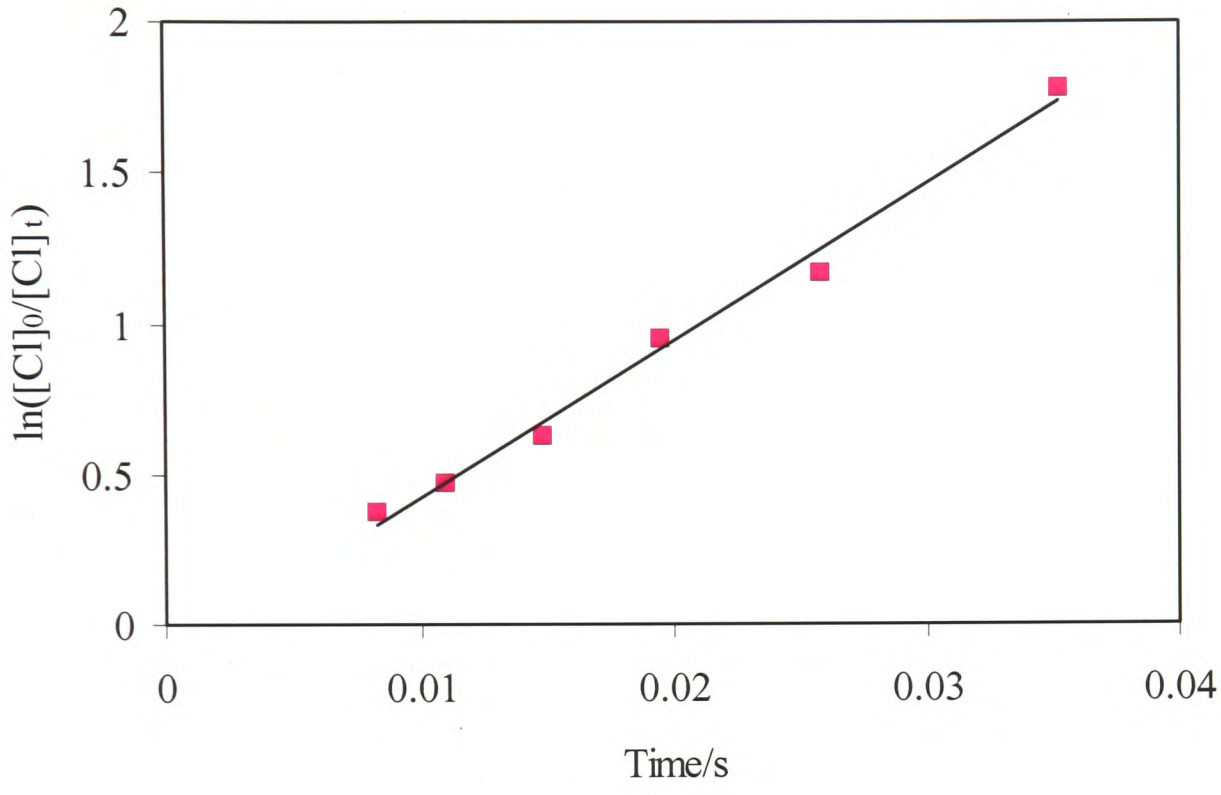

Figure 4.7. A typical first-order plot for the reaction of a high concentration of Cl atoms with acetone in the presence of oxygen. $[Cl] = 3.71 \times 10^{11}$ atom cm^{-3}, [acetone] = 3.14×10^{13} molecule cm^{-3} and $[O_2] = 2.77 \times 10^{15}$ molecule cm^{-3}.

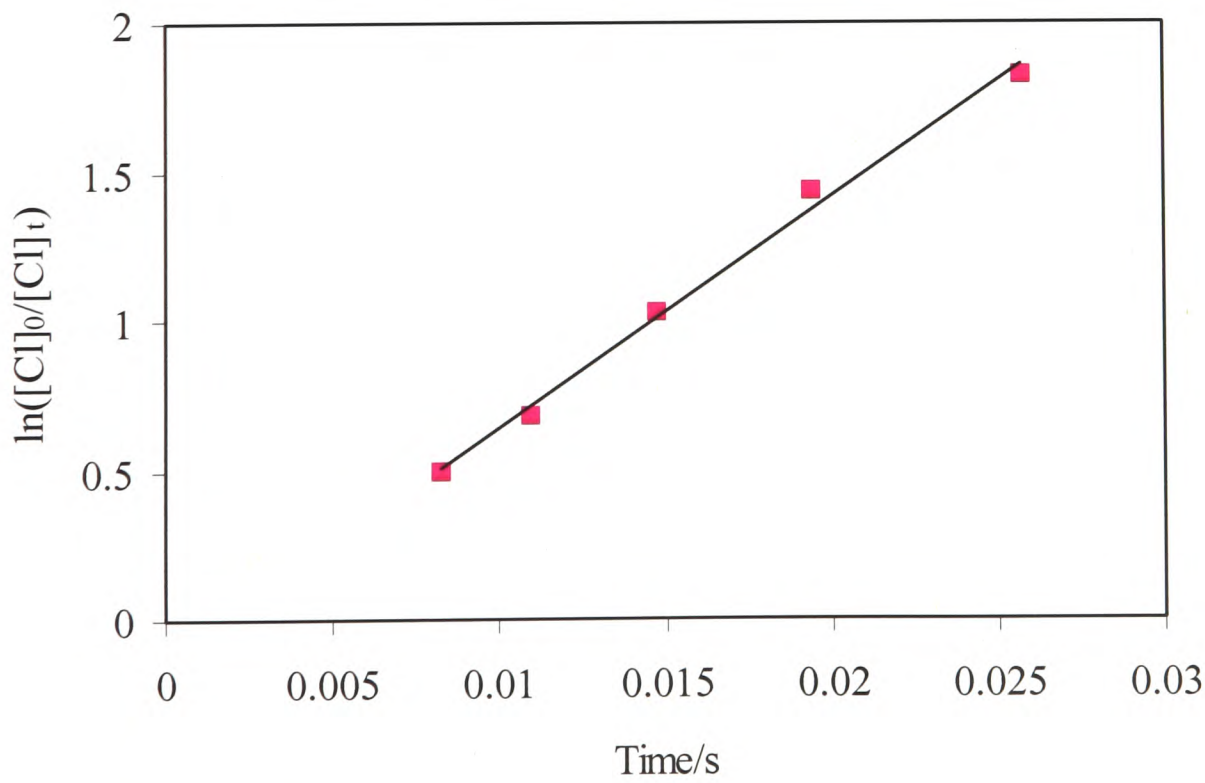

Figure 4.8. The second-order plot for the reaction of a low concentration of Cl atoms with acetone in the absence of oxygen. [Cl] = $(1.39 - 3.43) \times 10^{10}$ atom cm^{-3}. The unbroken line passes through the origin and the dashed line does not.

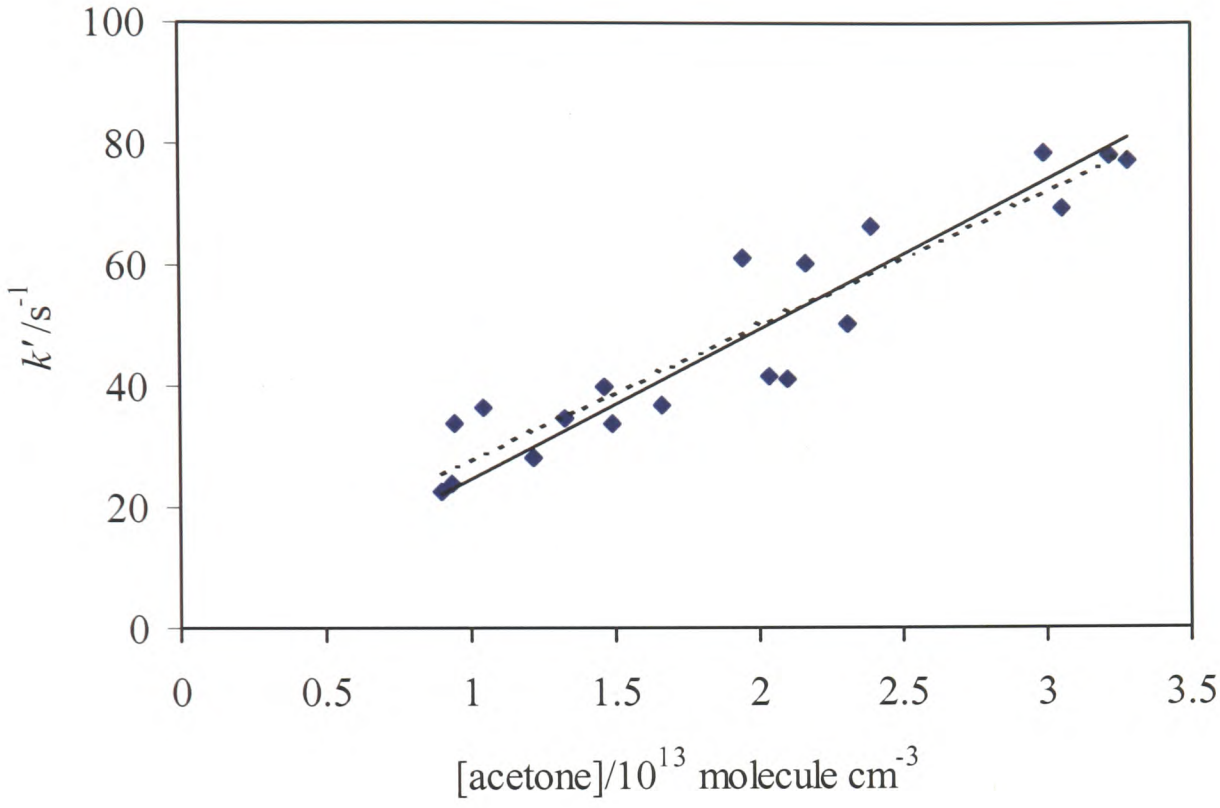

Figure 4.9. The second-order plot for the reaction of a high concentration of Cl atoms with acetone in the absence of oxygen. [Cl] = $(3.01 - 4.31) \times 10^{11}$ atom cm^{-3}. The unbroken line passes through the origin and the dashed line does not.

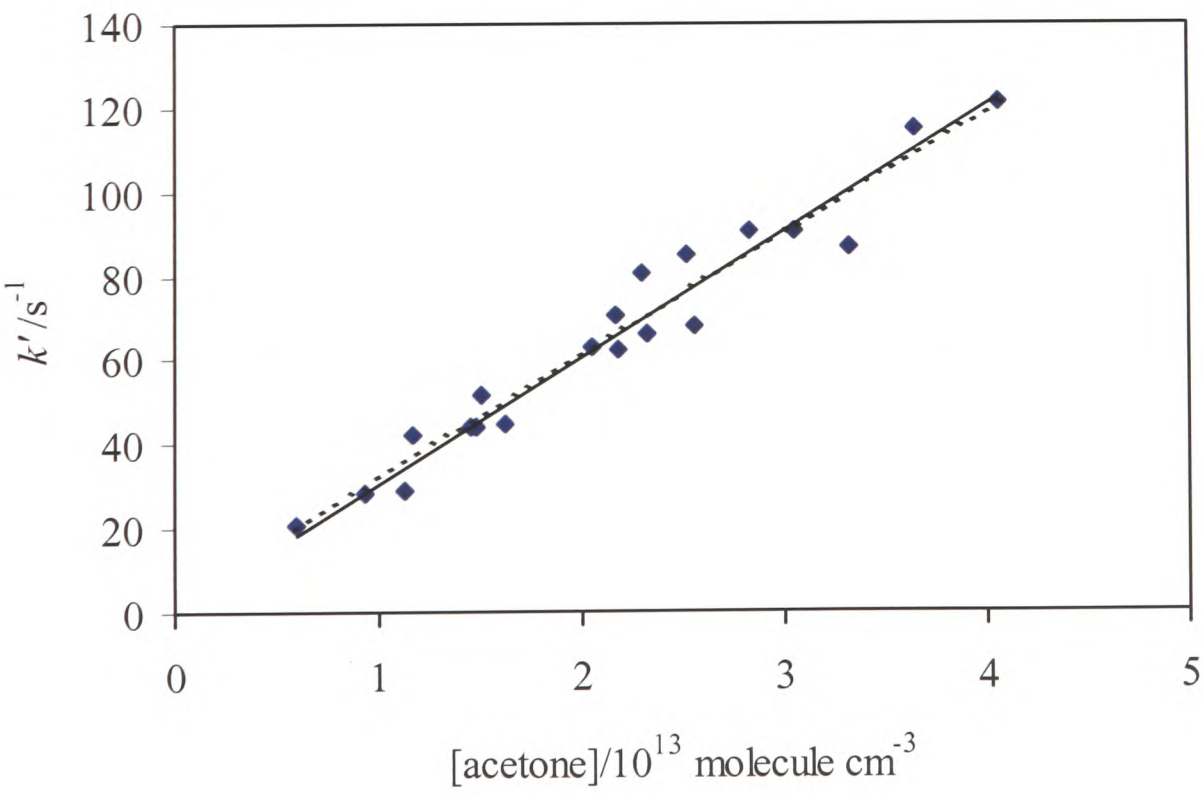

Figure 4.10. A second-order plot for the reaction of a low concentration of Cl atoms with acetone in the presence of oxygen. [Cl] = (1.70 – 2.33) × 10^{10} atom cm^{-3} and $[O_2]$ = (2.25 – 3.15) × 10^{15} molecule cm^{-3}. The unbroken line passes through the origin and the dashed line does not.

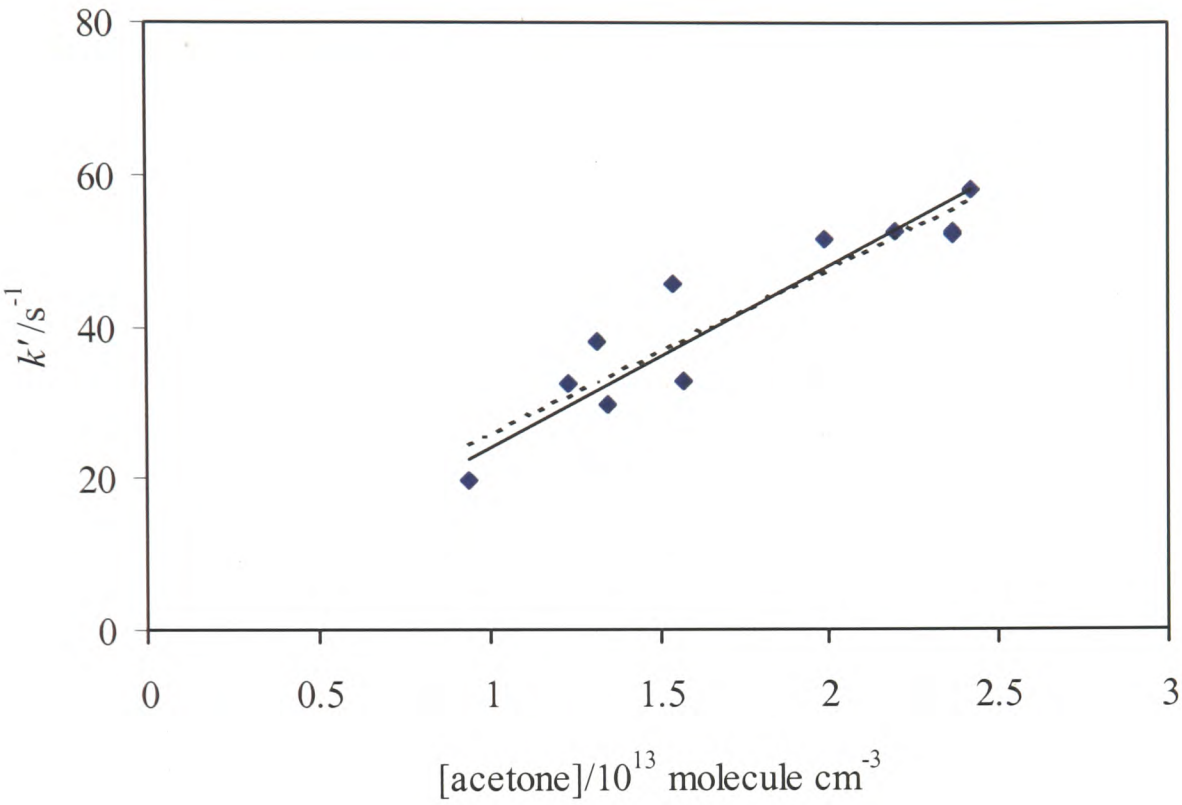

Figure 4.11. A second-order plot for the reaction of a high concentration of Cl atoms with acetone in the presence of oxygen. [Cl] = (3.23 – 3.71) × 10^{11} atom cm^{-3} and $[O_2]$ = (2.77 – 2.89) × 10^{15} molecule cm^{-3}. The unbroken line passes through the origin and the dashed line does not.

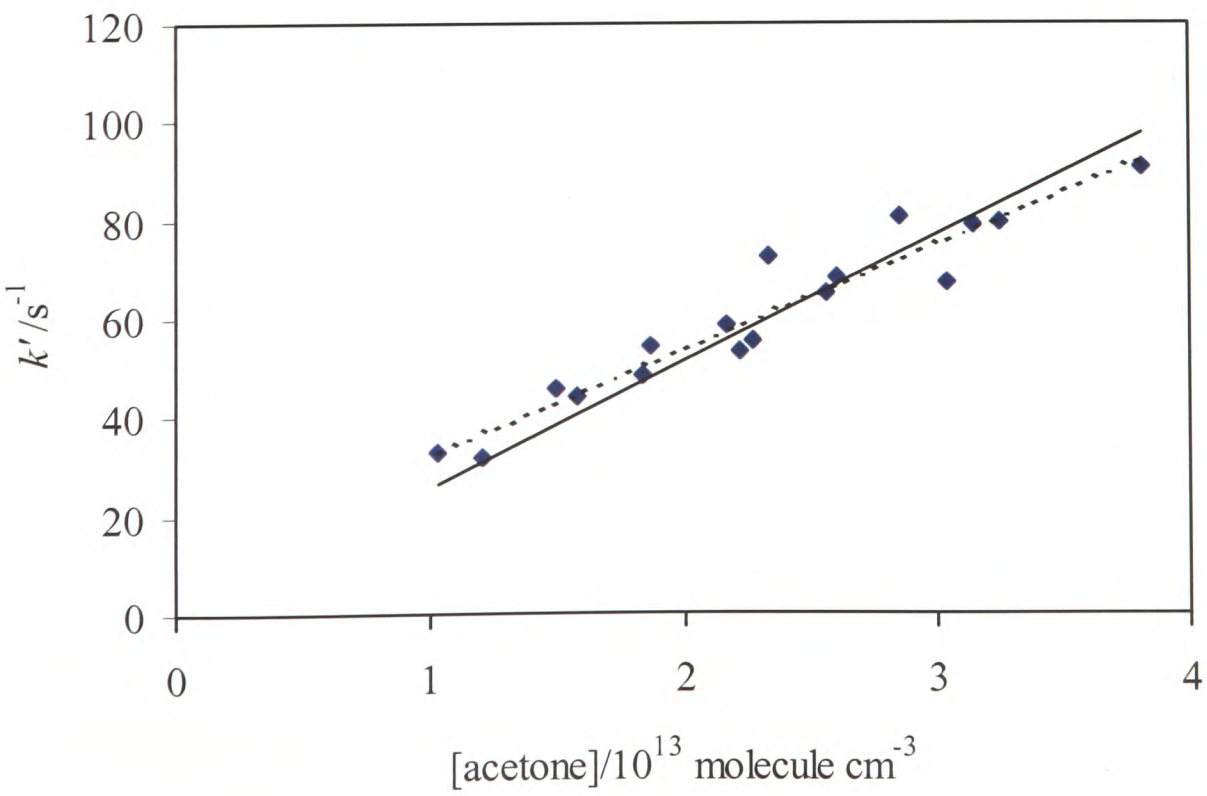

4.3.2 The reaction of Cl with butanone

A typical first-order plot and the second-order plot for the experiment involving butanone are shown in figures 4.12 and 4.13. The rate constant is $(4.31 \pm 0.87) \times 10^{-11}$ cm^3 molecule^{-1} s^{-1}, where the quoted errors are equal to the 95 % confidence limits and an additional ± 10 % equating to the estimated systematic error.

4.4 Discussion

4.4.1 The reaction of Cl with acetone

4.4.1.1 Data analysis

The values of k' were obtained from the first-order plots by applying a linear least-squares fit of the form $y = mx + c$, where m is the gradient (equal to k') and c is the intercept on the y axis. The fit should pass through the origin because at time $t = 0$ s the value of $\ln([Cl]_0/[Cl]_t)$ should also be zero. However, all the plots had negative values of c. Such intercepts are indicative of secondary chemistry and/or errors in the measurement of absolute time. It was thought that most plots were not affected by the former (see section 4.4.1.3) and instead that the latter was the correct explanation. Absolute time was poorly defined in two ways: first, the detection point, $t = 0$ s, was not a sharp point but instead a diffuse detection region, and secondly, the measurement of the period between the injection point and the detection region did not take account of the time taken for the acetone to mix into the flow-tube gases. The intercept on the x axis equates to these errors and in most plots it was 2 – 3 ms. However, as the time taken for acetone to mix should be the same at each port, the measurement of the relative values of time, *i.e.* the periods between injection ports, should be correct. Thus a $y = mx + c$ fit is the appropriate method by which to obtain k'.

The equations of the linear least-squares fits to the second-order plots obtained with and without forcing the line through the origin are listed in table 4.4. The quoted errors are the 95 % confidence limits. Both fits are also displayed on the second-order plots (the unbroken lines pass through the origin and the dashed lines do not). The $y = mx + c$ fits

Figure 4.12. A typical first-order plot for the reaction of Cl atoms with butanone. [Cl] = 3.23×10^{10} atom cm^{-3} and [butanone] = 2.16×10^{12} molecule cm^{-3}.

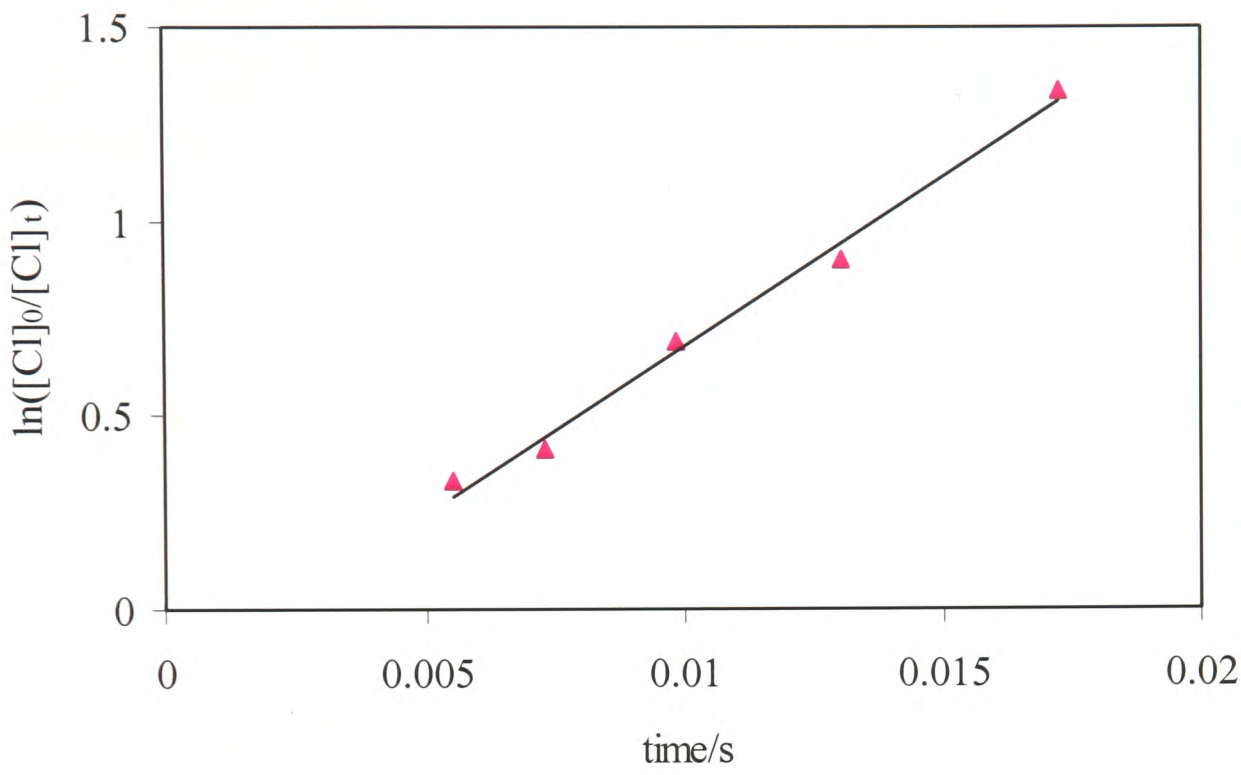

Figure 4.13. The second-order plot for the reaction of Cl atoms with butanone. [Cl] = $(3.03 - 3.81) \times 10^{10}$ atom cm^{-3}. The unbroken line passes through the origin and the dashed line does not.

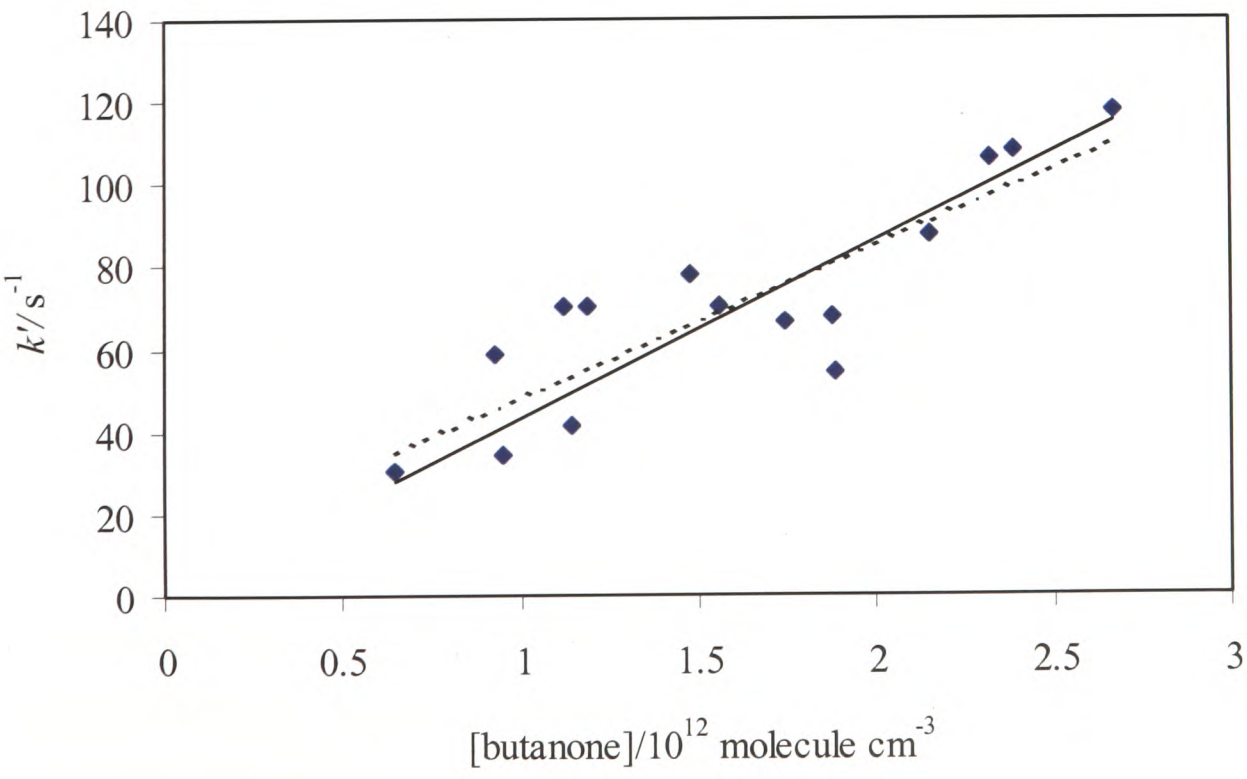

should pass through the origin as there should be no loss of Cl atoms as a result of reaction when [acetone] = 0. It can be seen that the intercepts are small and the origin falls within the error limits for experiments 1, 2 and 3. In experiment 4, a larger intercept was obtained with error limits that did not include the origin, which could suggest that some species in the flow tube was causing an extra loss of Cl atoms to the walls. However, as the addition of acetone in the other experiments did not cause such a loss, it is more likely that the intercept of experiment 4 is a result of scatter in the data. It can be concluded that a $y = mx$ fit is the correct method of analysis for all the experiments.

Table 4.4. The equations of the linear least-squares fit of the second-order plots obtained with and without forcing the line through the origin.

	[Cl]/10^{10} atom cm^{-3} **[O_2]/10^{15} molecule cm^{-3}**	***m*/cm^3 molecule^{-1} s^{-1} from a $y = mx$ fit**	***m*/cm^3 molecule^{-1} s^{-1} + *c* /s^{-1} from a $y = mx + c$ fit**
1	[Cl] = 1.39 – 3.43 no O_2	$(2.47 \pm 0.16) \times 10^{-12}$	$(2.23 \pm 0.42) \times 10^{-12}$ $+ (5.53 \pm 8.08)$
2	[Cl] = 30.1 – 43.1 no O_2	$(3.01 \pm 0.12) \times 10^{-12}$	$(2.92 \pm 0.32) \times 10^{-12}$ $+ (2.35 \pm 6.90)$
3	[Cl] = 1.70 – 2.33 [O_2] = 2.25 – 3.15	$(2.39 \pm 0.17) \times 10^{-12}$	$(2.16 \pm 0.63) \times 10^{-12}$ $+ (4.40 \pm 11.11)$
4	[Cl] = 32.3 – 37.1 [O_2] = 2.77 – 2.89	$(2.56 \pm 0.13) \times 10^{-12}$	$(2.14 \pm 0.36) \times 10^{-12}$ $+ (10.74 \pm 8.23)$

4.4.1.2 Comparison with literature values

The value of $k_{4.1}$ will be taken as that obtained in experiment 1, as the conditions were such that the extent of secondary reactions involving Cl atoms could not be significant. The value is listed in table 4.5 along with others from the literature. It can be seen that there is good agreement with the previous studies (including Notario *et al.*, 2000), although the value obtained by Olsson *et al.* (1997) is a little low.

Table 4.5. A comparison of the rate constants for the reaction of Cl with CH_3COCH_3 obtained in this work and those listed in the literature.

Method	**$k_{4.1}/10^{-12}$ cm^3 molecule^{-1} s^{-1}**	**Reference**
Absolute Discharge-flow tube/RF	2.47 ± 0.41	This work
RR Photolysis/FTIR	2.37 ± 0.12 [h] (2.37 ± 0.59)	Wallington *et al.* (1990)[a]
RR Pulsed-laser photolysis/absorption	1.69 ± 0.32	Olsson *et al.* (1997)[b]
Absolute Pulsed-laser photolysis/RF	3.06 ± 0.38	Notario *et al.* (2000)[c]
RR Photolysis/FTIR	2.2 ± 0.4	Christensen *et al.* (2000)[d]
RR Photolysis/FTIR	2.0 ± 0.3	Orlando *et al.* (2000)[e]
Absolute Pulsed-laser photolysis/RF	2.93 ± 0.20[h]	Albaladejo *et al.* (in press)[f]
RR Photolysis/GC and FTIR	2.20 ± 0.44	Carr *et al.* (in preparation)[g]

Notes: RR – relative rate; [a]295 K and 700 Torr; [b]294 K and 1 atmosphere; [c]298 K and 15 – 60 Torr, [d]296 K and 700 Torr; [e]298 K and 1 atmosphere; [f]conditions unknown, and [g]298K and 760 Torr. [h]The error limits of these rate constants are equal to 2σ and do not include the systematic errors, although Wallington *et al.* (1990) estimate these to be ± 20 % in their work. The value in brackets includes this estimate. The systematic errors of the value obtained by Albaladejo *et al.* (in press) are not known.

4.4.1.3 Secondary chemistry

The second-order rate constants obtained in the four acetone experiments agree with each other when the estimated systematic error is taken into account (see table 4.3), which could indicate that there is no difference in the extent of secondary chemistry between the

experiments conducted at a low and high [Cl], and that the addition of O_2 had no effect. However, when the data are compared only on the basis of the 95 % confidence limits, it can be seen that the rate constant obtained in the experiment performed with a high [Cl] in the absence of O_2 (experiment 2) is larger than the other values. This difference could be the result of chemistry involving the reaction of Cl atoms with a product of the primary step. Thus it was possible that the reaction:

$$CH_3COCH_2 + Cl \rightarrow \text{products} \qquad \text{(R4.6)}$$

was taking place. The rate constant obtained in experiment 4 (a high [Cl] in the presence of O_2) agrees with those acquired in the low-[Cl] experiments, which based on the previous statement would suggest that the addition of oxygen suppresses the secondary chemistry. (As stated in section 4.2.4, the concentration of oxygen added to the flow tube was sufficient to ensure that:

$$CH_3COCH_2 + O_2 + M \rightarrow CH_3COCH_2O_2 + M \qquad \text{(R4.5)}$$

occurred at a much higher rate than R4.6). The agreement also suggests that there is no difference in the extent of secondary reactions involving Cl atoms in these experiments.

Further evidence for the presence of secondary processes in experiment 2 can be found in the first-order plots. Many of the plots for only this experiment appeared to be curved, with intercepts on the x axis that were on average about 1 ms larger than in the other experiments. Such curvature indicates that the rate of loss of Cl was increasing with increasing time. This situation only arises when the rate of the secondary reaction is comparable with the rate of the primary step. If the secondary chemistry is fast, then the first-order plot will be linear but the gradient will be equal to $2k'_{\text{primary}}$. The first-order plots of the other experiment performed with a high concentration of Cl (experiment 4) were linear but had intercepts and gradients of similar size to the low-[Cl] experiments. This observation supports the previous statement that secondary chemistry was not occurring in experiment 4.

A simple test of the possibility of secondary chemistry in experiment 2 was performed. As stated in the previous paragraph, the rate of loss of Cl appeared to be increasing with increasing time. Thus if the contact time of the experiment was reduced, the effect of secondary reactions on the loss of Cl atoms should also be reduced and the derived rate constant should differ less from those produced in the low-[Cl] experiments. The data obtained in experiment 2 were adjusted to exclude those collected through the use of the three ports furthest from the detection cell. This analysis reduced the maximum contact time from 39 ms to 15 ms. The derived rate constant was $(2.51 \pm 0.11) \times 10^{-12}$ cm^3 molecule^{-1} s^{-1}. The quoted errors are the 95 % confidence limits. This value is in excellent agreement with those obtained in the low-[Cl] experiments. It would appear that an extra process was indeed occurring in experiment 2.

In an attempt to quantify the secondary chemistry, a simple numerical model was generated with the FACSIMILE software package (version 3.0.30, AEA Technology): see appendix III. The model contained only the reactions:

$$Cl + CH_3COCH_3 \rightarrow HCl + CH_3COCH_2 \qquad (R4.1a)$$

$$Cl + CH_3COCH_2 \rightarrow \text{products.} \qquad (R4.6)$$

The value of $k_{4.1a}$ employed was taken as being equal to that obtained for $k_{4.1}$ in this work. The parameter-fitting option was used to obtain $k_{4.6}$ from the experimental data. A value of $(7 \pm 2) \times 10^{-11}$ cm^3 molecule^{-1} s^{-1} was derived. There are no previous determinations of this rate constant in the literature. Figure 4.14 shows a typical first-order plot from experiment 2 and those produced by model simulations where $k_{4.6} = 0$, 3, 7 and 11×10^{-11} cm^3 molecule^{-1} s^{-1}. The initial concentrations of Cl and acetone were 3.6×10^{11} atom cm^{-3} and 2.2×10^{13} molecule cm^{-3}, respectively. It can be seen that this particular experimental data set indicate a value of $k_{4.6}$ that is slightly larger than 7×10^{-11} cm^3 molecule^{-1} s^{-1}.

Figure 4.14. An example of a first-order plot from experiment 2 (a high [Cl] in the absence of O_2) and those produced by a model that simulates the reactions of Cl atoms with acetone (R4.1a) and the acetonyl radical (R4.6). The initial concentrations of Cl and acetone were 3.6×10^{11} atom cm^{-3} and 2.2×10^{13} molecule cm^{-3}, respectively. The value of $k_{4.1a}$ used in the model was 2.47×10^{-12} cm^3 molecule^{-1} s^{-1}. Several model simulations were performed where $k_{4.6} = 0$, 3, 7 and 11×10^{-11} cm^3 molecule^{-1} s^{-1}.

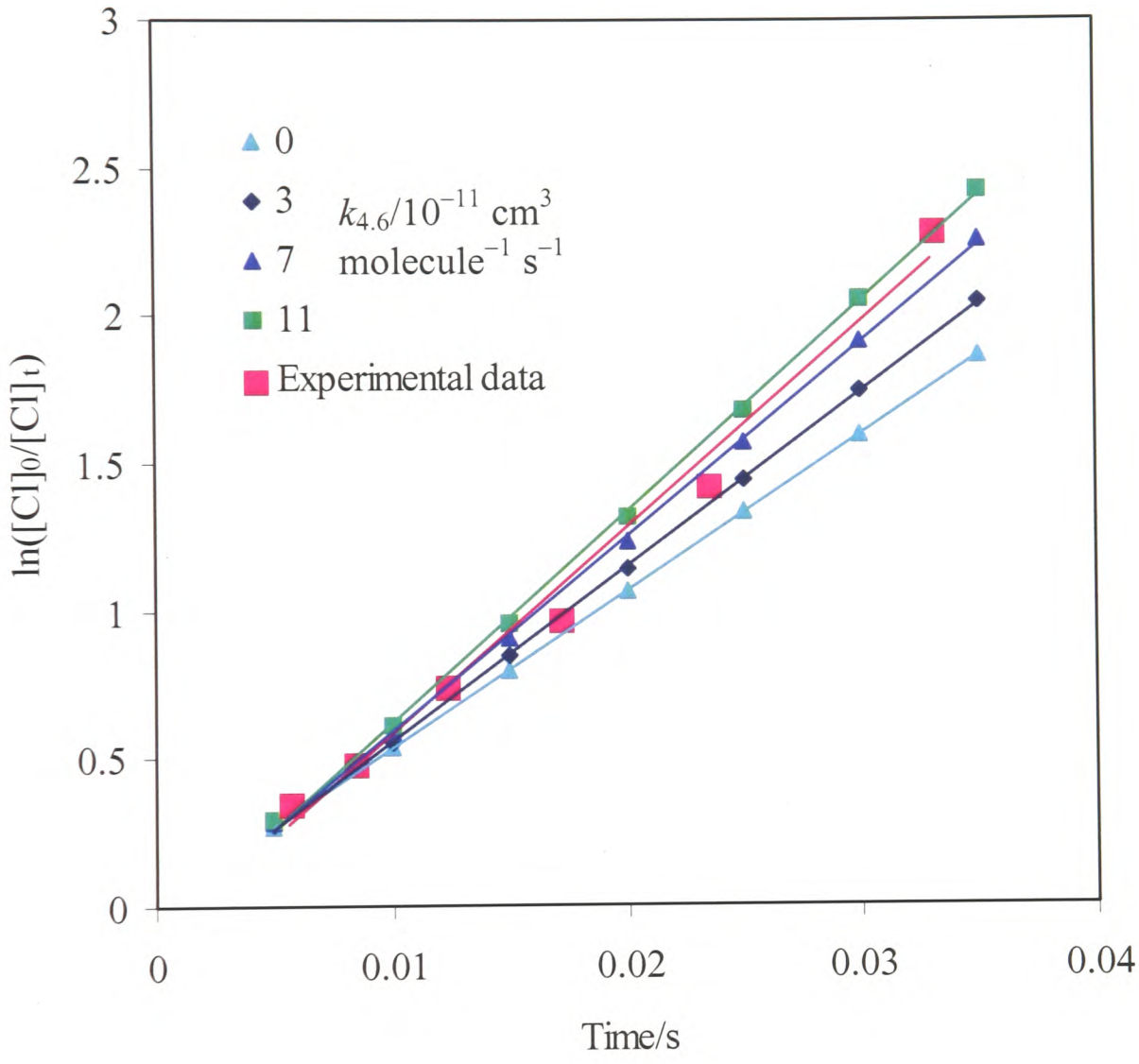

Although the reaction of Cl atoms with the acetonylperoxy radical (R4.2) was not observed in experiment 4, some kinetic information regarding this chemistry can still be deduced. As previously discussed, the addition of O_2 to the system suppressed the rate of R4.6 because the CH_3COCH_2 radicals were converted to $CH_3COCH_2O_2$. The absence of any indication of secondary chemistry in experiment 4 therefore suggests that $k_{4.2}$ is smaller than $k_{4.6}$. Modelling work was undertaken in an attempt to reduce the range of

possible values for the rate constant. A numerical model was generated with FACSIMILE that contained the reactions:

$$Cl + CH_3COCH_3 + O_2 \rightarrow HCl + CH_3COCH_2O_2 \qquad (R4.7)$$

$$CH_3COCH_2O_2 + Cl \rightarrow \text{products.} \qquad (R4.2)$$

$k_{4.7}$ was taken to be equal to $k_{4.1a}$. Several model simulations were performed where $k_{4.2}$ = 0, 1, 3.5 and 7×10^{-11} cm^3 molecule^{-1} s^{-1}. These data are presented in figure 4.15 along with a typical first-order plot from experiment 4. The initial concentrations of Cl and acetone were 3.7×10^{11} atom cm^{-3} and 2.3×10^{13} molecule cm^{-3}, respectively. It can be seen that the data produced by the model where $k_{4.2} = 7 \times 10^{-11}$ cm^3 molecule^{-1} s^{-1} (the derived value of $k_{4.6}$) differ greatly from the experimental data. By comparing the plots by eye, it can be said that the rate of R4.2 can not be faster than 1×10^{-11} cm^3 molecule^{-1} s^{-1}.

The rate constant for R4.2 could possibly be determined by conducting an experiment with a higher concentration of Cl than used in experiment 4. These conditions would generate more CH_3COCH_2 and therefore more $CH_3COCH_2O_2$, which would allow the reaction of the peroxy radical with Cl to compete with the primary process. This experiment was simulated with the model just described. The upper limit for $k_{4.2}$ was employed. Model results indicated that a very large concentration of Cl atoms of about 10^{13} molecule cm^{-3} are necessary for the effect of R4.2 on the concentration–time profiles of Cl to be observed. Higher concentrations would probably be required for the rate constant to be determined with a satisfactory level of precision.

4.4.2 The reaction of Cl with butanone

The data for this reaction were treated in the same manner as those for the reaction of Cl with acetone. The values of k' were obtained from the first-order plots by applying a linear least-squares fit of the form $y = mx + c$. An intercept of about 2 ms was once again apparent. The equations of the linear least-squares fits to the second-order plots obtained with and without forcing the line through the origin are $(4.31 \pm 0.44) \times 10^{-11}$ cm^3 molecule^{-1} s^{-1} and $(3.71 \pm 1.29) \times 10^{-11}$ cm^3 molecule^{-1} s^{-1} + (11.02 ± 20.70) ^{12} s^{-1},

Figure 4.15. An example of a first-order plot from experiment 4 and those produced by a model that simulates the reactions of Cl atoms with acetone in the presence of oxygen (R4.7) and the acetonylperoxy radical (R4.2). The initial concentrations of Cl and acetone were 3.7×10^{11} atom cm^{-3} and 2.3×10^{13} molecule cm^{-3}, respectively. The value of $k_{4.7}$ used in the model was 2.47×10^{-12} cm^3 molecule^{-1} s^{-1}. Several model simulations were performed where $k_{4.2} = 0$, 1, 3.5 and 7×10^{-11} cm^3 molecule^{-1} s^{-1}.

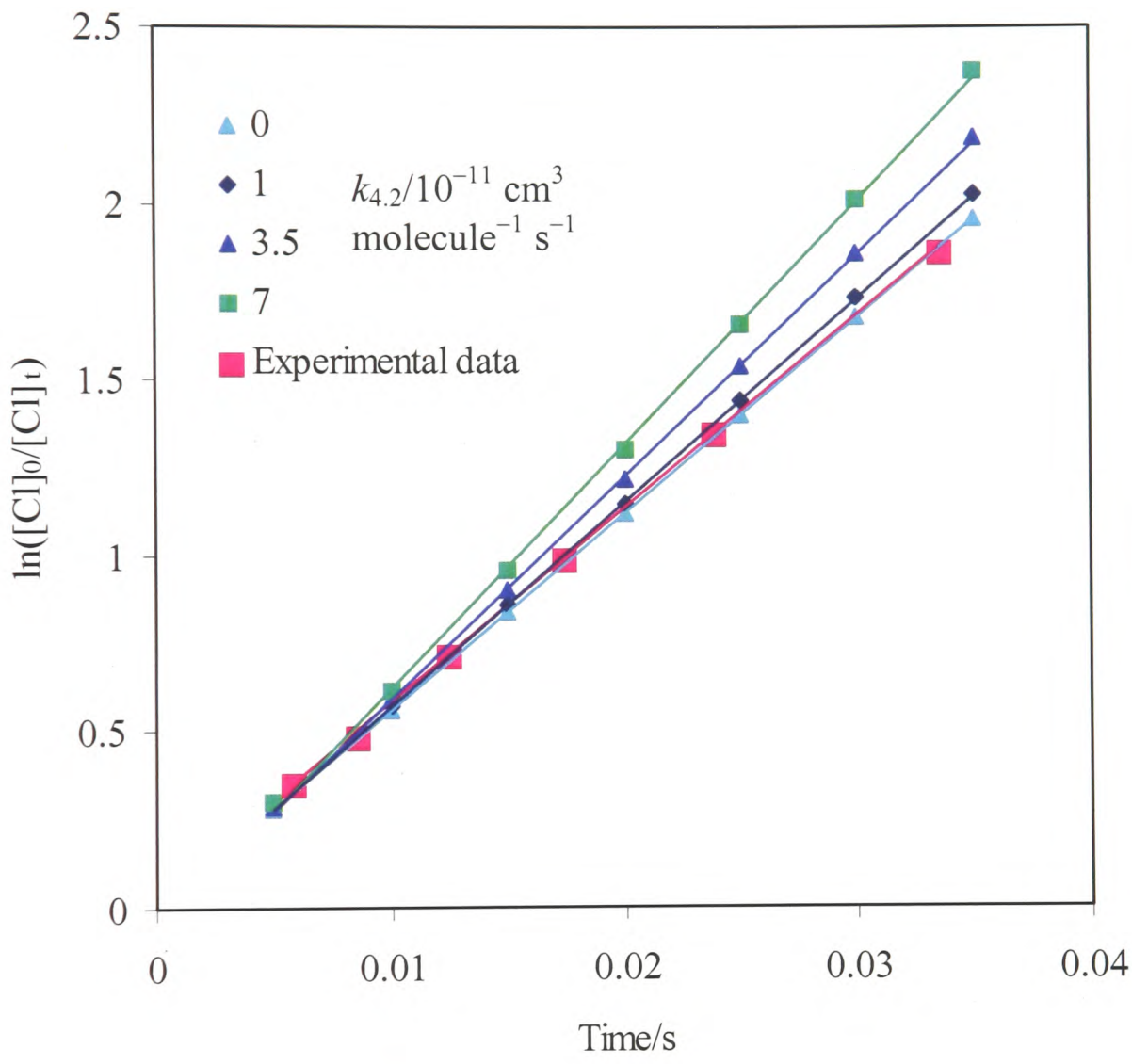

respectively. The quoted errors are the 95 % confidence limits. Although the intercept of the $y = mx + c$ fit is large, the origin does fall within the error limits and thus it can be assumed that it is a result of scatter in the data and that a $y = mx$ fit is applicable. The concentration of butanone added was in a sufficient excess to minimize the extent of secondary chemistry.

The rate constant obtained in this work is listed in table 4.6 along with the literature values. The study by Albaladejo *et al.* (2003) was published after this work was performed. It can be seen that there is good agreement with the other values.

Table 4.6. A comparison of the rate constants for the reaction of Cl with $CH_3COCH_2CH_3$ obtained in this work and those listed in the literature.

Method	$k_{4.3}/10^{-11}$ **cm^3 molecule^{-1} s^{-1}**	**Reference**
Absolute Discharge-flow tube/RF	4.31± 0.87	This work
RR Photolysis/FTIR	4.13 ± 0.57 [d] (4.13 ± 1.40)	Wallington *et al.* (1990)[a]
Absolute Pulsed-laser photolysis/RF	3.24 ± 0.38	Notario *et al.* (2000)[b]
Absolute Pulsed-laser photolysis/RF	3.30 ± 0.20[d]	Albaladejo *et al.* (2003)[c]

Notes: RR – relative rate; [a]295 K and 700 Torr; [b]298 K and 15 – 60 Torr, [c]298 K and 20 – 200 Torr; and [d]the error limits of these rate constants are equal to 2σ and do not include the systematic errors, although Wallington *et al.* (1990) estimate these to be ± 20 % in their work. The value in brackets includes this estimate. The systematic errors of the value obtained by Albaladejo *et al.* (2003) are not known.

4.4.3 The reactivity of ketones with chlorine atoms

The rate constant for the reaction of Cl with butanone is one order of magnitude greater than that for the reaction of Cl with acetone. A consideration of the deactivating effects of the carbonyl group and the number of CH_x groups present can explain this difference. As can be seen in table 4.7, Cl atoms react more slowly with ketones than with the corresponding alkanes. As the hydrogen atoms in the ketone are of the same type and number as those in the alkane, the difference in reactivity must be a result of the presence

Table 4.7. Rate constants for the reactions of atomic chlorine with several ketones and the corresponding alkanes.

Molecule	***k*(Cl + ketone) /10^{-11} cm^3 molecule^{-1} s^{-1}**	***k*(Cl + alkane) /10^{-11} cm^3 molecule^{-1} s^{-1}**	***k*(Cl + alkane)/ *k*(Cl + ketone)**
CH_3COCH_3	0.25[a]		23.0
CH_3CH_3		5.74[c]	
$CH_3COCH_2CH_3$	4.31[a]		3.2
$CH_3CH_2CH_3$		14.0[c]	
$CH_3COCH_2CH_2CH_3$	4.57[b]		4.7
$CH_3CH_2CH_2CH_3$		21.5[c]	
$CH_3COCH_2CH_2CH_2CH_3$	6.54[b]		3.8
$CH_3CH_2CH_2CH_2CH_3$		25.0[d]	

Notes: [a]this work; [b]Albaladejo *et al.* (2003), and [c]Tyndall *et al.* (1997), and [d]Hooshiyar *et al.* (1995).

of the carbonyl group. Olsson *et al.* (1997) remark that this observation is somewhat surprising, as the electron-withdrawing ability of the carbonyl group would be expected to weaken the C–H bonds, so allowing H abstraction to occur more easily. However, Albaladejo *et al.* (2003) counter this statement by proposing that the inductive effect of the carbonyl group reduces the reactivity of the hydrogens to an electrophilic species such as Cl. The workers strengthen their argument by stating that the C–H bond energies in ketones and alkanes are approximately equal. Further inspection of table 4.7 reveals that the rate constants increase as the number of CH_x groups in the ketone (or, indeed alkane) increase, but more interestingly, it can also been seen that the ratio of *k*(Cl + alkane) to *k*(Cl + ketone) generally decreases as the molecules get larger. The first trend is obviously a consequence of an increase in the number of sites for the Cl atom to attack. The second trend is thought to be the result of a weakening of the deactivation effect as the distance from the carbonyl group increases (Notario *et al.*, 2000 and Albaladejo *et al.*, 2003).

Wallington *et al.* (1990) and Olsson *et al.* (1997) state that there is no correlation between the reactivities of Cl atoms and OH radicals with ketones and alkanes. For example, table 4.7 shows that the reaction of Cl with ethane occurs 23 times faster than the reaction of Cl with acetone. As both Cl and OH react with these compounds predominantly *via* hydrogen abstraction, it would seem reasonable to predict that the reaction of OH with ethane would be faster than the reaction with acetone by a similar factor. However, the two reactions proceed at similar rates: k(OH + acetone) = 2.20×10^{-13} and k(OH + ethane) = 2.49×10^{-13} cm^3 molecule^{-1} s^{-1}, respectively (Atkinson *et al.*, 1997). This difference in reactivity between Cl and OH suggests that one (or both) of the species does not react with the organic compounds by a simple hydrogen-abstraction mechanism. Albaladejo *et al.* (2003) propose that it is the reactions of OH radicals with ketones that follow more complex routes. As previously stated, they suggest that the electron-withdrawing ability of the carbonyl group reduces the reactivity of ketones to electrophilic species. Of course, OH is one such species, but it overcomes the deactivation effect by forming a stable transition state with the ketone. This transition state takes the form of a ring involving a hydrogen bond between the H atom of the OH radical and the O atom of the carbonyl group. Cl atoms are not able to form such stabilised structures and thus the deactivating effect of the carbonyl group is not countered.

4.4.4 Atmospheric implications

The major loss processes for ketones, such as acetone and butanone, in the atmosphere are photolysis and reaction with OH (Seinfeld and Pandis, 1998). However, as discussed in chapter 1, oxidation by Cl atoms may be of importance in the marine boundary layer (MBL) where Cl concentrations of up to $10^4 - 10^5$ atom cm^{-3} may be present. Table 4.8 lists the rates of loss of the two ketones *via* photolysis in the winter and the summer, and oxidation by OH and Cl in the global troposphere and the MBL. The photolysis rates are for noontime at 40°N at sea level under cloudless conditions and, as such, should be regarded as the upper limits for that region at that particular time of year. The rate constants for the reactions of the two ketones with OH are from Le Calvé *et al.* (1998) ($k_{\text{acetone}} = 1.91 \times 10^{-13}$ and $k_{\text{butanone}} = 1.23 \times 10^{-12}$ cm^3 molecule^{-1} s^{-1}) and those for the reactions with Cl are from this work. The average global concentrations of OH and Cl in

the troposphere are 1.6×10^6 molecule cm^{-3} (Prinn *et al.*, 1995) and 5×10^3 atom cm^{-3} (Singh and Kasting, 1988), respectively. The abundance of the two oxidants in the MBL is taken as [Cl] = 1.3×10^5 atom cm^{-3} and [OH] = 3.9×10^5 molecule cm^{-3} (Spicer *et al.*, 1998). These are the concentrations shortly after sunrise, when [Cl] is at a maximum.

Table 4.8 The rates of loss of acetone and butanone as a result of photolysis in the winter and summer, and oxidation by OH and Cl in the global troposphere and the MBL.

Ketone	**Photolysis [a]**		**Reaction with OH[b]**		**Reaction with Cl[c]**	
	1st January	**1st July**	**Global**	**MBL**	**Global**	**MBL**
	$/s^{-1}$	**$/s^{-1}$**	**$/s^{-1}$ [d]**	**$/s^{-1}$ [f]**	**$/s^{-1}$ [e]**	**$/s^{-1}$ [f]**
Acetone	1.4×10^{-7}	5.9×10^{-7}	3.1×10^{-7}	7.5×10^{-8}	1.24×10^{-8}	3.2×10^{-7}
Butanone	1.2×10^{-6}	4.2×10^{-6}	2.0×10^{-6}	4.8×10^{-7}	2.16×10^{-7}	5.6×10^{-6}

Notes: [a]taken from Yujing and Mellouki (2000); [b]the rate constants for the reactions of OH with acetone and butanone are from Le Calve *et al.* (1998); [c]the rate constants for the reactions of Cl with acetone and butanone are from this work; [d]the average global concentration of OH radicals in the troposphere is 1.6×10^6 molecule cm^{-3} (Prinn *et al.*, 1995); [e]the average global concentration of Cl atoms in the troposphere is 5×10^3 atom cm^{-3} (Singh and Kasting, 1988); [f]the abundance of the two oxidants in the MBL is taken as [Cl] = 1.3×10^5 atom cm^{-3} and [OH] = 3.9×10^5 molecule cm^{-3} (Spicer *et al.*, 1998). These are the concentrations shortly after sunrise, when [Cl] is at a maximum.

It can be seen that, on a global scale, photolysis and reaction with OH are the main sinks of acetone and butanone, as previously stated. Loss *via* oxidation initiated by Cl atoms occurs at a rate that is about one order of magnitude slower than the main processes because the global concentration of Cl is much less than that of OH. However, in the MBL the situation changes — reaction with Cl is of greater importance than reaction with OH. Although the abundance of Cl atoms in this region is still lower than that of OH radicals, the difference in concentrations is not as large as in the global troposphere. As ketones react more rapidly with Cl than with OH, removal by reaction with the former is of greater importance. Indeed, reaction with Cl competes with photolysis to be the dominant mechanism.

4.5 Conclusions

This chapter describes the successful determination of the rate constants for the reactions of atomic chlorine with acetone and butanone using a discharge–flow tube coupled to a RF detection system. The values agree well with those published in the literature. The acetone study was extended in an attempt to obtain information concerning the chemistry of the acetonylperoxy radical. Experiments performed at elevated chlorine concentrations allowed an upper limit of 1×10^{-11} cm^3 molecule^{-1} s^{-1} to be derived for the rate constant of the reaction of Cl with $CH_3COCH_2O_2$. The rate constant for the reaction of chlorine atoms with acetonyl radicals was also determined: $k_{4.6} = (7 \pm 2) \times 10^{-11}$ cm^3 molecule^{-1} s^{-1}. The difference in reactivity between acetone and butanone with Cl and OH was discussed and the atmospheric implications of the work were described.

4.6 References

- Albaladejo, J., A. Notario, C. A. Cuevas, E. Jiménez, B. Cabanas and E. Martínez, *Atmos. Environ.*, 2003, **37**, 455
- Albaladejo, J., A. Notario, C. A. Cuevas, B. Ballesteros and E. Martínez, in press
- Atkinson, R., D. L. Baulch, R. A. Cox, R. F. Hampson Jr., J. A. Kerr, M. J. Rossi, and J. Troe, *J. Phys. Chem. Ref. Data*, 1997, **26**, 521
- Baulch, D. L., J. Duxbury, S. J. Grant and D. C. Montague, *J. Phys. Chem. Ref. Data*, 1981, **10**, 1
- Carr, S., C. E. Canosa-Mas, J. C. Wenger, H. W. Sidebottom, R. P. Wayne and D. E. Shallcross, in preparation
- Christensen, L. K., J. C. Ball and T. J. Wallington, *J. Phys. Chem. A*, 2000, **104**, 345
- Cotter, E. S. N., N. J. Booth, C. E. Canosa-Mas, D. J. Gray, D. E. Shallcross and R. P. Wayne, *Phys. Chem. Chem. Phys.*, 2001, **3**, 402
- Hooshiyar, P. A. and H. Niki, *Int. J. Chem. Kinet.*, 1995, **27**, 1197
- Le Calvé, S., D. Hitier, G. Le Bras and A. Mellouki, *J. Phys. Chem. A*, 1998, **102**, 4579
- Ljungström, E. and M. Hallquist, *Int. J. Chem. Kinet.*, 1998, **30**, 311
- Nielsen, O. J., M. S. Johnson, T. J. Wallington, L. K. Christensen and J. Platz, *Int. J. Chem. Kinet.*, 2002, **34**, 283

- Notario, A., A. Mellouki and G. Le Bras, *Int. J. Chem. Kinet.*, 2000, **32**, 62
- Okabi, H, *Photochemistry of Small Molecules*, John Wiley and Sons, New York, 1978
- Olsson, B. E. R., M. Hallquist, E. Ljungström and J. Davidsson, *Int. J. Chem. Kinet.*, 1997, **29**, 195
- Orlando, J. J., G. S. Tyndall, L. Vereecken and J. Peeters, *J. Phys. Chem. A*, **2000**, 104, 11588
- Prinn, R. G., R. F. Weiss, B. R. Miller, J. Huang, F. N. Alyea, D. M. Cunnold, P. J. Fraser, D. E. Hartley and P. G. Simmonds, *Science*, 1995, **269**, 187
- Seeley, J. V., J. T. Jayne and M. J. Molina, *J. Phys. Chem.*, 1996, **100**, 4019
- Seinfeld, J. H. and S. N. Pandis, *Atmospheric Chemistry and Physics*, John Wiley and Sons, Toronto, 1998
- Singh, H. B. and J. F. Kasting, *J. Atmos. Chem.*, 1988, **7**, 261
- Spicer, C. W., E. G. Chapman, B. J. Finlayson-Pitts, R. A. Plastridge, J. M. Hubbe, J. D. Fast and C. M. Berkowitz, *Nature*, 1998, **394**, 353
- Tyndall, G. S., J. J. Orlando, T. J. Wallington, M. Dill and E. W. Kaiser, *Int. J. Chem. Kinet.*, 1997, **29**, 43
- Wallington, T. J., J. M. Andino, J. C. Ball and S. M. Japar, *J. Atmos Chem.*, 1990, **10**, 301
- Wallington, T. J., A. Guschin and M. D. Hurley, *Int. J. Chem. Kinet.*, 1998, **30**, 309
- Yujing, M. and A. Mellouki, *J. Photochem. Photobiol. A*, 2000, **134**, 31

Chapter 5 The design, construction and commissioning of an electron-impact mass spectrometer

5.1 Introduction

This chapter is the first of three that discuss mass-spectrometric experiments. The aim of the work described here was to construct an electron-impact mass spectrometer (EIMS) and couple it to a discharge–flow tube. The EIMS would then be converted to a chemical-ionization mass spectrometer (CIMS), intended for the direct observation of peroxy radicals. The construction of a CI source is described in chapter 7. The use of the EIMS to detect peroxy species indirectly was also investigated: see chapter 6, which is concerned with the acetonylperoxy radical self-reaction.

The budget for this project was small and so much of the MS system was borrowed or built in-house. A 1974 Extranuclear Laboratories Type II EI Source and Quadrupole, complete with a Mullard Channel Electron Multiplier (CEM), were acquired from a colleague. These components are described in the next section. The design for the vacuum system in which these components were mounted is then explained. The control of the apparatus and the data acquisition and processing are discussed, and finally the performance of the EIMS is described.

5.2 The MS components

The source was a modified Extranuclear Laboratories Type II High Efficiency Electron Impact Ionizer. It was comprised of a filament, an extraction plate and three ion lenses: see figure 5.1. The filament was made of tungsten wire and operated at about 6 V and 5 A. The electrons emitted by the filament were accelerated toward the ion region plate. Sample molecules entered the ion source through the aperture of the filament plate and then collided with the electrons to form positive ions. These ions were accelerated away from the ion region by the extractor plate and focused into the quadrupole by the electrostatic lenses.

Figure 5.1. An exploded diagram of the EI source (scale 1:1).

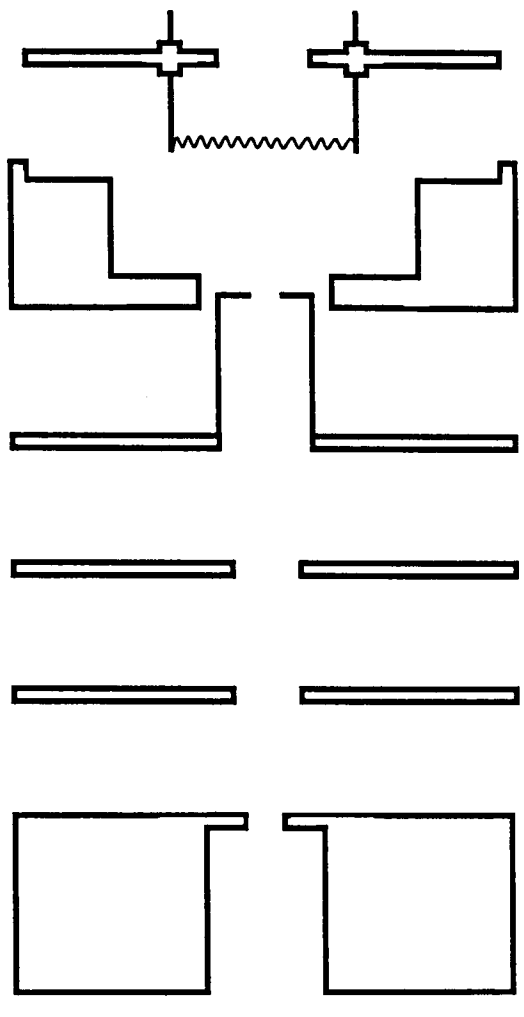

Filament plate
o.d. = 47 mm
i.d. = 9 mm

Filament shield
i.d. = 13 mm

Ion region
i.d. = 9 mm

Extractor
i.d. = 5 mm

Lens 1
i.d. = 6 mm

Lens 2
i.d. = 12 mm
(collimating aperture
= 5 mm i.d.)

Lens 3
i.d. = 12 mm

Notes: o.d. – outer diameter, and i.d. – inner diameter.

All the plates were made from stainless steel. The filament plate and filament shield were electrically connected. All other plates were electrically isolated by small ruby balls, with the plates approximately 1 mm apart. The EI source was held together and attached to the quadrupole canister by insulated screws.

The mass filter was an Extranuclear Laboratories Type II Quadrupole, model number 270-9. The stainless-steel poles were 210 mm long and 15.9 mm in diameter. The internal radius of the quadrupole was 68.4 mm. The poles were held in place by two

ceramic collars and housed in a stainless steel canister that had small apertures at either end to allow ions to pass through.

The CEM was a Mullard X959BL. It consisted of a planar spiral tube made of lead-doped glass with a 15 mm diameter cone for collecting the ions and a sealed end for collecting the electrons. The resistance of the device was ~ 5×10^8 Ω. When a potential difference of 2.5 kV was applied between its ends, the gain was of the order of 2×10^8. The CEM was housed in a stainless-steel box, which was attached to the quadrupole canister. Ions entered the box *via* a small opening in the front end. The CEM was positioned off-axis from the ion beam. This arrangement prevented neutral molecules from striking the CEM. Note that it is possible for neutral species with sufficient kinetic energy to pass through the quadrupole, collide with the CEM surface and cause electron emission. These species are of course unaffected by the quadrupole field as they do not carry charge. A thin stainless-steel plate with two holes was positioned in front of the CEM. It was possible to apply a potential to the plate to guide the ions through one hole and into the CEM. The other hole was on-axis and so allowed neutral species to pass through.

Figure 5.2. The EIMS components (scale 1:4).

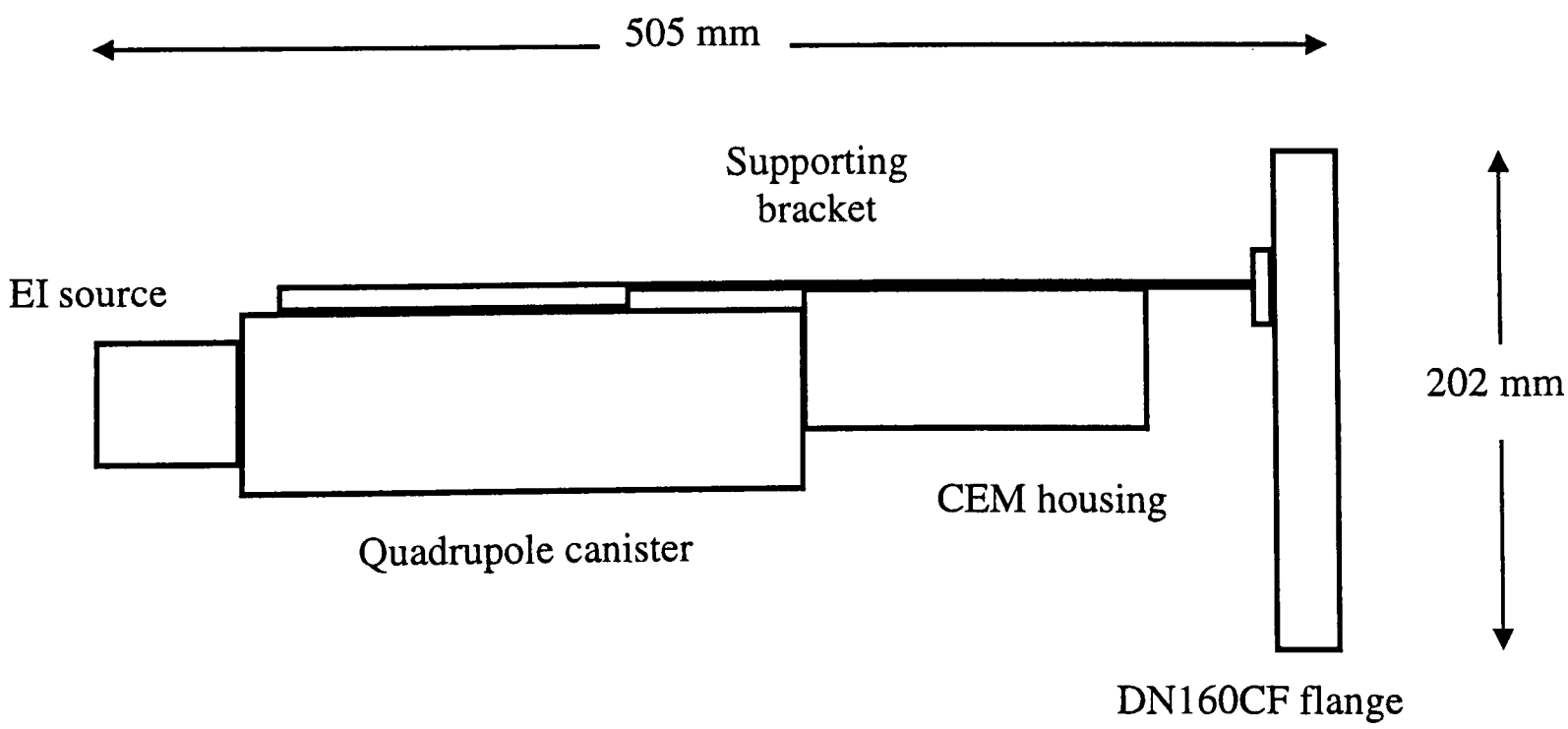

The EI source, quadrupole and CEM were supplied attached to a large flange (DN160CF) *via* a supporting bracket: see figure 5.2. This flange contained 7 sets of electrical feedthroughs. The MS components obtained also included one stainless-steel vacuum chamber: see figure 5.3, which will be discussed later. Note that this chamber had a smaller diameter front section that supported the ion source and quadrupole.

5.3 Vacuum-system design

When designing the vacuum system for the MS components, several matters required consideration.

First, as discussed in chapter 2, mass spectrometers operate at very high vacuum. This condition ensures that ions avoid collisions with other gaseous molecules. The desired pressure can be calculated from the mean free path, λ:

$$\lambda = \frac{k\,T}{\sqrt{2}\,\sigma\,p} \qquad \text{(E5.1)}$$

where k is the Boltzmann constant, T is the temperature, σ is the collision cross section, which is equal to πd^2, where d is the sum of the radii of the colliding ions or molecules, and p is the pressure (Atkins, 1994). The mean free path should be at least 1 m in a mass spectrometer (de Hoffmann and Stroobant, 2002). Using the collision cross section of nitrogen molecules, $\sigma = 4.3 \times 10^{-19}$ m^2, $p = 5 \times 10^{-5}$ Torr at 298 K. Thus, a very efficient pumping system was required.

Secondly, the desired operating pressure of the discharge–flow tube to be coupled to the MS was several orders of magnitude greater than the required MS pressure. It was decided to separate the two pieces of apparatus with a pinhole, which would allow a small fraction of the flow tube gases to be sampled, whilst the remainder was pumped away.

Finally, the smaller diameter section of the vacuum chamber that accompanied the borrowed MS components was not vacuum tight. Consequently, another chamber, which would couple the original chamber to the flow tube, had to be constructed. Both

chambers would be separately pumped. This differential pumping was considered necessary as preparation for when the EIMS was to be converted to a CIMS. CI sources operate at higher pressures than EI sources and thus the CI source would need to be placed outside the MS chambers. Ions would be drawn into the front chamber and focused into the back chamber by a set of ion optics. Obviously, some neutral species would also enter the MS. These would be removed by the front chamber pump.

The vacuum-system design is depicted in figure 5.3. The new parts, the flow-tube/MS coupling and the front chamber, were constructed from stainless steel. The flow-tube/MS coupling was a large Cajon-style vacuum fitting into which the discharge–flow tube adapter was placed. The fitting was mounted on a DN40KF flange, which held the ring and pinhole tight against the front chamber flange. The end of the flow tube was positioned about 10 mm away from the pinhole to allow gases to be sampled into the front chamber before being pumped away. The internal surface of the coupling piece was shaped to aid gas flow out of the flow tube, past the pinhole and round to the pump. Also, the dimensions of the flow-tube/MS coupling were such that after the pinhole region, the annular cross-sectional area through which the gas flowed was the same as that of the flow tube. This design generated a maximum linear flow velocity (LFV) of ~1200 cm s^{-1} at 5 Torr, which was suitable for the acetonylperoxy radical study. Despite the features intended to reduce the resistance to flow, the coupling piece did represent a considerable restriction, as without it an LFV of ~2000 cm s^{-1} was possible.

The front chamber was a 337 mm length of 152 mm wide tubing, with DN160KF and DN160CF flanges at the front and rear respectively. A gap of 60 mm was left between the front of the back chamber and the front flange to permit differential pumping. Like the original chamber, the new chamber had a small port to which pressure gauges could be attached. Thermal conductivity (Edwards Pirani PRM10) and cold-cathode ionization (Edwards Penning CP25EK) gauges were used.

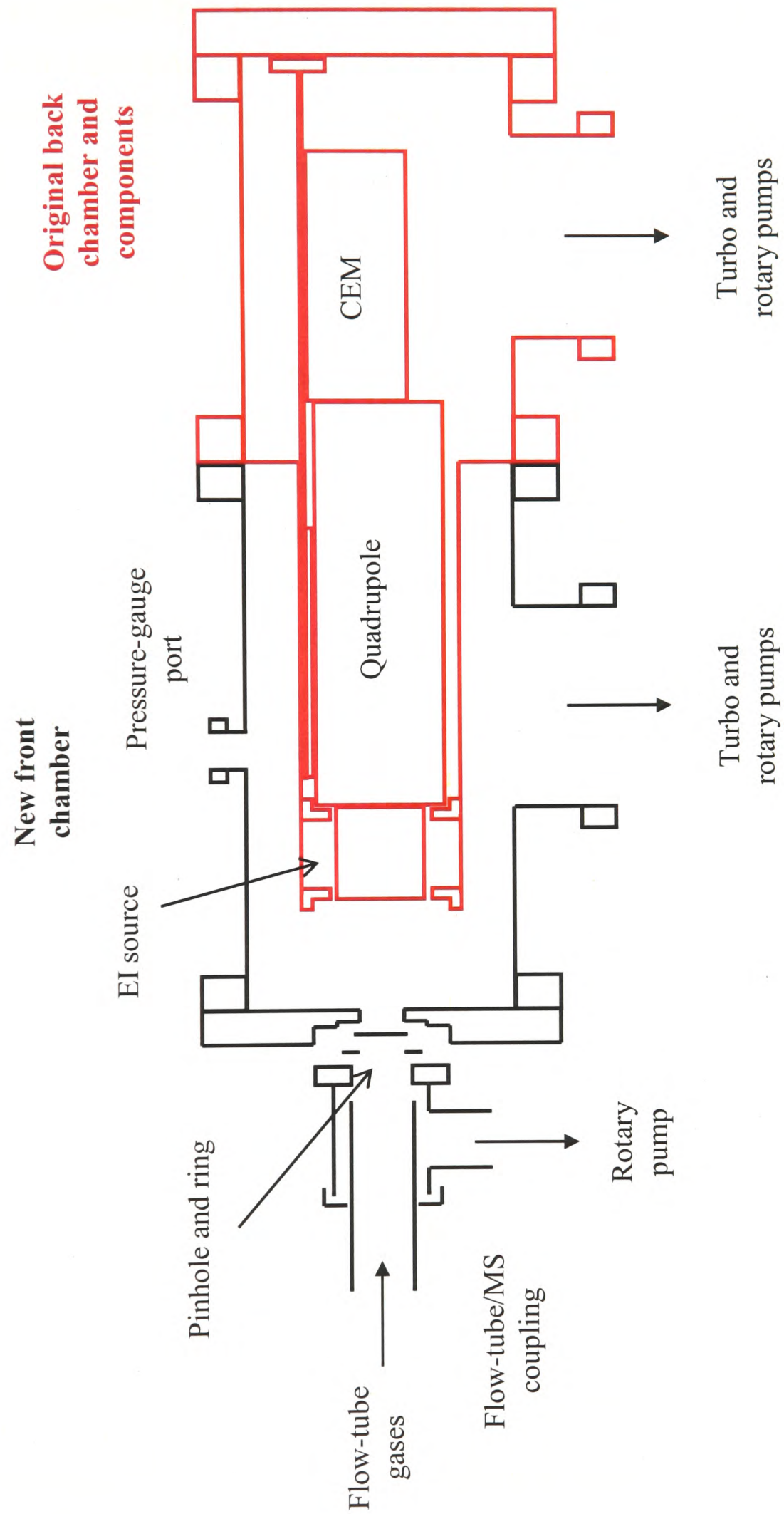

Figure 5.3. The MS vacuum chambers and flow-tube/MS coupling (scale 1:4).

Note: the part of the diagram corresponding to the flow-tube/MS coupling is exploded.

The pumping system was comprised of two turbomolecular pumps backed by rotary pumps. The front chamber was pumped by a Leybold Turbovac 360V and the back chamber was pumped by a Leybold Turbovac 361C. Both pumps ran at about 45,000 rpm with a pumping speed of approximately 345 L s^{-1}. The front-chamber pump was attached by DN100CF vacuum fittings, and the back-chamber pump was attached by 100 ISO-K vacuum fittings. The rotary pumps (Leybold D25B) were connected to the turbomolecular pumps by flexible stainless-steel tubing. Foreline traps (Edwards) were attached to the rotary pumps. These traps contained a plug of activated aluminium oxide that absorbed hydrocarbon species, thus reducing the backstreaming of rotary-pump oil into the turbomolecular pumps and the MS.

A pinhole size was selected that maintained an adequately high vacuum in the MS chambers whilst allowing the desired flow-tube pressures (FTP), 1 – 10 Torr, to be reached. As previously discussed, the back-chamber pressure must be kept below 5×10^{-5} Torr to minimise ion–molecule collisions. In fact, pressures of 10^{-6} Torr are preferred to maximise CEM performance. Pressures of more than 10^{-4} Torr should definitely be avoided as arcing would occur and damage the MS components. A pinhole diameter of 0.3 mm was found to provide the desired chamber pressures: see figure 5.4. Note also that the pinhole was chamfered so that it was indeed a hole and not a short tunnel in which radicals and ions would be lost.

5.4 MS control and signal processing

A schematic diagram of the devices used to control the MS and acquire and process the signals from the CEM is depicted in figure 5.5. These units shall be briefly discussed.

5.4.1 Ion-source control

Two in-house-built units supplied the filament current and the voltages to the ion source. The filament current could be varied to achieve five different electron-emission currents ranging from 10 μA to 1 mA. The electron current was measured on the ion region and held constant by feedback control. The voltage control unit supplied ±100 V to the filament, ion region and extractor plates, and the three lenses. The potential difference

Figure 5.4. The MS chamber pressures resulting from a flow-tube pressure (FTP) range of 0 – 12 Torr and a 0.3 mm pinhole.

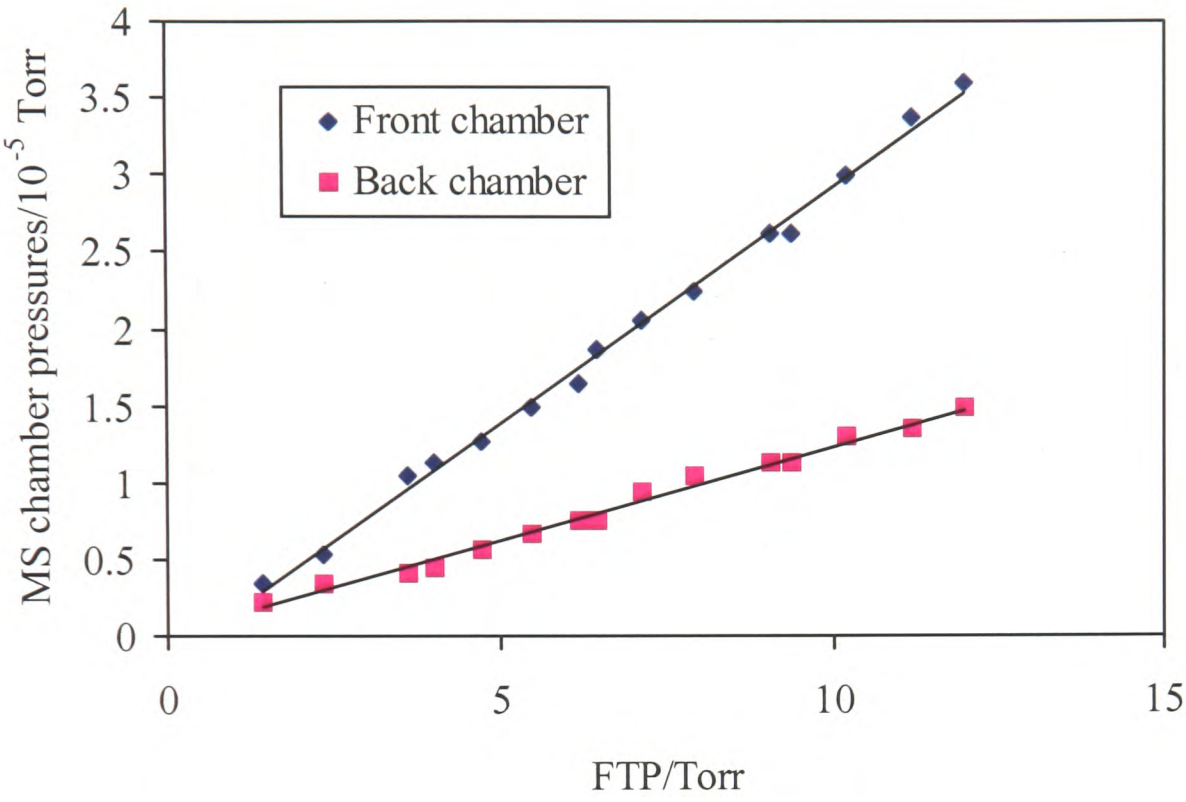

between the filament and ion region controlled the electron energy. The extractor and the three lenses were held at voltages that accelerated and focused the ions into the quadrupole. The selection of electron energies and currents with which to study flow-tube gases, particularly those involved in the acetonylperoxy radical study, is discussed in section 5.5.

5.4.2 Quadrupole control

An Extranuclear Laboratories High-Q Head, RF-power source and quadrupole control, and an in-house-built ramp generator were used to operate the quadrupole. The RF-power source applied a low-voltage, high-power RF frequency to the High-Q Head. This latter unit consisted of a parallel-resonant circuit, with the poles contributing to the total capacitance. High-voltage RF was generated by tuning the frequency of the RF to the resonance frequency of the High-Q Head/pole combination (Wayne, 1994). The High-Q Head also rectified a portion of this RF voltage to produce the DC voltage. The resolution was varied by adjusting the ratio of DC to RF voltages.

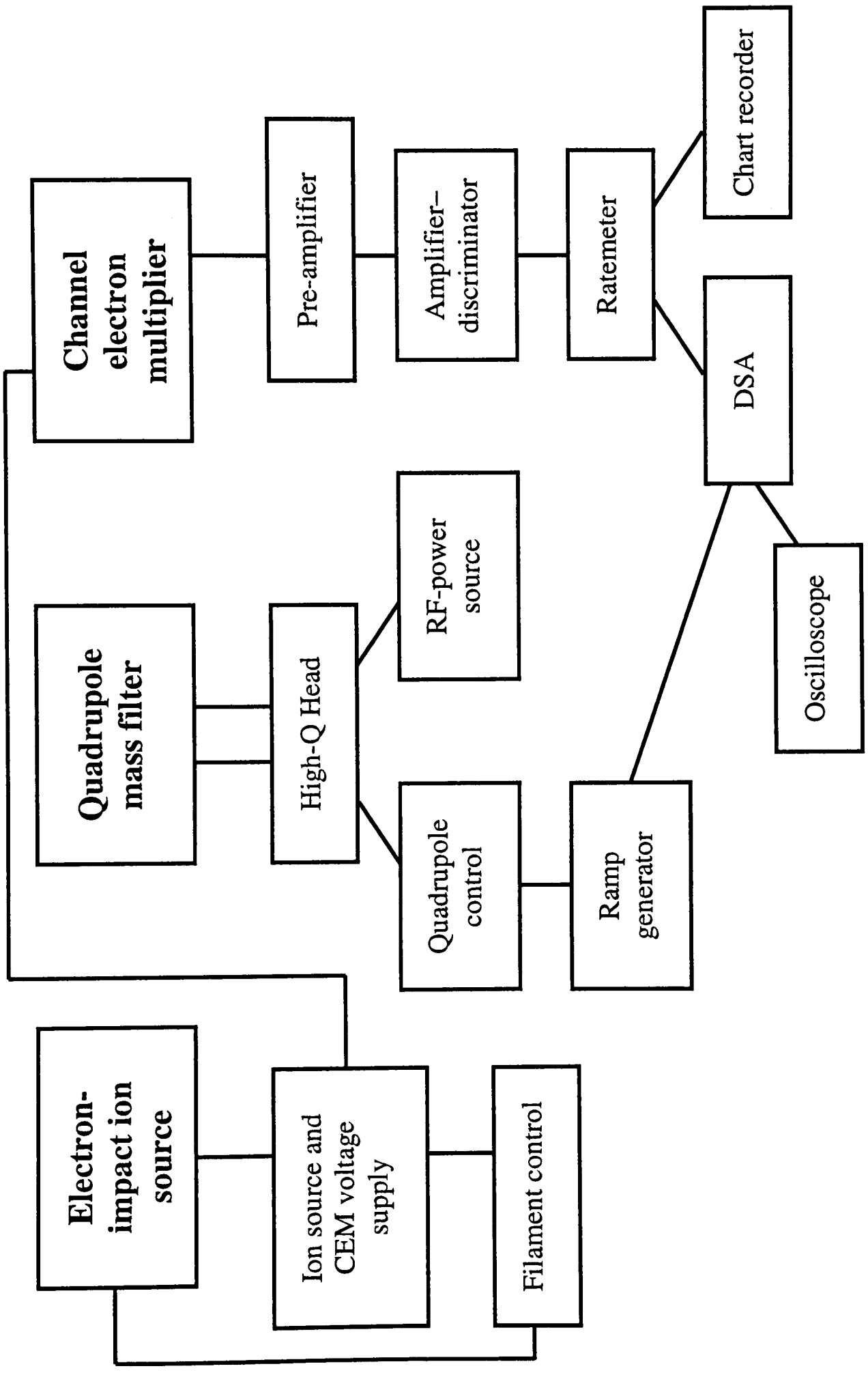

Figure 5.5. A schematic diagram depicting the devices used to control the MS and acquire and process the signals from the CEM.

Ions could be detected in two modes: automatic mass scanning and manual mass tuning. The former allowed a chosen mass range to be scanned repetitively and was controlled by the sweep generator, which applied a saw-tooth ramp voltage to the quadrupole control unit. The scan rate could be varied from 0.1 – 10 Hz. It was important to limit the speed of scanning to ensure that ions were subjected to several RF cycles in the quadrupole. This limit was of the order of 1 ms per amu (*Extranuclear Laboratories Quadrupole Power Supply Instruction Manual*, 1974). Faster scanning would have reduced the resolution and signal strength. The alternative mode, manual mass tuning, allowed individual ion peaks to be monitored.

The resolution was further controlled by operating in either constant Δm or constant $m/\Delta m$ mode. The former ensures that all peaks are separated by the same mass width. The latter represents constant resolution as the mass range is scanned.

5.4.3 CEM control

The CEM was controlled by a constant-voltage unit, which applied a large negative potential to the front end to attract the positive ions. Two different multipliers were used during the work and voltages between –2 and –3 kV were applied. The back end of the multiplier was held near ground potential to generate the electron cascade and act as the anode. The stainless-steel plate in front of the CEM was held at 0 V as this potential gave the largest signals.

5.4.4 Signal processing

The pulses of electron charge generated by the CEM were converted to voltages by an in-house-built pre-amplifier. The pre-amplifier also contained a low-pass filter, which removed some RF pick-up from the signal. A high-pass filter was also provided for flexibility in pulse shaping, but apparently had no useful effect. The signal was further processed by an Ortec 9302 amplifier–discriminator. The discriminator level could be set between 50 mV – 1 V to further remove RF interference. The count rate was measured by an Ortec 9349 Log/Lin ratemeter. Signals were recorded on a chart recorder (Venture

Servoscribe) or displayed on an oscilloscope (Tektronix 454). A digital storage adapter (Thurlby DSA524) manipulated the signal passed to the oscilloscope.

5.5 EIMS performance

The performance of the instrument can be described in terms of the mass range, resolution and sensitivity achieved.

5.5.1 Mass range

The mass range can be calculated as follows:

$$m_{max} = \frac{V_{max}}{7.219 r_0^2 f^2} \qquad \text{(E5.2)}$$

where m_{max} is the maximum mass that can be filtered, V_{max} is the peak RF voltage, r_0 is the internal radius of the quadrupole (cm) and f is the RF frequency (MHz) (*Extranuclear Laboratories Quadrupole Power Supply Instruction Manual*, 1974). r_0 is constant, whereas V_{max} and f are variable as they depend upon the identity of the components that comprise the resonant circuit in the High-Q Head.

Several High-Q Heads were acquired along with the MS components. A model E High-Q Head was initially used for the commissioning of the MS. The specified frequency and maximum voltage of this unit was ~1.6 MHz and ~3400 V respectively. Thus, a mass range of ~390 amu should have been possible. However, this range was not achieved because the maximum voltage could not be reached, possibly because of power losses in the system. Thicker conductor and dielectric cables were employed between the High-Q Head and the poles in an attempt to reduce the losses, but the nominal maximum mass was still not attained. It appears that there were either unexplained losses within the quadrupole itself or that the RF supply unit was no longer capable of delivering the specified power output.

The model E head was replaced with a model 12 head in preparation for the acetonylperoxy radical study. This unit nominally operated at ~3.5 MHz and ~3000 V and so should have been capable of offering a mass range of 72 amu, which was applicable to the study. The smaller mass range aided the task of manually tuning to a mass peak but more importantly, the higher frequency of operation improved the resolution. Higher frequencies cause ions to perform more oscillations in the quadrupole, thus improving the chance of species not of the selected *m/z* value being lost to the walls.

Unfortunately the power losses still prevailing in the system were such that a mass range of only 45 amu was achieved. The acetonylperoxy radical study required the detection of CO_2 nearly at the limit of this range, $m/z = 44$. The mass range was increased by addition of 50 pF capacitors to each set of poles. Increasing the capacitance lowers both the operating frequency and maximum voltage but as m_{max} is inversely proportional to the square of the frequency, an increase in mass range is achieved, in this case to 56 amu.

5.5.2 Resolution and sensitivity

The resolution and sensitivity of an MS is governed by many factors. As previously mentioned, inappropriate choice of the MS pressure and the scan rate can degrade the resolution and the transmission, i.e. signal strength. It is also important to correctly choose the ratio of DC to RF voltages, the RF frequency, and the $m/\Delta m$ setting. In addition, the potentials used to accelerate and focus the ions into the quadrupole impact upon the resolution and transmission: too high a kinetic energy will enable an ion not of the selected *m/z* value to reach the detector, and incorrect focusing can cause ions to enter the quadrupole off-center, so increasing their chance of being lost to the walls even if they are of the selected *m/z* value.

All these variables were adjusted for each experiment in which the EIMS was employed. Generally, the peaks of interest were separated from adjacent peaks whilst ensuring that signal strength was not greatly compromised. For example, in assessing the sensitivity of the EIMS to formaldehyde in preparation for the acetonylperoxy radical work, the resolution was set to the minimum level that ensured separation of the main formaldehyde peaks at $m/z = 29$ and 30. However, when testing new CI sources (see chapter 7) the

resolution was generally low: in fact, it was often set to zero by turning off the DC voltage. (Setting the DC to zero places the operating line along the x axis and so allows transmission of all masses: see figure 2.3). In this way, any ions generated by the new source had a higher chance of being detected.

The signal suffered from a great deal of RF interference, which was partially removed by the low-pass filter and the discriminator. This noise was also reduced at source by shielding the quadrupole, the CEM and the connecting wires. The remaining noise included statistical contributions. The signal-to-noise ratio was improved by adjusting the time constant of the ratemeter. A time constant of either 0.3 or 1 s was employed when monitoring individual ion peaks. Shorter and longer time constants were available but the former increased the noise and the latter increased the time taken for the signal to respond to a change in the chemical system to an unacceptable level.

Adjusting the electron energy and current also affected the S/N. These variables were investigated by following the formaldehyde signals at m/z = 29 and 30 (CHO^+ and CH_2O^+), and the carbon dioxide signal at m/z = 44 (CO_2^+), in preparation for the acetonylperoxy radical self-reaction study. The gases were prepared and introduced to the EIMS by the methods described in chapter 6. The electron energy was adjusted by changing the potential difference between the filament and the ion-region plates. In practise, the voltage applied to the filament plate was changed and the ion-region voltage kept constant, so as not to affect the fields involved in accelerating and focusing the ions into the quadrupole. The response of the formaldehyde signals at m/z = 29 and 30 to different potential differences between the filament and ion region is shown in figure 5.6. The concentration of formaldehyde was ~9.5×10^{12} molecule cm^{-3} and the electron current was 140 μA.

Figure 5.6 shows that the formaldehyde signals increased as the potential difference was reduced. The EIMS responded in a similar way to carbon dioxide and argon. Dobis and Benson (1990, 1991) witnessed similar behaviour in the parent molecular ions of ethane and ethene. The signal drops as the potential difference is increased because more energy is transferred to the molecule, thus causing more of the resulting ions to fragment. Figure 5.6 also shows that the largest signals were obtained at the lowest potential difference

Figure 5.6. Formaldehyde signals at *m/z* = 29 and 30 as a function of the potential difference between the filament and ion-region plates. The electron current was 140 μA.

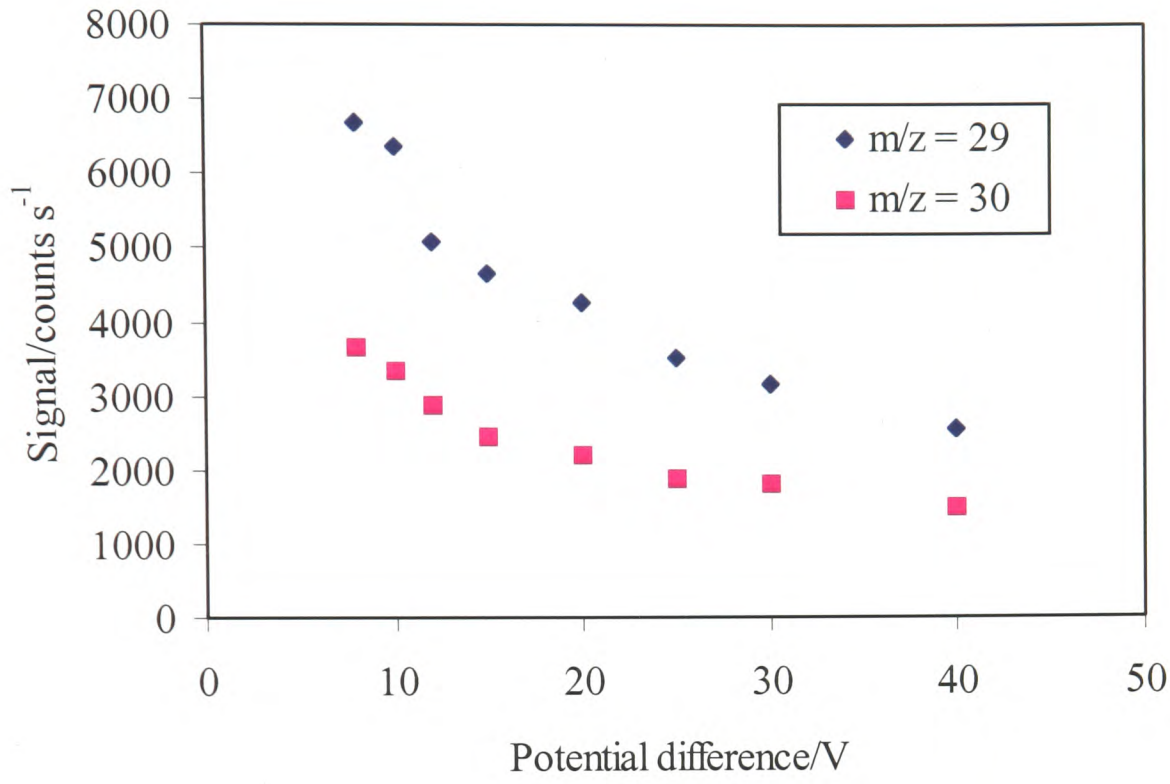

Figure 5.7. Calibrations of the formaldehyde signal at *m/z* = 30 for electron currents of 10, 50 140 and 500 μA.

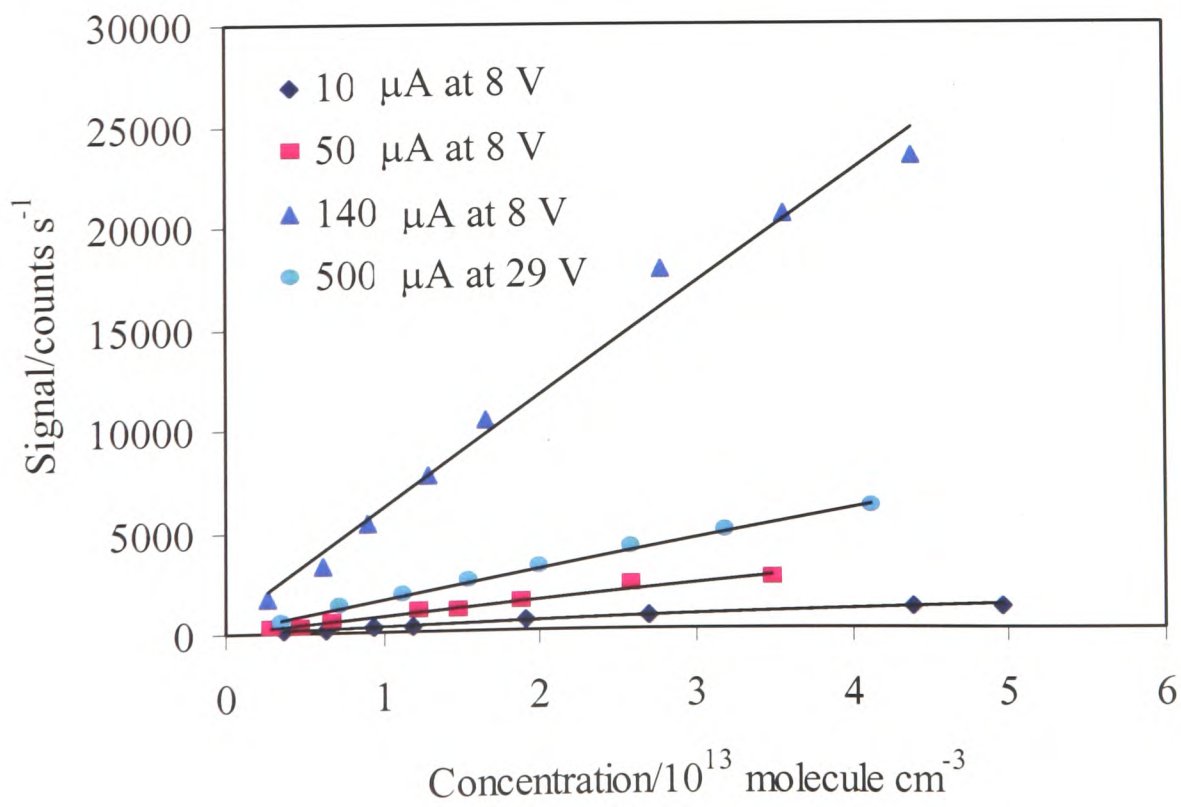

tested, 8 V. This value is lower than the ionization energy of formaldehyde (10.88 eV) and the appearance energy of CHO^+ (11.97 eV) (*NIST Standard Reference Database*, 2001). However, this discrepancy can be easily explained in that EI ionization generates electrons with a range of kinetic energies.

The effect of electron currents of 10, 50, 140 and 500 μA on the formaldehyde and carbon dioxide signals was investigated. The response of the formaldehyde signal at $m/z = 30$ is shown in figure 5.7. The potential difference between the filament and ion region was 8 V, except for the experiment conducted at 0.5 mA, which required a potential difference of 29 V. This voltage was the minimum at which the feedback mechanism designed to hold the current constant could operate at when the current was so high.

It can be seen that the largest signals were obtained by operating at an electron current of 140 μA. These signals were bigger than those generated by operating at 10 and 50 μA because increasing the number of electrons increases the number of collisions, which increases the number of ions. The highest current of 500 μA did not provide the largest signals because the higher potential difference between the filament and ion region caused a large loss in the parent molecular ion abundance. No attempt was made to adjust the filament control unit so that higher electron currents could be used at very low potential differences because high currents have a practical drawback in that they greatly reduce the filament lifetime.

At an electron current of 140 μA and a potential difference between the filament and ion region of 8 V, the sensitivity of the EIMS to formaldehyde at $m/z = 29$ and 30 was 3×10^{11} and 2×10^{11} molecule cm^{-3} respectively, for a signal-to-noise ratio of unity and an integration time of 60 s. The sensitivity to carbon dioxide at $m/z = 44$ was 1×10^{11} molecule cm^{-3}.

5.6 Conclusions

This chapter describes the successful design, construction and commissioning of an EIMS. The design of the vacuum system required several important factors to be taken into account, namely pressure requirements, sample introduction and flow-tube LFV. The design also had to be flexible as it was intended to convert the EIMS to a CIMS. The control units were connected to the MS and a means of acquiring and processing the signal was devised. The mass range, resolution and sensitivity of the EIMS are discussed with particular reference to the preparation of the instrument for the study of the acetonylperoxy radical self-reaction. The methods employed in adjusting the resolution, increasing the signal strength and reducing the noise are described.

Future work involves improving the mass range of the EIMS. The maximum mass ranges of the two High-Q Heads tested were not achieved because the maximum operating voltages could not be reached. Two possible explanations were provided for this shortcoming: either power losses were occurring within the quadrupole or the RF-power source was faulty. The cause can be identified by operating the RF-power source with a set of dummy poles. Once the problem has been solved, it will be necessary to improve the RF shielding of the CEM and connecting wires to reduce the interference from the larger RF voltages employed.

An important future aim is to improve the signal processing. The ratemeter and chart recorder could be replaced with a counter and computer.

5.7 References

- Atkins, P. W., *Physical Chemistry*, 5th Edition, Oxford University Press, Oxford, 1994
- de Hoffmann, E. and V. Stroobant, *Mass Spectrometry, Principles and Applications*, 2nd Edition, John Wiley and Sons, England, 2002
- Dobis, O. and S. W. Benson, *J. Am. Chem. Soc.*, 1990, **112**, 1023
- Dobis, O. and S. W. Benson, *J. Am. Chem. Soc.*, 1991, **113**, 6377

- *Extranuclear Laboratories Quadrupole Power Supply Instruction Manual,* Extranuclear laboratories, Pittsburgh, 1974
- *NIST Standard Reference Database*, Number 69, NIST, 2001, (http://webbook.nist.gov/chemistry)
- Wayne, R. P., *Chemical Instrumentation*, Oxford University Press, Oxford, 1994

Chapter 6 The self-reaction of the acetonylperoxy radical: an attempted discharge–flow tube/EIMS study

6.1 Introduction

The purpose of the work reported in this chapter was to determine the rate constant for the self-reaction of the acetonylperoxy radical using an electron-impact mass spectrometer (EIMS) coupled to a discharge–flow tube. The feasibility of the proposed aim was evaluated using a numerical model. The broad objective of the investigation was to determine whether the EIMS was a suitable tool with which to study such peroxy species. The complications that arose during the study illustrate the need for a more versatile form of mass spectrometry.

The self-reaction was the focus of the work for several reasons. As well as having some atmospheric importance, the reaction will contribute to the chemistry occurring in a laboratory investigation of the radical. Ideally, this chemistry should be understood before other reactants are added. Also, there is a conflict in the literature regarding the rate constant. Table 6.1 lists the results of the previous laboratory studies of the reaction. The apparent close agreement between Cox *et al.* (1990) and Bridier *et al.* (1993) is misleading. The two groups of workers measured the acetonylperoxy radical absorption spectrum to determine the rate constant. However, the values of the absorption cross-section used differ markedly and thus the agreement is fortuitous. It should be noted that the rate constant determined by Cox *et al.* (1990) is an upper limit as the secondary chemistry that contributes to the decay of the radical was not considered. Doubt has also been cast over the work of Bridier *et al.* (1993) as the acetonylperoxy radical absorption spectra determined by Sehested *et al.* (1998) and Nielsen *et al.* (2002) agree with that derived by Cox *et al.* (1990). Clearly further investigation of the rate constant and branching ratio was required.

Table 6.1. Previous laboratory studies of the acetonylperoxy radical self-reaction.

Study	Results	Technique used	Reference
Kinetic	$(8.3 \pm 1.6) \times 10^{-12}$ cm^3 molecule^{-1} s^{-1}	Pulse radiolysis of $CH_3COCH_3/O_2/SF_6$ and acetonylperoxy absorption at 310 nm	Cox *et al.* (1990) [a]
Kinetic	$(8.0 \pm 2.0) \times 10^{-12}$ cm^3 molecule^{-1} s^{-1} $k_a/k_b = 0.75 \pm 0.1$	Flash photolysis of $CH_3COCH_3/O_2/Cl_2$ and acetonylperoxy absorption at 230, 260 and 310 nm	Bridier *et al.* (1993) [b]
Product	Two channels identified: a) $2CH_3COCH_2O + O_2$ b) $CH_3COCHO + CH_3COCH_2OH + O_2$	Flash photolysis of $CH_3COCH_3/O_2/Cl_2$ and FTIR and UV-vis absorption	Jenkin *et al.* (1993) [b]

Notes: [a]1 bar and 298 K and [b]760 Torr and 298 K.

6.2 Feasibility study

The discharge–flow tube/EIMS system could not be used to monitor the acetonylperoxy radical directly. As discussed in chapter 2, it is not always possible to observe parent molecular ions using the EI technique. The method transfers more energy to the molecule than is required for ionization and the excess is sufficient to cause fragmentation. Observing a fragment of the radical was also not an option, as the EI mass spectrum is not known. Determining it would be a complex and probably not very worthwhile task, as it is highly likely that acetone and many of the intermediate and product species generated by the self-reaction would have similar spectra. Furthermore, any chance of observing $CH_3COCH_2O_2$ directly was negated by the possibility that the radical may not even survive the MS sampling process.

It was therefore necessary to devise an alternative method with which to obtain the rate constant. Two viable options existed: one was to titrate the acetonylperoxy radical with NO and monitor the NO_2 produced, and the second was to follow a product of the self-reaction. Before discussing the feasibility of these options, it would be useful to describe the acetonylperoxy radical self-reaction and subsequent chemistry.

6.2.1 The acetonylperoxy self-reaction

Jenkin *et al.* (1993) and Bridier *et al.* (1993) found that the self-reaction progresses *via* two pathways, with 75 % of the peroxy being converted to the oxy species and 25 % generating methyl glyoxal and hydroxyacetone:

$$2CH_3COCH_2O_2 \rightarrow 2CH_3COCH_2O + O_2 \qquad \text{(R6.1a)}$$

$$\rightarrow \underset{\text{methyl glyoxal}}{CH_3COCHO} + \underset{\text{hydroxyacetone}}{CH_3COCH_2OH} + O_2. \qquad \text{(R6.1b)}$$

The acetonoxy radical rapidly decomposes to generate formaldehyde and the acetyl radical, which in the presence of O_2 leads to the formation of the acetylperoxy radical:

$$CH_3COCH_2O + M \rightarrow CH_3CO + CH_2O + M \qquad \text{(R6.2)}$$

$$CH_3CO + O_2 + M \rightarrow CH_3COO_2 + M. \qquad \text{(R6.3)}$$

Note that the rate of reaction of the acetonoxy radical with oxygen has been found to be negligible (Jenkin *et al.* 1993 and Orlando *et al.* 2000), unlike the behaviour of other RO species.

The cross-reaction of the acetylperoxy and acetonylperoxy radicals propagates the chemistry. Acetonoxy and methyl radicals, carbon dioxide, acetic acid and more methyl glyoxal are generated:

$$CH_3COCH_2O_2 + CH_3COO_2 \rightarrow CH_3COCH_2O + CH_3 + CO_2 + O_2 \qquad \text{(R6.4a)}$$

$$\rightarrow CH_3COCHO + CH_3COOH + O_2. \qquad \text{(R6.4b)}$$

The decomposition of the acetonoxy radical formed in R6.4a leads to the regeneration of the acetylperoxy radical whilst the methyl radicals react with oxygen to produce a methylperoxy radical:

$$CH_3 + O_2 + M \rightarrow CH_3O_2 + M. \qquad \text{(R6.5)}$$

The cross-reaction of methylperoxy and acetonylperoxy radicals is also possible. It follows three channels, one forming radicals and two producing non-radical species:

$$CH_3COCH_2O_2 + CH_3O_2 \rightarrow CH_3COCH_2O + CH_3O + O_2 \qquad \text{(R6.6a)}$$

$$\rightarrow CH_3COCH_2OH + CH_2O + O_2 \qquad \text{(R6.6b)}$$

$$\rightarrow CH_3COCHO + CH_3OH + O_2. \qquad \text{(R6.6c)}$$

Methoxy radicals can react with O_2 to form HO_2:

$$CH_3O + O_2 \rightarrow CH_2O + HO_2. \qquad \text{(R6.7)}$$

Finally, the reaction of acetonylperoxy and hydroperoxy radicals yields stable products and so the chemistry is terminated:

$$CH_3COCH_2O_2 + HO_2 \rightarrow CH_3COCH_2O_2H + O_2. \qquad \text{(R6.8)}$$

6.2.2 The NO titration method

The NO titration method has been employed successfully many times in investigations of peroxy radicals. For example, Biggs *et al.* (1997a) used the technique to determine the rate constant for the self-reaction of CF_3O_2. The concentration of the radical was derived *via* EIMS and LIF detection of NO_2 and then concentration–time profiles were fitted to a numerical model that allowed for secondary chemistry. Biggs *et al.* (1999) used similar methods to determine the rate constants for the self-reaction of CH_2ClO_2 and $CHCl_2O_2$ radicals.

However, the NO titration method can not be applied to the study of the acetonylperoxy radical self-reaction because the concentration of NO_2 generated will not equal the concentration of acetonylperoxy in the flow tube. The other peroxy species present in the system, CH_3COO_2, CH_3O_2 and HO_2, will also react with NO to generate NO_2. Extracting the amount of NO_2 produced by reaction with the acetonylperoxy radical from the total NO_2 observed could not be achieved by the use of EIMS or the addition of another simple detection method.

6.2.3 Monitoring a product of the self-reaction

The second option for monitoring the acetonylperoxy radical self-reaction was to observe some product of the reaction. The feasibility of this option was evaluated using a numerical model generated with the FACSIMILE software package (version 3.0.30, AEA Technology).

6.2.3.1 The self-reaction model

Table 6.2 lists the chemical reactions and rate constants employed in the FACSIMILE model. The input file is shown in appendix IIII. The model not only simulates the self-reaction of the acetonylperoxy radical and subsequent chemistry but also includes the generation mechanism and peroxy radical cross-reactions.

It should be noted that the model represents only a simplified version of the oxidation scheme used for the purposes of the feasibility study. Regarding the generation mechanism, other reactions that would consume either F atoms or the acetonyl radical were not considered, as it was intended to adjust the flow-tube conditions in the experiments to minimize the extent of these reactions. Also, the minor pathways for the reaction of atomic fluorine and acetone:

$$F + CH_3COCH_3 \rightarrow CH_3 + CH_3COF \qquad \text{(R6.9b)}$$

$$k_{6.9b}/k_{6.9} = 0.08 \pm 0.01$$

$$\rightarrow CH_3F + CH_3CO \qquad \text{(R6.9c)}$$

$$k_{6.9c}/k_{6.9} < 0.02$$

Table 6.2. The chemical reactions and rate constants used to simulate the acetonylperoxy radical experiment.

	Reaction	Rate constant /cm^3 molecule^{-1} s^{-1}	Reference
	Generation		
(R6.9a)	$CH_3COCH_3 + F \rightarrow CH_3COCH_2 + HF$	1.35×10^{-10}	Cox *et al.* (1990)
(R6.10)	$CH_3COCH_2 + O_2 + M \rightarrow CH_3COCH_2O_2 + M$	1.45×10^{-12}	Cox *et al.* (1990)
	Self-reaction		
(R6.1a)	$2CH_3COCH_2O_2 \rightarrow 2CH_3COCH_2O + O_2$	6×10^{-12}	Bridier *et al.* (1993)
(R6.1b)	$\rightarrow CH_3COCHO + CH_3COCH_2OH + O_2$	2×10^{-12}	Bridier *et al.* (1993)
	Subsequent chemistry		
(R6.2)	$CH_3COCH_2O \rightarrow CH_3CO + CH_2O$	Rapid	
(R6.3)	$CH_3CO + O_2 + M \rightarrow CH_3COO_2 + M$	2×10^{-12}	Atkinson *et al.* (1992)
(R6.4a)	$CH_3COCH_2O_2 + CH_3COO_2 \rightarrow CH_3COCH_2O + CH_3 + CO_2 + O_2$	1×10^{-11}	Orlando *et al.* (2000)
(R6.4b)	$\rightarrow CH_3COCHO + CH_3COOH + O_2$	1×10^{-12}	Orlando *et al.* (2000)
(R6.11)	$2CH_3COO_2 \rightarrow 2CH_3COO + O_2$	1.6×10^{-11}	Atkinson *et al.* (1992)
(R6.12)	$CH_3COO \rightarrow CH_3 + CO_2$	Rapid	
(R6.5)	$CH_3 + O_2 + M \rightarrow CH_3O_2 + M$	6×10^{-14}	DeMore *et al.* (1997)
(R6.6a)	$CH_3COCH_2O_2 + CH_3O_2 \rightarrow CH_3COCH_2O + CH_3O + O_2$	1.1×10^{-12}	Orlando *et al.* (2000)
(R6.6b)	$\rightarrow CH_3COCH_2OH + CH_2O + O_2$	1.4×10^{-12}	Orlando *et al.* (2000)
(R6.6c)	$\rightarrow CH_3COCHO + CH_3OH + O_2$	1.4×10^{-12}	Orlando *et al.* (2000)
(R6.13a)	$CH_3COO_2 + CH_3O_2 \rightarrow CH_3COO + CH_3O + O_2$	1.2×10^{-11}	Orlando *et al.* (2000)
(R6.13b)	$\rightarrow CH_3COOH + CH_2O + O_2$	1.2×10^{-12}	Orlando *et al.* (2000)
(R6.14a)	$2CH_3O_2 \rightarrow 2CH_3O + O_2$	1.6×10^{-13}	Orlando *et al.* (2000)
(R6.14b)	$\rightarrow CH_3OH + CH_2O + O_2$	3.2×10^{-13}	Orlando *et al.* (2000)
(R6.7)	$CH_3O + O_2 \rightarrow CH_2O + HO_2$	1.9×10^{-15}	Atkinson *et al.* (1992)

as measured by Nielsen *et al.* (2002), were not included. Reactions of the HO_2 radical were excluded as well because the scheme only predicts a low concentration of this species. The main limitation of the model was that the uncorroborated rate constant and branching ratio of Bridier *et al.* (1993) was used. It was intended to adjust the model should experimental evidence indicate that any parameters were incorrect.

6.2.3.2 Model results

Concentration–time profiles of the acetonylperoxy radical and the stable products of the self-reaction generated by the numerical model are depicted in figure 6.1. Stable products are defined as those that do not take part in other chemistry listed in the model. The initial concentrations of the reactants were [F] = 5×10^{12}, [CH_3COCH_3] = 5×10^{13} and [O_2] = 1×10^{15} molecule cm^{-3}. The model simulated the chemistry occurring between 0 and ~50 ms, which is comparable to the time range that can be observed experimentally.

Figure 6.1 shows that large quantities of formaldehyde and carbon dioxide, much lower concentrations of methyl glyoxal and hydroxyacetone, and very small amounts of acetic acid and methanol are generated. All these species are products of the major pathway of the acetonylperoxy self-reaction and the subsequent chemistry, whereas the minor channel only generates methyl glyoxal and hydroxyacetone.

The total conversion of $CH_3COCH_2O_2$ to the stable products was quantified by running the model for a period of time that allowed the reactions to go to completion — 10 s was sufficient. The quantities of the products generated per molecule of the acetonylperoxy radical and the equivalent carbon yields are shown in table 6.3. The initial concentration of $CH_3COCH_2O_2$ was equal to the initial concentration of F (5×10^{12} molecule cm^{-3}).

It can be seen that, according to the reaction scheme listed in the model, large quantities of formaldehyde are produced — 42 % of the carbon in $CH_3COCH_2O_2$ is converted to CH_2O. Interestingly, methanol, which is the least concentrated product when the reaction time is short (see figure 6.1), is the third most abundant product when the chemistry is allowed to go to completion, reflecting the fact that it continues to be generated after most of the other products have reached their limiting concentrations.

Figure 6.1 Concentration–time profiles of the acetonylperoxy radical and the stable products of the self-reaction generated by the numerical model. The initial concentrations of the reactants were [F] = 5×10^{12}, [CH_3COCH_3] = 5×10^{13} and [O_2] = 1×10^{15} molecule cm^{-3}.

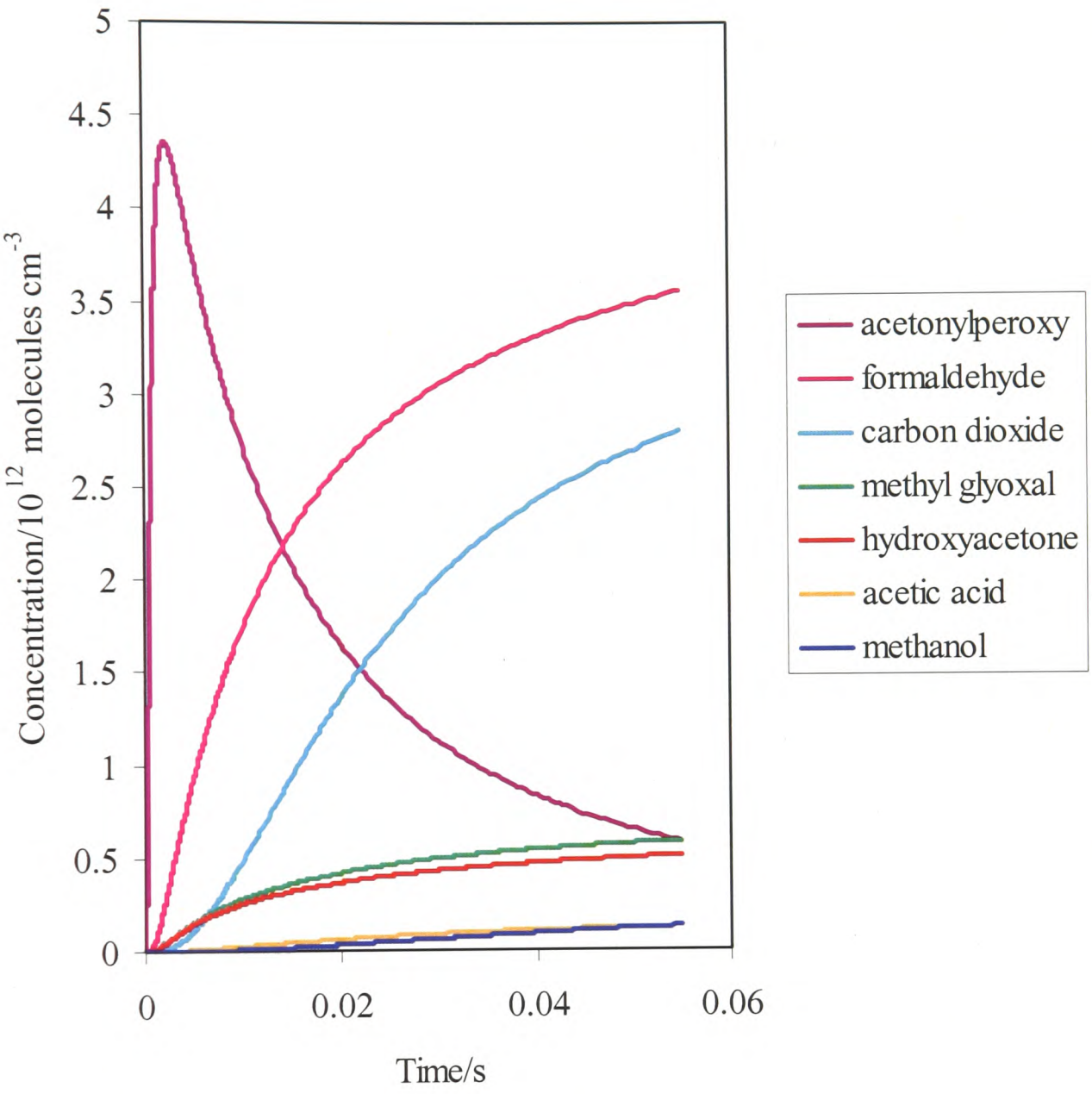

The large quantities of formaldehyde and carbon dioxide generated when the reaction time is comparable to the range that can be observed experimentally suggest that these two species would be good tracers for the self-reaction. The rate constant, $k_{6.1}$, could be obtained by fitting CH_2O and CO_2 concentration–time data to the model. Furthermore, it is possible that the branching ratio of R6.1 could be determined. Figure 6.2 shows the concentration–time profiles of formaldehyde when the rate constant and the branching

ratio are varied. Values of $k_{6.1}$ = 6, 8 and 10 × 10^{-12} cm^3 $molecule^{-1}$ s^{-1} and $k_{6.1a}/k_{6.1}$ = 0.25, 0.5 and 0.75 were used. A similar but slightly smaller set of curves can be generated for CO_2.

Table 6.3. The conversion of the acetonylperoxy radical to the stable products of the self-reaction: quantities per molecule of $CH_3COCH_2O_2$ and the equivalent carbon yield.

Product	**Final concentration /10^{12} molecule cm^{-3}**	**Product molecules per molecule of $CH_3COCH_2O_2$**	**Equivalent carbon yield**
CH_2O	6.25	1.25	0.42
CO_2	3.63	0.73	0.24
CH_3OH	0.84	0.17	0.06
CH_3COCHO	0.70	0.14	0.14
CH_3COCH_2OH	0.61	0.12	0.12
CH_3COOH	0.19	0.04	0.02

It can be seen that different combinations of the rate constant and branching ratio lead to differing concentration–time profiles of formaldehyde. The branching ratio has a particular effect on the profiles. For example, when $k_{6.1a}/k_{6.1}$ is small, more of the $CH_3COCH_2O_2$ reacts *via* R6.1b to form the stable products methyl glyoxal and hydroxyacetone, which leaves less peroxy available to produce CH_2O. This effect is well illustrated by comparing figures 6.1 and 6.3. As $k_{6.1a}/k_{6.1}$ is reduced from 0.75 (figure 6.1) to 0.5 and 0.25 (figure 6.3), the quantities of CH_2O and CO_2 generated are reduced, and [CH_3COCHO] and [CH_3COCH_2OH] are increased. Should the latter two species be produced in measurable concentrations, the extra data could be used in the model. However, for such concentrations of methyl glyoxal and hydroxyacetone to be generated, the branching ratio derived by Bridier *et al.* (1993) would need to be grossly inaccurate.

Figure 6.2. The concentration–time profiles of formaldehyde generated by the numerical model for $k_{6.1} = 6$, 8 and 10×10^{-12} cm^3 molecule^{-1} s^{-1} and $k_{6.1a}/k_{6.1} = 0.25$, 0.5 and 0.75.

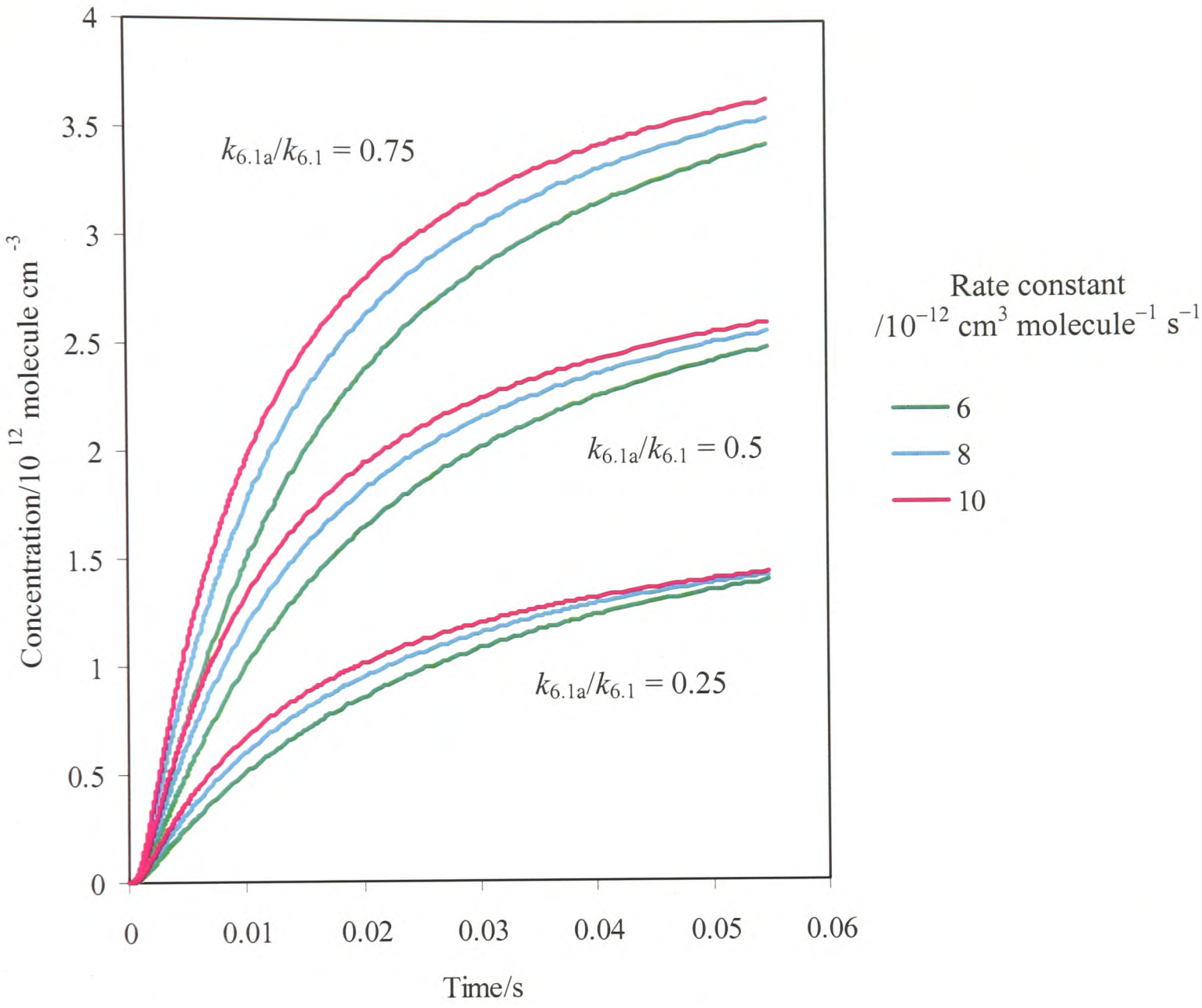

Of course, fitting concentration–time profiles to models to extract kinetic parameters requires the initial concentrations of the reactants to be known. The concentration of atomic fluorine could be easily quantified by titration with a mixture of H_2/NO_2 (Biggs *et al.,* 1997b). The F atoms react with H_2 to produce H atoms, which subsequently react with NO_2 to form OH. The OH could be monitored using OH resonance fluorescence.

Figure 6.3. Concentration–time profiles of the stable products of the self-reaction generated by the numerical model. $k_{6.1} = 8 \times 10^{-12}$ cm^3 molecule^{-1} s^{-1} and $k_{6.1a}/k_{6.1}$ = (a) 0.5 and (b) 0.25.

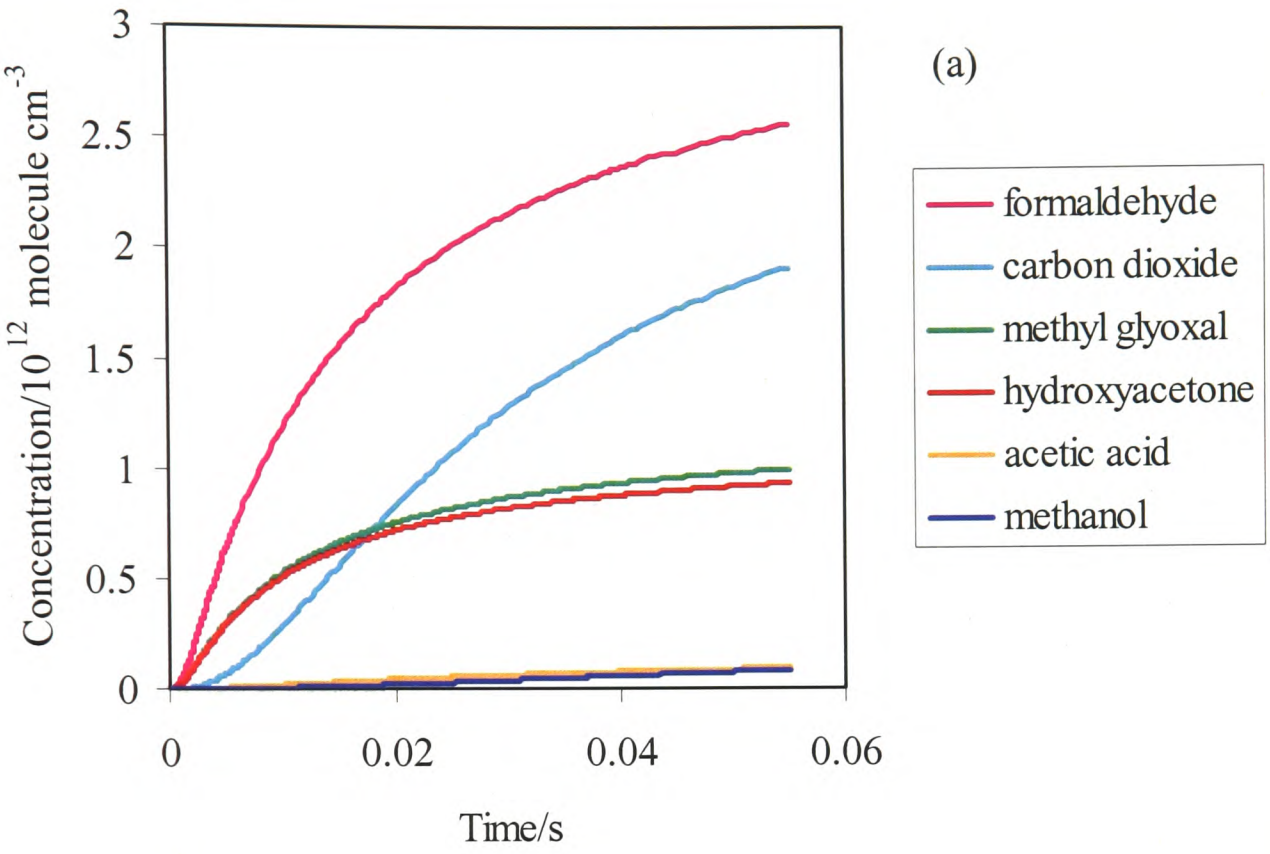

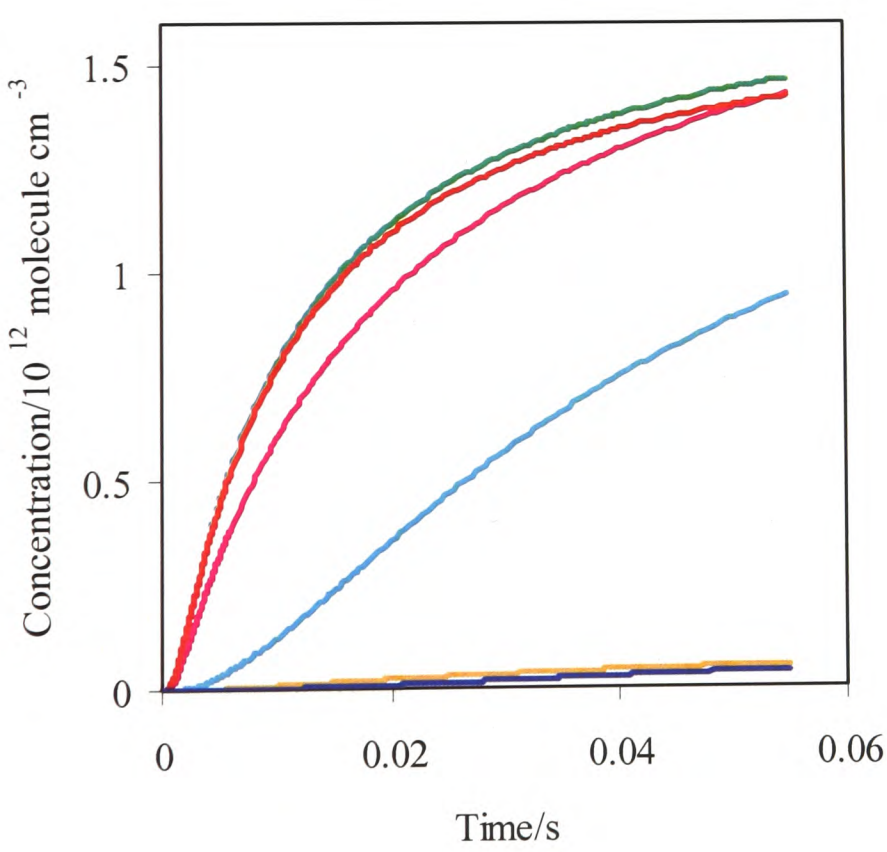

6.2.3.3 Testing the proposed method of extracting the kinetic parameters

It was decided to investigate the proposed method of obtaining the rate constant and branching ratio for R6.1. Some 'experimental data' were generated by taking the concentrations of formaldehyde and carbon dioxide produced by the model and then adding a random error of up to ±10 %. Note that the model used to generate the data was that in which $k_{6.1a} = 6 \times 10^{-12}$ and $k_{6.1b} = 2 \times 10^{-12}$ cm^3 molecule^{-1} s^{-1}. In total, seven data points were created for each species. The results of fitting these concentration–time profiles to the model are shown in table 6.4. The errors quoted are the 90% confidence limits. The point, time = 0 and concentration = 0, was also used in the fitting.

Table 6.4 The values of $k_{6.1a}$ and $k_{6.1b}$ derived from fitting concentration–time profiles of CH_2O and CO_2 to the model. See the text for details of how the data were produced.

Concentration–time profile used	**Value of $k_{6.1a}/10^{-12}$ cm^3 molecule^{-1} s^{-1} obtained**	**Value of $k_{6.1b}/10^{-12}$ cm^3 molecule^{-1} s^{-1} obtained**
[CH_2O]	5.65 ± 1.23	2.12 ± 1.13
[CO_2]	5.60 ± 1.41	2.18 ± 1.35
[CH_2O] and [CO_2]	5.62 ± 0.81	2.18 ± 0.75

The values of $k_{6.1a}$ and $k_{6.1b}$ produced by the parameter-fitting model agree within experimental error with those used in the model from which the data were obtained, although it must be said that $k_{6.1a}$ is slightly lower and $k_{6.1b}$ is a bit higher than the model values. It can also be seen that the choice of data set has little effect on the value derived. The only difference is in the error limits — those obtained with the formaldehyde data are smaller than those derived from the carbon dioxide data. Thus, formaldehyde is a better tracer for the self-reaction. As to be expected, using both sets of data for the fitting results in the smallest error limits.

6.2.3.4 EI mass spectra of the proposed tracers

The final part of the feasibility study was to determine which mass peaks to use to monitor the proposed tracers. The choice was greatly limited by the requirement to avoid the peaks of other species present. The mass spectra of formaldehyde, carbon dioxide, methyl glyoxal and hydroxyacetone, and the reactants and other stable products of the self-reaction are listed in table 6.5.

The best peak at which to monitor formaldehyde was m/z = 30, as there was no interference from any other species listed in the table. The base peak of formaldehyde, m/z = 29, was not an option as it is a minor peak of acetone. Although m/z = 29 is weak compared to other acetone peaks, the large concentration of acetone required to perform the experiment meant that the signal was not insignificant (~1500 counts s^{-1}). Hydroxyacetone, methyl glyoxal, acetic acid and methanol also have minor peaks at m/z = 29. The base peak of carbon dioxide, m/z = 44, is unaffected by any other species in the table. Of course, there was some contribution from the CO_2 in the residual air in the MS, but as it was small and constant, it should be subtractable from the signal generated by the self-reaction.

The only peaks in the spectra of CH_3COCHO and CH_3COCH_2OH that do not coincide with the peaks of the other species present are the parent molecular ions at m/z = 72 and 74. *The Eight Peak Index of Mass Spectra* (1991) lists these peaks as very weak because the spectra were taken with an electron energy of 70 eV, which means that the parent molecular ion has suffered extensive fragmentation. The intensity of the peaks at lower electron energies is not known. As the quantity of CH_3COCHO and CH_3COCH_2OH generated is likely to be low, and the observation of the molecules is not fundamental to the derivation of the kinetic information desired, it was decided to focus on the use of formaldehyde and carbon dioxide as tracers for the acetonylperoxy self-reaction.

The mass spectra of several species, mainly the peroxy and oxy radicals, generated by the acetonylperoxy self-reaction are not listed in table 6.5 because they are not known. However, it is probable that these species will not interfere with m/z = 30 and 44 as they

have similar structures to acetone and the other stable products of the reaction, and hence should have similar spectra. It is also by no means certain that such radical species will survive the MS sampling process.

Table 6.5 The mass spectra of reactants and stable products involved in the study of the acetonylperoxy radical self-reaction.

Species	**Mass spectral peaks/*m/z***							
Tracers								
CH_2O	29	30	28	27	26	(15)	(13)	(12)
CO_2	44	(28)	(16)	(22)	(12)	(45)		
CH_3COCHO	43	15	29	45	(42)	(28)	(72)	(60)
CH_3COCH_2OH	43	31	28	29	(74)	(42)	(27)	(32)
Reactants								
F_2	38	19						
CH_3COCH_3	43	58	15	(42)	(28)	(27)	(29)	(26)
O_2	32	(16)						
Other stable products								
CH_3OH	31	32	29	15	28	(33)	(14)	(13)
CH_3COOH	43	45	60	15	42	29	(28)	(14)

Notes: all data is from *The Eight Peak Index of Mass Spectra* (1991) except that for methyl glyoxal, which was listed in *NIST Standard Reference Database* (2001), and that for molecular fluorine, which was obtained in this work; the mass peaks are listed in order of intensity, with the largest peak first, and brackets indicate peaks that are ≤ 10 % of the base peak.

6.3 Experimental details

The experiments were performed using a discharge–flow tube/EIMS apparatus, the details of which have already been presented in previous chapters: see chapter 3 for a description of the flow tube and chapter 5 for a discussion of the EIMS. However, a brief

description of the apparatus is provided here in addition to the experimental details pertinent to this investigation.

The experimental system consisted of a Pyrex flow tube connected to an EI quadrupole MS. The flow tube was 1.1 m long and had an internal diameter of 36.8 mm. Gases were introduced *via* a double-nested sliding injector, a large side arm and six smaller ports. The tube was pumped downstream of the EIMS by a two-stage rotary pump (Edwards E2M80). A linear flow velocity (LFV) of 1150 – 1250 cm s^{-1} and a flow tube pressure (FTP) of 5.0 ± 0.2 Torr were employed during the experiments. The FTP was measured using a 10 Torr capacitance manometer (Edwards Barocel 600) located approximately halfway along the tube.

The flow-tube gases were sampled into the EIMS through a 0.3 mm pinhole. A portion of these gases passed through the front chamber and into the large opening of the back chamber, where they were ionized, mass filtered and detected. The pressures in the front and back chambers were ~ 1×10^{-5} and ~ 5×10^{-6} Torr respectively. As discussed in the preceding chapter, an electron current of 0.14 mA and a potential difference of 8 V between the filament and grid were found to be the best conditions with which to monitor CH_2O and CO_2. For a signal-to-noise ratio of unity and an integration time of 60 s, the sensitivities to formaldehyde at m/z = 30 and carbon dioxide at m/z = 44 were 2×10^{11} and 1×10^{11} molecule cm^{-3}, respectively.

The maximum mass that could be observed was m/z = 56, which was unfortunate considering that acetone has a mass of 58. Adjustments had already been made to the MS, as discussed in section 5.5.1, to achieve this maximum mass. Of course, it was not necessary to be able to detect masses above 56 to monitor carbon dioxide and formaldehyde. Should the detection of the parent molecular ions of methyl glyoxal or hydroxyacetone be required, the High Q Head could be changed.

The front of the channel electron multiplier was held at approximately –2.1 kV to collect the positive ions. The signal generated by the detector was recorded on a chart recorder (Venture Servoscribe).

The helium carrier gas (BOC, 99.996 %) flowed directly from the cylinder, through a series of purification traps (silica gel, diphosphorus pentoxide, and sodium and calcium aluminosilicate molecular sieve (4A, 5A and 13X) cooled with liquid nitrogen (all trap materials were supplied by BDH)), and into the flow tube *via* the side arm. A 10 SLPM mass flow controller (Tylan FC2900) — a valve coupled to a thermal-conductivity flow sensor — regulated the flow and the backing pressure was monitored with a dial manometer (De Wit).

The flows of all other gases were controlled by ~0.05 and ~2.5 SLPM ball flow-meters (Jencons RS1 and RS2) fitted with needle valves (Nupro). The backing pressures were monitored by 1000 Torr capacitance manometers (Data Instruments) or as in the case of oxygen, with a 'bubbler' — a trap filled with dimethyl phthlate (BDH) through which the gas could escape and thus, keep the pressure in the line equal to the atmospheric pressure. Oxygen (BOC, 99.5 %) was delivered directly from the cylinder and purified in the same manner as helium, expect that the molecular sieve was not cooled. Gaseous mixtures of acetone (Aldrich, 99.9+ %), fluorine (Messer, 5 % in He), formaldehyde (Aldrich, 95%) and carbon dioxide (BOC, 99.99+ %) were stored in 6 L bulbs. These gases were purified and the mixtures prepared by the techniques described in Appendix I. The gases were delivered to the flow tube *via* the sliding injector and ports.

Atomic fluorine was generated by passing the mixture of molecular fluorine and a further flow of helium through a microwave-discharge cavity fitted to the flow-tube side arm. Acetone and oxygen, and another flow of helium, were introduced to the system through the sliding injector. Movement of the injector permitted control of the contact time between F atoms and acetone and oxygen. The sliding injectors and the internal surface of the flow tube were coated with a halocarbon wax (KMZ Chemicals Ltd) to create an inert surface that minimized the loss of radical species to the walls.

Unless otherwise stated, the initial concentrations of the reactants were similar to those used in the numerical model, i.e. $[F] = 5 \times 10^{12}$, $[CH_3COCH_3] = 5 \times 10^{13}$ and $[O_2] = 1 \times 10^{15}$ molecule cm^{-3}. As can be seen from figures 6.1 to 6.3, employing such a starting concentration of fluorine atoms leads to the generation of CH_2O and CO_2 concentrations

that are greater than the sensitivities for these species. The initial concentrations of acetone and oxygen were such that they would be in an excess over F and CH_3COCH_2 respectively, so as to minimize the extent of other possible reactions of these radicals. All experiments were conducted at 298 ± 2 K.

6.4 Results

6.4.1 The conversion of molecular fluorine to atomic fluorine

Molecular fluorine could be detected at m/z = 38 (F_2^+) and m/z = 19 (F^+). The signals at both peaks dropped dramatically when the microwave-discharge cavity was turned on: evidence that molecular fluorine was dissociated to atomic fluorine. Figure 6.4 shows the reduction in signal at m/z = 38 when the discharge was turned on. The decrease in signal for all concentrations of F_2 was found to be 95 ± 2 %. This figure was used in later work to estimate the maximum concentration of atomic fluorine. It should be noted that the concentration of fluorine atoms in the flow tube would be much less as a result of losses to the walls.

A decrease in signal would be expected at m/z = 38 but maybe not at m/z = 19. When F_2 was dissociated and acetone injected, reductions in the acetone signals were observed: see the next section. Therefore, fluorine atoms must have been present in the flow tube and so the signal at m/z = 19 should have increased. One possible explanation for the absence of signal from the fluorine radicals is that they were lost in the MS sampling process.

6.4.2 The reaction of atomic fluorine with acetone

A reduction in signal at several acetone peaks was observed when molecular fluorine was dissociated, indicating a reaction between F and acetone. Figure 6.5 shows the decrease at m/z = 43 as [F] was increased. The acetone concentration was 7.9×10^{12} molecule cm^{-3} and the contact time was 43 ms. Note that the rate constant can not be derived from this data because the fluorine atom concentration is an overestimation as it was based on the assumption that 95 % of the molecular fluorine was dissociated.

Figure 6.4 The F_2 signal at $m/z = 38$ with and without the microwave discharge on.

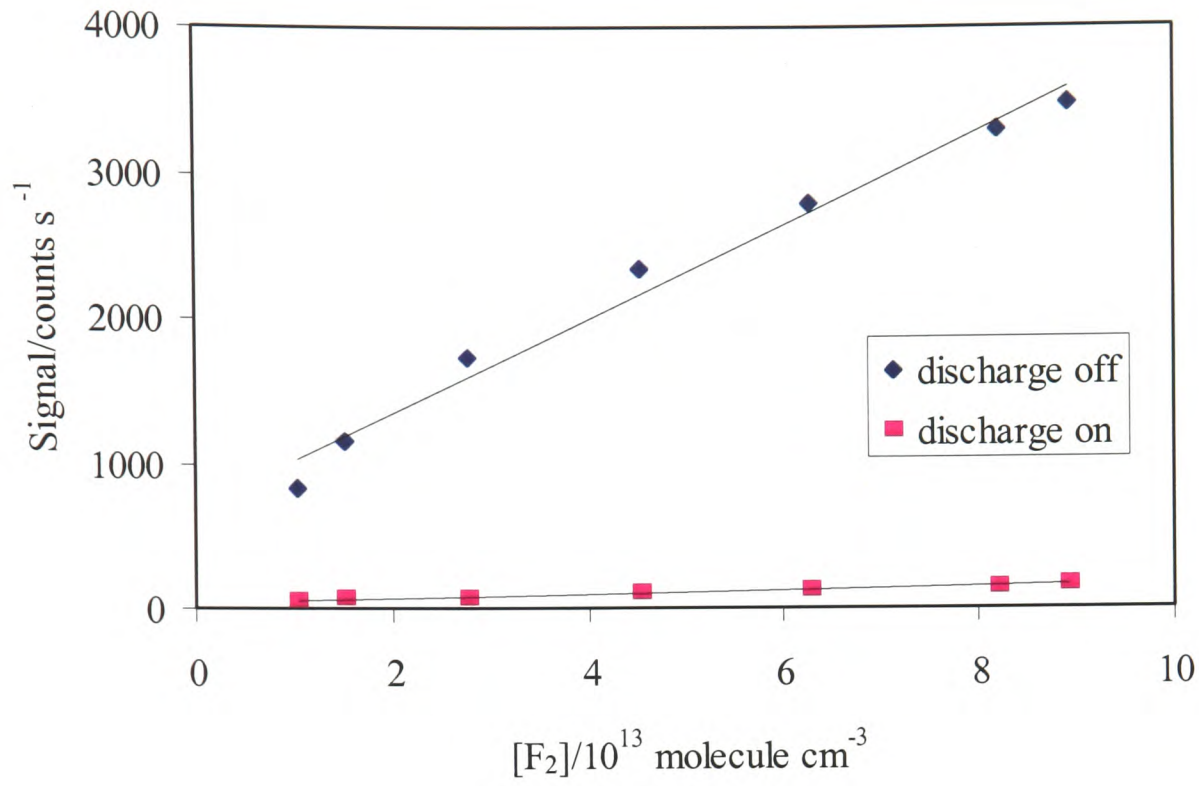

Figure 6.5 The drop in acetone signal at $m/z = 43$ on addition of atomic fluorine.

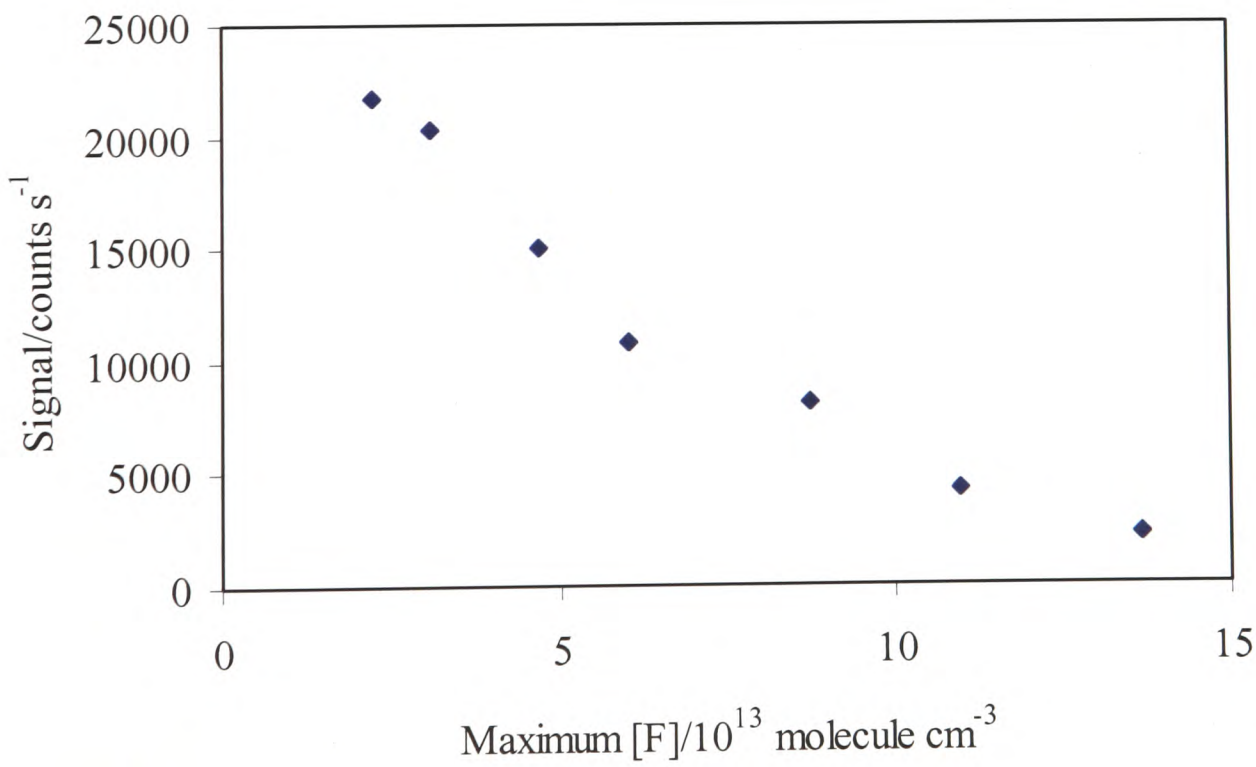

Tests were performed to check that the desired relative concentrations of F and acetone ([acetone] > [F]) were achieved in later experiments. The concentration of acetone was increased past the point where the addition of F had no observable effect on the acetone signals.

6.4.3 The interference of reactant species at *m/z* = 44

Unfortunately, the concentrations of acetone and oxygen required to study the acetonylperoxy radical self-reaction were observed to interfere with the signal at *m/z* = 44. Indeed, this mass peak behaved as if it were part of the spectra for acetone and oxygen, as the signal increased and decreased linearly in response to changes in concentration of the two species. These responses are shown in figures 6.6 and 6.7.

Further investigation of the effect of acetone upon this mass region revealed that the signal at *m/z* = 44 was a result of interference from the base peak in the spectrum of acetone, *m/z* = 43 (CH_3CO^+). The concentration of acetone necessary for the experiment was high enough to cause this peak to broaden to such an extent that it spilled over into *m/z* = 44.

Overlap of peaks was not the explanation for the response to oxygen, which was considerable. The mass peak neither corresponds to the mass spectrum of O_2 (peaks at *m/z* = 32 and 16) nor to a water-cluster ion involving oxygen. One possible explanation is that the signal is a response to CO_2, generated by the reaction of O_2 and carbon deposits burnt onto the filament. This hypothesis was tested by observing the signal with respect to time, with the expectation that the signal would decrease as the carbon source was depleted. However, no such reduction was seen in the time frame tested (~ 15 mins). Perhaps the carbon was present as an impurity in the tungsten wire instead. An MS with higher resolution would have revealed the elemental composition of the ion responsible for the signal.

The response of the signal at *m/z* = 44 to acetone and oxygen was so large that the detection of carbon dioxide generated by the self-reaction of the acetonylperoxy radical would have been very difficult. If the two explanations given above were correct then an

Figure 6.6 The response of the apparent signal at $m/z = 44$ to acetone.

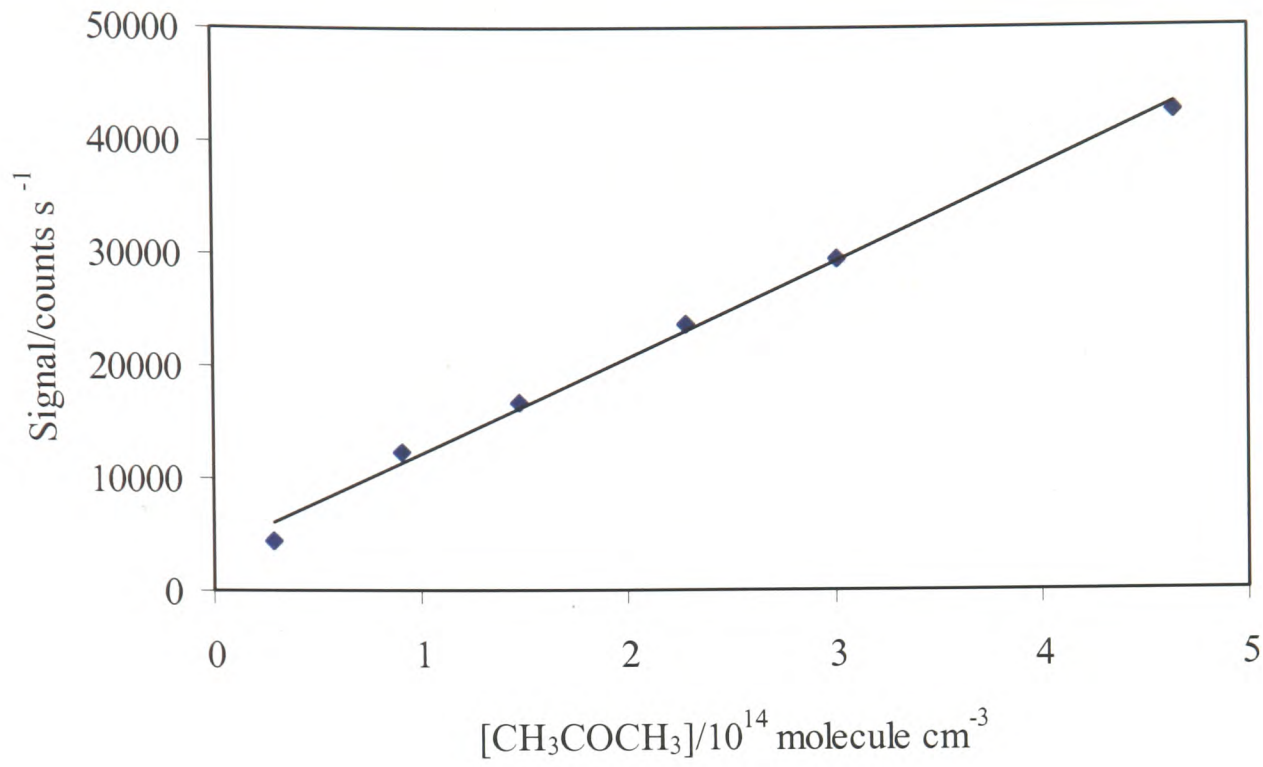

Figure 6.7 The response of the apparent signal at $m/z = 44$ to oxygen.

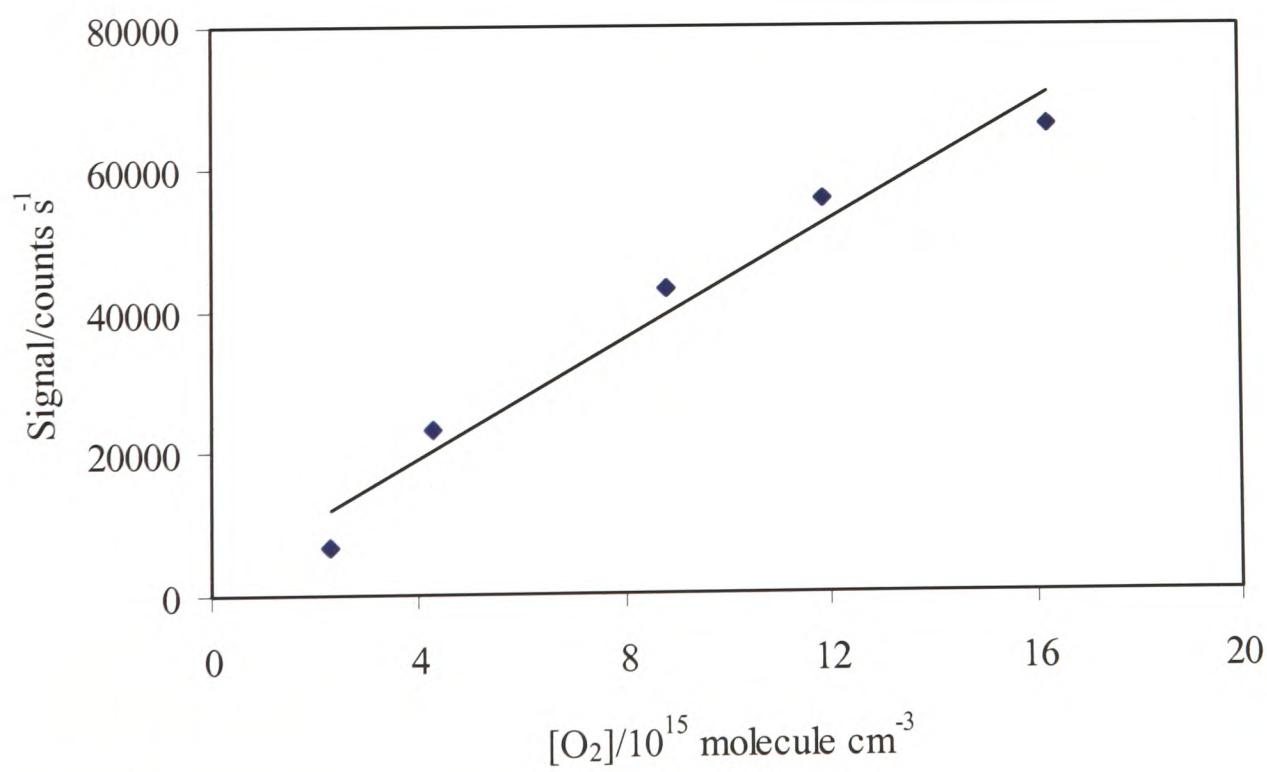

increase either in sensitivity (to reduce the reactant concentrations required) or in resolution (but without sacrificing sensitivity to CO_2), and either regular cleaning of the ion assembly or the use of a filament material with no impurities would be necessary. The use of other peaks in the CO_2 spectrum was not a viable alternative as they were very weak and corresponded to the spectra of other species in the flow tube. It was decided to focus on the use of $m/z = 30$ to follow the generation of formaldehyde.

6.4.4 Interference at $m/z = 30$

The signal at $m/z = 30$ did not suffer from interference from individual reactant species. However, an unexpected increase in signal was observed when acetone and atomic F were both injected into the flow tube in the absence of oxygen. The increase was of the order of several thousand counts per second. Similar behaviour was observed at $m/z = 29$ (after subtracting the acetone signal at this peak). The increase in signal was found to be dependent on acetone concentration but in a rather curious manner: see figure 6.8. A relationship to [F] could not be found. The addition of oxygen caused no change in the signal.

Mass 30 corresponds to CH_2O^+ and $CH_3CH_3^+$, and mass 29 corresponds to CHO^+ and $CH_3CH_2^+$. The signal at $m/z = 29$ in the spectrum of acetone is a result of the latter ion (N. Oldham, 2003, private communication). One possible explanation for the signals is that they are part of the spectra of the products of the reaction of F with acetone. However, this hypothesis is rather unlikely, as it is difficult to propose the identity of the molecules responsible for the ions, whose existence is independent of the presence of oxygen. Also, mechanisms for the re-arrangement reactions required to generate the ions from the species present in the flow tube are not known (N. Oldham, 2003, private communication).

Another explanation is that the signals were actually caused by formaldehyde somehow generated by the reaction of F with CH_3COCH_3. To test this hypothesis, the signals at $m/z = 29$ and 30 were recorded for different concentrations of F and CH_3COCH_3. The two mass peaks were then calibrated for their response to formaldehyde and these calibrations were used to obtain the concentration of formaldehyde that would correspond

to the signal from acetone and fluorine. If the signals at the two peaks were not in the same ratio as the calibrated signals for CH_2O, then the signal can not be due to CH_2O. The results are shown in table 6.6.

Figure 6.8 The signals at *m/z* = 29 and 30 when acetone and atomic fluorine were injected into the flow tube: the dependence on acetone concentration.

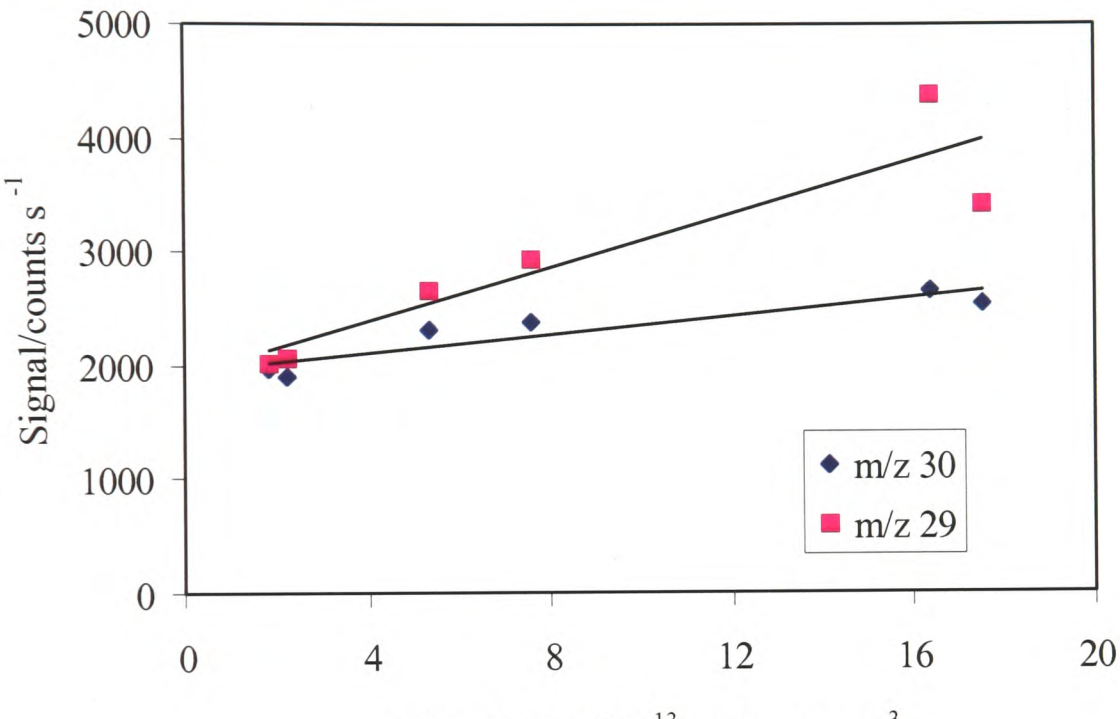

Although the ratio is quite close to unity at the lower count rates, there does seem to be a clear trend for an increase with increasing signal. According to the criterion just set forward, it must be concluded that the spurious signal does not arise from CH_2O.

With no proven explanation for the signals caused by the reaction of fluorine and acetone and no increase in signal from the addition of oxygen, it was felt that it would be useless to pursue the experiment any further.

Table 6.6 The signals generated at m/z = 29 and m/z = 30 when fluorine atoms and acetone were injected into the flow tube, and the concentrations of formaldehyde that the signals correspond to according to the formaldehyde calibrations.

$[CH_3COCH_3]$ /10^{13} molecule cm^{-3}	**Maximum [F]/10^{13} molecule cm^{-3}**	**Signal at m/z = 29 /counts s^{-1}**	**Signal at m/z = 30 /counts s^{-1}**	**Corresponding $[CH_2O]$ at m/z = 29 /10^{12} molecule cm^{-3} (A)**	**Corresponding $[CH_2O]$ at m/z = 30 /10^{12} molecule cm^{-3} (B)**	**A/B**
1.85	3.88	2025	1964	2.60	2.85	0.91
2.26	5.99	2059	1914	2.66	2.75	0.96
5.36	5.79	2666	2309	3.71	3.48	1.07
7.61	2.38	2936	2379	4.18	3.61	1.16
17.55	1.52	3409	2552	5.00	3.93	1.27
16.35	6.20	4388	2653	6.69	4.12	1.62

6.5 Discussion

This chapter describes an attempt to follow the acetonylperoxy radical self-reaction using an EIMS coupled to a discharge–flow tube. A numerical model identified formaldehyde and carbon dioxide as good tracers for the reaction. Evidence for the generation of fluorine atoms and their reaction with acetone was found. However, the rate constant for the self-reaction of acetonylperoxy was not derived because of interference from known and unknown sources at the mass peaks in question.

The success of previous workers in using discharge–flow tube/EIMS systems to investigate peroxy radical reactions is a result of studying simpler species with less complicated secondary chemistry. Biggs *et al.* (1997a) were able to study the CF_3O_2 self-reaction by the NO titration method because no other peroxy species were generated in the flow tube to interfere with the titration. In the investigation of the self-reaction of CH_2ClO_2, Biggs *et al.* (1999) again used the NO titration method but were able to eliminate the contribution of the only other peroxy produced by the chemistry (HO_2) by using OH resonance fluorescence, which is a very simple detection technique. Also, in

monitoring NO_2 at m/z = 46, Biggs *et al.* (1997a) avoided the possibility of interference from other species in the flow tube. The peak is neither close to the large reactant peaks nor corresponds to fluorine-containing fragments.

It was not possible to use the NO titration technique in this study as the contribution of the other peroxy species generated in the system to the concentration of NO_2 produced could not be assessed easily. The unsuitability of this technique was unfortunate because m/z = 46 is neither close to a reactant peak nor corresponds to the mass spectra of the stable products. Instead, the acetonylperoxy self-reaction was to be monitored by observing formaldehyde and carbon dioxide. Unfortunately, the base peak of CO_2 was too close to a large reactant peak and the mass peaks of formaldehyde were in a region where ions produced by the EI fragmentation of organic molecules are common.

Cox *et al.* (1990), Bridier *et al.* (1993) and Jenkin *et al.* (1993) were able to study the acetonylperoxy radical self-reaction because they could observe the radical directly, *via* its UV spectrum. The latter two workers also monitored several product species by their UV-vis and IR spectra, which allowed the numerical model used to derive the rate constant and branching ratio to be further constrained. Orlando *et al.* (2000) were able to investigate the chemistry of the acetonoxy radical with FTIR spectroscopy.

However, the use of UV absorption spectroscopy to monitor peroxy radicals is not without its problems, as illustrated by the disagreement between Cox *et al.* (1990) and Bridier *et al.* (1993) over the absorption cross section of $CH_3COCH_2O_2$. Simultaneously extracting the absorption cross-section and the desired rate constant, whilst taking account of the UV absorption of the other species (including other peroxy radicals) present, is an extremely complicated task. Mass spectrometry could be a less problematic technique. However, this study showed that EIMS was not appropriate because its use required the peroxy radical to be monitored indirectly, in a mass range cluttered with reactant and product peaks. A more versatile form of mass spectrometry is required.

Direct observation of the acetonylperoxy radical could be achieved with a chemical-ionization mass spectrometer (CIMS). CI produces ions with little excess energy, so less fragmentation occurs and the parent molecular ions can be observed.

Reduced fragmentation also means that CI spectra are less complicated than EI spectra, so the chances of the types of interference experienced in the EIMS study are reduced. As discussed in the next chapter, CIMS has been used to observe many peroxy species and the technique could be well applied to the acetonylperoxy radical. The most common peroxy CI scheme involves the production of molecular anions. The self-reaction of the acetonylperoxy radical could be followed by monitoring its molecular anion, as well as the acetylperoxy and methylperoxy anions. It may also be possible to monitor the stable products of the reaction. This proposal is discussed further in section 7.2.1. Fitting the concentration–time profiles to the numerical model would yield the rate constant. The conversion of the EIMS to a CIMS is the subject of the following chapter.

The experiments described in this chapter did show that the discharge–flow tube/EIMS system was a suitable technique with which to perform a kinetic study of the reaction between atomic fluorine and acetone. Peaks in the acetone spectrum decreased when fluorine atoms were injected into the flow tube. Such a study would be worthwhile as the rate constant for the reaction between F and CH_3COCH_3 is not well established. The work could be extended to include reactions of F or other halogen atoms with many organic species.

6.6 References

- Atkinson, R., D. L. Baulch, R. A. Cox, R. F. Hampson, J. A. Kerr and J. Troe, *J. Phys. Chem. Ref. Data*, 1992, **21**(6)
- Biggs, P., C. E. Canosa-Mas, J. M. Fracheboud, C. J. Percival, R. P. Wayne and D. E. Shallcross, *J. Chem. Soc., Faraday Trans.*, 1997a, **93**(3), 379
- Biggs, P., C. E. Canosa-Mas, D. E. Shallcross, A. Vipond and R. P. Wayne, *J. Chem. Soc., Faraday Trans.*, 1997b, **93**(16), 2701
- Biggs, P., C. E. Canosa-Mas, C. J. Percival, D. E. Shallcross and R. P. Wayne, *Int. J. Chem. Kinet.*, 1999, **31**, 433
- Bridier, I., B. Veyret, R. Lesclaux and M. E. Jenkin, *J. Chem. Soc. Faraday Trans.*, 1993, **89**(16), 2993

- Cox, R. A., J. Munk, O. J. Nielsen, P. Pagsberg and E. Ratajczak, *Chem. Phys. Lett.*, 1990, **173**(2,3), 206
- DeMore, W. B., S. P. Sander, D. M. Golden, R. F. Hampson, M. J. Kurylo, C. J. Howard, A. R. Ravishankara, C. E. Kolb and M. J. Molina, *Chemical Kinetics and Photochemical Data for Use in Stratospheric Modeling*, Evaluation Number 12, NASA, California, 1997
- Jenkin, M. E., R. A. Cox, M. Emrich and G. K. Moortgat, *J. Chem. Soc. Faraday Trans.*, 1993, **89**(16), 2991
- Nielsen, O. J., M. S. Johnson, T. J. Wallington, L. K. Christensen and J. Platz, *Int. J. Chem. Kinet.*, 2002, **34**, 283
- *NIST Standard Reference Database*, Number 69, NIST, 2001, (http://webbook.nist.gov/chemistry)
- Orlando, J. J., G. S. Tyndall, L. Vereecken and J. Peeters, *J. Phys. Chem. A.*, 2000, **104**, 11578
- Sehested, J., L. K. Christensen, O. J. Nielsen, M. Bilde, T. J. Wallington, W. F. Schneider, J. J. Orlando and G. S. Tyndall, *Int. J. Chem. Kinet.*, 1998, **30**, 475
- *Eight Peak Index of Mass Spectra*, 4th Edition, The Mass Spectrometry Data Centre, RSC, Cambridge, 1991

Chapter 7 The conversion of the mass spectrometer from an electron-impact to a chemical-ionization instrument

7.1 Introduction

The aim of this work was to convert the EIMS to a CIMS. One of the current research programmes in Oxford is the development of a CIMS that will be coupled to a discharge–flow tube to study reactions of the acetonylperoxy radical and other peroxy species. This chapter describes the beginning of the process, namely the design and construction of an external ion source. A brief overview of the important factors in discharge–flow tube/CIMS system design is given first.

7.2 Discharge–flow tube/CIMS systems

As discussed in chapters 2 and 5, mass spectrometers operate at high vacuum to ensure that collisions between ions and molecules, which reduce sensitivity and resolution, do not occur. However, ionization in a CIMS occurs *via* such collisions and so the CI source must operate at higher pressures. One method of accommodating this requirement is to separate the source from the MS chambers and devise a means of introducing the externally produced ions. Thus, the discharge–flow tube/CIMS technique involves the following sequence of events:

- Reagent-ion generation
- Ionization of the flow-tube gases
- Introduction of the ions to the MS
- Mass separation and detection.

The following sections discuss peroxy radical CI schemes, options for the source, and methods of introducing the ions to the MS. Mass separation and detection were to be achieved using the quadrupole and the channel electron multiplier (CEM) already discussed in chapter 5.

7.2.1 Peroxy radical CI schemes

Peroxy radical CI schemes used in previous discharge–flow tube/CIMS investigations are listed in table 7.1. It can be seen that most of the schemes involve the transfer of charge from a negative reagent ion, generally SF_6^- or O_2^-, to the peroxy radical. Such charge-transfer reactions are preferable to ion–molecule reactions involving proton transfer or some other chemical change as the peroxy radical is observed directly as the molecular anion. The stability of the molecular ion must mean that the enthalpy change of the reaction is low. Electron affinities (EAs) can be used to calculate the exothermicity of the reaction. (The EA is defined as the negative of the enthalpy change for the attachment of an electron to a molecule). However, the only peroxy species for which the EA has been determined is HO_2 (1.08 eV) (de Hoffmann and Stroobant, 2002). The EAs of the other peroxy radicals listed in table 7.1 must also be more positive than the EAs of SF_6 (1.07 eV) and O_2 (0.45 eV) (*NIST Standard Reference Database*, 2001) for the reactions to occur.

The use of a discharge–flow tube/CIMS system to study the self-reaction of the acetonylperoxy radical is proposed in chapter 6. The reaction could be followed by monitoring acetonylperoxy radicals, and the acetylperoxy and methylperoxy radicals that are generated. As can be seen from table 7.1, CH_3COO_2 has been successfully observed as its molecular anion following reaction with SF_6^-. It is highly likely that $CH_3COCH_2O_2$ and CH_3O_2 could be ionized in the same way. SF_6^- would also ionize any hydroperoxy radicals present in the flow tube, although this species would not be observed as its molecular anion but as $SF_4O_2^-$ instead. Further kinetic information could be obtained by monitoring the stable products of the acetonylperoxy radical self-reaction, namely formaldehyde, carbon dioxide, methanol, acetic acid, methyl glyoxal and hydroxyacetone. However, as the EA of CH_2O is –0.95 eV (Francisco and Thoman, 1999) and the EA of CO_2 is –0.6 eV (de Hoffmann and Stroobant, 2002), these two species could not be ionized by SF_6^-. The EAs of methanol and acetic acid are +1.6 eV and +3.1 eV respectively and thus, these species could be observed as their molecular anions. The ability to ionize CH_3COCHO and CH_3COCH_2OH with SF_6^- can not be predicted, as the EAs are not known.

Table 7.1. Peroxy radical CI schemes used in previous discharge–flow tube/CIMS investigations.

Peroxy radical	Ion source	CI reaction		Reference
HO_2	Corona discharge	$F^- + HO_2 \rightarrow HF + O_2^-$	(R7.1)	Seeley *et al.* (1996)
	Corona discharge	$SF_6^- + HO_2 \rightarrow \rightarrow SF_4O_2^-$	(R7.2)	Elrod *et al.* (1996)
	Filament	$(HO_2 + NO \rightarrow OH + NO_2)$	(R7.3)	Lovejoy *et al.* (1990)
		$SF_6^- + NO_2 \rightarrow SF_6 + NO_2^-$	(R7.4)	
CH_3O_2	Filament	$O_2^+ + CH_3O_2 \rightarrow O_2 + CH_3O_2^+$ (~75 %)	(R7.5a)	Villalta *et al.* (1995)
		$\rightarrow 2O_2 + CH_3^+$ (~25 %)	(R7.5b)	
	Polonium cartridge	$H_3O^+(H_2O)_3 + CH_3O_2 \rightarrow H_2O + CH_3OOH^+(H_2O)_3$	(R7.6)	Elrod *et al.* (2001)
CF_3O_2	Filament	$SF_6^- + CF_3O_2 \rightarrow SF_6 + CF_3O_2^-$	(R7.7)	Bevilacqua *et al.* (1993)
	Filament	$I^- + CF_3O_2 \rightarrow IO + CF_3O^-$	(R7.8)	Turnipseed *et al.* (1995)
$C_2H_5O_2$	Filament	$O_2^- + C_2H_5O_2 \rightarrow O_2 + C_2H_5O_2^-$	(R7.9)	Eberhard and Howard (1996)
	Polonium cartridge	$H_3O^+(H_2O)_3 + C_2H_5O_2 \rightarrow H_2O + C_2H_5O_2H^+(H_2O)_3$	(R7.10)	Ranschaert *et al.* (2000)
CH_3COO_2	Filament	$SF_6^- + CH_3COO_2 \rightarrow SF_6 + CH_3COO_2^-$	(R7.11)	Villalta and Howard (1996)
		$I^- + CH_3COO_2 \rightarrow IO + CH_3COO^-$	(R7.12)	
		$O_3^- + CH_3COO_2 \rightarrow 2O_2 + CH_3COO^-$	(R7.13)	
	Corona discharge	$SF_6^- + CH_3COO_2 \rightarrow SF_6 + CH_3COO_2^-$	(R7.14)	Moise *et al.* (1999)
n-$C_3H_7O_2$	Filament	$O_2^- + n\text{-}C_3H_7O_2 \rightarrow O_2 + n\text{-}C_3H_7O_2^-$	(R7.15)	Eberhard and Howard (1996)
$(CH_3)_2CHO_2$	Filament	$O_2^- + (CH_3)_2CHO_2 \rightarrow O_2 + (CH_3)_2CHO_2^-$	(R7.16)	Eberhard *et al.* (1996)
$C_2H_5COO_2$	Filament	$SF_6^- + C_2H_5COO_2 \rightarrow SF_6 + C_2H_5COO_2^-$	(R7.17)	Froyd and Lovejoy (1999)
		$I^- + C_2H_5COO_2 \rightarrow IO + C_2H_5COO^-$	(R7.18)	
$CH_2CHCH_2O_2$	Filament	$O_2^- + CH_2CHCH_2O_2 \rightarrow O_2 + CH_2CHCH_2O_2^-$	(R7.19)	Eberhard and Howard (1997)
t-$C_4H_9O_2$		$O_2^- + t\text{-}C_4H_9O_2 \rightarrow O_2 + t\text{-}C_4H_9O_2^-$	(R7.20)	
c-$C_5H_9O_2$		$O_2^- + c\text{-}C_5H_9O_2 \rightarrow O_2 + c\text{-}C_5H_9O_2^-$	(R7.21)	
2-$C_5H_{11}O_2$		$O_2^- + 2\text{-}C_5H_{11}O_2 \rightarrow O_2 + 2\text{-}C_5H_{11}O_2^-$	(R7.22)	
$CH_2C(CH_3)COO_2$	Filament	$SF_6^- + CH_2C(CH_3)COO_2 \rightarrow SF_6 + CH_2C(CH_3)COO_2^-$	(R7.23)	de Gouw and Howard (1997)
$C_5H_8OHO_2$	Corona discharge	$SF_6^- + C_5H_8OHO_2 \rightarrow SF_6 + C_5H_8OHO_2^-$	(R7.24)	Zhang *et al.* (2001)

7.2.2 CI sources

Three types of ion source have been used in discharge–flow tube/CIMS systems, namely filaments, corona discharges and radioactive materials. Table 7.1 shows that all three sources have been used in peroxy radical studies. Both positive and negative reagent ions can be generated either by electron impact or electron capture. The ionizing electrons arise from a carrier gas and are of a much lower energy than those usually generated by an EI filament. Electron capture processes require very low energy electrons. Associative capture only occurs when molecules with a high electronegativity are ionized by such electrons (de Hoffmann and Stroobant, 2002). Collisions with the carrier gas are also required to stabilise the anions. Some electron capture processes occur with sufficient energy to cause the anion to dissociate.

Carrier gas ionization:	$He \rightarrow He^+ + e^-$	(R7.25)
Electron impact:	$O_2 + e^- \rightarrow O_2^+ + 2e^-$	(R7.26)
Associative electron capture:	$SF_6 + e^- + M \rightarrow SF_6^- + M$	(R7.27)
Dissociative electron capture:	$CF_3I + e^- \rightarrow CF_3 + I^-$	(R7.28)

The filament source is similar to the conventional electron-impact source (Gleason *et al.*, 1987). It is commonly housed in a separate 'ion flow tube'. A large flow of carrier gas is introduced to the ion flow tube. The filament bombards the carrier gas with electrons, generating positive ions and low energy electrons. Reagent ions are produced by introducing a small flow of the reagent gas to the flow tube just before or after the filament (Villalta *et al.*, 1995). The discharge–flow tube gases are sampled into the ion flow tube further downstream.

The corona discharge source consists of a steel needle, held at typically –4 kV, inside a grounded stainless-steel tube (Elrod *et al.*, 1996). A glass tube separates the two electrodes. A large flow of carrier gas is passed through the source and ions and electrons are produced in the resulting discharge. A small quantity of reagent gas is added to the carrier gas either before or after the source (Suh *et al.*, 2000). Generally, the corona discharge is excited in a separate tube and the ions are added to the downstream end of the discharge–flow tube.

The radioactive source generally consists of a foil of polonium-210, an alpha emitter. The foil is housed in a cartridge through which a large flow of carrier gas is passed (Percival *et al.*, 1997). Ions and electrons are generated when the carrier gas is bombarded by high-energy (5.305 MeV) alpha particles. The reagent gas is also passed through the source (Jayne *et al.*, 1997). Usually, the ions are produced in a separate tube and added to the downstream end of the discharge–flow tube.

7.2.3 Ion sampling

The techniques used by different workers to transport the externally produced ions from the CI region into the MS chambers are very similar (see Seeley *et al.* (1996), Jayne *et al.* (1997) and Suh *et al.* (2000)). A pinhole is employed between the flow tube and the MS to allow a sample of the flow tube gases to be admitted. The pinhole is held at a potential of up to ±200 V to draw the ions into the MS. The mass analyser and detector are held in a second chamber, separated from the first by another pinhole or a cone. This differential pumping allows the neutral flow-tube species that have effused through the front pinhole to be pumped away. However, the distance between the front and back apertures, typically 5 cm, is sufficient to demand the use of ion optics to prevent ions from being either lost to the chamber walls or pumped away. A series of electrostatic lenses, an einzel lens and an electrostatic ion guide (EIG) have been used to focus the ions. An einzel lens is a particular arrangement of three cylindrical lenses or apertures (Cerezo and Miller, 1991). An EIG is comprised of a cylindrical mesh and a central wire (Zhang *et al.*, 1998). The back pinhole or cone is of a similar diameter to the first and also held at a potential that aids ion sampling.

7.3 CIMS design

The first step in the development of the discharge–flow tube/CIMS apparatus was the conversion of the EIMS to a CIMS. It was intended to operate the CIMS initially in positive-ion mode. The system would be converted to detect negative ions when externally produced positive ions had been successfully detected. This conversion would involve changes in the CEM control and signal processing. The external source and ion optics designs are described.

7.3.1 Ion-source design

The polonium-210 cartridge was chosen as the source because of its simplicity. Filament sources require current and voltage supplies, a collector plate and a feedback mechanism to regulate the electron emission. Discharge sources require a high-voltage supply. The polonium cartridge is a less complicated device and only requires a low-voltage source (to supply a potential to the cartridge to create an electric field that aids ion sampling).

The cartridge (Stat Attack Nuclecel P-2031) contained 20 mCi of polonium. It consisted of a stainless-steel tube, 66 mm long and 25 mm in diameter, with the radioactive material encapsulated in a strip of copper mounted inside. The cartridge was placed inside a mini flow tube, which was coupled to the MS: see figure 7.1. The mini flow tube was a ~200 mm long section of 34 mm internal diameter Pyrex tubing. The polonium cartridge was attached to a length of ¼ inch diameter stainless-steel tube, which was connected to the glass tube by a ¼ – ½ inch Cajon vacuum fitting. Gases flowed through the steel tube and cartridge, and one of the side arms, into the mini flow tube. The tube was pumped downstream of the MS by a two-stage rotary pump (Edwards E2M80). Linear flow velocities (LFVs) of 600 to 1000 cm s^{-1} and flow-tube pressures (FTPs) of ≤ 10 Torr were employed during the experiments. The pressure was monitored by a 10 Torr capacitance manometer (Leybold CTR90 Ceravac).

7.3.2 Ion-optics design

The flow-tube gases were sampled into the MS through a 0.3 mm chamfered pinhole. The pinhole was isolated from the flange in which it was mounted by Teflon spacers. A potential difference of up to 500 V was applied between the pinhole and polonium cartridge. Positive potentials are required on the pinhole to force cations through to the MS chambers (R. Burke, private communication, 2003) — negative potentials attract cations to the pinhole plate where they are lost. The cartridge was held at a more positive potential to accelerate the ions towards the pinhole.

An electrostatic ion guide (EIG) was placed between the front pinhole and the back chamber: see figure 7.1. As previously stated, an EIG is comprised of an outer mesh

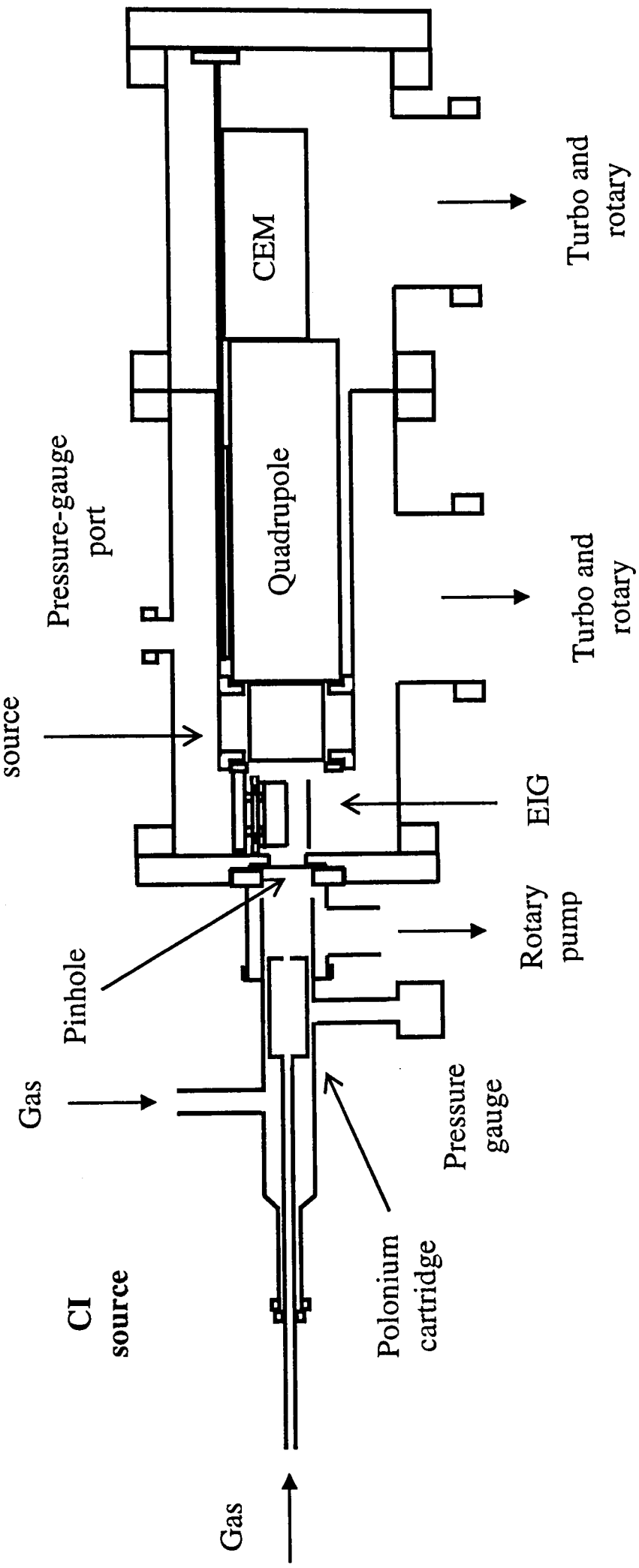

Figure 7.1. The coupling of the polonium CI source to the EIMS (scale 1:5).

Note: see figure 7.2 for a larger scale drawing of the EIG.

cylinder and a central wire. A small potential difference is applied between the two components. Ions that effuse through the front pinhole are caught in the resulting electric field and are transmitted through the EIG. Calculations by Zhang *et al.* (2000) showed that the ions perform spiral motions around the central wire. Neutral species that enter the EIG are pumped away through the mesh.

The EIG was chosen as it has several advantages over einzel lenses and other electrostatic plate arrangements. First, the guide has been shown to be effective at transporting ions over a variety of distances (Bondarenko and Macfarlane, 1997). Thus, a design that filled the gap between the pinhole and the first plate of the EI source could be easily selected. A design for an electrostatic plate system would have required careful consideration of the number, size and spacing of the individual elements required to successfully transmit the ions across the gap (Cerezo and Miller, 1991). Secondly, precise alignment of the guide with the entrance and exit apertures was not necessary. Ions that are displaced from the z axis and/or have trajectories diverging from the z axis when they enter the guide are successfully transmitted to the exit plate (Zhang *et al.*, 1998). Indeed, Zhang *et al.* (2000) found the guide to be more efficient than electrostatic lenses in capturing and transporting ions in a rapidly expanding beam (as produced by the front chamber pinhole). Finally, the guide is less of an obstruction to pumping than other lenses as neutral species can easily pass through the mesh cylinder. In conclusion, the EIG is an efficient ion optic and was easy to design and position.

The EIG used in this work was based upon designs by Bondarenko and Macfarlane (1997) and Zhang *et al.* (1998): see figure 7.2. The cylinder was 47 mm long, 38 mm in diameter and constructed from a stainless-steel mesh. 0.2 mm diameter nichrome wire was positioned along the central axis of the cylinder. The wire was supported at both ends by 0.13 mm diameter nylon threads. At the back of the EIG, three nylon threads were tied to a loop at the end of the central wire. At the front, two nylon thread supports were attached to the wire, and the wire itself provided the third supporting line. The ends of the supporting wires were threaded through holes in the mesh cylinder and anchored to nylon screws. Tightening the screws pulled the central wire taut and held it in position. The screws were mounted in rods, which were supported by larger rods that were attached to a ring. This supporting structure was constructed from PEEK (polyaryletheretherketone), a plastic suitable for high vacuum applications. The EIG was

Figure 7.2. The electrostatic ion guide (scale 1:1.5).

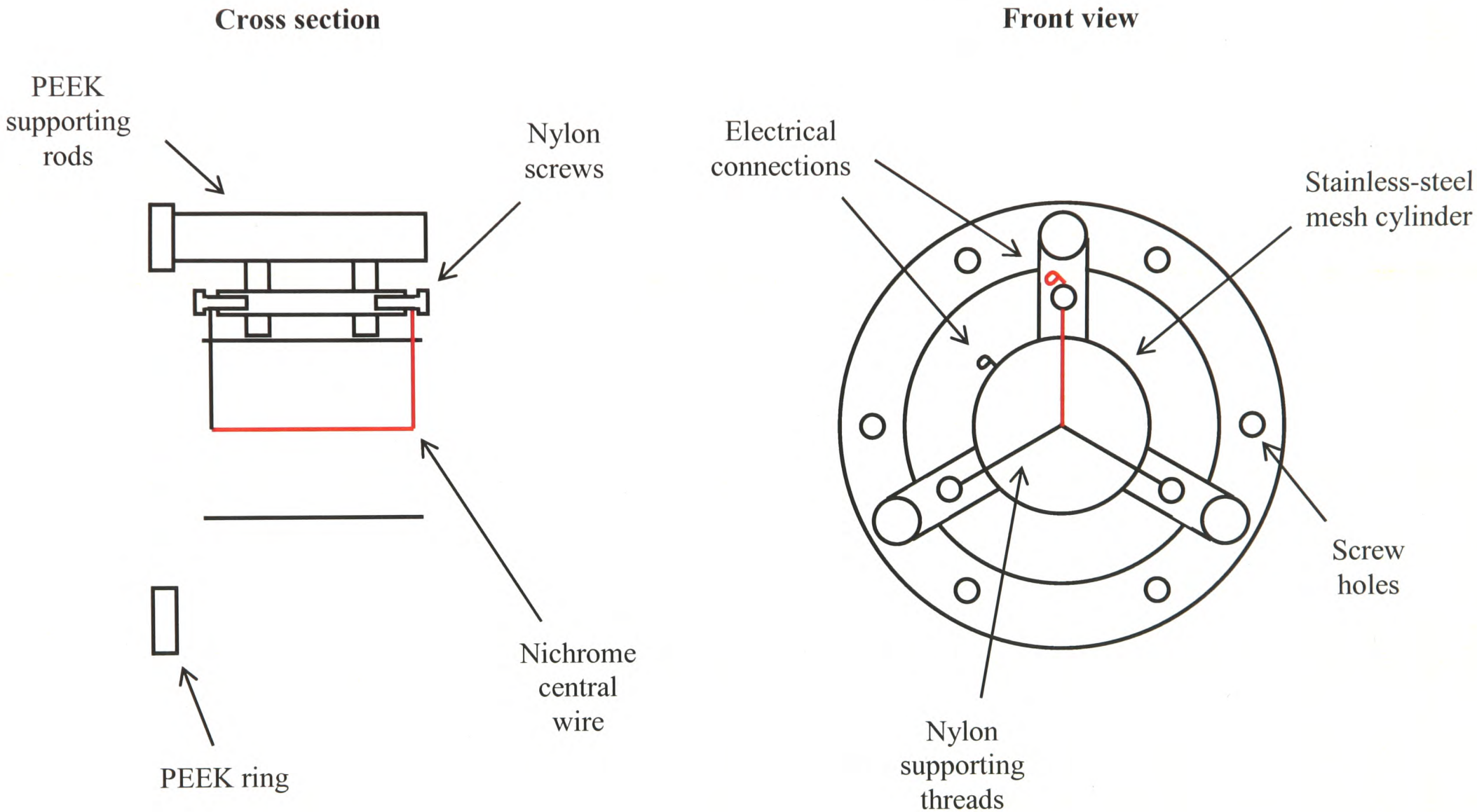

held in place by bolting the ring to the back-chamber opening. The length of the EIG was such that the ends were as close as possible to the pinhole and first element of the EI source (the filament plate), so that ions could be easily captured and passed to the filament plate. Electrical connections were made to the cylinder and central wire at the front of the EIG. A potential difference of up to 100 V was applied between the cylinder and wire. For positive ion transmission, the EIG cylinder should be more positive than the central wire.

The EI source, (see figure 7.1), was also used to focus the ions into the quadrupole. Voltages of up to ±100 V were applied to the individual elements. It was likely that only the voltage applied to the front element, the filament plate, would need to be changed from that used in EI mode. Once the external ions reached the ion region, they should be carried through by the same electric field used in EI mode.

7.3.3 Other experimental details

Ions were generated by passing helium (BOC, 99.996 %) and argon (BOC, 99.999 %) through the ion source. The gases flowed directly from the cylinders and through a series of purification traps (silica gel, diphosphorus pentoxide, and sodium and calcium aluminosilicate molecular sieve (4A, 5A and 13X) (all trap materials were supplied by BDH)). The gas flows were controlled by ~0.05 and ~2.5 SLPM ball-flow meters (Jencons RS1 and RS2) fitted with needle valves (Nupro). The backing pressures were monitored with a dial manometer (De Wit).

High-Q Heads 12 and E were used in the experiments. These units offered mass ranges of ~55 and ~300 amu respectively. However, the choice of High-Q Head was not an important consideration during this work because the DC supply was generally turned off so that the quadrupole did not function as a mass filter. Instead, the application of just the RF voltage converted the quadrupole into an ion guide that transported all masses to the detector.

The front of the CEM was held at approximately –2.5 kV. The signal was processed and then displayed on an oscilloscope (Tektronix 454). See chapter 5 for further details of the MS.

7.4 Ion-source performance

A great deal of time was spent adjusting the conditions in the source, and the ion sampling and focusing, but only ~50 counts per minute were observed (DC off). There were two possible explanations: either the source was not generating enough ions, or the ions were being incorrectly sampled and focused. To find the answer, it was decided to see if the ions could be detected externally to the MS, as a current on the pinhole.

The circuitry used to monitor the ion currents is shown in figure 7.3. A picoammeter (Keithley 480) was connected to the pinhole. The polarity of the ammeter was such that positive ions were measured as a negative current. A voltage of 100 V was applied to the cartridge using a simple battery pack and the pinhole was held at ground. Thus, positive ions were accelerated towards the pinhole.

Figure 7.3. The circuitry used to monitor ion currents on the MS pinhole.

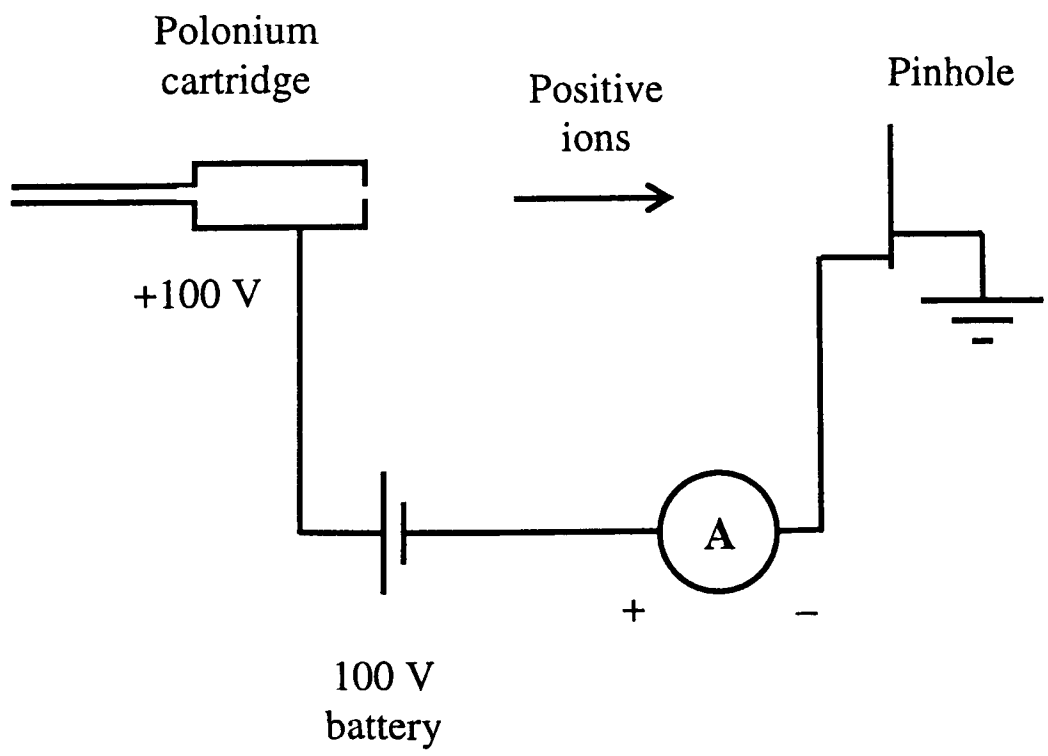

Initial experiments involved passing helium through the source at an FTP of ~5 Torr and an LFV of ~700 cm s^{-1}. Ion currents of about –20 pA were measured. Changing the flow of helium had a dramatic effect on the current and so it was decided to undertake a thorough investigation of the response of the ion source to different gas pressure and velocity conditions. The effect of adjusting the potential difference between the cartridge and the pinhole was also studied.

A few simple adaptations were made to the CI source in preparation for these experiments. The pinhole was replaced with a blank disc so that a wide pressure range could be investigated without damaging the turbomolecular pumps. A 1000 Torr capacitance manometer (Leybold CTR90 Ceravac) was attached to the flow tube to monitor the pressure.

7.4.1 The effect of potential difference

The voltage applied to the cartridge was varied from +100 V to –100 V with the blank pinhole held at ground. The resulting ion currents are shown in figure 7.4. Data were obtained at 50 and 100 Torr of helium and the LFV in both experiments was 34 cm s^{-1}.

As just discussed, when the cartridge was held at a positive voltage, cations were accelerated towards the blank pinhole and recorded as a negative current. Positive currents were also measured when the cartridge was held at negative voltages. The positive ions were attracted to the cartridge and thus, the current flowed in the opposite direction to that occurring when the cartridge was held at a positive voltage. The positive current could not be the result of a flow of negative ions towards the pinhole because helium does not form anions. However, impurities such as O_2 do, but the probability of O_2^- being generated in equal quantities to He^+, as required by the symmetrical nature of the positive and negative current curves in figure 7.4, is low. Furthermore, the rate of a termolecular process, such as the formation of O_2^-, increases with the square of the pressure (Wayne, 2000), and no such pressure dependence was observed.

Figure 7.4 shows that only a small potential difference of about 10 V was required to observe the ion current on the pinhole. The application of potential differences greater

than 20 V did not greatly increase the current. Thus, 10 – 20 V was sufficient to accelerate the ions towards the pinhole at the pressure and flow conditions employed. It can also be seen that the ion currents measured at 100 Torr were greater than those measured at 50 Torr — the effect of pressure is discussed in the next section.

Figure 7.4. Ion currents as a function of the voltage applied to the cartridge. The blank pinhole was held at ground. The LFV was 34 cm s^{-1}.

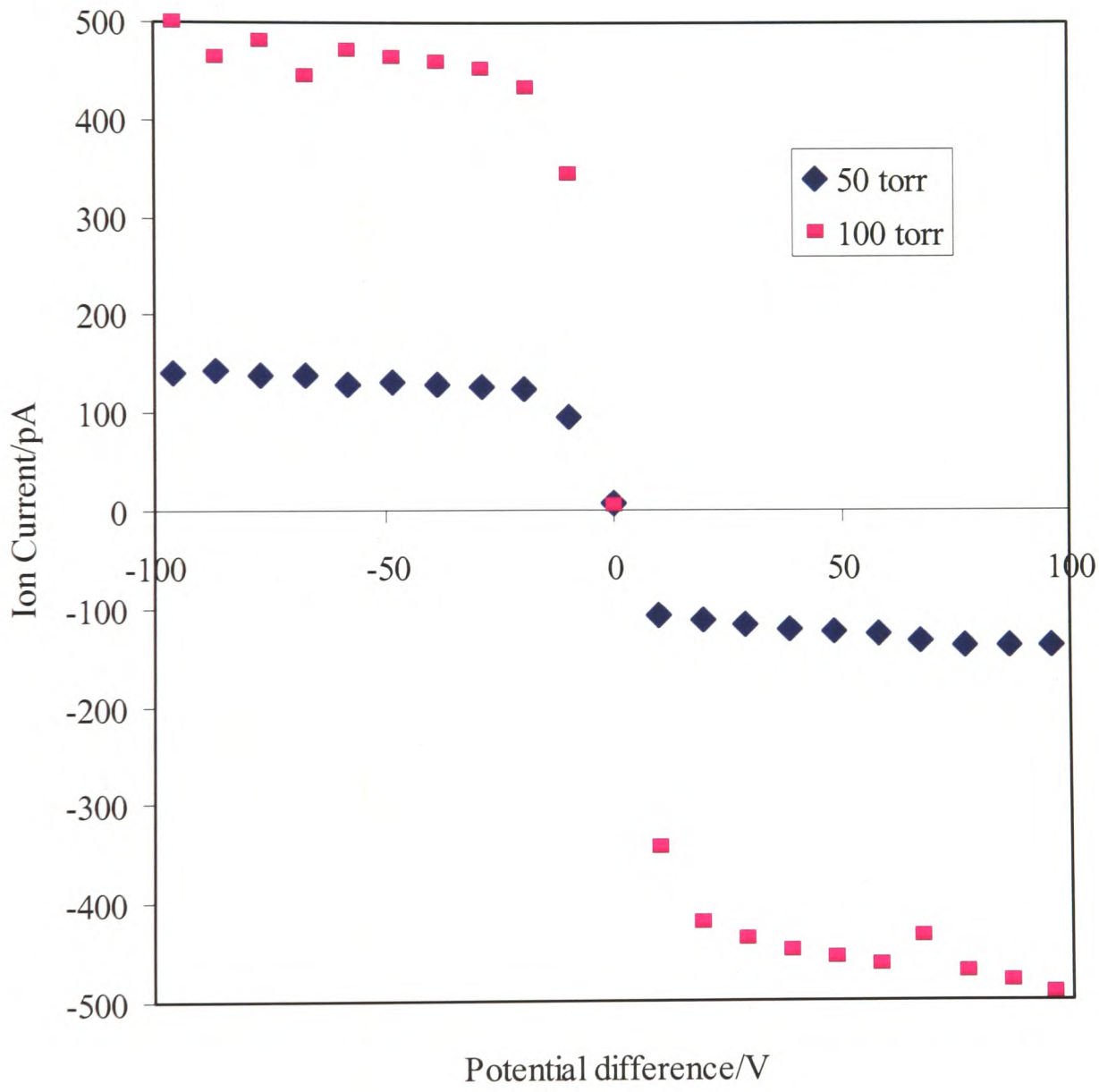

7.4.2 The effect of pressure

The ion currents measured on the blank pinhole for an FTP range of 0 – 430 Torr of He are shown in figure 7.5. Data were obtained for three different gas velocities. The voltage applied to the cartridge was either +100 V or –100 V and the pinhole was held at ground.

Figure 7.5. The ion currents measured on the blank pinhole as a function of flow-tube pressure.

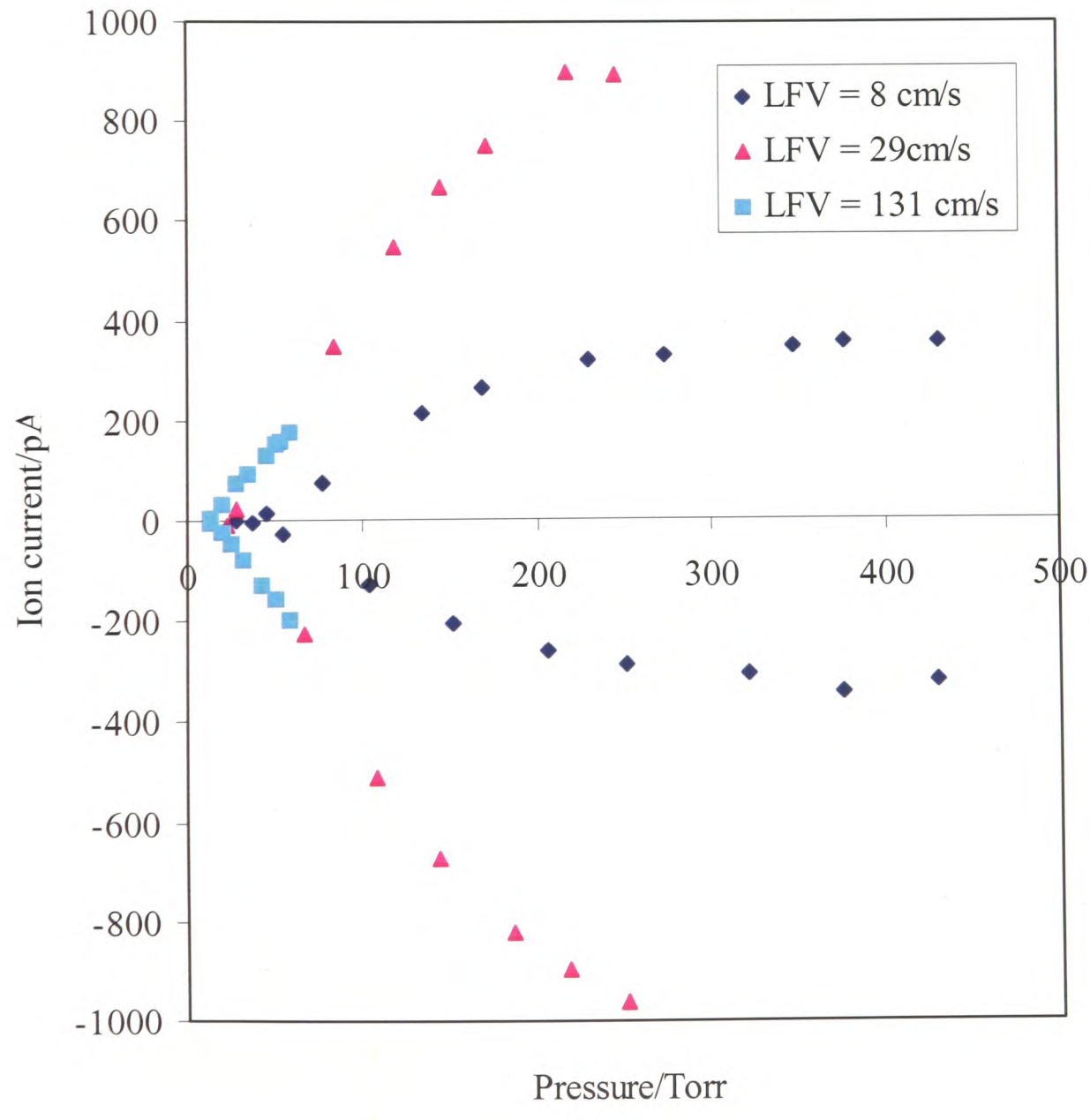

It can be seen that the ion current increased as the pressure was increased. This effect is a result of greater ion production rates at higher pressures owing to an increase in the number of collisions between alpha particles and helium atoms. Figure 7.5 also shows that the ion currents measured when the LFV was 29 cm s^{-1} were greater than those observed at 8 cm s^{-1}. It is anticipated that the largest ion currents would have been generated by employing high pressures at the fastest LFV tested, 131 cm s^{-1}. However, such conditions could not be attained with the pumping system employed.

7.4.3 The effect of LFV

The effect of LFV is better illustrated by figure 7.6. Data were obtained for several different pressures of helium. The voltage applied to the cartridge was either +100 V or −100 V and the blank pinhole was held at ground.

The ion current increased as the LFV was increased because reducing the time taken for the ions to travel from the source to the pinhole reduces the opportunity for wall losses to occur. It should be noted that the gas velocity has a particular importance with regard to the efficiency of cation transportation because the rate of wall loss is greater for positive ions than for neutral or negatively charged species (Smith and Adams, 1979). The phenomenon of ambipolar diffusion is responsible for this enhanced loss. The electrons produced in the ionization process are able to diffuse to the flow-tube walls much more quickly than atoms or molecules because of their small size. As the electrons crash out on the flow-tube glass a negative charge builds up, which attracts the positive ions and thus increases the number lost to the walls.

It can be seen that the curves in figure 7.6 reach a point where an increase in LFV no longer increases the ion current. A possible explanation is that the current is limited by the rate of ion production at the prevailing pressure. It can also be seen that the curves corresponding to 25 Torr are not symmetrical about the x axis. These data can be seen more clearly in figure 7.7, which also presents the measurements taken at 10 Torr. These lower pressures allowed the pumping system to produce much higher gas velocities. Figure 7.7 shows that the negative currents increase as the LFV is increased, whereas the positive currents do not respond in the same way. The current measured at 25 Torr

reaches a maximum at about 100 cm s^{-1} and the current measured at 10 Torr is extremely small. It is possible that the gas (ion) velocity in these experiments was large enough to overcome the attraction of the cations to the negatively biased cartridge and thus reduce the current flow.

Figure 7.6. The ion currents measured on the blank pinhole as a function of linear flow velocity.

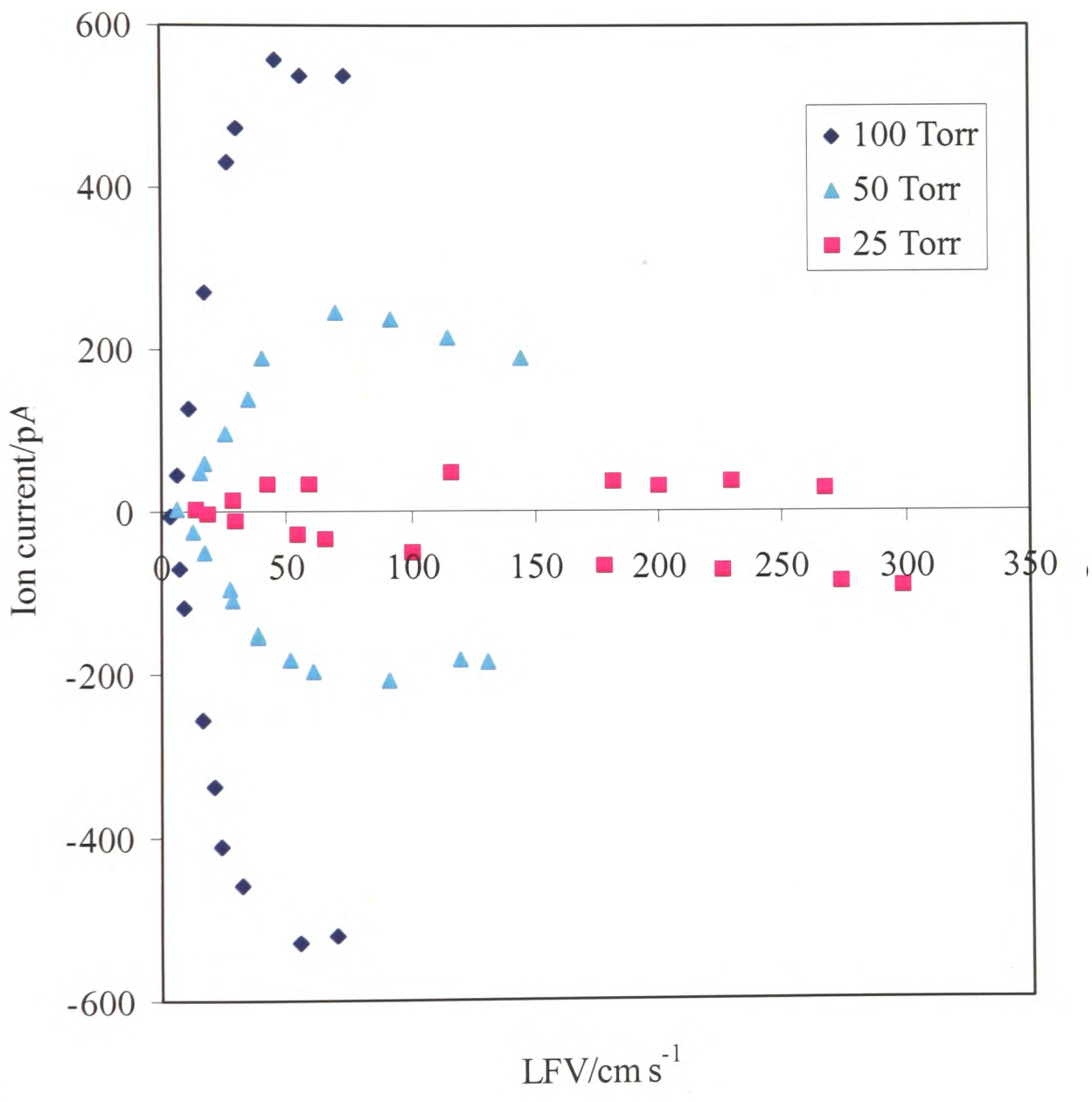

Figure 7.7 The ion currents measured on the blank pinhole as a function of linear flow velocity at 25 and 10 Torr.

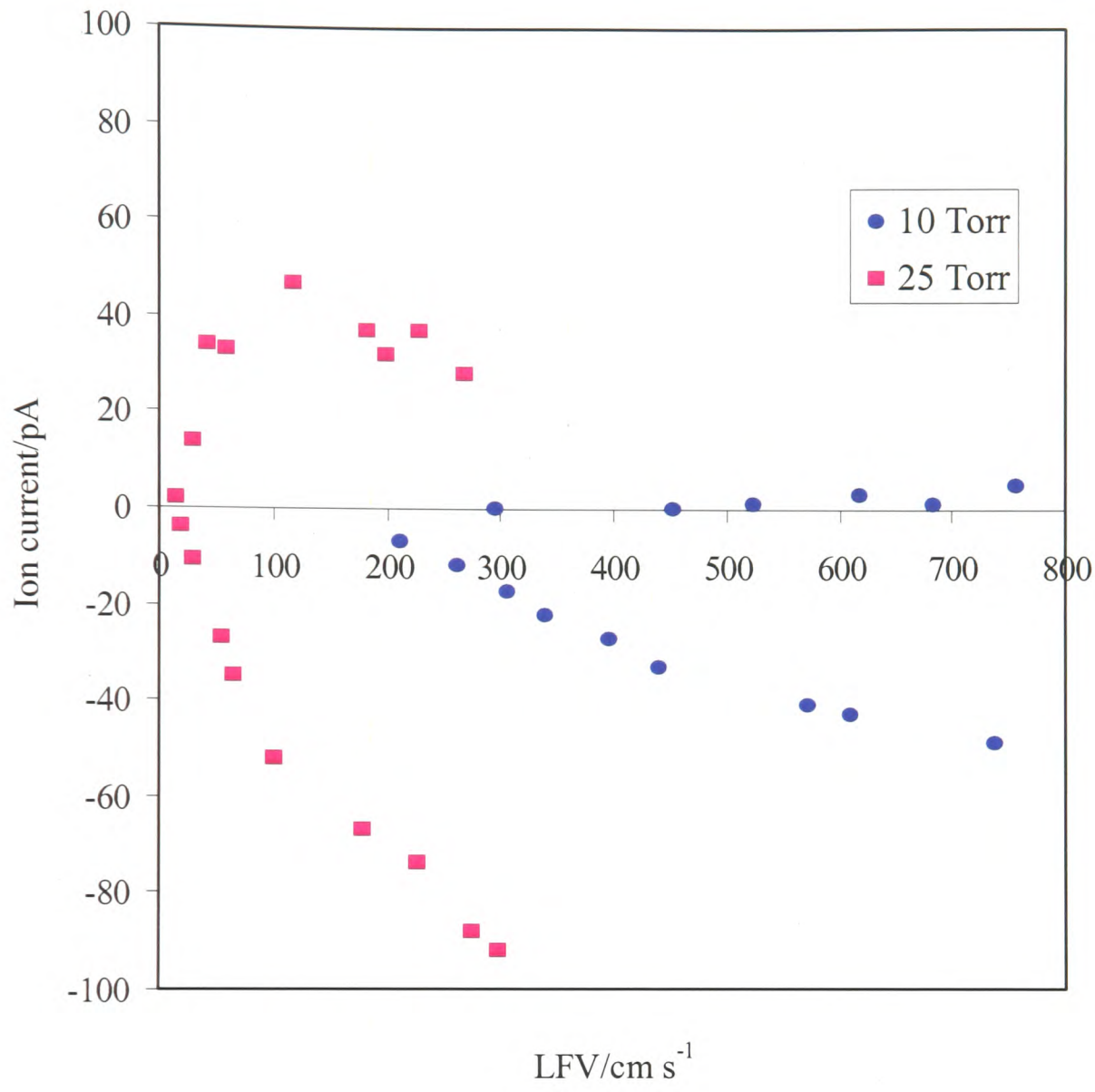

7.4.4 Discussion

The ion currents produced by the polonium cartridge were greatly affected by the operating conditions. A potential difference of up to 100 V between the cartridge and the pinhole, with the cartridge the more positive element, was seen to accelerate the ions towards the pinhole. In addition, a high LFV (strictly speaking, a short transportation time from the source) was shown to increase the number of ions reaching the pinhole. These conditions were in fact those employed when the CEM registered a signal (LFV ≈ 1000 cm s^{-1} (which equated to a transportation time of about 7 ms), FTP ≈ 1 Torr, polonium cartridge potential = +100 V and pinhole potential = 0 V). Previous discharge–

flow tube/CIMS investigations have employed potential differences of a similar magnitude and ion transportation times of a few milliseconds (e.g. see Jayne *et al.*, 1997 and Seeley *et al.*, 1996).

It was also shown that the ion production capacity of the polonium cartridge was severely limited by employing low pressures of gas. It was therefore possible that the FTP of 1 Torr was responsible for the low count rate. The ion source could have been adapted to operate at both high-pressure and high-LFV conditions, but such adaptations would have been expensive, as a bigger flow-tube pump and smaller pinholes would have been required. Furthermore, it was likely that such a design would be incompatible with the low-pressure flow tube for which the source was intended. It was decided to investigate alternative methods of generating ions, as it was possible that other ion sources would produce greater numbers of ions at low pressures. It should be noted incorrect sampling and focusing of the ions was also still a plausible explanation for the low count rate.

7.5 Alternative ion sources

The apparatus could be easily adapted to employ a discharge ion source. The polonium cartridge was removed and a microwave-discharge cavity was fitted to the gas inlet. Argon was passed through the cavity. The FTP was ~1 Torr and the LFV was about 1000 cm s^{-1}. A discharge was created when 40 W was applied to the cavity, using an EMS Microtron 200 microwave power supply.

The ion current was measured on the pinhole using the picoammeter. The pinhole was held at ground and 100 V was applied to a Cajon vacuum fitting just before the microwave cavity. Ion currents of about −0.6 μA were measured. Ions were also detected by the CEM but only when the EIG was employed. No signal was observed when the EIG was removed. About 20 counts s^{-1} were measured at m/z = 40 (Ar^+). It was necessary to apply a large positive potential, ~190 V, to the pinhole to observe these ions. The EIG central wire was held at ground and 10 V was applied to the mesh cylinder. The voltages applied to the EI source did not need to be greatly adjusted from those used to observe ions in EI mode.

7.6 Conclusions

This chapter describes the design and construction of an external ion source and an ion sampling and focusing system. The source that employed the polonium cartridge produced extremely small ion count rates. A thorough study of the effect of the operating conditions on the ion currents measured on the blank pinhole was undertaken. It was shown that the ion generation capability of the cartridge was severely limited at low pressures. As the discharge–flow tube was to be operated at such pressures, it was decided to investigate alternative ion sources.

A simple discharge source was constructed and briefly tested. Argon was passed through the discharge cavity at an FTP of ~1 Torr and an LFV of ~1000 cm s^{-1} to produce ion currents of about –0.6 μA. These currents were five orders of magnitude greater than those produced by the polonium source at similar operating conditions, (–20 pA was measured when helium was passed through the source at an FTP of ~5 Torr and an LFV of ~700 cm s^{-1}). A small signal, 10 – 20 count s^{-1}, was produced at m/z = 40 with the discharge source, which again was much larger than the ~50 count min^{-1} generated with the polonium cartridge, observed when the quadrupole DC voltage was turned off. It can be concluded that the discharge is the more appropriate ion source for low-pressure conditions. However, much work is required to improve the signal size.

One likely explanation for the low count rate is poor ion sampling and focusing. Both ion sources produced a great number of ions but they were not getting through to the CEM. Focusing may be less to blame because the EIG was shown to work — without it, no signal was observed with either source in place. Instead, it is possible that the ions were being lost in the sampling process. Indeed, a recent development in the ongoing CIMS project in Oxford has been the introduction of a stainless-steel cone, which has improved the count rate. Cones are preferable to pinholes because they project into the gas flow. Pinholes have a particular disadvantage in that a stagnant layer of gas can exist in front of the pinhole plate, which prevents ions from passing through the hole, (R. Burke, private communication, 2003). A cone with a molybdenum tip has also been constructed, as molybdenum has been shown to reduce ion-sampling losses, although the exact reason for

this phenomenon is not known (Smith and Adams, 1979). At the time this thesis was written, the Mo-tipped cone had not yet been tested.

Other recent developments in the laboratory have involved the testing of corona discharge and filament sources, and the introduction of a mesh cylinder in the mini flow tube to reduce wall losses. A small positive potential is applied to the mesh to repel positive ions and so combat the phenomenon of ambipolar diffusion. These improvements have resulted in an increase in signal size to 10^4 count s^{-1} (DC voltage on), although there have been problems with signal stability. Once this issue has been dealt with, the next stage of the project is to chemically ionize a species introduced downstream of the ion source.

7.7 References

- Bevilacqua, T. J., D. R. Hanson and C. J. Howard, *J. Phys. Chem.*, 1993, **97**, 3750
- Bondarenko, P. V. and R. D. Macfarlane, *Int. J. Mass Spectrom. Ion Processes*, 1997, **160**, 241
- Cerezo, A. and M. K. Miller, *Surface Science*, 1991, **246**, 450
- de Gouw, J. A. and C. J. Howard, *J. Phys. Chem. A*, 1997, **101**, 8662
- de Hoffmann, E. and V. Stroobant, *Mass Spectrometry, Principles and Applications*, 2nd Edition, John Wiley and Sons, England, 2002
- Eberhard, J., P. W. Villalta and C. J. Howard, *J. Phys. Chem.*, 1996, **100**, 993
- Eberhard, J. and C. J. Howard, *Int. J. Chem. Kinet*, 1996, **28**, 731
- Eberhard, J. and C. J. Howard, *J. Phys. Chem. A*, 1997, **101**, 3360
- Elrod, M. J., R. F. Meads, J. B. Lipson, J. V. Seeley and M. J. Molina, *J. Phys. Chem.*, 1996, **100**, 5808
- Elrod, M. J., D. A. Ranschaert and N. J. Schneider, *Int. J. Chem. Kinet*, 2001, **33**, 363
- Francisco, J. S. and J. W. Thomas Jr., *Chem. Phys. Letts.*, 1999, **300**, 553
- Froyd, K. D. and E. R. Lovejoy, *Int. J. Chem. Kinet*, 1999, **31**, 221
- Gleason, J. F., A. Sinha and C. J. Howard, *J. Phys. Chem.*, 1987, **91**, 719
- Jayne, J. T., U. Poschl, Y. Chen, D. Dai, L. T. Molina, D. R. Worsnop, C. E. Kolb and M. J. Molina, *J. Phys. Chem. A*, 1997, **101**, 10000
- Lovejoy, E. R., T. P. Murrells, A. R. Ravishankara and C. J. Howard, *J. Phys. Chem.*, 1990, **94**, 2386

- Moise, T., W. Denzer and Y. Rudich, *J. Phys. Chem. A*, 1999, **103**, 6766
- *NIST Standard Reference Database*, Number 69, NIST, 2001, (http://webbook.nist.gov/chemistry)
- Percival, C. J., G. D. Smith, L. T. Molina and M. J. Molina, *J. Phys. Chem. A*, 1997, **101**, 8830
- Ranschaert, D. L., N. J. Schneider and M. J. Elrod, *J. Phys. Chem. A*, 2000, **104**, 5758
- Scholtens, K. W., B. M. Messer, C. D. Cappa and M. J. Elrod, *J. Phys. Chem. A*, 1999, **103**, 4378
- Seeley, J. V., R. F. Meads, M. J. Elrod and M. J. Molina, *J. Phys. Chem.*, 1996, **100**, 4026
- Smith, D. and N. G. Adams, in *Gas Phase Ion Chemistry*, ed. M. T. Bowers, Academic Press, New York, 1979
- Suh, I. And R. Zhang, *J. Phys. Chem. A*, 2000, **104**, 6590
- Turnipseed, A. A., S. B. Barone, N. R. Jensen, D. R. Hanson, C. J. Howard and A. R. Ravishankara, *J. Phys. Chem.*, 1995, **99**, 6000
- Villalta, P. W., L. G. Huey and C. J. Carleton, *J. Phys. Chem.*, 1995, **99**, 12829
- Villalta, P. W. and C. J. Howard, *J. Phys. Chem.*, 1996, **100**, 13624
- Wayne, R. P., *Chemistry of Atmospheres*, Oxford University Press, Oxford, 2000
- Zhang, R., L. T. Molina and M. J. Molina, *Rev. Sci. Instrum.*, 1998, **69**, 4002
- Zhang, R., W. Lei, L. T. Molina and M. J. Molina, *Int. J. Mass Spectrom.*, 2000, **194**, 41
- Zhang, D., R. Zhang, C. Church and S. W. North, *Chem. Phys. Letts.*, 2001, **343**, 49

Appendix I The purification of materials and preparation of gaseous mixtures

In experiments such as those described in this thesis, it is necessary to employ gases that are as pure as possible to minimise the extent of side reactions that could interfere with the chemistry of interest. As such, the gases used were purchased in the purest form permitted by budget constraints and then a variety of techniques were used to purify them further. These methods are described below.

If a large quantity of gas was required, as was the case for helium when it was used as a carrier gas, it was delivered directly from the cylinder to the flow tube. The gas was purified by passing it through a series of traps containing sodium and calcium aluminosilicate molecular sieve cooled with liquid nitrogen, and silica gel and diphosphorus pentoxide, which removed H_2O, CO_2 and hydrocarbons. All trap materials were supplied by BDH. If only small quantities of gas were needed, as was typical of most of the reactants used in the experiments, mixtures of the gas were prepared and stored in 6 L pyrex bulbs. An inert gas, generally helium, was used to dilute the reactant. The concentration of the mixture was selected to provide the quantity desired in the flow tube. The mixture was delivered to the flow tube from the bulb. The methods for preparing these mixtures are now described.

The storage bulb was attached to a gas-handling manifold, which was constructed from pyrex. The manifold and bulb were evacuated with a small rotary pump. The vacuum was monitored with a Pirani gauge (Edwards PRM10). A small quantity of the reactant was admitted to the manifold. Gaseous species could be admitted directly from the cylinder *via* a port on the manifold. Liquid and solid reactants were placed in a small trap, which could be attached to the manifold, and then gently heated to generate the gaseous form. The gas was then purified by the freeze-pump-thaw technique: the gas was frozen down into a manifold trap cooled with liquid nitrogen, the manifold was pumped upon to remove any species that had not solidified, and then the reactant was gently heated to once more form a gas. Several freeze-pump-thaw cycles could be performed.

A capacitance manometer (MKS Baratron Type 626A or Leybold CTR90 Ceravac) of the appropriate range was used to measure out the required quantity of reactant. Helium, purified in the manner previously described, was added to the reactant to achieve the required concentration. The gaseous mixtures were allowed to mix for at least two hours before being used in an experiment.

It should be noted that the gases employed in resonance-fluorescence lamps were purified and prepared by similar methods.

Appendix II An example of an input file, executable in a FACSIMILE parameter-fitting model, designed to quantify processes other than the self-reaction of IO that contributed to the loss of the radical in the discharge-flow tube

```
* Generated by FACSIMILE Reaction Wizard -
Tuesday, June 03, 2003 ;

EXECUTE ;
OPEN 8 "C:\kirsteniodinefitting_calc.out";
OPEN 9 "C:\kirsteniodinefitting_resid.out";
OPEN 10 "C:\kirsteniodinefitting_plot.out";
**;


PARAMETER
 K1f  9.3e-11  K2f  60
;

VARIABLE
IO       products1 products2
;

INTEGER #COUNT ;

COMPILE INITIAL;
IO = 2.6e11 ;
**;

COMPILE EQUATIONS ;
% K1f  : IO + IO = products1;
% K2f  : IO = products2;
**;

SETPSTREAM 1 8;
**;
SETPSTREAM 2 9;
**;

DATA 0.1 ;
TIME IO ;
RANGE  1.957E+11 ;
 0.004 1.957e11 ;
 0.006 1.729e11 ;
```

```
0.008 1.316e11 ;
0.011 1.066e11 ;
0.013 8.481e10 ;
0.016 7.176e10 ;
0.018 5.980e10 ;
0.021 4.893e10 ;

**;
SETVARY K2f ;
BEGIN;
COMPILE INSTANT ;
WRITE 1=10, " PRINT STREAM NO. " % ;
WRITE 2=10, "TIME IO IO(obs) " % ;
#COUNT=0;
**;
COMPILE PRINT;
* Output routine called during the final phase;
#COUNT=#COUNT+1;
DO 10 FOR #2=#COUNT-1 ;
WRITE 1=10, ((E14,6))TIME, IO, VOBS<0,#2> ;
LABEL 10;
**;
SETNOFIT;
WHENEVER TIME = TOBS % CALL PRINT;
**;

BEGIN;
STOP;
```

Appendix III An example of an input file, executable in a FACSIMILE parameter-fitting model, designed to quantify secondary chemistry in a study of the reaction of Cl atoms with acetone

```
* Generated by FACSIMILE Reaction Wizard -
Wednesday, April 09, 2003 ;

EXECUTE ;
OPEN 8 "C:\highcllplusacetone1_calc.out";
OPEN 9 "C:\highcllplusacetone1_resid.out";
OPEN 10 "C:\highcllplusacetone1_plot.out";
**;


PARAMETER
 K1f  2.47e-12    K2f  1e-11
;

VARIABLE
CH3COCH2  CH3COCH3  Cl      HCl      products
;

INTEGER #COUNT ;

COMPILE INITIAL;
CH3COCH3 = 6.030e12 ;
Cl = 3.564e11 ;
**;

COMPILE EQUATIONS ;
% K1f  : Cl  + CH3COCH3 = HCl + CH3COCH2;
% K2f  : Cl + CH3COCH2 = products;
**;

SETPSTREAM 1 8;
**;
SETPSTREAM 2 9;
**;

DATA 0.1 ;
TIME Cl ;
RANGE  3.564E+11 ;
 0 3.564e11 ;
```

```
0.0084 3.080e11 ;
0.0123 2.905e11 ;
0.0172 2.703e11 ;
0.0237 2.327e11 ;
0.0333 1.856e11 ;

**;

SETVARY K2f ;
BEGIN;
COMPILE INSTANT ;
WRITE 1=10, " PRINT STREAM NO. " % ;
WRITE 2=10, "TIME Cl Cl(obs) " % ;
#COUNT=0;
**;
COMPILE PRINT;
* Output routine called during the final phase;
#COUNT=#COUNT+1;
DO 10 FOR #2=#COUNT-1 ;
WRITE 1=10, ((E14,6))TIME, Cl, VOBS<0,#2> ;
LABEL 10;
**;
SETNOFIT;
WHENEVER TIME = TOBS % CALL PRINT;
**;

BEGIN;
STOP;
```

Appendix IV An example of an input file, executable in a FACSIMILE simulation model, which describes the acetonylperoxy radical self-reaction and subsequent chemistry

```
* Generated by FACSIMILE Reaction Wizard -
Friday, March 14, 2003 ;

EXECUTE OPEN 8 "C:\EIMS.out";


PARAMETER
K79a 1.35e-10 K710 1.45e-12 K71a 6e-12 K71b 2e-12
K73 2e-12 K74a 1e-11 K74b 1e-12 K711 1.6e-11 K75 6e-14
K76a 1.1e-12 K76b 1.4e-12 K76c 1.4e-12 K713a 1.2e-11
K713b 1.2e-12 K714a 1.6e-13 K714b 3.2e-13 K77 1.9e-15
;

PERMIT +- ;
VARIABLE
CH3    CH3CO   CH3COCH2  CH3COCH2O2  CH3COCH2OH  CH3COCH3
CH3COCHO CH3COO2 CH3COOH CH3O   CH3O2   CH3OH   CO2
F      HCHO    HF      O2          HO2
;

COMPILE INSTANT;
CH3COCH3 = 5e13 ;
F = 5e12 ;
O2 = 1e15 ;
**;

COMPILE EQUATIONS ;
% K79a  : CH3COCH3 + F = CH3COCH2 + HF;
% K710  : CH3COCH2 + O2 = CH3COCH2O2;
% K71a  : CH3COCH2O2 + CH3COCH2O2 = CH3CO + CH3CO + HCHO + HCHO +
O2;
% K71b  : CH3COCH2O2 + CH3COCH2O2 = CH3COCHO + CH3COCH2OH + O2;
% K73  : CH3CO + O2 = CH3COO2;
% K74a  : CH3COCH2O2 + CH3COO2 = CH3CO + HCHO + CH3 + CO2 + O2;
% K74b  : CH3COCH2O2 + CH3COO2 = CH3COCHO + CH3COOH + O2;
% K711  : CH3COO2 + CH3COO2 = CH3 + CH3 + CO2 + CO2 + O2;
% K75  : CH3 + O2 = CH3O2;
% K76a  : CH3COCH2O2 + CH3O2 = CH3CO + CH3CO + HCHO + O2;
% K76b  : CH3COCH2O2 + CH3O2 = CH3COCH2OH + HCHO + O2;
% K76c  : CH3COCH2O2 + CH3O2 = CH3COCHO + CH3OH + O2;
% K713a  : CH3COO2 + CH3O2 = CH3 + CO2 + CH3O + O2;
```

```
% K713b  : CH3COO2 + CH3O2 = CH3COOH + HCHO + O2;
% K714a  : CH3O2 + CH3O2 = CH3O + CH3O + O2;
% K714b  : CH3O2 + CH3O2 = CH3OH + HCHO + O2;
% K77  : CH3O + O2 = HCHO + HO2;
**;

SETPSTREAM 1 8 ;
TIME          CH3     CH3CO    CH3COCH2  CH3COCH2O2 CH3COCH2OH
CH3COCH3   CH3COCHO CH3COO2  CH3COOH  CH3O     CH3O2
CH3OH     CO2         F       HCHO    HF      O2     HO2      ;
**;

COMPILE OUT ;
PSTREAM 1 ;
**;

WHENEVER TIME=
101 * (+0.0005) 0  %
CALL OUT;
**;

BEGIN;
STOP;
```